Aspects of neutrino flavor propagation in binary neutron star merger remnants

Inauguraldissertation

zur

Erlangung der Würde eines Doktors der Philosophie
vorgelegt der
Philosophisch-Naturwissenschaftlichen Fakultät
der Universität Basel

von

Maik Uwe Frensel

aus Schopfheim (Deutschland) und Liesberg (BL)

Basel, 2017

Genehmigt von der Philosophisch-Naturwissenschaftlichen Fakultät
auf Antrag von

Prof. Dr. Friedrich-Karl Thielemann
Fakultätsverantwortlicher

Dr. Cristina Volpe
Korreferentin

Basel, den 13.12.2016

Prof. Dr. Jörg Schibler
(Dekan)

Für meine Grosseltern.

Table of Contents

Abstract

In this thesis we study the neutrino flavor evolution in the neutrino-driven wind from a binary neutron star merger remnant consisting of a massive neutron star surrounded by an accretion disk. With the neutrino emission characteristics and the hydrodynamical profile of the remnant consistently extracted from a three-dimensional simulation, we compute the flavor evolution by taking into account neutrino coherent forward scattering off ordinary matter and neutrinos themselves. We employ a "single-trajectory" approach to investigate the dependence of the flavor evolution on the neutrino emission location and angle. We also show that the flavor conversion in the merger remnant can affect the (anti)neutrino absorption rates on free nucleons and may thus impact the r-process nucleosynthesis in the wind. We discuss the sensitivity of such results on the change of neutrino emission characteristics, also from different neutron star merger simulations. Furthermore, we discuss the adiabaticity of the evolution, compare two- and three-flavor calculations, and present a first investigation of CP violation.

Overview

> *[...] es könnten elektrisch neutrale Teilchen, die ich Neutronen nennen will, in den Kernen existieren, welche den Spin 1/2 haben und das Ausschliessungs-prinzip befolgen*
>
> WOLFGANG PAULI
> Open letter to the group of radioactive people
> at the Gauverein meeting in Tübingen (1930)

1.1 A brief note on history

In 1930, it was Wolfgang Pauli who raised the hypothesis that neutrinos[1] - electrically neutral, spin-$\frac{1}{2}$ particles obeying the exclusion principle, could exist. By introducing such particles he tried to save fundamental conservation laws, which seemed to be violated in nuclear beta-decay processes: It turned out that the thereby produced electrons possess a continuous energy spectrum, which was different from what one was expecting from two-body kinematics provided that the conservation of energy and linear momentum holds. With the introduction of the neutrino, these laws could be rescued, however in the physics community, this idea was received with skepticism. Nevertheless, in 1934 Enrico Fermi introduced a theory of beta-decay in which the interaction is expressed as the product of four spinor fields and he incorporated Pauli's proposed neutrino. Today we know that this Fermi theory manifest itself as a low energy limit of the weak interaction.

However, the neutrino remained a hypothetical particle until Cowan and Reines [2] provided the first experimental evidence for neutrinos, or to be more precise, for electron antineutrinos in their project "poltergeist" in 1956 through the observation of inverse beta-decay processes. Later, in 1962, Lederman, Schwartz and Steinberger discovered the muon neutrino in pion-decay processes [3].

In 1969, Davis detected neutrinos from the Sun and recognized that the solar neutrino flux is too small compared to what was expected from standard solar model predictions. Several subsequent experiments confirmed this so-called "solar neutrino problem" [4].

The existence of the tau neutrino was conjectured with the discovery of the tau lepton by Perl

---

[1] Actually he called them neutrons, which were not yet discovered by James Chadwick at that time. Later, the term "neutrino" was actually coined by Edoardo Amaldi who used this name humorously during a discussion with Enrico Fermi in order to distinguish it from Chadwick's neutron. As noted in [1], the word "neutrino" is a contraction (though grammatically incorrect) of the Italian word "neutronino", which is in turn the diminutive of neutron. Ultimately, it was Fermi who made it popular by using it at conferences in 1932 and 1933 (see footnote 277 in [1]). Also Pauli adopted this terminology.

in 1976, but the first direct evidence was provided by the DONUT Collaboration in 2000. In 1987, the first detection of supernova neutrinos by the Kamiokande Collaboration was a milestone and triggered a huge torrent of research activities in the astro- and particle physics community.

Besides the fact that neutrinos exist in (at least) three flavors, they have the peculiar property to actually change their flavor. Already in 1957 Bruno Pontecorvo mentioned for the first time the possible existence of neutrino-antineutrino conversions in close analogy to K^0-$\bar{K}^0$ oscillations [5, 6]. Since at that time only the electron flavor was known, he considered only the possibility of $\nu_e \leftrightarrow \bar{\nu}_e$ oscillations[2]. Shortly after the existence of the muon neutrino was established, Maki, Nakagawa and Sakata [7] introduced the concept of flavor mixing in 1962 and outlined the possibility of $\nu_e \leftrightarrow \nu_\mu$ and $\bar{\nu}_e \leftrightarrow \bar{\nu}_\mu$ oscillations[3,4]. Independently from Maki et al., though a few years later (1967), Pontecorvo also considered $\nu_e \leftrightarrow \nu_\mu$ oscillations and proposed the Sun as "the ideal object" for observations. In the same work he discussed transitions of the form $\nu_{\alpha,\mathrm{L}} \leftrightarrows \bar{\nu}_{\alpha,\mathrm{L}}$ ($\alpha = e, \mu$) and introduced the notion of "sterile" neutrinos. Probably the first modern treatment was provided by Gribov and Pontecorvo in 1969 [9]. Many subsequent papers advanced the idea of flavor mixing and oscillations with important phenomenological consequences for particle-/astrophysics and cosmology. Some of the more recent developments contributing to this field are subject of this work. Here, we will focus on the study of the neutrino flavor evolution in an astrophysical setting, namely binary neutron star mergers, which we will describe briefly in the following section.

1.2 Binary neutron star mergers

If in a binary system, consisting of two massive stars, both stars undergo supernova explosions, the outcome will be a binary system of compact objects. Each of the latter can be a neutron star or a black hole and both rotate around the center of mass of the system.

The total orbital energy $E_{\mathrm{orb}} = -GM_1M_2/(2a)$ (including kinetic and potential energies), where G denotes the gravitational constant, M_1 and M_2 the masses of both compact objects[5], and a the orbital radius (here the "semi-major axis"[6]), is reduced due to emission of gravitational waves[7] which carry away energy and angular momentum from the binary system. This will decrease the spatial separation of both objects and therefore increase the frequency $\omega_{\mathrm{orb}} = \sqrt{GM/a^3}$ (Kepler's third law, where $M = M_1 + M_2$) of their orbital motion. This

---

[2] In fact, in his 1958 paper [6], Pontecorvo considered neutrinos and antineutrinos, produced in weak interaction processes, as linear combinations of two Majorana neutrinos (ν_1^{M} and ν_2^{M}): $\nu = (\nu_1^{\mathrm{M}} + \nu_2^{\mathrm{M}})/\sqrt{2}$, $\bar{\nu} = (\bar{\nu}_1^{\mathrm{M}} - \bar{\nu}_2^{\mathrm{M}})/\sqrt{2}$.

[3] which the authors called "virtual transmutations".

[4] It should be noted that in the same year (1962), but shortly prior to the work of Maki et al., Katayama, Matsumoto, Tanaka and Yamada also introduced two-flavor mixing [8].

[5] Note that in our discussion, we treat both masses as point-like, i.e., we neglect any possible impact from their internal structure, in order to give some rough estimates.

[6] Here we considered a circular orbit, but for elliptical orbits also the eccentricity e will change as the system evolves. However, the eccentricity will decrease when the compact objects approach each other and the orbits become almost circular $e = 0$.

[7] which are predicted by Einstein's theory of general relativity.

process, in turn, will boost the gravitational wave emission even more until both objects finally merge.

An estimate for the inspiral time until coalescence for circular ($e = 0$) and elliptical orbits ($0 < e < 1$) is given by [10]

$$\tau_{\text{coal}} \simeq 9.83 \times 10^6 \text{ years} \left(\frac{T_0}{1 \text{ hour}}\right)^{8/3} \left(\frac{\mathcal{M}_\odot}{M}\right)^{2/3} \left(\frac{\mathcal{M}_\odot}{\mu}\right)(1 - e^2)^{7/2}, \tag{1.1}$$

where $T_{\text{orb}} = 2\pi/\omega_{\text{orb}}$ denotes the initial orbital period, $\mu = M_1 M_2/(M_1 + M_2)$ the reduced mass, e the initial eccentricity, and $\mathcal{M}_\odot \simeq 1.99 \times 10^{33}$ g corresponds to the mass of the sun. For a binary on a circular orbit ($e = 0$) with $M_1 = M_2 = 1.4\,\mathcal{M}_\odot$ and $T_0 = 8$ hours we have $\tau_{\text{coal}} \sim \mathcal{O}(10^9)$ years while for a binary with the same parameters, but on an elliptical orbit with $e = 0.99$ the time until coalescence is substantially reduced: $\tau_{\text{coal}} \sim \mathcal{O}(10^3)$ years. Remarkably, if the compact objects (with both $1.4\,\mathcal{M}_\odot$) are separated by 100 km, their orbital period is $T_{\text{orb}} \simeq 0.01$ s and it will take only 0.34 s until they merge.

The GW frequency can approximately be written in the form [10]:

$$f_{\text{GW}}(\tau_{\text{coal}}) \simeq 134 \text{ Hz} \left(\frac{1.2\,\mathcal{M}_\odot}{\mathcal{M}_c}\right)^{5/8} \left(\frac{1 \text{ s}}{\tau_{\text{coal}}}\right)^{3/8}, \tag{1.2}$$

where we introduced the chirp mass $\mathcal{M}_c := \mu^{3/5} M^{2/5}$ and $\mathcal{M}_c \approx 1.2\,\mathcal{M}_\odot$ corresponds to a $2 \times 1.4\,\mathcal{M}_\odot$ binary. This means that at $f_{\text{GW}} \simeq 10$ Hz we would measure waves at $\tau_{\text{coal}} \simeq 17$ min and at 1 kHz waves at $\tau_{\text{coal}} \simeq 5$ms. From Kepler's third law, we can find the separation of the compact objects: In case of a $2 \times 1.4\,\mathcal{M}_\odot$ binary, the objects would be separated by a distance of $\simeq 34$ km. Note that here we used the relation $\omega_{\text{GW}} = 2\omega_{\text{orb}}$ which holds for circular orbits [10]. The frequency and amplitude of GWs will increase until coalescence. Note that current Earth-based interferometers like Advanced LIGO [11] are sensitive to frequencies between 10 Hz and 7 kHz. Also Advanced Virgo [12] will have a similar range (10 Hz - 10 kHz). In the future, space-based detectors like eLISA (Evolved Laser Interferometer Space Antenna) [13] would have access to very low frequencies ranging from 0.1 mHz to 1 Hz at redshifts of $z = 15$.

Key quantities that determine the evolution of a compact object merger, are the ratio of the initial masses, the equation of state and the total mass of both binaries just before the end of the merger phase. After the compact objects finally merged, the system can either directly collapse to a black hole or find itself in a quasi-stable configuration (on dynamical timescales), but can lose stability on longer timescales which are determined by processes like magnetic fields or gravitational wave emission leading to a reduction of angular-momentum which is necessary for the stability. In the latter case, we expect the formation of a massive neutron star (MNS) if the sum of both NS masses does not exceed a certain threshold which depends on the equation of state (EOS). We use the term "MNS" to collectively refer to supra- and hypermassive neutron stars [14]. For the numerical studies presented in this work it does not

matter if we have a supra- or hypermassive NS. What we need in this work, is just a central compact object surrounded by a disk.

Roughly speaking, only 3 out of 10 binary neutron star systems are expected to directly collapse to a black hole[8] [15]. Note that the period until a black hole forms has rich phenomenological consequences e.g., for the launch of short gamma ray bursts (sGRB) or the neutrino-driven wind that eventually forms, and the subsequent nucleosynthesis. In addition, if a MNS is present for a sufficiently long time, it could produce radiative signatures and can contribute to cosmic rays [15]. In both cases, prompt or delayed collapse, the central object accretes the disrupted neutron star matter that is floating around. However, this will usually not happen immediately, since the matter has still some angular momentum left. Instead a disk (torus) forms around the central object. In figure 1.1 we show schematically different evolution phases of a compact object merger.
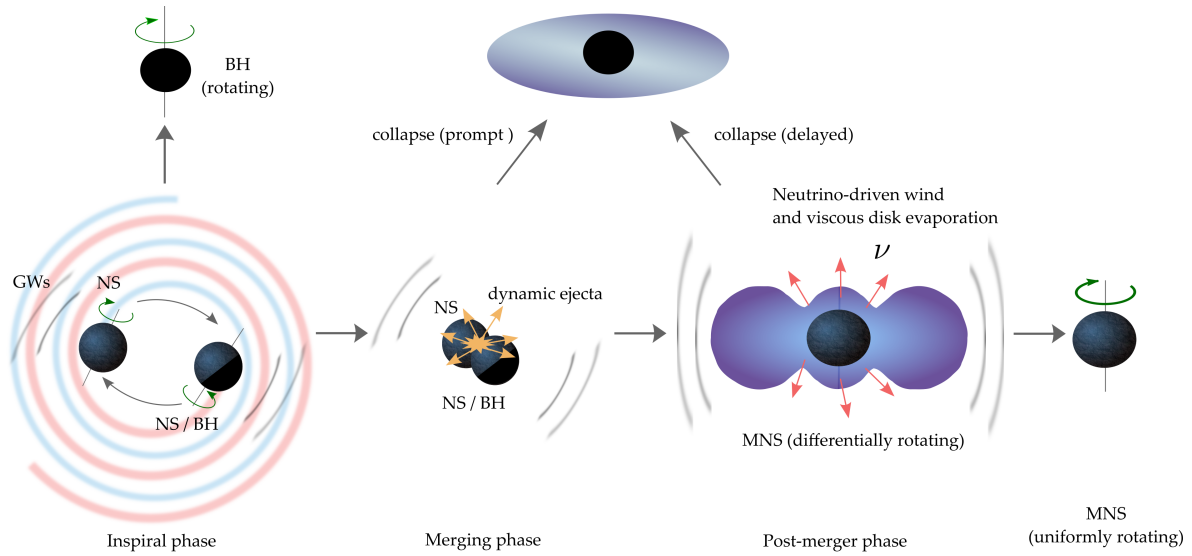
Figure 1.1.: Evolution phases of a compact object merger with either two neutron stars or a neutron star and a black hole.

Another scenario, which we will not discuss in this work, but on which we are going to comment on briefly is the merger of a neutron star and a black hole (NS-BH). Starting from a NS-BH system, there are two possibilities how it can evolve[9]: If the BH is sufficiently more massive than the NS, the BH can "consume" the NS without tidal disruption [16]. Because this scenario does neither produce an outflow nor an accretion disk, it is less interesting for our studies. If, however, the BH is sufficiently small compared to the mass of the NS or if the NS radius is sufficiently large, the NS will be destroyed and the matter will be swallowed by the BH. The resulting system consists of a BH surrounded by an accretion disk.

---

[8] Indeed, this provides only a rough estimate, since there are large uncertainties with respect to the binary neutron star masses.
[9] The outcome is mainly determined by the masses M_{NS} and M_{BH}, the BH spin, and the NS compactness M_{NS}/R_{NS} [16].

Due to their neutron richness, neutron star mergers are expected to provide the right thermodynamical conditions to allow the formation of heavy elements and are considered as a likely site for the rapid neutron capture process (*r*-process). As candidates, they were proposed in e.g., [17–20]. On the other hand, BNS mergers could be useful to infer information about the structure of neutron stars (e.g., EOS or NS radius [21]) by studying the gravitational wave shapes from the inspiral and merger phases. Typical frequencies are above 1 kHz which makes a detection rather difficult. Also note that BNS systems are expected to occur much less frequent than other scenarios, since they are the result of a binary star system that experienced two supernova explosions.

Since observational data is limited, we need to rely on numerical simulations. The latter are computationally demanding so that simplifications are necessary. For example, the neutrino transport has to be simplified, or only a certain part of the space-time domain can be studied with the currently available computational resources.

With respect to observations, a complementary measurement of a gravitational wave signal and electromagnetic counterparts (GRBs, kilonova/macronova[10]) can provide valuable information: It is necessary for identifying the source of gravitational waves [16] and we can infer information about the amount of *r*-process elements from the brightness of the kilonova/macronova [24].

In this work, we will use the detailed simulations of [25] as a basis for studying the neutrino flavor evolution in a BNS merger remnant consisting of a MNS and an accretion disk accompanied by the neutrino-driven wind.

1.3 Outline

The thesis is organized as follows. In Chapter 2 we will review some general aspects on neutrino flavor mixing and how the Standard Model of Particle Physics can be extended in order to account for massive neutrinos. Neutrino oscillations in vacuum and in ordinary matter are discussed. We comment on the current status and open issues. Furthermore, the mechanism behind adiabatic flavor transformation through the MSW effect is introduced and the neutrino flavor isospin formalism is employed. In Chapter 3, we will extend our discussion and include so-called neutrino self-interactions, i.e., we study coherent neutrino forward scattering off neutrinos themselves. We describe typical assumptions and follow a mean-field approach. In the context of neutrino self-interactions, collective effects are discussed and applications to core-collapse supernovae are shown for illustrative purposes. Some key aspects of matter-neutrino resonances are discussed within toy models using the framework of the neutrino flavor isospin. In Chapter 4, we investigate the trajectory dependence of the neutrino flavor evolution in binary neutron star merger remnants using matter profiles obtained from state-of-the-art hydrodynamical simulations. We discuss uncertainties in the

---

[10] A kilonova [22] (or macronova [23]) represents an electromagnetic transient in the optical and near-infrared bands originating from the radioactive decay of heavy elements that are produced in the neutron-rich ejecta of the merger due to the *r*-process.

emission parameters and review the employed assumptions. Beside calculations with three flavor neutrinos we show results obtained with a two-flavor approximation and comment on the adiabaticity. Finally, we present a first investigation of possible CP violation in binary neutron star mergers. To ensure readability we illustrate and discuss some aspects in more detail in the appendices.

During the course of this thesis, codes for the numerical calculations have been developed by the author using Fortran, Python, and C++. These programs account for the flavor evolution in models of binary neutron star merger remnants and supernovae, for studying the evolution in toy models, and for neutrino optical depth calculations. Note that parts of this thesis are reproduced from the author's work which has been published as [26]

> Maik Frensel, Meng-Ru Wu, Cristina Volpe, Albino Perego:
> *Neutrino flavor evolution in binary neutron star merger remnants*,
> Phys. Rev. D **95**, 023011 (2017),
> arXiv: 1607.05938 [astro-ph.HE].

If not stated otherwise, we will use natural units $\hbar = c = k_B = 1$.

Neutrino Flavor Mixing and Oscillations

> *How puzzling all these changes are! I'm never sure what I'm going to be, from one minute to another!*
>
> LEWIS CAROLL
> Alice's Adventures in Wonderland (1865)

2.1 Introduction

The Standard Model (SM) of Particle Physics describes three fundamental interactions: the electromagnetic, weak and the strong interaction. The underlying gauge group is described by the direct product $SU(3)_c \times SU(2)_L \times U(1)_Y$ which is spontaneously broken down to $SU(3)_c \times U(1)_Q$ using the Higgs mechanism. The non-Abelian gauge group of quantum chromodynamics, the color (c) group $SU(3)_c$, describes strong interactions while in the electroweak theory the corresponding gauge group is $SU(2)_L \times U(1)_Y$ and describes the electroweak interaction. The subscript L denotes left-handedness while Y refers to weak hypercharge. In the SM model there exist fundamental spin-$\frac{1}{2}$ particles, the quarks and leptons, which come in three generations (also called families). Each generation consists of two types of quarks or two types of leptons. In case of leptons, these correspond to a neutrino and its corresponding charged lepton partner, i.e., depending on the generation either an electron, a muon or a tau. To each generation, another neutrino flavor is associated. In the first generation, the neutrino is referred to as electron neutrino (ν_e) while in second generation as muon neutrino (ν_μ), and in the third generation as tau neutrino (ν_τ), respectively. Between the families the interactions of the particles are the same, but they possess different flavor numbers and masses. While quarks from different families are allowed to mix in the SM, there is no such mixing in the lepton sector. Within the SM neutrinos are assumed to be massless and flavor lepton number is conserved exactly, with other words, in each interaction process, neutrinos cannot change their flavor into another.

However, in 1969 Raymond Davis made a crucial observation that should raise doubts about this picture. Davis studied neutrinos radiated from the Sun. Indeed, the main energy source of the Sun is a nuclear fusion reaction which converts four protons into a helium nucleus and thereby releasing an energy of about 26.73 MeV and electron neutrinos [4]:

$$2e^- + 4p \rightarrow {}^4\text{He} + 2\nu_e + 26.73\,\text{MeV}. \tag{2.1}$$
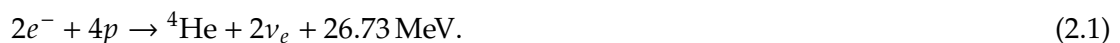
This proton-proton fusion reaction (the so called pp-chain) is the dominant process in the Sun and Sun-like stars[1].

In the so-called Standard Solar Model, established by John Bahcall, which describes the internal structure and the evolution of the Sun by solving the stellar structure equations. Thereby, one assumes [4] hydrostatic equilibrium, energy transport proceeds dominantly through radiation and convection, energy generation due to thermonuclear reactions, and that the Sun's primordial interior possesses a homogeneous chemical composition. Key input quantities are the Sun's current mass, radius, luminosity, and age. Furthermore, the initial chemical composition is needed.

To observe solar neutrinos, Davis used a radiochemical technique[2] used in the Homestake experiment where electron neutrinos are captured via the process

$$^{37}\text{Cl} + \nu_e \rightarrow {}^{37}\text{Ar} + e^- \tag{2.2}$$

in order to measure ^{8}B-neutrinos that are produced by one branch of the pp-chain. Davis found that the measured flux of solar ^{8}B-neutrinos was less than expected by the Standard Solar Model. This mismatch, which is referred to as the "solar neutrino problem", was also confirmed by other experiments: SAGE and GALLEX which both used gallium as target material, and Kamiokande-II, where elastic scattering processes between neutrinos and electrons were studied in a Cherenkov detector. Accordingly, the measured flux was between 1/3 and 1/2 of the theoretical prediction.

Ones needs to stress that detecting MeV (or sub-MeV) neutrinos is a challenging task due to the very low cross sections. This makes it necessary to construct huge detectors in which one can only register a few events in a short period. In addition, one needs to take care of the background and needs to avoid reactions that could mimic neutrino interactions and produce a fake signal. Besides this major problems, a high degree of purity of the material used in the experimental setup and an effective shielding from cosmic rays becomes necessary. Most adequate for the solar neutrino detection are therefore experiments that are based underground.

In the theoretical predictions one assumed that neutrinos from the Sun arrive at Earth without any change of their fundamental properties. A way that suggested itself to resolve the solar neutrino problem was offered by neutrino flavor oscillations. But in order to allow for such oscillations, neutrino flavors need to mix. And necessary for flavor mixing are finite neutrino masses contradicting the SM. This would mean that the conservation of flavor lepton number, which holds exactly in the SM, is violated.

At this point, it is worth mentioning how the particle physics community thought about the solar neutrino problem. While neutrino flavor oscillations were discussed as something more exotic, many particle physicists searched for alternative solutions such as neutrino magnetic

---

[1] In heavier stars it is expected that the CNO cycle plays the dominant role.
[2] The technique was suggested by Bruno Pontecorvo in 1946 [27].

moments like in the work of Howard Georgi and Michael Luke from 1990 [28]. They write in their introduction "*Most likely, the solar neutrino problem has nothing whatever to do with particle physics*", which is just one example showing the skepticism of leading scientists in the particle physics community about the idea of flavor oscillations as a possible solution to the solar neutrino puzzle.

However, in 1998 the situation changed. Super-Kamiokande [29] detected variations in the flux ratio of atmospheric ν_μ over ν_e as a function of their propagation distance and energy, L/E. The found patterns were consistent with neutrino flavor oscillation predictions [30] and indeed, this was the first observation of such oscillations. Furthermore, in 2001, the Sudbury Neutrino Observatory (SNO) found evidence for the flavor change of solar neutrinos.

Since these major achievements, it was realized that the SM is not complete and many open questions remain. As we will describe in the following section, the Higgs mechanism can be used to account for massive neutrinos. We stress that the non-alignment between mass and weak interaction eigenstates, which leads to neutrino mixing, is a simple consequence of the symmetry breaking mechanism as it is in the case of quarks.

2.2   Beyond the Standard Model of Particle Physics

The discovery of neutrino oscillations and hence the existence of massive neutrinos is the simplest example for physics beyond the SM. There are different theories in which neutrinos become massive. Probably the most trivial approach is to add right-handed neutrinos to the SM and therefore extend the particle spectrum[3]. Since these right-handed neutrinos are singlets with respect to the SM gauge group, they are also called sterile[4] with respect to the SM interactions. In this case, neutrino masses are generated by the Higgs mechanism like the masses of quarks and charged leptons.

In the SM, the Higgs-lepton Yukawa Lagrangian density is given by[5]:

$$\mathcal{L}_{\text{Yuk,lep}}^{\text{SM}} = - \sum_{\alpha,\beta=e,\mu,\tau} \tilde{Y}_{\alpha\beta}^{(\text{lep})} \overline{L'_{\alpha\text{L}}} \, \Phi \, l'_{\beta\text{R}} + \text{h.c.} \quad . \tag{2.3}$$

The primes on the fields indicate weak interaction eigenstates which do not have definite masses (see below). The Higgs doublet $\Phi(x)$ consists of a charged complex scalar field $\phi^+(x)$ and a neutral complex scalar field $\phi^0(x)$. The meanings of the quantities above are listed in table 2.1. The complex 3×3 matrix of charged lepton Yukawa couplings is denoted by $\tilde{Y}^{(\text{lep})}$.

---

[3] In what follows, we introduce three right-handed neutrinos for simplicity. But we stress that in principle, a single right-handed neutrino would be sufficient. In the general case, we would have a $(3 \times N_{\nu,\text{RH}})$-Yukawa-matrix.

[4] To be precise, they are not really sterile, since they can mix with the active flavor neutrinos.

[5] Remark on notation: For a Dirac field ψ, the Dirac adjoint is denoted by $\bar{\psi} \equiv \psi^\dagger \gamma^0$ while $\psi_\text{L} \equiv \frac{1-\gamma^5}{2} \psi$ and $\psi_\text{R} \equiv \frac{1+\gamma^5}{2} \psi$ are the left (L)- and right (R)-handed components where $\gamma^5 = i\gamma^0\gamma^1\gamma^2\gamma^3$ corresponds to the usual product of Dirac matrices.

Note that only left-handed parts of the three neutrinos take part in weak interactions due to the chiral nature of the theory[6].

Now if we add right- handed neutrinos we obtain

$$\mathcal{L}_{\text{Yuk,lep}} = - \sum_{\alpha,\beta=e,\mu,\tau} \tilde{Y}^{(\text{lep})}_{\alpha\beta} \overline{L'_{\alpha L}} \Phi l'_{\beta R} - \sum_{\alpha,\beta=e,\mu,\tau} \tilde{Y}^{(\nu)}_{\alpha\beta} \overline{L'_{\alpha L}} \tilde{\Phi} \nu'_{\beta R} + \text{h.c.}, \tag{2.4}$$

where $\tilde{Y}^{(\nu)}$ denotes the matrix of neutrino Yukawa couplings. In order to have a gauge-invariant Yukawa coupling term, we need a doublet which transforms as Φ under the gauge group SU(2), i.e., as **2**, but with opposite hypercharge. This properties are satisfied by the conjugated Higgs doublet $\tilde{\Phi} \equiv i\sigma_2 \Phi^*$, where σ_2 corresponds to the second Pauli matrix and * to complex conjugation[7]. The second Yukawa coupling term in eq. (2.4) is indeed gauge-invariant, because there is a singlet on the right-hand side of

$$(\bar{\mathbf{2}}, +1) \otimes (\bar{\mathbf{2}}, -1) \otimes (\mathbf{1}, 0) = (\mathbf{1}, 0) \oplus (\mathbf{3}, 0). \tag{2.5}$$

Note that these right-handed neutrinos are sterile ($I_3 = Y = 0$) with respect to weak interactions.

For convenience we introduce vectors of fields:

$$l'_{\text{L(R)}} \equiv \begin{pmatrix} e'_{\text{L(R)}} \\ \mu'_{\text{L(R)}} \\ \tau'_{\text{L(R)}} \end{pmatrix}, \qquad \nu'_{\text{L(R)}} \equiv \begin{pmatrix} \nu'_{e\text{L(R)}} \\ \nu'_{\mu\text{L(R)}} \\ \nu'_{\tau\text{L(R)}} \end{pmatrix}. \tag{2.6}$$

In the following we use the unitary gauge rendering only the physical degrees of freedom of the theory and where the Higgs doublet takes the form

$$\Phi(x) = \frac{1}{\sqrt{2}} \begin{pmatrix} 0 \\ H(x) + v \end{pmatrix} \tag{2.7}$$

after spontaneous symmetry breaking of the electroweak gauge group to the gauge group of quantum electrodynamics, $\text{SU}(2)_{\text{L}} \times \text{U}(1)_Y \to \text{U}(1)_Q$. Here, $H(x)$ is a real scalar field and $v \approx 246\,\text{GeV}$ corresponds to the vacuum expectation value (VEV) $\langle \Phi \rangle_0$ of the Higgs fields [31]. Applying the unitary gauge, we write the Yukawa term above in matrix form:

$$\mathcal{L}_{\text{Yuk,lep}} = - \left(\frac{H+v}{\sqrt{2}} \right) \left[\bar{l}'_{\text{L}} \tilde{Y}^{(\text{lep})} l'_{\text{R}} + \bar{\nu}'_{\text{L}} \tilde{Y}^{(\nu)} \nu'_{\text{R}} \right] + \text{h.c.} \quad . \tag{2.8}$$

---

[6] In principle one needs to distinguish between chirality and helicity, but in the massless case they are the same. We will therefore use both terms interchangeably (note that in the ultrarelativistic limit, they are approximately equal).

[7] Note that the fundamental representation **2** and the conjugate representation $\bar{\mathbf{2}}$ of SU(2) are equivalent. This can be shown explicitly by using the matrix $i\sigma_2$.

The terms proportional to the VEV of the Higgs doublet, v, are mass terms for the lepton fields. The terms proportional to the Higgs boson field H give trilinear couplings and are not of our interest. For our purposes, we only consider the Dirac mass term for neutrinos

$$\mathcal{L}_{\text{Yuk,lep}} \supset \mathcal{L}_{\text{Dirac},\nu} \equiv -\frac{v}{\sqrt{2}} \bar{\nu}'_{\text{L}} \tilde{Y}^{(\nu)} \nu'_{\text{R}} + \text{h.c.} \quad . \tag{2.9}$$

Now we want to consider the theory in the mass eigenstate basis. In order to this, we diagonalize the Yukawa matrix $\tilde{Y}^{(\nu)}$ by a bi-unitary transformation, i.e., we perform a singular value decomposition:

$$\left(V_{\text{L}}^{(\nu)} \right)^{\dagger} \tilde{Y}^{(\nu)} V_{\text{R}}^{(\nu)} =: Y^{(\nu)}, \qquad \text{with } Y_{kj}^{(\nu)} = y_k^{(\nu)} \delta_{kj} \quad (k, j = 1, 2, 3), \quad y_k^{(\nu)} \in \mathbb{R}_{>0}. \tag{2.10}$$

The matrices $V_{\text{L}}^{(\nu)}$ and $V_{\text{R}}^{(\nu)}$ are appropriate 3×3 unitary matrices. Similarly, we can proceed with $\tilde{Y}^{(\text{lep})}$:

$$\left(V_{\text{L}}^{(\text{lep})} \right)^{\dagger} \tilde{Y}^{(\text{lep})} V_{\text{R}}^{(\text{lep})} =: Y^{(\text{lep})}, \qquad \text{with } Y_{kj}^{(\text{lep})} = y_k^{(\text{lep})} \delta_{kj} \quad (k, j = 1, 2, 3), \quad y_k^{(\text{lep})} \in \mathbb{R}_{>0}. \tag{2.11}$$

The SM Lagrangian density contains a term

$$\mathcal{L}^{\text{SM}} \supset -\frac{g}{2\sqrt{2}} j_{W,\text{L}}^{\lambda} W_{\lambda} + \text{h.c.}, \tag{2.12}$$

where

$$j_{W,\text{L}}^{\lambda} = 2 \sum_{\alpha} \overline{\nu'_{\alpha\text{L}}} \gamma^{\lambda} l'_{\alpha\text{L}} \tag{2.13}$$

denotes the leptonic weak charge current, W the W-boson field and g the weak gauge coupling constant.

By defining massive chiral neutrino vectors

$$\nu_{\text{L(R)}} = \left(V_{\text{L(R)}}^{(\nu)} \right)^{\dagger} \nu'_{\text{L(R)}} =: \begin{pmatrix} \nu_{1\text{L(R)}} \\ \nu_{2\text{L(R)}} \\ \nu_{3\text{L(R)}} \end{pmatrix} \tag{2.14}$$

and vectors for the charged leptons

$$l_{\text{L(R)}} = \left(V_{\text{L(R)}}^{(\text{lep})} \right)^{\dagger} l'_{\text{L(R)}} =: \begin{pmatrix} e_{1\text{L(R)}} \\ \mu_{2\text{L(R)}} \\ \tau_{3\text{L(R)}} \end{pmatrix}, \tag{2.15}$$

we can re-express the current as

$$j^\lambda_{W,L} = 2\overline{\nu'_L}\gamma^\lambda l'_L \tag{2.16}$$

$$= 2\overline{\nu_L}(V^{(\nu)}_L)^\dagger V^{(\text{lep})}_L \gamma^\lambda l_L \equiv 2\overline{\nu_L}\mathsf{U}^\dagger\gamma^\lambda l_L. \tag{2.17}$$

In the latter expression, the matrix $\mathsf{U} := (V^{(\text{lep})}_L)^\dagger V^{(\nu)}_L$ appears, which corresponds to the neutrino mixing matrix relating weak interaction eigenstates (flavor eigenstates) and mass eigenstates. It is called Pontecorvo-Maki-Nakagawa-Sakata (PMNS) matrix[8]. As we will see below, it is this matrix, which appears in weak charged-current interactions. At this point, it is convenient to introduce the flavor fields

$$\nu^{(f)}_L \equiv \begin{pmatrix} \nu_{eL} \\ \nu_{\mu L} \\ \nu_{\tau L} \end{pmatrix} = \mathsf{U}\nu_L = (V^{(\text{lep})}_L)^\dagger \nu'_L. \tag{2.18}$$

Then the charged current reads as

$$j^\lambda_{W,L} = 2\overline{\nu^{(f)}_L}\gamma^\lambda l_L = 2\sum_\alpha \overline{\nu^{(f)}_{\alpha L}}\gamma^\lambda l_{\alpha L}. \tag{2.19}$$

Now let us have a look on the masses. Introducing the mass matrix $\mathsf{M} \equiv \mathsf{Y}^{(\nu)}v/\sqrt{2} \equiv \text{diag}(m_1, m_2, m_3)$, the neutrino Dirac mass term reads

$$\mathcal{L}_{\text{Dirac},\nu} = -\bar{\nu}_L \mathsf{M}\nu_R + \text{h.c.} \quad . \tag{2.20}$$

If we use Dirac neutrino fields $\nu_k \equiv \nu_{kL} + \nu_{kR}$, $k = 1, 2, 3$ we can also write this as

$$\mathcal{L}_{\text{Dirac},\nu} = -\sum_{k=1}^3 m_k \bar{\nu}_k \nu_k. \tag{2.21}$$

To end this section we note that the masses of charged leptons and quarks are proportional to the Higgs VEV v. Because the masses of neutrinos are known to be much smaller than the masses of charged leptons and quarks, the Yukawa couplings $y^{(\nu)}_k$ are expected to be unnaturally small which leads to a hierarchy problem. To illustrate this, we consider the ratio [32] $y^{(\nu)}_k/y_e = m_k/m_e \lesssim 0.5\,\text{eV}/(0.5\,\text{MeV}) = 10^{-6}$, where y_e denotes the Yukawa coupling related to the electron. However, the approach described above does not explain this smallness. One possible way out of this dilemma could be to consider neutrino masses as a low-energy manifestation of physics beyond the SM and their smallness is due to a suppression generated by a new high-energy scale, possibly related to the unification of forces. In this context, seesaw

---

[8] Note that sometimes the basis where $Y^{(\text{lep})}$ is diagonal and $V^{(\text{lep})}_L = \mathbb{1}$ is chosen and the neutrino mixing matrix becomes simply $\mathsf{U} = V^{(\nu)}_L$. However, it should be stressed that the charged lepton sector could contribute to leptonic flavor mixing as well. For this reason, one should use the product $(V^{(\text{lep})}_L)^\dagger V^{(\nu)}_L$ in order to account for leptonic flavor mixing.

mechanisms provide a formalism to include massive neutrinos. The basic idea is to add new, heavy particles into the SM and allow the violation of the global B-L symmetry[9]. The smallness of the three SM neutrinos is then associated with those heavy degrees of freedom and the lepton number violation [32]. There are different types of seesaw mechanisms, for a review we refer to [34].

For a consistent quantum field theory, it is necessary that the SM possesses a $\mathrm{SU(2)_L \times U(1)_Y}$ gauge symmetry and Lorentz invariance. Since the SM does not include right-handed neutrinos, Dirac mass terms for neutrinos are not permitted. Furthermore, since only a single Higgs doublet is included, gauge-invariant Majorana mass terms are not allowed as well. Note that the SM is renormalizable. To account for massive neutrinos, we need to abandon one of these assumptions. If we regard the SM as a low-energy effective theory and do not demand renormalizability, we are allowed to introduce an operator with mass dimension 5 [35],

$$\mathcal{L}_{\mathrm{eff}} = \mathcal{L}_{\mathrm{M}} + \delta\mathcal{L}^{\mathrm{d=5}}, \tag{2.22}$$

where Λ corresponds to a "cut-off scale" and $\delta\mathcal{L}^{\mathrm{d=5}}$ denotes the Weinberg operator

$$\delta\mathcal{L}^{\mathrm{d=5}} = \frac{1}{2}c^{\mathrm{d=5}}_{\alpha\beta}(\overline{L^c_{\alpha\mathrm{L}}}\tilde{\Phi}^*)(\tilde{\Phi}^\dagger L_{\beta\mathrm{L}}) + \mathrm{h.c.} \quad . \tag{2.23}$$

For the coefficients of the complex and symmetric matrix $c^{\mathrm{d=5}}_{\alpha\beta}$ we have the relation $|c^{\mathrm{d=5}}_{\alpha\beta}| \sim \mathcal{O}(1/\Lambda)$. The cut-off scale Λ should be below the Planck-scale $\Lambda_{\mathrm{Planck}} = \sqrt{\hbar c/G} = 1.2 \times 10^{19}\,\mathrm{GeV}$, where G denotes the gravitational constant, since the dimension-five operator described above would lead to Majorana neutrino masses $m_\nu \sim \mathcal{O}(v^2/\Lambda_{\mathrm{Planck}}) \simeq 10^{-6}\,\mathrm{eV}$. For the heaviest neutrino mass, we can extract a lower bound from the largest mass-squared difference $(|\Delta m^2_{\mathrm{atm}}| \approx 2.43 \times 10^{-3}\,\mathrm{eV}^2)$ $m_\nu > \sqrt{|\Delta m^2_{\mathrm{atm}}|} \approx 0.05\,\mathrm{eV}$ which excludes the validity of the effective theory up to the Planck scale.

After spontaneous symmetry breaking we obtain a mass term of the form:

$$\mathcal{L}_{\mathrm{Majorana},\nu} = -\frac{1}{2}(\mathsf{M}_\nu)_{\alpha\beta}\overline{\nu^c_{\alpha\mathrm{L}}}\nu_{\beta\mathrm{L}} + \mathrm{h.c.}, \tag{2.24}$$

where

$$(\mathsf{M}_\nu)_{\alpha\beta} := -\frac{v^2}{2}c^{\mathrm{d=5}}_{\alpha\beta}. \tag{2.25}$$

The particle-antiparticle-conjugate field $(\nu_{\mathrm{L}})^c := \mathsf{C}\overline{\nu_{\mathrm{L}}}^{\mathrm{T}}$, where C denotes the conjugation matrix, corresponds to the right-handed component of ν^c: $(\nu_{\mathrm{L}})^c = (\nu^c)_{\mathrm{R}}$. With other words, chirality is flipped. Note that charge conjugation $\mathcal{C}$ transforms particles into antiparticles by inverting all additive quantum numbers (like electric charge, baryon number, strangeness,

---

[9] Indeed, it is the absence of right-handed neutrinos and the exact conservation of baryon-minus-lepton (B-L) number in the SM which makes neutrinos strictly massless in the SM (see, e.g., [33]).

etc.) and preserving momentum and spin. In particular, we have[10] $\nu_{L,R} \overset{\mathcal{C}}{\mapsto} (\nu^c)_{L,R} = (\nu_{R,L})^c$. Thereby, the field $\nu \equiv \nu_L + e^{i\alpha}(\nu_L)^c$ satisfies the Majorana condition $(\nu')^c = e^{-i\alpha}\nu'$ [38], where α is an arbitrary phase [39]. With other words, the particle-antiparticle-conjugate of a Majorana field corresponds (up to a phase factor) to the field itself - a Majorana particle is its own antiparticle.

The Weinberg operator also appears in see-saw models. Even tough the seesaw mechanisms can explain the smallness of neutrino masses, there are still drawbacks: The mixing angle is still a free parameter and needs to be adjusted manually. Typical energy scales of conventional seesaw scenarios are close to the grand unified theory scale. This involves the problem that direct experimental studies are not accessible. In addition, the SM Higgs mass will be affected by quantum corrections due to the heavy degrees of freedom. For this seesaw-induced hierarchy problem [32] a possible solution could be offered by supersymmetry, but we stress that experimental support for the latter is still missing.

	Symbol	Representation with respect to $\mathrm{SU(2)_L \times U(1)}_Y$
Left-handed weak isospin doublet	$L'_{\alpha L} \equiv \begin{pmatrix} \nu'_{\alpha L} \\ \alpha'_L \end{pmatrix}$	$(\mathbf{2}, -1)$
Right-handed weak isospin singlet	$l'_{\beta R} \equiv \beta'_R$	$(\mathbf{1}, -2)$
Right-handed neutrino field	$\nu'_{\beta R}$	$(\mathbf{1}, 0)$
Higgs doublet	$\Phi \equiv \begin{pmatrix} \phi^+ \\ \phi^0 \end{pmatrix}$	$(\mathbf{2}, +1)$
Conjugate Higgs doublet	$\tilde{\Phi} \equiv i\sigma_2 \Phi^*$	$(\bar{\mathbf{2}}, -1)$

Table 2.1.: Particle content of the lepton sector in the SM and corresponding representations with respect to the electroweak gauge group $\mathrm{SU(2)_L \times U(1)}_Y$. The subscript L in the notion of the weak isospin group $\mathrm{SU(2)_L}$ indicates that the group elements act in a non-trivial manner only on left-handed chiral components of the fermion fields. The symmetry group $\mathrm{U(1)}_Y$ is generated by the weak hypercharge operator Y which is related to the weak isospin I_3 and the electric charge Q via the electroweak interactions analog of the Gell-Mann-Nishijima relation $Q = I_3 + Y/2$. The indices α and β run over e, μ, τ. In addition, we also list the Higgs doublet in the complex conjugated representation $(\bar{\mathbf{2}}, -1)$.

---

[10] Since $\nu_{L,R}$ and $(\nu_{L,R})^c$ have opposite helicities, one should avoid to denote ν_L^c the charge conjugate of ν_L. Some authors call it CPT-conjugate (e.g., [36]) or just conjugate (e.g. [37]).

2.3 Neutrino flavor mixing and masses

In practice, neutrinos always start and end as pure weak interaction eigenstates. Typically, they are produced via weak interaction processes like pion (see figure 2.1)- or muon-decays and are detected via inverse-beta- and inverse-muon-decay processes, in which they are transformed back to their charged lepton partners[11].
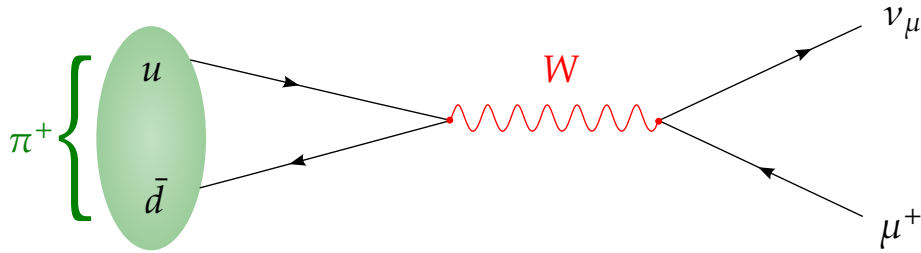

Figure 2.1.: Feynman diagram for pion decay $\pi^+ \to \mu^+ + \nu_\mu$ at tree-level.

From the formal point of view the mixing between neutrinos does not differ from the mixing between quarks. But in contrast to neutrinos, quarks being part of composite particles like protons or neutrons always start and end as pure mass eigenstates. It is the action of the weak interaction that reflects the fact that quarks are mixtures of weak eigenstates: If a neutron decays, the d-quark transforms into a u-quark and the degree to which a d-quark is composed of the weak eigenstate d' can only be determined by a measurement of the decay rate [41]. Furthermore, the quark mixing angles are small and possess a strong hierarchy. In contrast, neutrinos have relatively large mixing angles (two angles are "large", one angle is "small")[12]. This suggests that the source of quark and neutrino mixing is different [43]. Another major difference are the tiny masses of neutrinos. Measurements of the electron energy spectrum in tritium β-decays, $^3\mathrm{H} \to {}^3\mathrm{He} + e^- + \bar{\nu}_e$, provide the most strict upper limits of the lightest neutrino mass. From the results obtained by the Troitsk and Mainz groups one infers an upper bound of $m_{\min} \lesssim 2.2\,\mathrm{eV}$ [44]. This value can be improved by one order of magnitude with the currently running experiment KATRIN reaching a sensitivity of $0.2\,\mathrm{eV}$ [31].

Possible natural explanations for the smallness of neutrino masses usually suppose a violation of the total lepton number at large energy scales ($10^{15} - 10^{16}\,\mathrm{GeV}$). Indeed, if this is the case, then neutrinos are Majorana particles which could be experimentally accessed via the neutrinoless double β-decay $(A, Z) \to (A, Z + 2) + e^- + e^-$, where, A and Z denote the mass and atomic numbers, respectively, and where lepton number is violated by two units. Experiments targeting this problem are e.g., GERDA, KamLAND-Zen, EXO, and SNO+.

---

[11] Note that neutrinos produced and detected in weak interaction processes are in general not correctly described by the weak states $|\nu_\alpha\rangle$ as pointed out in [40]. If the differences between the neutrino masses are negligible with respect to the neutrino momentum (which is the case in the ultrarelativistic limit), the weak states $|\nu_\alpha\rangle$ can be used to describe approximately the neutrinos detected in the weak-interaction process under consideration. For a detailed discussion on the nature of neutrino states that are produced and detected in weak interaction processes see [39, 40].

[12] In order to give a number: From current oscillation data [31], the angle θ_{23} is expected to lie between $38°$ and $53°$ [42] while the corresponding angle in the quark sector is only about $2.4°$.

In the case of three flavors, the weak eigenstates $|\nu_\alpha\rangle$ ($\alpha \in \{e, \mu, \tau\}$) are linked to the mass eigenstates $|\nu_k\rangle$ ($k \in \{1, 2, 3\}$) via

$$|\nu_\alpha\rangle = \sum_{j=1}^{3} \mathsf{U}_{\alpha j}|\nu_j\rangle. \tag{2.26}$$

Here, U denotes the unitary matrix[13] $\mathsf{U}^*_{\text{PMNS}}$, where

$$\mathsf{U}_{\text{PMNS}} = \begin{pmatrix} 1 & 0 & 0 \\ 0 & c_{23} & s_{23} \\ 0 & -s_{23} & c_{23} \end{pmatrix} \begin{pmatrix} c_{13} & 0 & s_{13}\mathrm{e}^{-i\delta} \\ 0 & 1 & 0 \\ -s_{13}\mathrm{e}^{i\delta} & 0 & c_{13} \end{pmatrix} \begin{pmatrix} c_{12} & s_{12} & 0 \\ -s_{12} & c_{12} & 0 \\ 0 & 0 & 1 \end{pmatrix} \begin{pmatrix} 1 & 0 & 0 \\ 0 & \mathrm{e}^{i\alpha_1/2} & 0 \\ 0 & 0 & \mathrm{e}^{i\alpha_2/2} \end{pmatrix} \tag{2.27}$$

with $c_{ij} \equiv= \cos\theta_{ij}$ and $s_{ij} \equiv \sin\theta_{ij}$ for $ij = 12, 13, 23$. This is the standard parametrization for the mixing matrix [31]. Note that there exist different types of parametrizations, but because all of them are equivalent from the mathematical point of view, one usually chooses the one which is most convenient for studying a given problem.

The three mixing angles approximately correspond to the mixing angles found in atmospheric ($\theta_{23} = \theta_{\text{atm}}$), reactor ($\theta_{13}$) and solar ($\theta_{12} = \theta_\odot$) neutrino oscillations experiments. The last factor on the right-hand side of eq. 2.27 corresponds to the Majorana phase matrix[14] and is not relevant for the discussion of neutrino oscillations [32] and hence, we will neglect it. To sum up, we have three mixing angles ($\theta_{12}, \theta_{13}, \theta_{23}$), one Dirac and two Majorana CP-violating phases and three neutrino masses (m_1, m_2, m_3). Hence, 7 (Dirac case) or 9 (Majorana case) additional parameters have to be added to the 13 free parameters of the lepton and quark sector of the SM (3 charged-lepton masses, 6 quark masses, 3 CKM mixing angles, 1 CKM CP-violating phase). These parameters have to be determined by experiments. Still, it remains an open question why there are so many parameters in the flavor sector of the SM.

The mixing angles can be defined such that they all lie in the first quadrant [32] while the three CP-violating phases can take any values between 0 and 2π.

If we ignore the Majorana phases α_1 and α_2, we end up with the following three-flavor mixing matrix:

$$\mathsf{U}_{\text{mixing}} = \begin{pmatrix} c_{12}c_{13} & s_{12}c_{13} & s_{13}\mathrm{e}^{-i\delta} \\ -s_{12}c_{23} - c_{12}s_{13}s_{23}\mathrm{e}^{i\delta} & c_{12}c_{23} - s_{12}s_{13}s_{23}\mathrm{e}^{i\delta} & c_{13}s_{23} \\ s_{12}s_{23} - c_{12}s_{13}c_{23}\mathrm{e}^{i\delta} & -c_{12}s_{23} - s_{12}s_{13}c_{23}\mathrm{e}^{i\delta} & c_{13}c_{23} \end{pmatrix} \tag{2.28}$$

In table 2.2 we summarize the best-fit values obtained from a global fit of current neutrino oscillation parameters [45].

---

[13] The neutrino flavor fields and massive fields are linked via U_{PMNS}, eq. (2.18), while in the transformation of the states $\mathsf{U}^\dagger_{\text{PMNS}}$ appears leading to a complex conjugation in eq. (2.26), $\mathsf{U} = \mathsf{U}^*_{\text{PMNS}}$. This is related to the fact, that the quantum field $\overline{\nu_{\alpha L}}$, appearing in the charged-current eq. (2.19), contains the creation operator for a massive neutrino field ν_k, i.e., a flavor state is produced via $\sum_k \mathsf{U}^*_{\alpha k}\bar{\nu}_{kL}$.

[14] which is equal to the identity in case of Dirac neutrinos as in section 2.2.

Parameter	Best-fit value $\pm 1\sigma$	3σ range
$\Delta m_{21}^2\,[\mathrm{eV}^2]$	$7.50^{+0.19}_{-0.17} \times 10^{-5}$	$(7.03 - 8.09) \times 10^{-5}$
$\Delta m_{31}^2\,[\mathrm{eV}^2]\,(\mathrm{NH})$	$2.524^{+0.039}_{-0.040} \times 10^{-3}$	$(2.407 - 2.643) \times 10^{-3}$
$\Delta m_{32}^2\,[\mathrm{eV}^2]\,(\mathrm{IH})$	$-2.514^{+0.038}_{-0.041} \times 10^{-3}$	$-(2.635 - 2.399) \times 10^{-3}$
$\theta_{12}\,[°]$	$33.56^{+0.77}_{-0.75}$	$31.38 - 35.99$
$\theta_{13}\,[°]\,(\mathrm{NH})$	$8.46^{+0.15}_{-0.15}$	$7.99 - 8.90$
$\theta_{13}\,[°]\,(\mathrm{IH})$	$8.49^{+0.15}_{-0.15}$	$8.03 - 8.93$
$\theta_{23}\,[°]\,(\mathrm{NH})$	$41.6^{+1.5}_{-1.2}$	$38.4 - 52.8$
$\theta_{23}\,[°]\,(\mathrm{IH})$	$50.0^{+1.1}_{-1.4}$	$38.8 - 53.1$
$\delta\,[°]\,(\mathrm{NH})$	261^{+51}_{-59}	$0 - 360$
$\delta\,[°]\,(\mathrm{IH})$	277^{+40}_{-46}	$145 - 391$

Table 2.2.: Global fit results from [45] of experimentally obtained data of the oscillation parameters along with the 3σ allowed ranges.

The current data obtained from solar (ν_e), reactor ($\bar{\nu}_e$), atmospheric and accelerator (both ν_μ and $\bar{\nu}_\mu$) neutrino experiments are consistent with a three-flavor neutrino mixing framework[15]. Within a three-flavor treatment, there exist two independent mass-squared differences Δm_{21}^2 and Δm_{31}^2. In this work, we choose the convention, where $m_1 < m_2$ such that $|\Delta m_{21}^2| < |\Delta m_{31}^2|$. The smaller mass-squared difference Δm_{21}^2 accounts for solar electron neutrino oscillations and reactor electron antineutrino oscillations (KamLAND) while the larger mass-squared difference corresponding to $|\Delta m_{31}^2|$ or $|\Delta m_{32}^2|$ is linked to atmospheric and accelerator neutrino oscillations (ν_μ and $\bar{\nu}_\mu$) and reactor neutrino oscillations ($\bar{\nu}_e$) at short baselines (about 1 km).

The experimentally observed impacts of the mass-squared differences Δm_{31}^2 or Δm_{32}^2 on solar neutrino oscillations (ν_e), and of Δm_{21}^2 on atmospheric and accelerator neutrino oscillations (in both cases ν_μ and $\bar{\nu}_\mu$), or on $\bar{\nu}_e$-oscillations from reactors at short baselines are only minor [31]. This is mainly due to the fact that the scales of both mass-squared differences are largely separated $|\Delta m_{21}^2/\Delta m_{31(32)}^2| \sim \mathcal{O}(10^{-2})$ and because in these cases the source-detector distance L, the neutrino energy E and their ratios L/E differ significantly [31].

Until the beginning of 2000, it was found that the values for the mixing angles θ_{12} and θ_{23} are relatively large. While the knowledge of these angles improved over the subsequent years, there was only an upper bound on the θ_{13} mixing angle, provided by the CHOOZ experiment with reactor $\bar{\nu}_e$. The early results from its successor Double Chooz in 2011

---

[15] Some experimental data could indicate the possible existence of one or two light sterile neutrinos with masses of $m_\nu \sim \mathcal{O}(1)\,\mathrm{eV}$, for reviews, see [46–48] and references therein.

suggested the possible existence of a non-vanishing θ_{13}. It turned out that these results were consistent with the statistically significant measurements of Daya Bay and RENO indicating that $\sin \theta_{13}$ is relatively small. With these experiments one entered the field of high precession measurements allowing to study effects beyond the leading approximation where one assumes that $\sin^2 \theta_{13} = 0$ [49]. This is necessary to explore three flavor effects, the mass ordering, and CP violation.

The relative smallness of $\sin \theta_{13}$ allows the description of the dominant effects in solar and atmospheric neutrino oscillations by an effective two-flavor mixing scheme where the mixing angle θ_{12} is linked to solar ν_e oscillations while the angle θ_{23} is connected to atmospheric ν_μ and $\bar{\nu}_\mu$ oscillations. For this reason, it is convenient to call $\theta_{12} \equiv \theta_\odot$ "solar" mixing angle and $\theta_{23} \equiv \theta_{\text{atm}}$ "atmospheric" mixing angle. Correspondingly, one introduces the solar $\Delta m_\odot^2 \equiv \Delta m_{21}^2$ and atmospheric $\Delta m_{\text{atm}}^2 \equiv \Delta m_{31}^2$ mass-squared differences.

The present experiments do not reach the necessary sensibility to access the difference between $|\Delta m_{31}^2|$ and Δm_{32}^2. Due to the relation $\Delta m_{21}^2 \equiv \Delta m_{31}^2 - \Delta m_{32}^2 \ll \Delta m_{31(32)}^2$ we infer $\Delta m_{32}^2 \simeq \Delta m_{31}^2$. While solar neutrino experiments are able to determine the sign of Δm_{21}^2, we do not yet know the sign of Δm_{31}^2 (or $|\Delta m_{32}^2|$) resulting in two possible scenarios as shown in figure 2.2. The
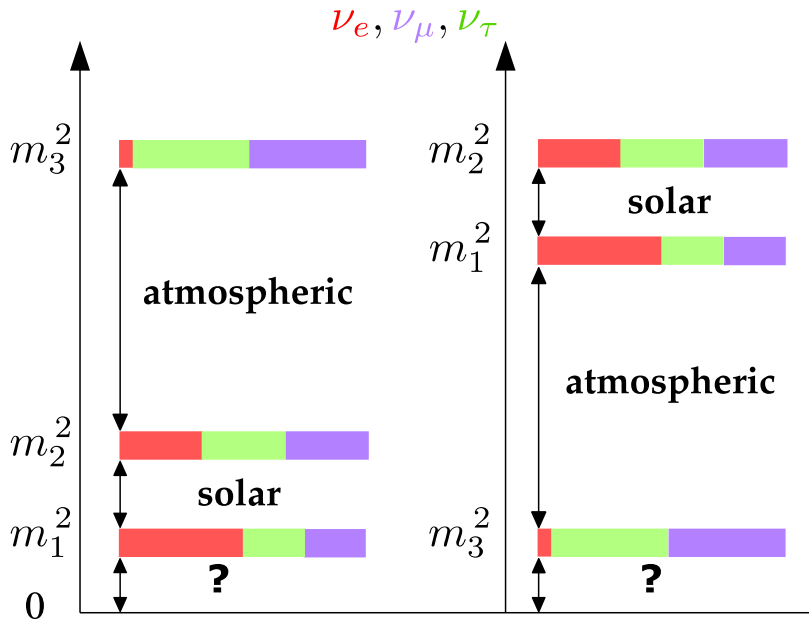

Figure 2.2.: Neutrino mass hierarchy: normal (left) and inverted (right). The colors show a schematic representation of the flavor content of the mass eigenstates, where red corresponds to electron neutrinos, violet to muon neutrinos, and green to tau neutrinos.

case where both are positive is referred to as the normal mass hierarchy (NH) while the case where both are negative, is referred to as inverted mass hierarchy (IH). The determination of the mass hierarchy is of fundamental importance [50]:

- to find extensions of the SM in order to include neutrino masses accompanied with an appropriate mechanism to explain the smallness of the neutrino masses (so far there are many different models and the mass hierarchy would provide a constrain);

- for the reduction of experimental uncertainties in measuring the CP-violating phase;

- for core-collapse supernova, remnants of compact object mergers and stellar collapses.

Note that neutrino masses are not necessarily hierarchical, but could be quasi-degenerate [31]. Current data from atmospheric neutrinos by Super-Kamiokande slightly prefer the normal mass hierarchy. The same is true for accelerator neutrinos from the long baseline experiment NOνA. However, in both cases the statistical significance is still too low and more data has to be collected. Promising future experiments that should be able to resolve the mass ordering are DUNE/LBNF (accelerator neutrinos), PINGU, ORCA, INO, Hyper-Kamiokande (atmospheric neutrinos), and JUNO, RENO-50 (reactor neutrinos). For a review, see [51].

Another unknown is the CP-violating phase which has not been determined yet, but there exist some constraints (still the statistics is rather poor) suggesting a CP phase of $\delta \simeq 3\pi/2$. A corresponding measurement is one of the major goals of near future experiments. More on CP violation will be discussed in section 4.8.

In table 2.3 we list the parameter values used in the numerical calculations of this thesis, which are consistent with the current best-fit values [31, 45].

Parameter	Value
Δm_{21}^2	$7.59 \times 10^{-5}\,\mathrm{eV}^2$
$\lvert\Delta m_{31}^2\rvert$	$2.43 \times 10^{-3}\,\mathrm{eV}^2$
θ_{12}	0.60
θ_{13}	0.15
θ_{23}	$\frac{\pi}{4}$

Table 2.3.: Parameters used in this work. Note that they are consistent with current best-fit values [31, 45].

2.4 Neutrino propagation equation in vacuum

Neutrino flavor oscillations are a consequence of non-degenerate neutrino masses and flavor mixing[16]. In the following we want to derive a formal equation for the evolution of neutrinos in vacuum. The discussion is based on [39, 52, 53]. Until today the nature of neutrinos remains unknown. They may be Dirac or Majorana particles, but for the propagation of ultrarelativistic neutrinos ($v/c \approx 1$) the full spin structure does not need to be taken into account [52]. Moreover, for ultrarelativistic particles, chirality conservation is good to the order m/E (cf. [52]) and furthermore, weak interactions couple only to the left-handed component of the neutrino field. Altogether, for neutrinos with $E \gg m$, only the propagation of the left-handed component is relevant [52].

---

[16] Note that at least two different neutrino masses are required in order to allow for oscillations. If the masses are completely degenerate, i.e., all masses have the same value m, then the mass matrix $M = m\mathbb{1}$ remains invariant under unitary transformations $UMU^\dagger = M$, in particular it is flavor diagonal and flavor oscillations cannot occur.

Now it is convenient to work with neutrino state vectors. Note that the one-neutrino mass eigenstate $|\nu_k(t)\rangle$ ($k = 1, 2, 3$) is created by the field operator $\nu_k^\dagger(t)$ acting on the vacuum state[17]. Because of the remarks outlined above, a freely propagating neutrino described by the mass eigenstate $|\nu_k(t)\rangle$ satisfies the Klein-Gordon equation

$$(\Box + m_k^2) |\nu_k(t)\rangle = 0, \tag{2.29}$$

which is independent of the Dirac or Majorana nature. In the latter expression, $\Box \equiv \partial_\mu \partial^\mu = \partial_t^2 - \nabla^2$ denotes the d'Alembert operator. Equivalently, we can write

$$\left(\partial_t^2 - \nabla^2\right) |\nu_k(t)\rangle = -m_k^2 |\nu_k(t)\rangle. \tag{2.30}$$

Now we assume that all mass eigenstates have the same three-momentum $\mathbf{p}$, which is accurate up to small corrections for ultrarelativistic neutrinos [52]. Hence, the free solutions (corresponding to plane waves) of the Klein-Gordon equation above can be written as $|\nu_k(t)\rangle = e^{i(\mathbf{p}\cdot\mathbf{x} - E_k t)} |\nu_k\rangle$, where $E_k = (\mathbf{p}^2 + m_k^2)^{1/2}$. Inserting the solutions into the wave equation we obtain

$$\left(\partial_t^2 + \mathbf{p}^2\right) |\nu_k(t)\rangle = -m_k^2 |\nu_k(t)\rangle. \tag{2.31}$$

In the following we will use the decomposition [53]

$$\left(\partial_t^2 + \mathbf{p}^2\right) = -\left(i\partial_t - p\right)\left(i\partial_t + p\right) \tag{2.32}$$

and the Taylor expansion $E_k = (p^2 + m_k^2)^{1/2} \simeq p$ for ultrarelativistic neutrinos where higher order terms $\mathcal{O}(m_k^2/p^2)$ are omitted due to $p = |\mathbf{p}| \gg m_k$. On the Hilbert space of mass eigenstates, we can replace $i\partial_t$ by p in the second factor of the decomposition in eq. (2.32) because of $i\partial_t |\nu_k(t)\rangle = E_k |\nu_k(t)\rangle \simeq p |\nu_k(t)\rangle$, while we keep the differential operator in the first factor which corresponds to a difference (between energy and momentum) term:

$$\left(\partial_t^2 + \mathbf{p}^2\right) \mapsto -2p\left(i\partial_t - p\right). \tag{2.33}$$

This leads us to a Schrödinger-like equation for the mass eigenstates:

$$i\partial_t |\nu_k(t)\rangle = \left(p + \frac{m_k^2}{2p}\right) |\nu_k(t)\rangle. \tag{2.34}$$

We note that the p-term can be absorbed into a phase factor which is identical for all mass eigenstates [52, 55]:

$$|\tilde{\nu}_k(t)\rangle := e^{ipt} |\nu_k(t)\rangle \tag{2.35}$$

---

[17] We skip the technical details, but stress that the construction of a physical Fock space for flavor states is problematic [40, 54]

Since such global phase factors are unobservable we will simply drop this term (instead of redefining the mass eigenstates as in eq. (2.35)). This leads us to

$$i\partial_t \left|\nu_k(t)\right\rangle = \frac{m_k^2}{2p} \left|\nu_k(t)\right\rangle. \tag{2.36}$$

The negative energy solutions $\left|\bar{\nu}_k(t)\right\rangle = e^{-i(\mathbf{p}\cdot\mathbf{x} - E_k t)} \left|\bar{\nu}_k\right\rangle$, associated with antiparticles, lead to a global minus sign

$$i\partial_t \left|\bar{\nu}_k(t)\right\rangle = -\frac{m_k^2}{2p} \left|\bar{\nu}_k(t)\right\rangle, \tag{2.37}$$

where we used

$$\left(\partial_t^2 + \mathbf{p}^2\right) \mapsto +2p\left(i\partial_t - p\right). \tag{2.38}$$

To end this section we remark that in practice we usually deal with stationary neutrino sources with non-trivial spatial variations [32, 53]. In this case the neutrino energy spectrum is fixed and we measure the propagation in space rather than in time [32, 53, 55]. In either case we will obtain the same oscillation probabilities in the light-ray approximation [39] $t \approx x = |\mathbf{x}|$. In this context, we stress the fact that the latter approximation is unjustified and we should rather describe neutrinos by wave packets. Furthermore, note that the latter approximation is also inappropriate when neutrinos travel large distances between source and detection, e.g., neutrinos from astrophysical sources. This is due to the fact, that the individual velocities of the mass eigenstates will differ and the mass eigenstates will be spatially separated leading to a loss of quantum mechanical coherence. For a proper wave packet treatment of neutrino oscillations and discussions concerning problems with the (unrealistic) equal momentum (used above) and equal energy assumption we refer to [39, 56].

2.5   Neutrino oscillations in vacuum

In order to simplify the discussion, we first study neutrinos with two flavors only and consider the propagation of a stationary neutrino beam in vacuum. The relation between flavor eigenstates ($\left|\nu_e\right\rangle$ and $\left|\nu_\mu\right\rangle$) and mass eigenstates ($\left|\nu_1\right\rangle$ and $\left|\nu_2\right\rangle$) is given by the unitary transformation:

$$\begin{pmatrix} \left|\nu_e\right\rangle \\ \left|\nu_\tau\right\rangle \end{pmatrix} = \mathsf{U} \begin{pmatrix} \left|\nu_1\right\rangle \\ \left|\nu_2\right\rangle \end{pmatrix} \equiv \begin{pmatrix} \cos\theta & \sin\theta \\ -\sin\theta & \cos\theta \end{pmatrix} \begin{pmatrix} \left|\nu_1\right\rangle \\ \left|\nu_2\right\rangle \end{pmatrix}. \tag{2.39}$$

The unitary mixing matrix is a two-dimensional version of the neutrino mixing matrix (see eq. (2.28)) appropriate for a two-flavor description of neutrino oscillations. Effectively, we set $\theta_{23} = 0$ and define [57] the states $\left|\nu_\mu^*\right\rangle \equiv (\left|\nu_\mu\right\rangle - \left|\nu_\tau\right\rangle)/\sqrt{2}$ and $\left|\nu_\tau^*\right\rangle \equiv (\left|\nu_\mu\right\rangle + \left|\nu_\tau\right\rangle)/\sqrt{2}$. Then only the mixing $\nu_e \rightleftarrows \nu_\tau^*$ becomes important and we can use $\theta \approx \theta_{13}$ as effective two-flavor

mixing angle. In what follows, we will simply write ν_τ instead of ν_τ^*. Though neutrino masses may not be relevant for the dynamics of astrophysical settings like supernovae or compact object mergers, the mass-squared differences are likely sufficiently large to allow for significant flavor transformations. This in turn, can crucially affect e.g., supernova shock re-heating or nucleosynthesis.

Because neutrinos propagate in their mass eigenstates $|\nu_k(t)\rangle$, their evolution is described by the Schrödinger-like equation (cf. eq. (2.36))

$$
i\frac{\partial}{\partial t}\begin{pmatrix}|\nu_1(t)\rangle \\ |\nu_2(t)\rangle\end{pmatrix} = \mathsf{H}_{\mathrm{vac}}^{(\mathrm{m})}\begin{pmatrix}|\nu_1(t)\rangle \\ |\nu_2(t)\rangle\end{pmatrix} \tag{2.40}
$$

$$
= \frac{1}{2p}\mathsf{M}^2\begin{pmatrix}|\nu_1(t)\rangle \\ |\nu_2(t)\rangle\end{pmatrix} \equiv \frac{1}{2p}\begin{pmatrix}m_1^2 & 0 \\ 0 & m_2^2\end{pmatrix}\begin{pmatrix}|\nu_1(t)\rangle \\ |\nu_2(t)\rangle\end{pmatrix}, \tag{2.41}
$$

where $\mathsf{H}_{\mathrm{vac}}^{(\mathrm{m})} = \mathsf{M}^2/(2p)$ denotes the Hamiltonian in the mass basis. Multiplying both sides of the last equation by U we find

$$
i\frac{\partial}{\partial t}\begin{pmatrix}|\nu_e(t)\rangle \\ |\nu_\tau(t)\rangle\end{pmatrix} = \frac{1}{2p}\mathsf{U}\begin{pmatrix}m_1^2 & 0 \\ 0 & m_2^2\end{pmatrix}\mathsf{U}^\dagger\begin{pmatrix}|\nu_e(t)\rangle \\ |\nu_\tau(t)\rangle\end{pmatrix}. \tag{2.42}
$$

Finally, we write the effective Hamiltonian in the flavor basis as

$$
\mathsf{H}_{\mathrm{vac}}^{(\mathrm{f})} = \frac{1}{2p}\mathsf{U}\mathsf{M}^2\mathsf{U}^\dagger = \frac{m_1^2+m_2^2}{4p}\mathbb{1} + \frac{\Delta m^2}{4p}\begin{pmatrix}-\cos 2\theta & \sin 2\theta \\ \sin 2\theta & \cos 2\theta\end{pmatrix}, \tag{2.43}
$$

where we used the trigonometric identities

$$
\sin^2\theta = \frac{1}{2}(1 - \cos 2\theta), \tag{2.44}
$$

$$
\cos^2\theta = \frac{1}{2}(1 + \cos 2\theta), \tag{2.45}
$$

$$
\sin\theta\cos\theta = \frac{1}{2}\sin 2\theta. \tag{2.46}
$$

In the Hamiltonian above, the mass-squared difference is given by $\Delta m^2 \equiv m_2^2 - m_1^2$. We assume without loss of generality $\Delta m^2 > 0$ and $0 \le \theta \le \pi/2$. Furthermore, the first term in $\mathsf{H}_{\mathrm{vac}}$ is proportional to the identity matrix and can be absorbed into a global phase factor which does not contribute to the flavor evolution. For this reason, we neglect this term and define the Hamiltonian as follows:

$$
\mathsf{H}_{\mathrm{vac}}^{(\mathrm{f})} = \frac{\omega}{2}\begin{pmatrix}-\cos 2\theta & \sin 2\theta \\ \sin 2\theta & \cos 2\theta\end{pmatrix}, \tag{2.47}
$$

where we set $E \equiv p$ and $\omega \equiv \Delta m^2/(2E)$. We remark that the angle θ obviously satisfies the relation

$$\tan 2\theta = \frac{2[\mathsf{H}^{(f)}_{\text{vac}}]_{e\tau}}{[\mathsf{H}^{(f)}_{\text{vac}}]_{\tau\tau} - [\mathsf{H}^{(f)}_{\text{vac}}]_{ee}}, \tag{2.48}$$

where $[\mathsf{H}^{(f)}_{\text{vac}}]_{\alpha\beta}$ denotes the elements of the matrix $\mathsf{H}^{(f)}_{\text{vac}}$ with $\alpha, \beta = e, \tau$.

In the rest of the work, we will suppress the index (f) and if not otherwise stated, we will work in the flavor basis.

2.5.1 Three flavor case

Sometimes it is convenient to introduce the following basis [32]:

$$\begin{pmatrix} |\nu_e\rangle \\ |\nu_x\rangle \\ |\nu_y\rangle \end{pmatrix} = \begin{pmatrix} 1 & 0 & 0 \\ 0 & c_{23} & -s_{23} \\ 0 & s_{23} & c_{23} \end{pmatrix} \begin{pmatrix} |\nu_e\rangle \\ |\nu_\mu\rangle \\ |\nu_\tau\rangle \end{pmatrix}. \tag{2.49}$$

Effectively, this corresponds to setting $\theta_{23} = 0$ in eq. (2.26). Due to the fact that ν_μ- and ν_τ have the same interactions with ordinary matter (at least at leading order), this choice of basis is particularly convenient for studying neutrino oscillations in matter [58, 59].

Starting from the Hamiltonian $\mathsf{H}^{(m)}_{\text{vac}} = \mathsf{M}^2/(2E)$ in the mass basis, we can write the effective Hamiltonian for vacuum oscillations in the new flavor basis as $\mathsf{H}^{(f')}_{\text{vac}} = \tilde{\mathsf{U}}\mathsf{M}^2\tilde{\mathsf{U}}^\dagger/(2E)$ with

$$\tilde{\mathsf{U}} := \begin{pmatrix} c_{13} & 0 & s_{13} \\ 0 & 1 & 0 \\ -s_{13} & 0 & c_{13} \end{pmatrix} \begin{pmatrix} c_{12} & s_{12} & 0 \\ -s_{12} & c_{12} & 0 \\ 0 & 0 & 1 \end{pmatrix} = \begin{pmatrix} c_{12}c_{13} & s_{12}c_{13} & s_{13} \\ -s_{12} & c_{12} & 0 \\ -s_{13}c_{12} & -s_{12}s_{13} & c_{13} \end{pmatrix}, \tag{2.50}$$

or explicitly:

$$\mathsf{H}^{(f')}_{\text{vac}} = \omega_{\text{L}} \begin{pmatrix} s_{12}^2 c_{13}^2 & s_{12}c_{12}c_{13} & -s_{12}^2 s_{13}c_{13} \\ s_{12}c_{12}c_{13} & c_{12}^2 & -s_{12}c_{12}s_{13} \\ -s_{12}^2 s_{13}c_{13} & -s_{12}c_{12}s_{13} & s_{12}^2 s_{13}^2 \end{pmatrix} + \omega_{\text{H}} \begin{pmatrix} s_{13}^2 & 0 & s_{13}c_{13} \\ 0 & 0 & 0 \\ s_{13}c_{13} & 0 & c_{13}^2 \end{pmatrix} + \frac{m_1^2}{2E} \begin{pmatrix} 1 & 0 & 0 \\ 0 & 1 & 0 \\ 0 & 0 & 1 \end{pmatrix}, \tag{2.51}$$

where $\omega_{\text{L}} \equiv \Delta m_{21}^2/(2E)$ and $\omega_{\text{H}} \equiv \Delta m_{31}^2/(2E)$ are the low and high oscillation frequencies [32]. Note that we set the Dirac phase to zero ($\delta = 0$) and the third term on the right-hand side of the last equation is not relevant for neutrino oscillations and will be omitted.

For a fixed energy and with the values $|\Delta m_{31}^2| \approx 2.43 \times 10^{-3} \text{ eV}^2$ and $\Delta m_{21}^2 \approx 7.59 \times 10^{-5} \text{ eV}^2$, we have $|\omega_{\text{H}}| \gg \omega_{\text{L}}$, so the leading contribution to the Hamiltonian originates from the ω_{H}-term.

This allows us to approximate the three-flavor oscillations by an effective two-flavor description with mixing parameters θ_{13} and Δm_{31}^2, i.e.,

$$\begin{pmatrix} |\nu_e\rangle \\ |\nu_y\rangle \end{pmatrix} = \begin{pmatrix} c_{13} & s_{13} \\ -s_{13} & c_{13} \end{pmatrix} \begin{pmatrix} |\nu_1\rangle \\ |\nu_3\rangle \end{pmatrix}. \tag{2.52}$$

2.5.2 Vacuum oscillation probabilities

Solving the evolution equation yields

$$|\nu_k(t)\rangle = \exp\left(-i\frac{m_k^2 t}{2E}\right)|\nu_k(t)\rangle, \tag{2.53}$$

where we set $E \approx |\mathbf{p}|$. If we expand a flavor state into the mass basis,

$$|\nu_\alpha\rangle = \sum_{k=1}^{3} \mathsf{U}_{\alpha k}^* |\nu_k\rangle, \tag{2.54}$$

where U denotes the mixing matrix U_{PMNS}, we can compute the probability to find a neutrino with energy E and initial flavor[18] α in a flavor β after some t:

$$P(\nu_{\underline{\alpha}} \to \nu_\beta)(E, t) = |\langle \nu_\beta | \nu_\alpha(t)\rangle|^2 \tag{2.55}$$

$$= \sum_{j,k=1}^{3} \mathsf{U}_{\alpha j}\mathsf{U}_{\alpha k}^*\mathsf{U}_{\beta j}^*\mathsf{U}_{\beta k}\exp\left(-i\frac{\Delta m_{kj}^2 t}{2E}\right). \tag{2.56}$$

In this expression we introduced the mass-squared difference $\Delta m_{kj}^2 \equiv m_k^2 - m_j^2$. Because for practical applications, it is more convenient to use the propagation distance L (e.g., the distance between the neutrino source and detector), we will use L instead of the time t using the approximation $t \approx L$. The phase appearing in eq. (2.56), $-\Delta m_{kj}^2 L/(2E)$ is then determined by the distance and neutrino energy. It is also convenient to introduce the oscillation length[19]

$$L_{kj}^{\text{osc}} \equiv 4\pi E/\Delta m_{kj}^2 \tag{2.57}$$

so that the probability turns into

$$P(\nu_{\underline{\alpha}} \to \nu_\beta)(E, L) = \sum_k |\mathsf{U}_{\alpha k}|^2|\mathsf{U}_{\beta k}|^2 + 2\,\Re \sum_{k>j} \mathsf{U}_{\alpha j}\mathsf{U}_{\alpha k}^*\mathsf{U}_{\beta j}^*\mathsf{U}_{\beta k}\mathrm{e}^{-2\pi i L/L_{kj}^{\text{osc}}}. \tag{2.58}$$

In an experimental setting, one needs to take into account uncertainties originating from the finite resolution of the detector and the fact that a neutrino beam is not perfectly

---

[18] The underline refers to the initial flavor.

[19] Sometimes it is convenient to write $L_{kj}^{\text{osc}} = \frac{4\pi E\hbar c}{\Delta m_{kj}^2} \approx 2.48\,\mathrm{m}\frac{E}{\mathrm{MeV}}\frac{\mathrm{eV}^2}{\Delta m_{kj}^2}$.

monochromatic. Another one comes from the fact that the regions where neutrinos are produced and detected have a finite size. This makes it necessary to perform averages over the uncertainties in the energies and distances of the oscillation probability resulting in

$$\langle P(\nu_{\underline{\alpha}} \rightarrow \nu_\beta)(E, L)\rangle = \sum_k |U_{\alpha k}|^2 |U_{\beta k}|^2, \tag{2.59}$$

where the phase is effectively averaged out. Note that the latter expression is independent of the energy and the propagation distance. Furthermore, it applies for incoherent production and detection as well [60].

Due to the unitarity of the mixing matrix, $UU^\dagger = \mathbb{1}$, or equivalently,

$$\delta_{\alpha\beta} = \left(UU^\dagger\right)_{\alpha\beta} = \sum_{j=1}^3 U_{\alpha j} \left(U^\dagger\right)_{j\beta} = \sum_{j=1}^3 U_{\alpha j} U_{\beta j}^*, \tag{2.60}$$

the following two sum rules hold:

$$\sum_\beta P(\nu_{\underline{\alpha}} \rightarrow \nu_\beta) = 1, \qquad \sum_\alpha P(\nu_{\underline{\alpha}} \rightarrow \nu_\beta) = 1. \tag{2.61}$$

If we use the squared modules of eq. (2.60),

$$\delta_{\alpha\beta} = \left| \sum_j U_{\alpha j} U_{\beta j}^* \right|^2 \tag{2.62}$$

$$= \sum_k |U_{\alpha k}|^2 |U_{\beta k}|^2 + 2\Re \sum_{k>j} U_{\alpha j} U_{\beta j}^* U_{\alpha k}^* U_{\beta k}, \tag{2.63}$$

we can write eq. (2.58) in the form

$$
\begin{aligned}
P(\nu_{\underline{\alpha}} \rightarrow \beta)(E, L) = \delta_{\alpha\beta} &- 4 \sum_{k>j} \Re(U_{\alpha j} U_{\alpha k}^* U_{\beta j}^* U_{\beta k}) \sin^2\left(\frac{\pi L}{L_{kj}^{\mathrm{osc}}}\right) \\
&+ 2 \sum_{k>j} \Im(U_{\alpha j} U_{\alpha k}^* U_{\beta j}^* U_{\beta k}) \sin\left(\frac{2\pi L}{L_{kj}^{\mathrm{osc}}}\right).
\end{aligned}
\tag{2.64}
$$

In case of antineutrinos, $P(\bar\nu_{\underline{\alpha}} \rightarrow \bar\nu_\beta)(E, L)$, one obtains the same expression as for neutrinos, but with a minus sign in front of the term involving the imaginary part. Similarly, one can derive an expression for the survival probability in case of only two flavors [39]:

$$P(\nu_{\underline{\alpha}} \rightarrow \nu_\alpha)(E, L) = 1 - \sin^2 2\theta \sin^2\left(\frac{\Delta m^2 L}{4E}\right), \tag{2.65}$$

and for the transition probability ($\alpha \neq \beta$):

$$P(\nu_{\underline{\alpha}} \rightarrow \nu_\beta)(E, L) = \sin^2 2\theta \sin^2\left(\frac{\Delta m^2 L}{4E}\right). \tag{2.66}$$

The averaged transition probability turns out to be

$$\langle P(\nu_{\underline{\alpha}} \rightarrow \nu_\beta)(E, L) \rangle = \frac{1}{2} \sin^2 2\theta. \tag{2.67}$$

2.6 Neutrino oscillations in matter

As first noted by Lincoln Wolfenstein [61], neutrinos on their way through matter can undergo coherent forward elastic scattering[20] off the medium particles which effectively changes their propagation. We consider electrically neutral, ordinary matter consisting of electrons and nucleons. Figure 2.3 shows the Feynman diagrams for elastic neutrino-fermion scattering on tree level. For antineutrinos similar diagrams can be drawn. Here, we have neutral-current (NC) contributions $\nu_\alpha + f \longrightarrow \nu_\alpha + f$ from all flavors $\alpha = e, \mu, \tau$, where f can be any fermion that is part of the medium (e.g., electrons, protons, neutrons) while the only charged-current (CC) contributions originates from the process $\nu_\alpha + l_\alpha^- \longrightarrow \nu_e + l_\alpha^-$. Note that processes like $\nu_{\mu,\tau}$-e^--scattering can only proceed via NC interactions, because at each vertex flavor lepton number has to be conserved. Furthermore, neutrino-proton or neutrino-neutron scattering are only possible via NC processes and there is no ν_μ-μ scattering (similar for ν_τ-τ), since μ- and τ-leptons are too heavy ($m_\mu \approx 106\,\text{MeV}$ and $m_\tau \approx 1.777\,\text{MeV}$) to be produced in the astrophysical environments we are studying[21].

The effective potentials on the mean-field level turn out to be [32, 39]:

$$V_\alpha^e = \sqrt{2} G_F n_e \left(\delta_{\alpha e} - \frac{1}{2} + 2 \sin^2 \theta_W \right) \tag{2.68}$$

in case of neutrino-electron scattering,

$$V_\alpha^n = -\sqrt{2} G_F \frac{n_n}{2} \tag{2.69}$$

for neutrino-neutron scattering,

$$V_\alpha^p = \sqrt{2} G_F n_p \left(\frac{1}{2} - 2 \sin^2 \theta_W \right) \tag{2.70}$$

for neutrino-proton scattering, where θ_W denotes the Weinberg angle, $n_e = n_{e^-} - n_{e^+}$ the net electron number density (n_n and n_p correspond to the net number densities for neutrons and protons, respectively), and α refers to the flavor of the propagating neutrino. In case of a propagating antineutrino, the potentials have the opposite sign. The total effective potential for electron neutrinos is given by the sum $V_e = V_e^e + V_e^n + V_e^p = \sqrt{2} G_F n_e + V_e^n$, where we used $n_e = n_p$ which holds because we are considering an electrically neutral medium. For ν_μ

---

[20] mediated by charged and/or neutral current interaction.

[21] For a non-degenerate fermion and using a Fermi-Dirac distribution, the mean energy can approximately related to the local matter temperature via $\langle E \rangle \approx 3.15\,T$. Only in the central regions of settings like supernovae, the temperatures are sufficiently high to allow a thermal population of muons [62]. At the ν_μ-surface, the temperatures are too low and muons are not important for our discussion.

and ν_τ, we only have NC potential contributions $V_\mu = V_\tau = V_\tau^e + V_\tau^n + V_\tau^p$. Because the NC contributions for the interaction with the medium are the same for all flavors, we can absorb them into a global phase factor. As a consequence we will ignore it in the following. What is important for the flavor evolution are the differences of the potentials, i.e., the energy shifts $V_e - V_\mu = V_e - V_\tau = \sqrt{2}G_\mathrm{F}n_e$.

Note that there are different approaches to compute the effective potentials leading to the same results, e.g., by computing scattering amplitudes and refractive indices[22] (e.g., [61]), by considering free neutrinos propagating in an effective potential (e.g., [39]), or by using thermal quantum field theory methods and compute the neutrino self-energy (e.g., [63]).
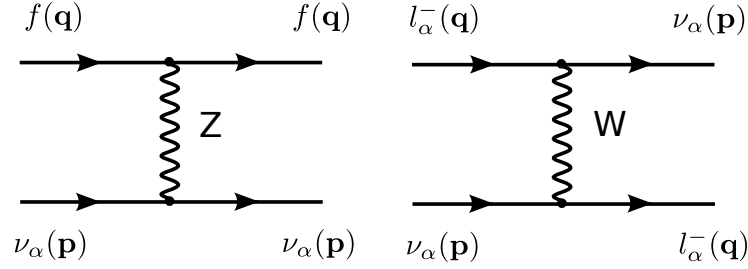
Figure 2.3.: Feynman diagrams for elastic neutrino-electron scattering on tree level. Neutral current (left) and charged current (right) contributions, where $\alpha = e, \mu, \tau$ and f can be any fermion that constitutes the medium.

Before we discuss the flavor evolution in matter, we first elaborate on the nature of the scattering process itself. By forward scattering we refer to small scattering angles θ with $\theta < \pi/2$ while for $\theta > \theta/2$ we talk about backward scattering [64, 65]. Elastic scattering usually proceeds in a coherent way, i.e., neutrinos remain in phase after the scattering event, and for low scattering angles it proceeds mainly in the forward direction[23]. If elastic scattering occurs at larger scattering angles $\theta \gtrsim 10°$, the process becomes more incoherent.

If a particle, like a neutrino, is propagating in a medium and interacting with the background particles, coherence of the scattering implies that the medium does not change and scattered and unscattered wave functions of the neutrino can interfere. The neutrinos interact with the background particles by forward elastic scattering, since the initial and final states coincide [66].

For a coherent process, the total amplitude $\mathcal{M}$ is a coherent sum over n amplitudes $\mathcal{M}_i$, $\mathcal{M} = \sum_{i=1}^{n} \mathcal{M}_i$, for the interaction of a neutrino with one of the n scattering centers (the background particles) [67] like depicted in figure 2.4. The interaction probability is thus given by $|\mathcal{M}|^2 \propto n^2$. Note that in case of incoherent scattering, where we have momentum transfer, $|\mathcal{M}|^2 = \sum_{i=1}^{n} |\mathcal{M}_i|^2 \propto n$ holds. With other words, it is the amplification of the probability due to coherent scattering, which makes the latter of vital importance for practical applications, e.g., in astrophysical settings.

---

[22] In appendix A we will comment on the relation of neutrino propagation and the meaning of the refractive index in this context.

[23] Note that coherent elastic scattering describes two complementary properties: "Elastic" which refers to the particle nature and "coherent" which refers to the wave nature.
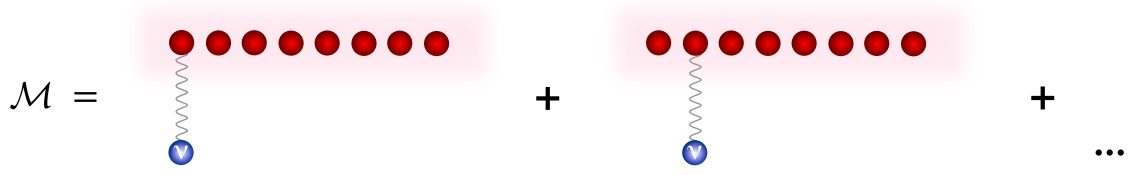
Figure 2.4.: Illustration of the coherent sum of amplitudes for a neutrino interacting with a background (consisting, e.g., of electrons).

We describe coherent forward scattering of neutrinos in ordinary matter by the effective potential $V_{cc} = \sqrt{2}G_F n_e$, where n_e denotes the number density of electrons. In the evolution equation we then need to add the term $\mathrm{diag}(V_{cc}, 0)$. But since a term proportional to the identity does not affect the flavor evolution, we can subtract $V_{cc}\mathbb{1}_2/2$ and define the matter Hamiltonian as

$$\mathsf{H}_{\mathrm{matt}} := \frac{1}{2}\begin{pmatrix} V_{cc} & 0 \\ 0 & -V_{cc} \end{pmatrix}.$$ (2.71)

In the following we consider a two-flavor scheme and we expand the state vector of the neutrino system in the flavor basis:

$$|\psi(t)\rangle = a_{\nu_e}(t)|\nu_e\rangle + a_{\nu_\tau}(t)|\nu_\tau\rangle.$$ (2.72)

In this case, the Schrödinger-like equation with the Hamiltonian $\mathsf{H} = \mathsf{H}_{\mathrm{vac}} + \mathsf{H}_{\mathrm{matt}}$ for the amplitudes is given by

$$i\partial_t \begin{pmatrix} a_{\nu_e}(t) \\ a_{\nu_\tau}(t) \end{pmatrix} = \left\{ \frac{\omega}{2}\begin{pmatrix} -\cos 2\theta & \sin 2\theta \\ \sin 2\theta & \cos 2\theta \end{pmatrix} + \frac{1}{2}\begin{pmatrix} V_{cc} & 0 \\ 0 & -V_{cc} \end{pmatrix} \right\} \begin{pmatrix} a_{\nu_e}(t) \\ a_{\nu_\tau}(t) \end{pmatrix}.$$ (2.73)

2.6.1 Constant matter density

Now we study a constant, i.e., independent of time and space, electron number density n_e. Similar to the case of vacuum oscillations, we diagonalize H in order to find the effective neutrino masses and effective mixing angle in matter. Because the matrix H is a real symmetric (2×2)-matrix, $\mathsf{H}^T = \mathsf{H}$, where ^{T} denotes transposition, and according to the spectral theorem (e.g., see [68]) it can be diagonalized by a similarity transformation with a real orthogonal matrix $\mathsf{U}_m \in O(2)$:

$$\mathsf{H}^{(m)} := \mathsf{U}_m^T \mathsf{H} \mathsf{U}_m = \frac{1}{2E}\mathrm{diag}(\tilde{m}_1^2, \tilde{m}_2^2),$$ (2.74)

where $\tilde{m}_{1,2}^2/(2E)$ correspond to the eigenvalues of H. The latter can be found by the usual procedure, i.e., solving the characteristic equation, $\det[\mathsf{H} - \lambda\mathbb{1}] = 0$, or equivalently:

$$\lambda^2 - \lambda\,\mathrm{tr}\,\mathsf{H} + \det\mathsf{H} = \lambda^2 - \frac{1}{4}(V_{\mathrm{cc}} - \omega\cos 2\theta)^2 - \frac{1}{4}\omega^2\sin^2 2\theta = 0. \tag{2.75}$$

If we express the eigenvalues, which represents energy shifts, in terms of mass shifts, $\lambda_{1,2} =: \delta\tilde{m}_{1,2}^2/(2E)$, we find

$$\delta\tilde{m}_1^2 = -E\sqrt{(V_{\mathrm{cc}} - \omega\cos 2\theta)^2 + \omega^2\sin^2 2\theta}, \tag{2.76}$$

$$\delta\tilde{m}_2^2 = +E\sqrt{(V_{\mathrm{cc}} - \omega\cos 2\theta)^2 + \omega^2\sin^2 2\theta}. \tag{2.77}$$

Introducing the effective mass splitting[24]

$$\Delta\tilde{m}^2 \equiv \delta\tilde{m}_2^2 - \delta\tilde{m}_1^2 = 2E\sqrt{(V_{\mathrm{cc}} - \omega\cos 2\theta)^2 + \omega^2\sin^2 2\theta}, \tag{2.78}$$

allows us to write

$$\mathsf{H}^{(\mathrm{m})} = \frac{1}{4E}\mathrm{diag}(-\Delta\tilde{m}^2, \Delta\tilde{m}^2). \tag{2.79}$$

Since $\mathsf{U}_{\mathrm{m}} \in O(2)$, we can introduce an effective mixing angle in matter, θ_{m}, through the following parametrization w.l.o.g.:

$$\mathsf{U}_{\mathrm{m}} = \begin{pmatrix} \cos\theta_{\mathrm{m}} & \sin\theta_{\mathrm{m}} \\ -\sin\theta_{\mathrm{m}} & \cos\theta_{\mathrm{m}} \end{pmatrix}. \tag{2.80}$$

Finally, the Hamiltonian assumes a similar form as in vacuum

$$\mathsf{U}_{\mathrm{m}}\mathsf{H}^{(\mathrm{m})}\mathsf{U}_{\mathrm{m}}^{\mathsf{T}} = \frac{\omega}{2}\begin{pmatrix} -\cos 2\theta_{\mathrm{m}} & \sin 2\theta_{\mathrm{m}} \\ \sin 2\theta_{\mathrm{m}} & \cos 2\theta_{\mathrm{m}} \end{pmatrix} \tag{2.81}$$

and an analogous relation to eq. (2.48) holds:

$$\tan 2\theta_{\mathrm{m}} = \frac{2\mathsf{H}_{e\tau}}{\mathsf{H}_{\tau\tau} - \mathsf{H}_{ee}} = \frac{\omega\sin 2\theta}{\omega\cos 2\theta - V_{\mathrm{cc}}}, \tag{2.82}$$

$$\sin 2\theta_{\mathrm{m}} = \frac{\omega\sin 2\theta}{\sqrt{(\omega\cos 2\theta - V_{\mathrm{cc}})^2 + \omega^2\sin^2 2\theta}}. \tag{2.83}$$

As eq. (2.82) indicates, the "most dramatic" change of the mixing angle appears if the resonance-condition

$$\omega\cos 2\theta = V_{\mathrm{cc}} \tag{2.84}$$

---

[24] Note that in the vacuum limit, $V_{\mathrm{cc}} \to 0$, we recover $\Delta\tilde{m}^2 \to \Delta m^2$ and $\mathsf{U}_{\mathrm{m}} \to \mathsf{U}$.

is satisfied, or in other words, if the electron number density reaches the critical value

$$n_e = \frac{\Delta m^2 \cos 2\theta}{2\sqrt{2}G_F E}.$$

(2.85)

In this case, the difference of the eigenvalues of H is minimal. At resonance, even for a small vacuum mixing angle θ, we obtain $\theta_m = \pi/4$ corresponding to maximal mixing between ν_e and ν_τ. Note that in the limit of a strong matter effect ($V_{cc} \to \infty$) we have $\theta_m \to \pi/2$.

2.6.2 Slowly-varying matter density

In what follows we consider a more realistic matter density, i.e., a time-dependent n_e. For a specific neutrino source (e.g., the Sun), the time dependence (t) should be understood as the distance (r) dependence of n_e, if we assume that the emitted neutrinos are relativistic.

Because the mass states in matter are not eigenstates during the whole evolution, but only for a given moment in time, we call them instantaneous mass eigenstates in matter (or propagation eigenstates). They are related to the flavor eigenstates via:

$$\begin{pmatrix} |\nu_e\rangle \\ |\nu_\tau\rangle \end{pmatrix} = U_m \begin{pmatrix} |\tilde{\nu}_1\rangle \\ |\tilde{\nu}_2\rangle \end{pmatrix} = \begin{pmatrix} \cos\theta_m & \sin\theta_m \\ -\sin\theta_m & \cos\theta_m \end{pmatrix} \begin{pmatrix} |\tilde{\nu}_1\rangle \\ |\tilde{\nu}_2\rangle \end{pmatrix},$$

(2.86)

where $\theta_m = \theta_m(t)$ varies with time.

Expanding the state vector in both, the instantaneous mass and flavor basis,

$$|\psi(t)\rangle = a_1(t)|\tilde{\nu}_1\rangle + a_2(t)|\tilde{\nu}_2\rangle$$

(2.87)

$$= a_{\nu_e}(t)|\nu_e\rangle + a_{\nu_\tau}(t)|\nu_\tau\rangle,$$

(2.88)

we find for the amplitudes:

$$\begin{pmatrix} a_{\nu_e}(t) \\ a_{\nu_\tau}(t) \end{pmatrix} = U_m \begin{pmatrix} a_1(t) \\ a_2(t) \end{pmatrix}.$$

(2.89)

Writing the Schrödinger-like equation (2.73) in a more compact form,

$$i\partial_t \begin{pmatrix} a_{\nu_e}(t) \\ a_{\nu_\tau}(t) \end{pmatrix} = \frac{1}{2E} \left\{ U_m \begin{pmatrix} \tilde{m}_1^2 & 0 \\ 0 & \tilde{m}_2^2 \end{pmatrix} U_m^\dagger \right\} \begin{pmatrix} a_{\nu_e}(t) \\ a_{\nu_\tau}(t) \end{pmatrix},$$

(2.90)

and using eq. (2.89) we arrive at the equation:

$$i\partial_t \begin{pmatrix} a_1(t) \\ a_2(t) \end{pmatrix} = i\partial_t \left[\mathsf{U}_{\mathrm{m}}^\dagger \begin{pmatrix} a_{\nu_e}(t) \\ a_{\nu_\tau}(t) \end{pmatrix} \right] \tag{2.91}$$

$$= \left\{ i\left(\partial_t \mathsf{U}_{\mathrm{m}}^\dagger\right)\mathsf{U}_{\mathrm{m}} + \frac{1}{2E}\begin{pmatrix} \tilde{m}_1^2 & 0 \\ 0 & \tilde{m}_2^2 \end{pmatrix} \right\} \begin{pmatrix} a_1(t) \\ a_2(t) \end{pmatrix} \tag{2.92}$$

$$= \frac{1}{2E}\begin{pmatrix} \tilde{m}_1^2 & -i2E\dot{\theta}_{\mathrm{m}}(t) \\ i2E\dot{\theta}_{\mathrm{m}}(t) & \tilde{m}_2^2 \end{pmatrix} \begin{pmatrix} a_1(t) \\ a_2(t) \end{pmatrix}, \tag{2.93}$$

where $\dot{\theta}_{\mathrm{m}}(t) \equiv \partial[\theta_{\mathrm{m}}(t)]/\partial t$. Making use of eq. (2.78) and dropping terms proportional to the identity matrix leads us:

$$i\partial_t \begin{pmatrix} a_1(t) \\ a_2(t) \end{pmatrix} = \begin{pmatrix} -\Delta\tilde{m}^2/(4E) & -i\dot{\theta}_{\mathrm{m}}(t) \\ i\dot{\theta}_{\mathrm{m}}(t) & \Delta\tilde{m}^2/(4E) \end{pmatrix} \begin{pmatrix} a_1(t) \\ a_2(t) \end{pmatrix}. \tag{2.94}$$

If for a given neutrino energy, the external conditions, such as density and electron fraction, change sufficiently slowly so that the system has enough time to adapt, the off-diagonal elements of the Hamiltonian are small compared to the relevant energy scales of the system. This yields the so-called adiabaticity condition $|\dot{\theta}_m(t)| \ll |\Delta\tilde{m}^2|/(4E)$.

By computing the eigenvalues of the Hamiltonian, i.e.,

$$\pm\sqrt{\left(\frac{\Delta\tilde{m}^2}{4E}\right)^2 + \dot{\theta}_{\mathrm{m}}(t)^2} = \pm\sqrt{\left(\frac{\tilde{m}_2^2 - \tilde{m}_1^2}{4E}\right)^2 + \dot{\theta}_{\mathrm{m}}(t)^2}, \tag{2.95}$$

we recognize that the only relevant energy quantity [37, 69] is given by the energy gap $|\tilde{m}_2^2 - \tilde{m}_1^2|/(2E)$ between the energy levels corresponding to $\tilde{m}_1^2/(2E)$ and $\tilde{m}_2^2/(2E)$, respectively. In the adiabatic approximation, the evolution equations for the instantaneous mass eigenstates decouple resulting in two homogeneous linear differential equations of first order. In other words, there are no transitions between mass eigenstates and they propagate independently. As a consequence, we can simply integrate eq. (2.94) and find the solutions:

$$a_1(t) = a_1(t_0)\exp\left(+i\int_{t_0}^t \mathrm{d}t' \frac{\Delta\tilde{m}^2(t')}{4E}\right), \tag{2.96}$$

$$a_2(t) = a_2(t_0)\exp\left(-i\int_{t_0}^t \mathrm{d}t' \frac{\Delta\tilde{m}^2(t')}{4E}\right). \tag{2.97}$$

We emphasize the fact that also the masses $\tilde{m}_1$ and $\tilde{m}_2$ become time-dependent. Furthermore, note that during the adiabatic evolution we neglect the derivative $\mathrm{d}\theta_{\mathrm{m}}/\mathrm{d}t$, but still take

the variation of the mixing angle $\theta_m(t)$ with the density into account. Consequently, the amplitudes to find the neutrino in a specific flavor (e, τ) are:

$$a_{\nu_e}(t) = \cos\theta_m a_1(t) + \sin\theta_m a_2(t), \tag{2.98}$$

$$a_{\nu_\tau}(t) = -\sin\theta_m a_1(t) + \cos\theta_m a_2(t). \tag{2.99}$$

If we impose the initial condition where we have only electron neutrinos at $t = t_0$,

$$a_{\nu_e}(t_0) = 1 \quad \text{and} \quad a_{\nu_\tau}(t_0) = 0, \tag{2.100}$$

we obtain $a_1(t_0) = \cos\theta_m(t_0)$ and $a_2(t_0) = \sin\theta_m(t_0)$. This allows us to compute the survival probability of electron neutrinos:

$$P(\nu_{\underline{e}} \rightarrow \nu_e)(t) = |a_{\nu_e}(t)|^2 \tag{2.101}$$

$$= \frac{1}{2}\left[1 + \cos 2\theta_m(t) \cos 2\theta_m(t_0)\right]$$

$$+ \frac{1}{2}\sin 2\theta_m(t)\sin 2\theta_m(t_0)\cos\left(\int_{t_0}^{t} dt' \frac{\Delta\tilde{m}^2(t')}{2E}\right). \tag{2.102}$$

For neutrinos produced in a very dense medium, where we can take $n_e(t_0) \rightarrow \infty$, the initial neutrino mixing is expected to be $\theta_m(t_0) = \pi/2$. On the other hand, the final mixing angle should assume its value in vacuum, $\theta_m(t) = \theta$, because in practice, the final angle is usually measured by detectors below the Earth's surface like IceCube [39].

In addition, we note that for realistic experiments, only the probability averaged over the energy spectrum and detection time is relevant and therefore, the last term in eq. (2.102) will vanish:

$$\langle P(\nu_{\underline{e}} \rightarrow \nu_e)\rangle = \frac{1}{2}\left[1 - \cos 2\theta\right] = \sin^2\theta. \tag{2.103}$$

This can be understood as follows. In the high density region where $\theta_m \rightarrow \pi/2$, the $|\nu_e\rangle$ is initially produced in the mass eigenstate $|\tilde{\nu}_2\rangle$ whereas $|\nu_\tau\rangle$ corresponds to $-|\tilde{\nu}_1\rangle$. While the matter density decreases in a very slowly manner such that the adiabatic condition is satisfied, the initial neutrino state $|\nu_e\rangle$ will remain in the same mass eigenstate $|\tilde{\nu}_2\rangle$ during its propagation through the density gradient. As we arrive in vacuum, we end up with the mass eigenstate $|\nu_2\rangle$ implying that the probability of finding it there as the electron neutrino is just $|\langle\nu_e|\tilde{\nu}_2(t)\rangle|^2 = \sin^2\theta$. This is the so-called resonant conversion phenomenon or MSW effect (after Stanislav Mikheyev, Alexei Smirnov and Lincoln Wolfenstein) [70, 71] (for a review, see [69]), which is most effective for a very small mixing angle θ leading to almost complete flavor conversions: $\nu_e \rightarrow \nu_\tau$. In figure 2.5 we qualitatively show this evolution in a diagram of the eigenvalues of $H^{(m)}$.

Note that far above the resonance, $V_{cc} \gg \omega \cos 2\theta$, the mass squared value $\tilde{m}_2^2(V_{cc})$ depends linearly on V_{cc} and because of $V_{cc} \propto n_e$ also linearly on the matter number density n_e while $\tilde{m}_1^2$ becomes independent of V_{cc}. These quantities are also called matter-induced [52] or effective

[72] mass squared values of the ν_e and ν_τ, respectively.

If we follow these matter-induced values (the blue dashed lines in figure 2.5) beginning in the high density region, we recognize that the value of ν_e starts higher than that of ν_τ, but with the decrease of n_e, the difference between the two effective values also decreases. At the resonance it is even vanishing. Arriving at very low densities or in vacuum, we see that the value of ν_τ has finally overtaken that of ν_e. Note that this phenomenon was identified with avoided level-crossing [73].
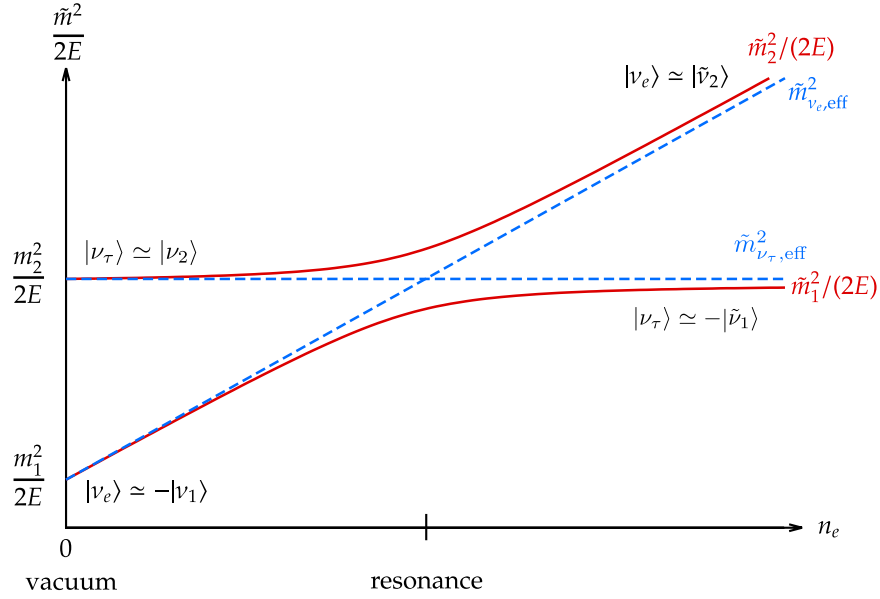
Figure 2.5.: Eigenvalue diagram of the matter Hamiltonian $H^{(m)}$. The instantaneous mass eigenstates propagate through the density gradient leading to an adiabatic flavor conversion. The red solid lines correspond to the mass squared values of the mass eigenstates, while the blue dashed lines correspond to the effective mass squared values of the ν_e and ν_τ, respectively.

The crucial point during this evolution is the validity of the adiabaticity condition $|\dot{\theta}_m(t)| \ll |\Delta\tilde{m}^2|/(4E)$. Note that a larger splitting $\Delta\tilde{m}^2$ at resonance will lead to a more adiabatic flavor evolution [57].

Using eqs. (2.78) and (2.82) with $\theta_m = \theta_m(t)$, $V_{cc} = V_{cc}(t)$ and $\Delta\tilde{m}^2 = \Delta\tilde{m}^2(t)$ we find

$$\dot{\theta}_m(t) = \frac{2E^2\omega\sin 2\theta}{[\Delta\tilde{m}^2(t)]^2}\dot{V}_{cc}(t) = \sqrt{2}G_F E\frac{\Delta m^2\sin 2\theta}{[\Delta\tilde{m}^2(t)]^2}\dot{n}_e(t). \tag{2.104}$$

The last equation allows us to express the adiabaticity condition in terms of the oscillation lengths in vacuum, $\lambda \equiv 4\pi E/(\Delta m^2)$ (see also eq. (2.57)), and in matter, $\lambda_m \equiv 4\pi E/(\Delta\tilde{m}^2)$ (cf. [52]):

$$\sqrt{2}G_F|\dot{n}_e(t)| \ll \frac{4\pi^2\lambda}{\lambda_m^3\sin 2\theta}. \tag{2.105}$$

However at the resonance point $t = t_r$, i.e., $A(t_r) = \Delta m^2 \cos 2\theta$ where the oscillation length λ_m becomes maximal, the adiabaticity condition might be violated. On the resonance we may define the so-called adiabaticity parameter [32, 52]

$$\gamma \equiv \frac{1}{4E} \left[\left| \frac{\Delta \tilde{m}^2(t)}{\dot{\theta}_m(t)} \right| \right]_{t=t_r} = \frac{\Delta m^2 \sin^2 2\theta}{2E \cos 2\theta} \left[\frac{|\dot{n}_e(t)|}{n_e(t)} \right]_{t=t_r}^{-1} , \tag{2.106}$$

where now the adiabaticity condition reads as $\gamma \gg 1$. If γ is of $\mathcal{O}(1)$, the off-diagonal matrix elements in eq. (2.94) will no longer be negligible. In this non-adiabatic region a transition between the instantaneous mass eigenstates $|\tilde{\nu}_1\rangle$ and $|\tilde{\nu}_2\rangle$ takes place, so the oscillation probabilities will be significantly modified. Before we briefly comment on non-adiabatic flavor transformations, we stress the fact that adiabatic flavor conversion can occur practically without oscillations.

2.6.3 Adiabatic flavor transformation

Analogously as shown in [74], we schematically present different conversion patterns that could appear during an adiabatic flavor evolution. In order to simplify the discussion, we focus on a monotonically decreasing matter profile[25], but applications to other types of profiles are straightforward. We can differ between three cases:

1. If the initial electron number density n_e^i strongly exceeds the resonance number density n_e^{res} (top part of figure 2.6), mixing is initially suppressed. The electron flavor ν_e is mainly composed of the matter mass eigenstate ν_{2m}. When the neutrino goes through the resonance at $n_e^i \approx n_e^{res}$, the mixing becomes maximal. Far below the resonance number density $n_e \ll n_e^{res}$, the flavor eigenstate is still mainly composed of ν_{2m} (the other matter mass eigenstate ν_{1m} gives only a minor contribution), so interference, or with other words, oscillations are practically suppressed. In this case neutrinos undergo a non-oscillatory flavor transition.

   If we consider the limit $n_e \to 0$, i.e., if we arrive in vacuum, then $\nu_{2m} \to \nu_2$ and we have

$$P(\nu_{\underline{e}} \to \nu_e)(r) = |\langle \nu_e | \nu_{\underline{e}}(r)\rangle|^2 \tag{2.107}$$

$$\approx |\langle \nu_e | \nu_{2m}(r)\rangle|^2 \xrightarrow{n_e \to 0} |\langle \nu_e | \nu_2\rangle|^2 = \sin^2 \theta. \tag{2.108}$$

   As outlined in [74], deviations from this value point to oscillations.

2. If the electron number density only slightly exceeds the resonance density, the initial mixing is not suppressed. Still, ν_{2m} dominates the initial flavor state ν_e, but in contrast to the first case, the other matter mass eigenstate gives a sufficiently large contribution so that the interference between the two matter mass eigenstates is not negligible. As

---

[25] Here we study the dependence on the distance, rather than on time.

a result, the flavor transformation is due to both, adiabatic resonant conversion and oscillations.

3. If the electron number density is below the resonance density, the resonance region will not be encountered, and hence, only oscillations (which are modified due to matter compared to the vacuum case) are present.
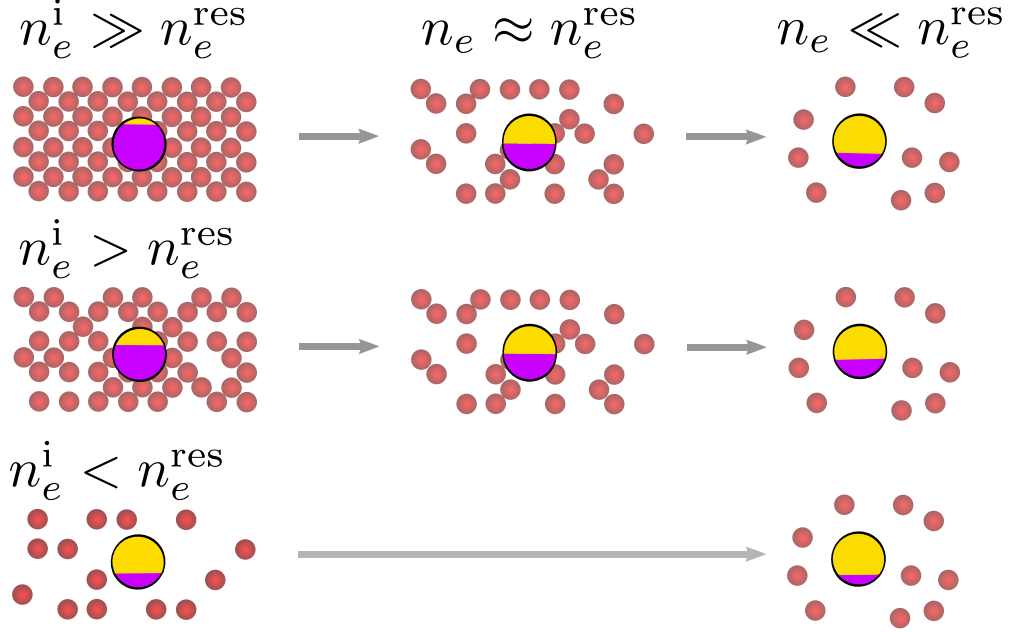

Figure 2.6.: Pattern of adiabatic flavor conversion in matter.

At this point we want to stress, that the results on solar neutrinos obtained by SNO are mainly a consequence of resonant flavor conversion through the MSW mechanism. The measurements are indeed consistent with this picture: As outlined above (point 1), the survival probability for electron neutrinos turns out to be $P_{\text{res}}(\nu_e \to \nu_e) = \sin^2 \theta_{12} \approx 0.32$, i.e., it is essentially determined by the solar mixing angle θ_{12}. On the other hand, the experimentally obtained value by SNO yields [75] $P_{\text{SNO}}(\nu_e \to \nu_e) = \phi_{\text{CC}}/\phi_{\text{NC}} = 0.340 \pm 0.023\,(\text{stat.})^{+0.029}_{-0.031}\,(\text{syst.})$, where ϕ_{CC} corresponds to the charged current contribution which is only sensitive to ν_e while ϕ_{NC} denotes the neutral current flux of all neutrino flavors. The small deviations between P_{SNO} and P_{res} originate from averaged oscillations and from regeneration effects of ν_e in the Earth matter [76]. The latter effect can be explained as follows. If solar neutrinos are measured at night, they will pass through the Earth before they reach the detector. Since in this case the encountered matter densities are not negligible[26], the MSW effect can be efficient. This means that ν_μ and ν_τ coming from $\nu_e \to \nu_\mu$ and $\nu_e \to \nu_\tau$ transitions, respectively, can be transformed back to ν_e (so-called ν_e-regeneration).

The bottom line of the discussion is that the dominant contribution to P_{SNO} is due the MSW effect and oscillations only play a minor role. Strictly speaking, while Super-Kamiokande has

---

[26] In contrast, during the day neutrinos only pass through a relatively thin layer of Earth crust matter which is located just above the underground detector [39]. The different types of behaviors lead to a so-called day-night asymmetry.

discovered neutrino flavor oscillations, SNO essentially found flavor transformations (which are almost non-oscillatory) due to the MSW effect (for a pedagogical discussion, see [76]).

2.6.4 Non-adiabatic flavor transformation

In what follows we will briefly comment on non-adiabatic flavor evolutions. In section 2.6.2 we inferred from eq. (2.102) the averaged probability[27]

$$\langle P(\nu_{\underline{e}} \to \nu_e)\rangle = \frac{1}{2}\left(1 + \cos 2\theta_{\mathrm{m}}(r)\cos 2\theta\right) \tag{2.109}$$

which describes the neutrino propagation through matter and the flavor transformation due to the MSW effect. It is valid as long as the adiabatic approximation applies. However, if the latter is not justified one needs to solve the equation of motion directly (usually a numerical treatment becomes necessary[28]). Still, there exists an analytical formula for $\langle P(\nu_{\underline{e}} \to \nu_e)\rangle$ that takes into account non-adiabatic effects [77]. Typically such effects become important only in a small region around the resonance location while outside the adiabatic approximation might still hold.

In case where the scale of the off-diagonal elements in eq. (2.94) becomes comparable to that of the diagonal elements (i.e., $\gamma \approx 1$), we can describe corrections to the adiabatic approximation by a level crossing, i.e., a flip between instantaneous mass eigenstates $|\tilde{\nu}_1\rangle \leftrightarrow |\tilde{\nu}_2\rangle$. The probability P_{c} for such a crossing takes the form

$$P_{\mathrm{c}} = |\langle \tilde{\nu}_2(r_+)|\tilde{\nu}_1(r_-)\rangle|^2, \tag{2.110}$$

where $r_+ \gg r_{\mathrm{res}}$ and $r_- \ll r_{\mathrm{res}}$ denote two locations far away from the resonance point located at r_{res} and where the adiabatic description holds. The probability for $\tilde{\nu}_1$ or $\tilde{\nu}_2$ to remain in its propagation eigenstate is consequently given by $1 - P_{\mathrm{c}}$ [52].

With these considerations we can "generalize" eq. (2.109) to the Parke formula [77]

$$\langle P(\nu_e \to \nu_e)\rangle = \frac{1}{2} + \left(\frac{1}{2} - P_{\mathrm{c}}\right)\cos 2\theta_{\mathrm{m}}(r)\cos 2\theta, \tag{2.111}$$

which effectively takes into account non-adiabatic corrections that are hidden in the expression for P_{c}. An explicit expression for P_{c} is usually obtained numerically. In the adiabatic limit ($\gamma \gg 1$ and $P_{\mathrm{c}} = 0$), eq. (2.111) reduces to eq. (2.109).

For narrow resonances one could approximately use a simple analytical function to describe the density profile within the resonance region. This way one can obtain analytical expressions

---

[27] As in the previous section, we consider the dependence on distance, rather than on time. Furthermore we take $\theta_{\mathrm{m}}(r_0) = \theta$.

[28] But for a few matter density profiles the equation of motion can yield exact solutions.

for P_c. For linear profiles one finds the so-called Landau-Zener formula [78, 79] (see also Stückelberg (1932) [80], Majorana (1932) [81])[29]:

$$P_c = \exp\left(-\frac{\pi}{2}\gamma\right).$$ (2.112)

In some practical applications it can already yield a sufficiently accurate approximation.

For a more detailed discussion of non-adiabatic neutrino flavor transformations we refer to [32, 39, 52] and references therein.

2.6.5 Numerical calculations

In the following we solve the evolution equation eq. (2.90) for neutrinos propagating in an ordinary matter background. We consider the two-flavor case with Δm_{31}^2 and θ_{13} in the normal mass hierarchy. In particular we consider the case when neutrinos are streaming off a supernova core. For this purpose, we use the late-time spectra of the form

$$f_\alpha(E) = N\left(\frac{E}{\langle E\rangle}\right)^\alpha e^{-(\alpha+1)E/\langle E\rangle},$$ (2.113)

$$N^{-1} \equiv \int_0^\infty dE \left(\frac{E}{\langle E\rangle}\right)^\alpha e^{-(\alpha+1)E/\langle E\rangle} = (\alpha+1)^{-(\alpha+1)}\Gamma(\alpha+1)\langle E\rangle,$$ (2.114)

with a parametrization according to table 6, $p = 10$, $q = 3.5$ in [83] which is summarized in table 2.4. Like in [84] and motivated by the neutrino-driven wind studies in [85], we employ

Neutrino species	$\langle E_\nu\rangle$ [MeV]	$(L_\nu/10^{51})$ [erg / s]	α []
ν_e	9.4	4.1	5.0
$\bar{\nu}_e$	13.0	4.3	3.4
ν_x	15.8	7.9	3.1

Table 2.4.: Parametrization for neutrino spectra.

the following baryon-density profile

$$\rho(r) = 10^8 \, \text{g cm}^{-3} \left(\frac{10\,\text{km}}{r^3}\right)$$ (2.115)

and set the electron fraction to $Y_e = 0.4$.

The results are presented in figure 2.7, where in the upper panel the matter and vacuum potentials are shown. Here, $\lambda \equiv V_{cc}$ corresponds to the charged current potential for ν_e-e

---

[29] Note that this formula is well-known in studies of two-level problems in quantum mechanics and has various fields of applications. In the theory of atomic and molecular collisions it has been studied independently by Landau, Zener, and Stückelberg while Majorana obtained similar results in the context of the dynamics of spin-$\frac{1}{2}$ particles in time-varying magnetic fields. For a discussion of the individual contributions and historical notes, see [82].

scattering. In the lower panel, we show the energy-dependent electron neutrino survival probabilities. It is evident that the location of the resonances is different for each neutrino energy. To make this even more transparent, we show in figure (2.8), the survival probabilities as a function of the distance and energy. The white line corresponds to the position in the E-r plane where the resonance condition is satisfied. Note that for antineutrinos the resonance condition is not satisfied, because the corresponding matter potential is negative $V_{cc} < 0$.
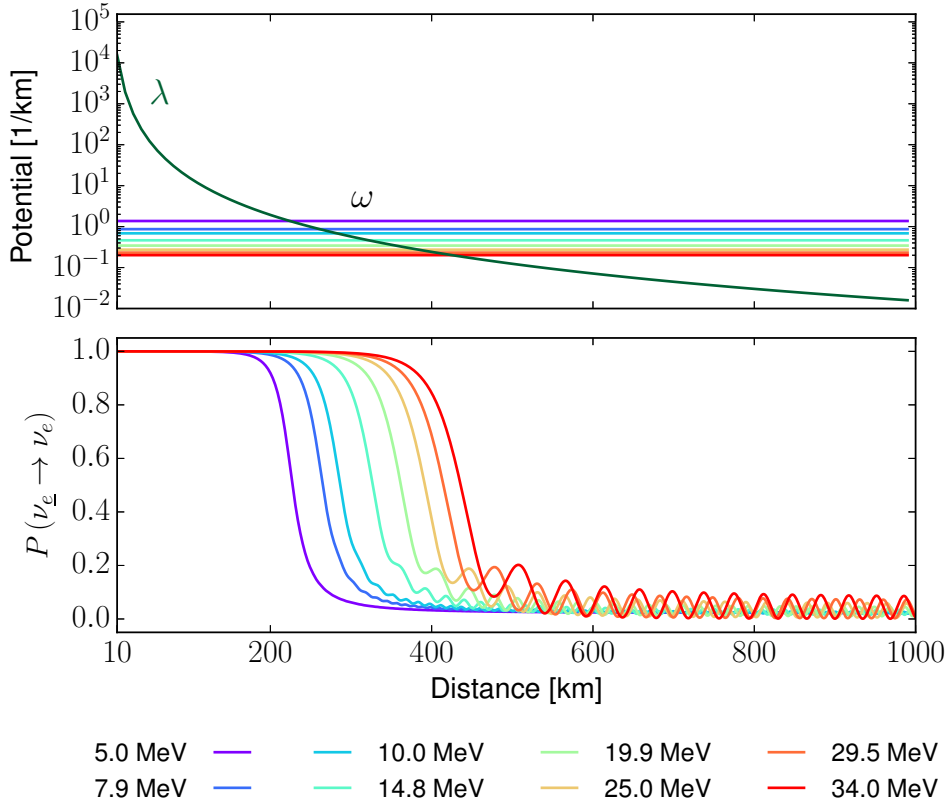
Figure 2.7.: The upper panel shows the matter and the vacuum potential for different energies while the lower panel shows the energy-dependent survival probabilities. The results are obtained in the two-flavor approximation and NH.

In figure 2.9, we show $\sin^2(2\theta_{\text{eff}})$, where θ_{eff} denotes the effective mixing angle in matter, as function of λ/ω. The resonance shape is immediately visible and the resonance width at half maximum[30] corresponds to $2\sin(2\theta)$. Similarly, we can give the width in the scale of the potential: $\Delta V = \omega \sin 2\theta$. Furthermore, we show in in figure 2.10, the effective masses, or to be precise, the energy shifts $\tilde{E}_k$ corresponding to the eigenvalues of the propagation Hamiltonian, as function of λ showing a similar behavior as in figure 2.5 and explained in section 2.6.2.

---

[30] The resonance width at half maximum can be obtained from the relation for the in-medium mixing angle eq. (2.83) and solving $\sin^2(2\theta_m) = 1/2$ for λ/ω. A straightforward calculations yields $(\lambda/\omega)_\pm = \cos 2\theta \pm \sin 2\theta$ and for the width $(\lambda/\omega)_+ - (\lambda/\omega)_- = 2\sin 2\theta$.
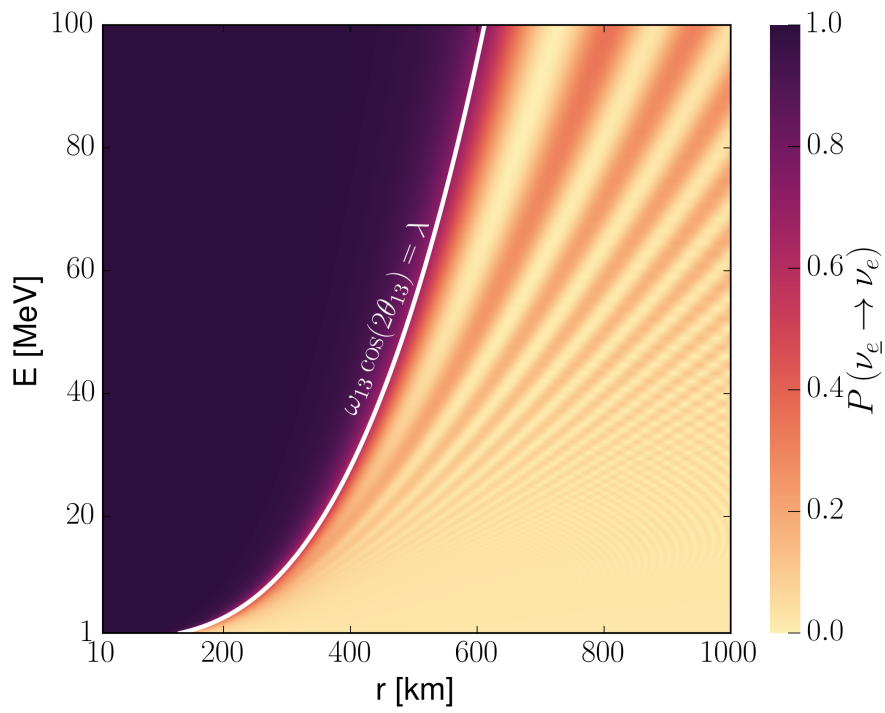
Figure 2.8.: Electron neutrino survival probability as a function of distance and energy. Adiabatic flavor conversion through the MSW mechanism for two flavors.
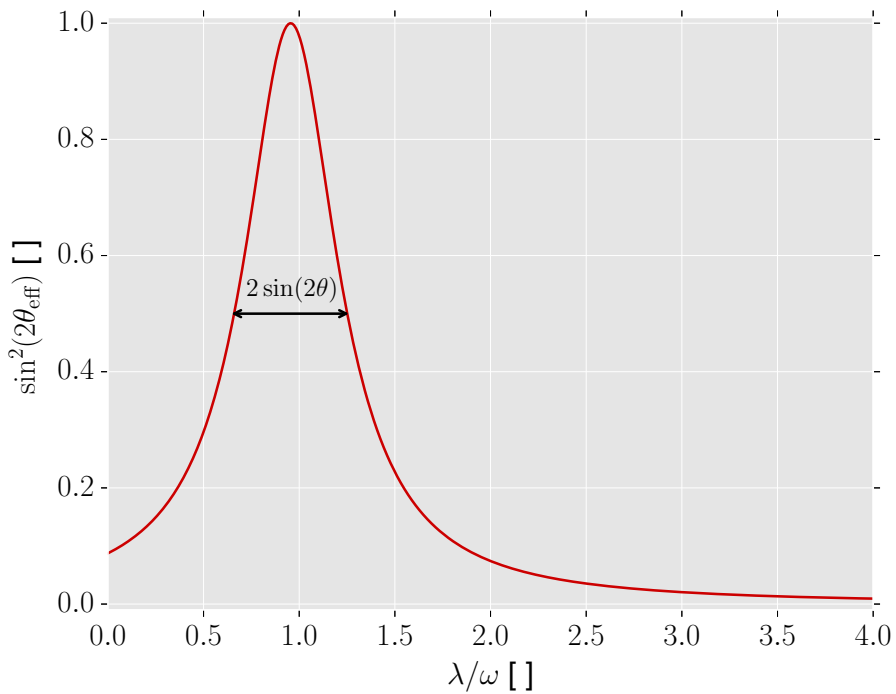
Figure 2.9.: Effective mixing angle $\sin^2(2\theta_{\text{eff}})$ as function of the ratio λ/ω.
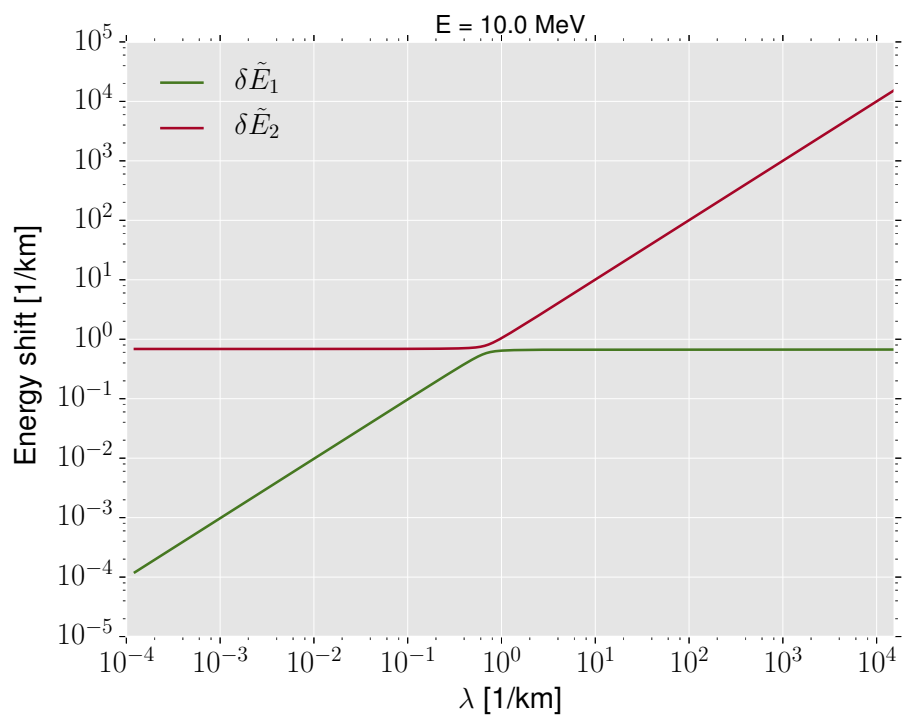
Figure 2.10.: Energy shifts $\tilde{E}_k$ as functions of the matter potential λ.

2.7 Neutrino flavor isospin

> ❝
>
> *To 'gyre' is go to round and round like a gyroscope.*
>
> ❞
>
> Lewis Caroll
>
> Through the Looking-Glass, and What Alice Found There (1871)

If we consider the two-flavor case, there exists an elegant geometrical way to describe neutrino oscillations and resonance phenomena. In the following we will make use of the fact that the Pauli matrices together with the identity $\mathbb{1}$ form a complete basis of the vector space $\mathrm{Mat}(2, \mathbb{C})$ of all complex 2×2 matrices. In particular, every $\mathcal{M} \in \mathrm{Mat}(2, \mathbb{C})$ can be decomposed as

$$\mathcal{M} = \frac{1}{2}\left(\mathrm{tr}[\mathcal{M}] \cdot \mathbb{1} + \sum_{k=1}^{3} \mathrm{tr}[\mathcal{M}\sigma_k]\sigma_k\right) \tag{2.116}$$

$$= \frac{1}{2}\left(\mathrm{tr}[\mathcal{M}] \cdot \mathbb{1} + \mathbf{M} \cdot \boldsymbol{\sigma}\right), \tag{2.117}$$

where $\mathbf{M} \equiv \mathrm{tr}[\mathcal{M}\boldsymbol{\sigma}] \in \mathbb{R}^3$.

This immediately allows the application on to the problem of neutrino flavor evolution. Let us consider an arbitrary traceless Hamiltonian H. Then, we can perform the decomposition[31] $\mathsf{H} = -\frac{1}{2}\mathbf{H} \cdot \boldsymbol{\sigma}$, where

$$\mathbf{H} := -\mathrm{tr}(\mathsf{H}\boldsymbol{\sigma}) = -\begin{pmatrix} 2\,\mathrm{Re}(\mathsf{H}_{\tau e}) \\ 2\,\mathrm{Im}(\mathsf{H}_{\tau e}) \\ \mathsf{H}_{ee} - \mathsf{H}_{\tau\tau} \end{pmatrix}. \tag{2.118}$$

Essentially this means we can equivalently describe a (2×2)-Hamiltonian in terms of a vector which is part of a real, three-dimensional flavor space with basis vectors denoted by

$$\hat{\mathbf{e}}_x^{\mathrm{f}} = \begin{pmatrix} 1 \\ 0 \\ 0 \end{pmatrix}, \quad \hat{\mathbf{e}}_y^{\mathrm{f}} = \begin{pmatrix} 0 \\ 1 \\ 0 \end{pmatrix}, \quad \hat{\mathbf{e}}_z^{\mathrm{f}} = \begin{pmatrix} 0 \\ 0 \\ 1 \end{pmatrix}. \tag{2.119}$$

Applied on the vacuum Hamiltonian,

$$\mathsf{H}_{\mathrm{vac}} = \frac{\omega}{2}\begin{pmatrix} -\cos 2\theta & \sin 2\theta \\ \sin 2\theta & \cos 2\theta \end{pmatrix}, \tag{2.120}$$

---

[31] Note that the minus sign is only convention.

this yields

$$\mathbf{H}_{\text{vac}} := -\text{tr}\left(H_{\text{vac}}\sigma\right) \tag{2.121}$$

$$= \omega \begin{pmatrix} -\sin 2\theta \\ 0 \\ \cos 2\theta \end{pmatrix} \tag{2.122}$$

$$=: \omega \hat{\mathbf{H}}_{\text{vac}}. \tag{2.123}$$

As an interesting fact, we note that since SU(2) is the two-fold covering group of SO(3), the angle between the mass $\hat{\mathbf{H}}_{\text{vac}}$ and the flavor direction $\hat{\mathbf{e}}_z^f$ corresponds to twice the vacuum mixing angle (2θ).

Similarly, we consider the matter term

$$H_{\text{matt}} = \sqrt{2}G_F n_e \begin{pmatrix} 1/2 & 0 \\ 0 & -1/2 \end{pmatrix} \tag{2.124}$$

and introduce

$$\mathbf{H}_{\text{matt}} := -\text{tr}\left(H_{\text{matt}}\sigma\right) \tag{2.125}$$

$$= V_e \begin{pmatrix} 0 \\ 0 \\ -1 \end{pmatrix} \tag{2.126}$$

$$=: V_e \hat{\mathbf{H}}_{\text{matt}} \tag{2.127}$$

with $V_e \equiv \sqrt{2}G_F n_e$.

Instead of working with SU(2)-spinors

$$\psi_\nu = \begin{pmatrix} a_{\nu_e} \\ a_{\nu_\tau} \end{pmatrix}, \tag{2.128}$$

or state vectors $|\psi_\nu\rangle = a_{\nu_e}|\nu_e\rangle + a_{\nu_\tau}|\nu_\tau\rangle$, where $a_{\nu_\alpha} \in \mathbb{C}$ denotes the amplitude for a neutrino to be in flavor $\alpha \in \{e, \tau\}$ with $|a_{\nu_e}|^2 + |a_{\nu_\tau}|^2 = 1$, we will work with vectors $\in \mathbb{R}^3$. This can be achieved via the mapping

$$\mathbf{s}_\nu := \psi_\nu^\dagger \frac{\sigma}{2} \psi_\nu = \langle\psi_\nu|\frac{\sigma}{2}|\psi_\nu\rangle. \tag{2.129}$$

What we just introduced is an artificial spin, the so-called neutrino flavor isospin (NFIS)[32] [87].

---

[32] We note that the formalism is equivalent to the use of polarization vectors (e.g., [86]).

As we will see later, it turns out to be useful to work with flavor density matrices

$$\rho_\nu = \psi_\nu \cdot \psi_\nu^\dagger = \begin{pmatrix} |a_{\nu_e}|^2 & a_{\nu_e} a_{\nu_\tau}^* \\ a_{\nu_e}^* a_{\nu_\tau} & |a_{\nu_\tau}|^2 \end{pmatrix}. \tag{2.130}$$

They are related to the NFIS via the expectation value

$$s_\nu = \left\langle \frac{\sigma}{2} \right\rangle_{\rho_\nu} \equiv \frac{1}{2} \mathrm{tr}\left(\rho_\nu \sigma\right) = \frac{1}{2} \begin{pmatrix} 2\,\mathrm{Re}\,(\rho_\nu)_{\tau e} \\ 2\,\mathrm{Im}\,(\rho_\nu)_{\tau e} \\ (\rho_\nu)_{ee} - (\rho_\nu)_{\tau\tau} \end{pmatrix}, \tag{2.131}$$

while for antineutrinos we use the following definition:

$$s_{\bar\nu} := \left\langle \epsilon^{-1} \frac{\sigma}{2} \epsilon \right\rangle_{\bar\rho_{\bar\nu}} = \frac{1}{2} \mathrm{tr}\left(\epsilon \bar\rho_{\bar\nu} \epsilon^{-1} \sigma\right) \tag{2.132}$$

$$= \frac{1}{2} \mathrm{tr}\left(\bar\rho_{\bar\nu} \epsilon^{-1} \sigma \epsilon\right), \tag{2.133}$$

$$= -\frac{1}{2} \mathrm{tr}\left(\bar\rho_{\bar\nu} \sigma^*\right), \tag{2.134}$$

where $\epsilon := i\sigma_2$ and $\epsilon^{-1} \sigma \epsilon = -\sigma^*$ and

$$\bar\rho_{\bar\nu} = \rho_{\bar\nu}^* = \begin{pmatrix} |a_{\bar\nu_e}|^2 & a_{\bar\nu_e}^* a_{\bar\nu_\tau} \\ a_{\bar\nu_e} a_{\bar\nu_\tau}^* & |a_{\bar\nu_\tau}|^2 \end{pmatrix}. \tag{2.135}$$

With the ϵ-transformation we made use of the fact that the **2**- and the $\bar{\mathbf{2}}$-representation of SU(2) are equivalent. This has the advantage that the NFISs for both neutrinos and antineutrinos will transform in the same way under rotations and allows us to write the equations of motion on an equal footing. The z-component of the NFISs for neutrinos and antineutrinos are related to the survival probabilities by

$$P(\nu_{\underline{\alpha}} \to \nu_\alpha) = \frac{1}{2} + s_\nu \cdot \hat{\mathbf{e}}_z^{\mathrm{f}}, \tag{2.136}$$

$$P(\bar\nu_{\underline{\alpha}} \to \bar\nu_\alpha) = \frac{1}{2} - s_{\bar\nu} \cdot \hat{\mathbf{e}}_z^{\mathrm{f}}. \tag{2.137}$$

With other words, if s_ν points in the $\pm\hat{\mathbf{e}}_z^{\mathrm{f}}$-direction, the neutrino is in the $|\nu_e\rangle$ (+) or $|\nu_\tau\rangle$ (−) state, respectively. The mass eigenstates $|\nu_1\rangle$ and $|\nu_2\rangle$ correspond to a NFIS pointing in the direction $+\hat{\mathbf{H}}_{\mathrm{vac}}$ and $-\hat{\mathbf{H}}_{\mathrm{vac}}$. Note that a maximally mixed state corresponds to $s_\nu \cdot \hat{\mathbf{e}}_z^{\mathrm{f}} = 0$. Similarly, the weak eigenstates $|\bar\nu_e\rangle$ and $|\bar\nu_\tau\rangle$ are represented by a NFIS for antineutrinos $s_{\bar\nu}$ pointing in the direction of $-\mathbf{e}_z^{\mathrm{f}}$- and $+\mathbf{e}_z^{\mathrm{f}}$, respectively. Furthermore, we will use the convention that a NFIS with positive (negative) vacuum frequency $\omega \equiv \Delta m^2/(2E)$ represents a NFIS for neutrinos (antineutrinos). Note that we can associate an effective energy[33] to each NFIS: $\mathcal{E}_\omega^{\mathrm{eff}} = -s_\omega \cdot \mathbf{H}_\omega$.

---

[33] This is analogous to a magnetic dipole moment $\mathbf{m}$ in an external magnetic field $\mathbf{B}$. There, the potential energy is given by $-\mathbf{m} \cdot \mathbf{B}$, where the minus sign comes from the fact that the dipole tries to align in parallel with $\mathbf{B}$ in order to minimize the potential energy.

Instead of solving the Schrödinger-like equation,

$$i\frac{\mathrm{d}}{\mathrm{d}t}\psi_\nu = \mathsf{H}\psi_\nu, \tag{2.138}$$

we can equivalently solve a von-Neumann-like equation for the flavor density matrix:

$$\dot{\rho}_\nu = -i\left[\mathsf{H}, \rho_\nu\right]. \tag{2.139}$$

With the decomposition $\rho = \frac{1}{2}(\mathbb{1} + \mathbf{s}_\nu \cdot \boldsymbol{\sigma})$ we find

$$\frac{1}{2}\dot{\mathbf{s}}_\nu \cdot \boldsymbol{\sigma} = -\frac{i}{4}\left[-\mathbf{H} \cdot \boldsymbol{\sigma}, \mathbf{s}_\nu \cdot \boldsymbol{\sigma}\right] \tag{2.140}$$

$$= -\frac{1}{2}\sum_{j,k,l}\epsilon_{jkl}H_j s_{\nu,k}\sigma_l \tag{2.141}$$

$$= -\frac{1}{2}\left(\mathbf{H} \times \mathbf{s}_\nu\right) \cdot \boldsymbol{\sigma} \tag{2.142}$$

and finally we arrive at the equation of motion for the NFIS $\mathbf{s}_\nu$:

$$\dot{\mathbf{s}}_\nu = \mathbf{s}_\nu \times \mathbf{H}. \tag{2.143}$$

If $\mathbf{H} = \mathbf{H}_{\text{vac}}$, the equation of motion describes the precession of $\mathbf{s}_\nu$ around the vacuum mass direction $\hat{\mathbf{H}}_{\text{vac}}$, shown in figure 2.11. Note that this is similar to the precession of a spin in a magnetic field.
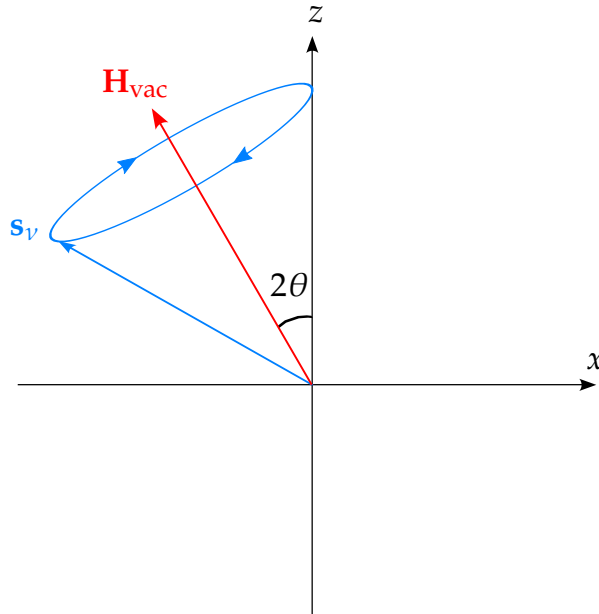
Figure 2.11.: NFIS representation of vacuum oscillations.

If we add the matter term, $\mathbf{H} = \mathbf{H}_{\text{vac}} + \mathbf{H}_{\text{matt}}$, we can obtain a simple geometric picture of adiabatic flavor conversion through the MSW mechanism, visualized in figure 2.12. If we follow an electron neutrino propagating from a high density region to a region of low

density, the NFIS $\mathbf{s}_\nu$ initially points into the direction of the heavy propagation eigenstate $\tilde{\nu}_2$, so it is initially antialigned with the effective field $\mathbf{H}$ and will precess around $-\mathbf{H}$. If the matter density is decreasing in such a way that the NFIS stays in its propagation eigenstate (adiabatically), or equivalently, stays antialigned with the effective field $\mathbf{H}$, the z-component of the NFIS will vanish as soon as $\mathbf{H} \cdot \hat{\mathbf{e}}_z^f = 0$. This corresponds to an MSW resonance[34]. Finally in vacuum (or in the low density regime), the NFIS has flipped its direction and is now precessing around the negative vacuum mass direction, $-\hat{\mathbf{H}}$, so it is essentially in the $|\nu_\tau\rangle$ state.
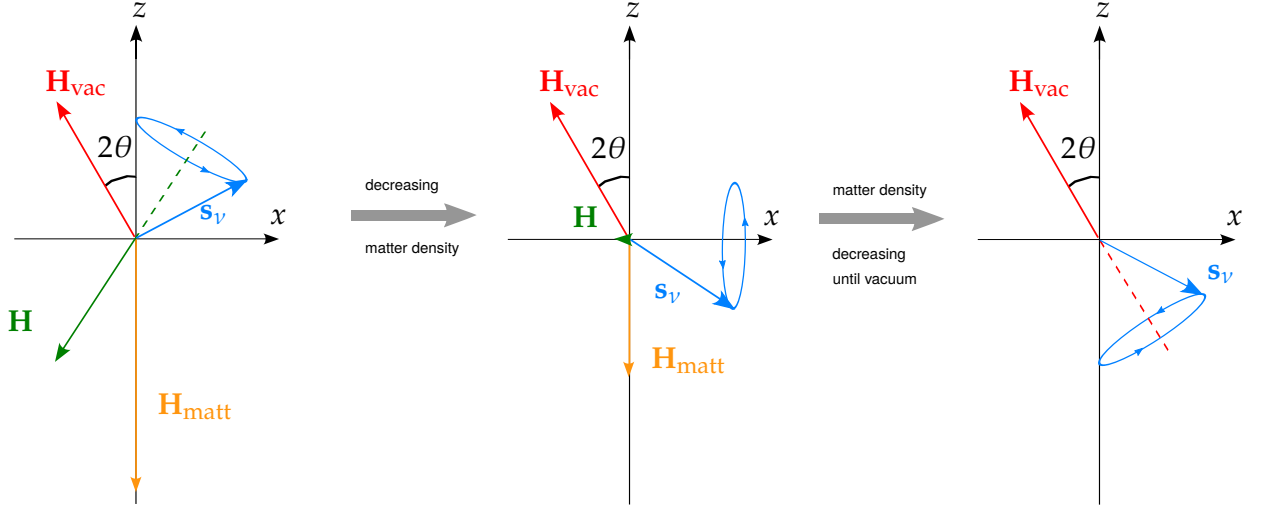
Figure 2.12.: NFIS representation of adiabatic flavor conversion through the MSW mechanism.

Furthermore, it is convenient to introduce an effective mixing angle via the relation:

$$\mathbf{H} \cdot \hat{e}_z = |\mathbf{H}| \cos(2\theta_{\text{eff}}), \tag{2.144}$$

or

$$\cos(2\theta_{\text{eff}}) = \frac{\mathsf{H}_{\tau\tau} - \mathsf{H}_{ee}}{2\sqrt{\left(\frac{\mathsf{H}_{\tau\tau} - \mathsf{H}_{ee}}{2}\right)^2 + |\mathsf{H}_{e\tau}|^2}}. \tag{2.145}$$

If the NFIS $\mathbf{s}_\nu$ and $\mathbf{H}$ are aligned and the evolution is adiabatic, then we have $P(\nu_{\underline{e}} \to \nu_e) = (1 + \cos(2\theta_{\text{eff}}))/2$.

We can also introduce an angle $\tilde{\theta}$ between NFIS $\mathbf{s}_\nu$ and Hamiltonian $\mathbf{H}$ which describes the alignment of the NFIS with its effective field:

$$\mathbf{s}_\nu \cdot \mathbf{H} = \frac{1}{2}|\mathbf{H}| \cos(2\tilde{\theta}). \tag{2.146}$$

---

[34] Note that $\mathbf{H} \cdot \hat{\mathbf{e}}_z^f = 0$ yields the usual resonance condition: $\omega \cos 2\theta = V_e$.

Neutrino Self-Interactions

> [...] *the most elementary and valuable statement*
> *in science, the beginning of wisdom, is, «I do not*
> *know».*
>

3.1 Preliminary remarks

Besides neutrino coherent scattering off background particles such as electrons and nucleons, it has been realized that in environments with high neutrino densities such as inside a supernovae, remnants from compact object mergers and stellar collapses, or in the early universe, neutrino coherent forward scattering off neutrinos themselves can play a key role, as first addressed in [63, 88] for supernovae[1]. However, those early works were incomplete, in the sense, that they lack an important ingredient, which is crucial for our discussion. This missing piece, namely the fact that coherent neutrino-neutrino scattering produces both flavor diagonal and *off*-diagonal contributions to the effective neutrino mass differences. The importance of the flavor off-diagonal terms was first pointed out by James Pantaleone [90] and has been considered later in [91], where the first extensive treatment of neutrino flavor transformation in the late time supernova epoch was given. Thereby, the authors made use of the formal approach developed in [92] and provided a more general framework for treating contributions to the neutrino propagation Hamiltonian from neutrino-neutrino forward scattering in the context of the MSW-like neutrino flavor transformations.

To make clear what we mean by flavor *off*-diagonal contributions we start our introduction by considering the NC scattering of a probe neutrino ν_α with flavor α on background neutrinos ν_b. It can proceed due to Z^0 exchange in the t- and u-channels, shown in figure 3.1. While the t-channel contribution is the same for all neutrino flavors, the u-channel contribution is flavor dependent: Because we are following a coherent scattering process, there is no exchange of momentum. Instead, we could interpret the u-channel contribution as an exchange of flavors.

One immediately recognizes that figure 3.1 (left) corresponds to the NC current graph in case of neutrino coherent scattering off ordinary matter, see figure 2.3 (left), when we identify the background fermion $f(\mathbf{q})$ with a neutrino $\nu(\mathbf{q})$. Note that this contribution

---

[1] Actually, the possible relevance of neutrino-neutrino scattering in supernovae was already pointed out in [89]. However, in this work only cross sections were computed and flavor conversion effects were not studied.

is flavor-diagonal, i.e., the same for all neutrino flavors. The crucial part now is that in addition, coherent interactions among neutrinos themselves, to which we refer to as neutrino self-interactions, have an additional exchange contribution corresponding to the u-channel graph in figure 3.1 (right). As mentioned above, the early works [63, 88] studied the case where $\alpha = \beta$, with other words, the propagating and the background neutrinos have the same flavor. Later, it was realized [90] that it is crucial to consider the off-diagonal, $\alpha \neq \beta$, contributions as well. Since coherence requires that the background state remains unchanged, we could interpret the off-diagonal parts, as a flavor-exchange. Due to the fact that neutrinos oscillate, we do not know the state of the background. Note that the situation is now very different from the case where ordinary matter constitutes the background. In the latter, we know the background state and can solve a linear equation to keep track of the neutrino flavor evolution. In the neutrino background case, the problem is intrinsically non-linear and requires a careful treatment. Pantaleone also pointed out the many-body nature of the problem.
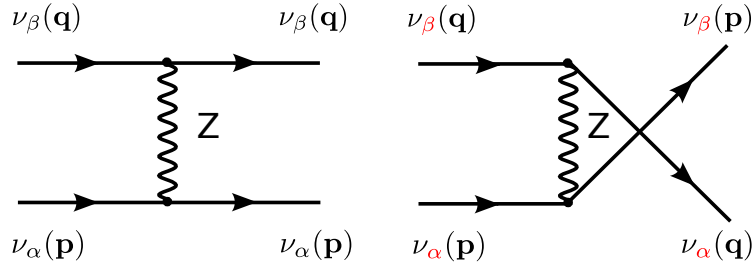
Figure 3.1.: Neutral current contributions: t-channel (left), u-channel (right).

In the next two sections, we want to emphasize why the off-diagonal contributions are indeed required.

3.2 Effective theory

For neutrino energies much lower than the mass of the neutral vector boson Z^0 ($m_{Z^0} \approx 91$ GeV), the effective interaction Hamiltonian density is given by the current-current term

$$\mathcal{H}_{\nu\nu}^{\mathrm{NC}} = -\mathcal{L}_{\nu\nu}^{\mathrm{NC}} \equiv \frac{G_{\mathrm{F}}}{\sqrt{2}} j^{\lambda} j_{\lambda} \tag{3.1}$$

$$= \frac{G_{\mathrm{F}}}{\sqrt{2}} \left(\frac{1}{2} \sum_{\alpha=e,\mu,\tau} \bar{\nu}_{\alpha} \gamma^{\lambda} \left(1 - \gamma^5 \right) \nu_{\alpha} \right) \left(\frac{1}{2} \sum_{\beta=e,\mu,\tau} \bar{\nu}_{\beta} \gamma_{\lambda} \left(1 - \gamma^5 \right) \nu_{\beta} \right), \tag{3.2}$$

where $\nu_{\alpha} = \overset{(-)}{\nu}_{\alpha}(x)$ are Dirac (anti)neutrino fields (see also 2.2) and $\bar{\nu}_{\alpha} = \nu_{\alpha}^{\dagger} \gamma^0$. The four-current j^{λ} reads as $j^{\lambda} = g_{\mathrm{L}}^{\nu} \sum_{\alpha=e,\mu,\tau} \bar{\nu}_{\alpha} \gamma^{\lambda} (1 - \gamma^5) \nu_{\alpha}$, where the vector coupling constant $g_{V,\mathrm{L}}^{\nu}$ for left-handed neutrinos corresponds to the third component I_3 of their weak isospin, $g_{V,\mathrm{L}}^{\nu} = I_3^{\nu} = 1/2$. Note that $\alpha \in \{e, \mu, \tau\}$ denotes a flavor index while $\lambda \in \{0, 1, 2, 3\}$ refers to

a Lorentz index[2]. If we use left-handed fields $\nu_{\alpha L} \equiv \frac{1}{2}(1 - \gamma^5)\nu_\alpha$ we can write eq. (3.2) in a more compact form:

$$\mathcal{H}_{\nu\nu}^{NC} = \frac{G_F}{\sqrt{2}} \left(\sum_{\alpha=e,\mu,\tau} \overline{\nu_{\alpha L}} \gamma^\lambda \nu_{\alpha L} \right) \left(\sum_{\beta=e,\mu,\tau} \overline{\nu_{\beta L}} \gamma_\mu \nu_{\beta L} \right), \tag{3.3}$$

Having a closer look on eq. (3.3), we realize that $\mathcal{H}_{\nu\nu}^{NC}$ remains invariant under a transformation of the form

$$\begin{pmatrix} \nu_{eL} \\ \nu_{\mu L} \\ \nu_{\tau L} \end{pmatrix} \mapsto U \begin{pmatrix} \nu_{eL} \\ \nu_{\mu L} \\ \nu_{\tau L} \end{pmatrix}, \tag{3.4}$$

where $U \in U(3)$ is in the fundamental representation[3] **3** of the unitary group U(3). Note that the vector containing the Dirac conjugate fields transforms according to the conjugated representation $\bar{\mathbf{3}}$ of U(3),

$$\begin{pmatrix} \overline{\nu_{eL}} \\ \overline{\nu_{\mu L}} \\ \overline{\nu_{\tau L}} \end{pmatrix} \mapsto U^* \begin{pmatrix} \overline{\nu_{eL}} \\ \overline{\nu_{\mu L}} \\ \overline{\nu_{\tau L}} \end{pmatrix}, \tag{3.5}$$

which is not equivalent to **3**. The transformation behavior can also be expressed for the individual ν_α and $\bar{\nu}_\alpha$,

$$\nu_{\alpha L} \mapsto \sum_\beta U_{\alpha\beta} \nu_{\beta L}, \tag{3.6}$$

$$\overline{\nu_{\alpha L}} \mapsto \left(\sum_\beta U_{\alpha\beta} \nu_{\beta L} \right)^\dagger \gamma^0 = \sum_\beta \overline{\nu_{\beta L}} U_{\alpha\beta}^*, \tag{3.7}$$

where we used $(U_{\alpha\beta})^\dagger = U_{\alpha\beta}^*$ in the last step. Using the unitarity relation $U^\dagger U = \mathbb{1}$, or equivalently,

$$\delta_{\alpha\beta} = \left(U^\dagger U \right)_{\alpha\beta} = \sum_{\lambda=e,\mu,\tau} \left(U^\dagger \right)_{\alpha\lambda} U_{\lambda\beta} = \sum_{\lambda=e,\mu,\tau} U_{\lambda\alpha}^* U_{\lambda\beta}, \tag{3.8}$$

---

[2] We suppressed the Lorentz indices on the fields and use the Einstein summation convention for Lorentz indices.
[3] As a consequence of the group isomorphism $U(3) \cong U(1) \times SU(3)$, we can decompose every element of U(3) into a phase factor $\exp(i\varphi)$ (with $\varphi \in \mathbb{R}$) times an element of SU(3). The fundamental representation $\mathbf{3}_{U(3)}$ of U(3) is therefore equivalent to $\mathbf{1}_{U(1)} \otimes \mathbf{3}_{SU(3)}$.

we can check the invariance of the Hamiltonian by a straightforward calculation:

$$\sum_{\alpha=e,\mu,\tau} \overline{\nu_{\alpha L}} \gamma^\lambda \nu_{\alpha L} \mapsto \sum_{\alpha,\rho,\sigma=e,\mu,\tau} \nu^\dagger_{\rho L} U^*_{\alpha\rho} \gamma^0 \gamma^\lambda U_{\alpha\sigma} \nu_{\sigma L} \tag{3.9}$$

$$= \sum_{\rho,\sigma=e,\mu,\tau} \overline{\nu_{\rho L}} \gamma^\lambda \left(\sum_\alpha U^*_{\alpha\rho} U_{\alpha\sigma} \right) \nu_{\sigma L} \tag{3.10}$$

$$= \sum_{\alpha=e,\mu,\tau} \overline{\nu_{\alpha L}} \gamma^\lambda \nu_{\alpha L} \tag{3.11}$$

Therefore, $H^{NC}_{\nu\nu}$ possesses a U(3) flavor symmetry.

3.3   Hamiltonian

In the following we make a simplified discussion that captures the basic idea behind neutrino self-interactions. We consider the interaction Hamiltonian density for neutral current neutrino-neutrino scattering for two flavors (the extension to three flavors is straightforward):

$$\mathcal{H}^{NC}_{\nu\nu} = \frac{G_F}{\sqrt{2}} \left(\sum_{\alpha=e,\mu} \overline{\nu_{\alpha L}} \gamma^\lambda \nu_{\alpha L} \right) \left(\sum_{\beta=e,\mu} \overline{\nu_{\beta L}} \gamma_\lambda \nu_{\beta L} \right), \tag{3.12}$$

$$= \frac{G_F}{\sqrt{2}} \left(\overline{\nu_{eL}} \gamma^\lambda \nu_{eL} \overline{\nu_{eL}} \gamma_\lambda \nu_{eL} + \overline{\nu_{\mu L}} \gamma^\lambda \nu_{\mu L} \overline{\nu_{\mu L}} \gamma_\lambda \nu_{\mu L} + 2\overline{\nu_{eL}} \gamma^\lambda \nu_{eL} \overline{\nu_{\mu L}} \gamma_\lambda \nu_{\mu L} \right), \tag{3.13}$$

where the last term can be rewritten using a Fierz transformation:

$$\overline{\nu_{eL}} \gamma^\lambda \nu_{eL} \overline{\nu_{\mu L}} \gamma_\lambda \nu_{\mu L} = \overline{\nu_{eL}} \gamma^\lambda \nu_{\mu L} \overline{\nu_{\mu L}} \gamma_\lambda \nu_{eL}. \tag{3.14}$$

Now we follow a mean field approach[4] and replace the left-handed neutrino currents by background averaged values[5] [93]:

$$\begin{aligned} \mathcal{H}^{NC}_{\nu\nu} \mapsto \frac{G_F}{\sqrt{2}} \Big(&4\langle\overline{\nu_{eL}} \gamma^\lambda \nu_{eL}\rangle \overline{\nu_{eL}} \gamma_\lambda \nu_{eL} + 4\langle\overline{\nu_{\mu L}} \gamma^\lambda \nu_{\mu L}\rangle \overline{\nu_{\mu L}} \gamma_\lambda \nu_{\mu L} \\ &+ 2\langle\overline{\nu_{eL}} \gamma^\lambda \nu_{eL}\rangle \overline{\nu_{\mu L}} \gamma_\lambda \nu_{\mu L} + 2\langle\overline{\nu_{\mu L}} \gamma^\lambda \nu_{\mu L}\rangle \overline{\nu_{eL}} \gamma_\lambda \nu_{eL} \\ &+ 2\langle\overline{\nu_{eL}} \gamma^\lambda \nu_{\mu L}\rangle \overline{\nu_{\mu L}} \gamma_\lambda \nu_{eL} + 2\langle\overline{\nu_{\mu L}} \gamma_\lambda \nu_{eL}\rangle \overline{\nu_{eL}} \gamma^\lambda \nu_{\mu L} \Big) + \text{const.} \end{aligned} \tag{3.16}$$

---

[4] Note that this is similar to the case where the neutral (V_{NC}) and charged current potentials (V_{CC}) for neutrino coherent scattering off electrons and nucleons were computed.

[5] We made use of the following relation for the background averaged values originating from a four-fermion interaction taking into account the Fermi statistics [93]:

$$\begin{aligned} \overline{\psi_{aL}} \gamma^\lambda \psi_{bL} \overline{\psi_{cL}} \gamma_\lambda \psi_{dL} \rightarrow &\langle\overline{\psi_{aL}} \gamma^\lambda \psi_{bL}\rangle \overline{\psi_{cL}} \gamma_\lambda \psi_{dL} + \overline{\psi_{aL}} \gamma^\lambda \psi_{bL} \langle\overline{\psi_{cL}} \gamma_\lambda \psi_{dL}\rangle \\ &+ \langle\overline{\psi_{aL}} \gamma^\lambda \psi_{dL}\rangle \overline{\psi_{cL}} \gamma_\lambda \psi_{bL} + \overline{\psi_{aL}} \gamma^\lambda \psi_{dL} \langle\overline{\psi_{cL}} \gamma_\lambda \psi_{bL}\rangle \\ &- \langle\overline{\psi_{aL}} \gamma^\lambda \psi_{bL}\rangle \langle\overline{\psi_{cL}} \gamma_\lambda \psi_{dL}\rangle - \langle\overline{\psi_{aL}} \gamma^\lambda \psi_{dL}\rangle \langle\overline{\psi_{cL}} \gamma_\lambda \psi_{bL}\rangle. \end{aligned} \tag{3.15}$$

This is similar to the case, where we start from the operator identity [94]

$$\hat{O}_1 \cdot \hat{O}_2 = \left(\hat{O}_1 - \langle\hat{O}_1\rangle\right)\left(\hat{O}_2 - \langle\hat{O}_2\rangle\right) + \langle\hat{O}_1\rangle\hat{O}_2 + \hat{O}_1\langle\hat{O}_2\rangle - \langle\hat{O}_1\rangle\langle\hat{O}_2\rangle \tag{3.17}$$

and apply a Hartree-Fock-like approximation [94]

$$\hat{O}_1 \cdot \hat{O}_2 \mapsto \langle\hat{O}_1\rangle\hat{O}_2 + \hat{O}_1\langle\hat{O}_2\rangle - \langle\hat{O}_1\rangle\langle\hat{O}_2\rangle, \tag{3.18}$$

i.e., fluctuations of the observables $\hat{O}_1$ and $\hat{O}_2$ around their background averaged values, $\hat{O}_1 - \langle\hat{O}_1\rangle$ and $\hat{O}_2 - \langle\hat{O}_2\rangle$, are neglected[6].

In virtue of the Hartree-Fock theory, the first two terms in eq. (3.16) constitute a "Hartree term" while the last two terms account for "exchange interactions" [93]. From $\mathcal{H}_{\nu\nu}^{\text{NC}}$, we define the following matrix in flavor space:

$$\mathsf{H}_{\nu\nu} = \frac{G_F}{\sqrt{2}} \begin{pmatrix} 4\langle\nu_{e\mathrm{L}}^\dagger \nu_{e\mathrm{L}}\rangle + 2\langle\nu_{\mu\mathrm{L}}^\dagger \nu_{\mu\mathrm{L}}\rangle & 2\langle\nu_{\mu\mathrm{L}}^\dagger \nu_{e\mathrm{L}}\rangle \\ 2\langle\nu_{e\mathrm{L}}^\dagger \nu_{\mu\mathrm{L}}\rangle & 2\langle\nu_{e\mathrm{L}}^\dagger \nu_{e\mathrm{L}}\rangle + 4\langle\nu_{\mu\mathrm{L}}^\dagger \nu_{\mu\mathrm{L}}\rangle \end{pmatrix}. \tag{3.19}$$

Note that the off-diagonal background averaged values $\langle\overline{\nu_{e\mathrm{L}}}\gamma^\lambda\nu_{\mu\mathrm{L}}\rangle$ and $\langle\overline{\nu_{\mu\mathrm{L}}}\gamma^\lambda\nu_{e\mathrm{L}}\rangle$ lead to flavor-mixing and cannot be set to zero (which would be possible for massless neutrinos) [93]. The constant term,

$$\begin{aligned} \text{const} \equiv -\frac{G_F}{\sqrt{2}} \Big(&2\langle\overline{\nu_{e\mathrm{L}}}\gamma^\lambda\nu_{e\mathrm{L}}\rangle\langle\overline{\nu_{e\mathrm{L}}}\gamma_\lambda\nu_{e\mathrm{L}}\rangle + 2\langle\overline{\nu_{\mu\mathrm{L}}}\gamma^\lambda\nu_{\mu\mathrm{L}}\rangle\langle\overline{\nu_{\mu\mathrm{L}}}\gamma_\lambda\nu_{\mu\mathrm{L}}\rangle \\ &+ 2\langle\overline{\nu_{e\mathrm{L}}}\gamma^\lambda\nu_{e\mathrm{L}}\rangle\langle\overline{\nu_{\mu\mathrm{L}}}\gamma_\lambda\nu_{\mu\mathrm{L}}\rangle + 2\langle\overline{\nu_{e\mathrm{L}}}\gamma^\lambda\nu_{\mu\mathrm{L}}\rangle\langle\overline{\nu_{\mu\mathrm{L}}}\gamma_\lambda\nu_{e\mathrm{L}}\rangle\Big), \end{aligned} \tag{3.20}$$

does not appear in the equations of motion[7] and consequently will not contribute to the dynamics. We will neglect it in what follows.

To sketch the basic idea, we follow [95] and consider a homogeneous gas of N_ν massless neutrinos (with flavor e and μ), described by plane waves, confined in a volume V and where coherent forward scattering takes place. In this case, only the temporal components of the averaged background four-current are non-vanishing $\langle\nu_\alpha\gamma^0\nu_\beta\rangle = \langle\nu_\alpha^\dagger\nu_\beta\rangle \neq 0$, where $\alpha, \beta \in \{e, \mu\}$. Since we assume a spatially homogeneous gas, the currents do not depend on position, but only on time. This suggests to replace

$$\langle\nu_\alpha^\dagger\nu_\beta\rangle(\mathbf{x}, t) \mapsto \langle\nu_\alpha^\dagger\nu_\beta\rangle(t) := \frac{1}{V}\int_V \mathrm{d}^3x\, \langle\nu_\alpha^\dagger\nu_\beta\rangle(\mathbf{x}, t). \tag{3.21}$$

If we follow the propagation of the ith neutrino, the background is given by

$$\langle\nu_\alpha^\dagger\nu_\beta\rangle(\mathbf{x}, t) = \sum_{j\neq i} \nu_e^{(j)*}\nu_\beta^{(j)}(\mathbf{x}, t), \tag{3.22}$$

---

[6] We assume that fluctuations are sufficiently small compared to the mean values. However, it should be stressed that this assumption needs to be reassessed by going beyond the mean field approximation.

[7] This term only provides a shift of the vacuum energy.

where $\nu_\alpha^{(j)}$ corresponds to one of the components of the jth neutrino:

$$\nu^{(j)}(\mathbf{x}, t) = \begin{pmatrix} \nu_e^{(j)}, \\ \nu_\mu^{(j)}, \end{pmatrix}. \tag{3.23}$$

with the unitarity relation [95] $|\nu_e^{(j)}|^2 + |\nu_\mu^{(j)}|^2 = 1/V$. The wave equation which governs the propagation in the gas reads as follows:

$$i\frac{\mathrm{d}}{\mathrm{d}t} \begin{pmatrix} \nu_e^{(i)} \\ \nu_\mu^{(i)} \end{pmatrix} = \mathsf{H}_{\nu\nu} \begin{pmatrix} \nu_e^{(i)} \\ \nu_\mu^{(i)} \end{pmatrix}, \tag{3.24}$$

where the background $\mathsf{H}_{\nu\nu}$ induces an effective mass matrix $2E\mathsf{H}_{\nu\nu}$ in flavor space. Explicitly, we find

$$\mathsf{H}_{\nu\nu} = \sqrt{2}\mathsf{G}_\mathrm{F} \sum_{j\neq i}^{N_\nu} \begin{pmatrix} 2|\nu_e^{(j)}|^2 + |\nu_\mu^{(j)}|^2 & \nu_e^{(j)}\nu_\mu^{(j)*} \\ \nu_e^{(j)*}\nu_\mu^{(j)} & |\nu_e^{(j)}|^2 + 2|\nu_\mu^{(j)}|^2 \end{pmatrix} \tag{3.25}$$

$$= \sqrt{2}\mathsf{G}_\mathrm{F} \left\{ \frac{N_\nu - 1}{V}\mathbb{1} + \sum_{j\neq i}^{N_\nu} \begin{pmatrix} |\nu_e^{(j)}|^2 & \nu_e^{(j)}\nu_\mu^{(j)*} \\ \nu_e^{(j)*}\nu_\mu^{(j)} & |\nu_\mu^{(j)}|^2 \end{pmatrix} \right\} \tag{3.26}$$

$$= \sqrt{2}\mathsf{G}_\mathrm{F} \left\{ \frac{N_\nu - 1}{V}\mathbb{1} + \sum_{j\neq i}^{N_\nu} \nu_e^{(j)} \cdot \nu_\mu^{(j)\dagger} \right\}. \tag{3.27}$$

From the latter equations, it is apparent that the flavor diagonal contributions correspond to neutrino number densities.

If we now perform an arbitrary U(2)-transformation $\nu^{(j)} \mapsto \mathsf{U}\nu^{(j)}$ of all neutrinos[8] $j = 1, \ldots N_\nu$, we can make the crucial observation that $\mathsf{H}_{\nu\nu}$ is form-invariant. Indeed, since we started from an U(2)-invariant theory, any derived description must respect this invariance. However, in earlier studies, only the flavor diagonal contributions were considered. But these will produce off-diagonal components and the U(2)-symmetry is not maintained.

3.4 Neutrino flavor transformation: Method

3.4.1 Equations of motion

We just considered a homogeneous ensemble of mixed neutrinos. The latter could be described with the density matrix formalism developed in [92]. However, if we want to investigate settings like supernovae or remnants of merging neutron stars, we have to take into account spatial variations. For this purpose one introduces so-called Wigner distributions[9],

---

[8] These include test and background neutrinos.
[9] For introductions, see also [96, 97] and the original work by Eugene Wigner [98].

represented by matrices $\rho(\mathbf{p}', \mathbf{x})$ with momentum $\mathbf{p}'$ at location $\mathbf{x}$ [92]. In flavor space[10], these represent generalized occupation number matrices. Attention has to be payed, however, because such a description is only valid if the ensemble's spatial inhomogeneities are large compared to the relevant scales set by the neutrino de Broglie wavelength[11] and oscillation length [99]. In this work, we do not consider any possible impact of small scale phase space fluctuations on the ensemble [100]. Furthermore, we restrict our discussion on stationary problems[12]. Therefore, in the neutrino free-streaming limit and with assuming the system in a stationary state, the spatial evolution of $\rho(\mathbf{p}', \mathbf{x})$ obeys the equation of motion at the lowest order [92],

$$\mathbf{v}_{\mathbf{p}'} \cdot \nabla_{\mathbf{x}} \rho(\mathbf{p}', \mathbf{x}) = -i \left[\mathsf{H}(\mathbf{p}', \mathbf{x}), \rho(\mathbf{p}', \mathbf{x}) \right], \tag{3.28}$$

where

$$\mathsf{H} = \mathsf{H}_{\text{vac}} + \mathsf{H}_{\text{matt}} + \mathsf{H}_{\nu\nu} \tag{3.29}$$

denotes the Hamiltonian including the vacuum, matter, and neutrino potentials. Notice that we do not include external forces (such as gravity) acting on neutrinos ($\nabla_{\mathbf{p}} \rho = 0$) and follow neutrinos on straight-line paths. An analogous relation holds for antineutrinos ($\bar{\rho}(\mathbf{p}', \mathbf{x})$). For the latter we employ the convention of [92] that ensures that both neutrinos and antineutrinos transform in the same way under SU(3). To be more explicit, $\rho_{\mathbf{p}}$ transforms with the fundamental representation of SU(3), $\rho_{\mathbf{p}} \mapsto \mathsf{U} \rho_{\mathbf{p}} \mathsf{U}^\dagger$, where we suppressed the flavor indices and where $\mathsf{U} \in SU(3)$. The corresponding matrix for antineutrinos should naturally transform with the conjugate fundamental representation. Here, however, we describe this matrix in the same representation as for neutrinos and consequently recover the same transformation law: $\bar{\rho}_{\mathbf{p}} \mapsto \mathsf{U} \bar{\rho}_{\mathbf{p}} \mathsf{U}^\dagger$. The reason why we use this convention is that it allows to write the equations of motion for both neutrinos and antineutrinos on an equal footing [86, 92]. Finally, an analogous equation to eq. (3.28) holds for antineutrinos with the replacement $\mathsf{H}_{\text{vac}} \mapsto -\mathsf{H}_{\text{vac}}$.

On the left hand side of eq. (3.28) one recognizes the drift term of the Liouville-Vlasov operator that is caused by the free streaming of neutrinos propagating with velocity $\mathbf{v}_{\mathbf{p}'}$. In the following we use the ultra-relativistic approximation[13] $|\mathbf{v}_{\mathbf{p}'}| \approx c$.

Before giving the explicit form of terms in eq. (3.29), we make a few remarks regarding eq. (3.28). First, this equation of motion is valid at the mean-field level. However, the most general mean-field approximation includes extra contributions, in particular neutrino-antineutrino pairing correlations and mass corrections [102–107]. The role of these terms still

---

[10] If not otherwise stated, we will work in flavor space.

[11] Recall that the de Broglie wavelength is given by $\lambda_{\text{de Broglie}} = 2\pi\hbar/p$ and corresponds to $\lambda_{\text{de Broglie}} \simeq 779\,\text{fm}$ for a 10 MeV neutrino.

[12] This prescription might be suitable if the emission properties of the source vary on a time scale greater than the relevant timescales of the problem.

[13] As noted in [101], time-of-flight effects become relevant when neutrinos propagate over large distances and hence, the approximation would not hold anymore and the drift term would gain a more complicated structure. However, the distances studied in this work are sufficiently small so that we can safely use it.

needs to be fully assessed. Second, we only study the limit where coherent forward scattering applies and sharply separate the dense region inside the neutrino surface, where neutrinos are trapped by collisions and the free streaming region. However, it was shown that in the context of core-collapse supernovae, the inclusion of a small backward scattered neutrino flux can affect the flavor evolution significantly [108]. Including these effects in numerical simulations is challenging and beyond the scope of this work. Future efforts along these lines may be necessary.

Now, let us discuss the different terms contributing to the Hamiltonian in eq. (3.29). The first one describes the vacuum term in the flavor basis, i.e.,

$$\mathsf{H}_{\text{vac}} = \frac{1}{2E} \mathsf{U} \tilde{\mathsf{M}}^2 \mathsf{U}^\dagger, \tag{3.30}$$

where $E \approx |\mathbf{p}'|$ corresponds to the energy of the neutrino and U denotes the unitary mixing matrix eq. (2.28) which links weak flavor and vacuum mass eigenstates. The quantity $\tilde{\mathsf{M}}^2 \equiv \text{diag}[0, \Delta m_{21}^2, \Delta m_{31}^2]$ essentially corresponds to the neutrino mass-squared matrix[14], where Δm_{21}^2 and Δm_{31}^2 denote the mass squared differences. The second term of the Hamiltonian eq. (3.29) takes into account neutrino coherent forward scattering off electrons, see section 2.6. Explicitly, we have

$$\mathsf{H}_{\text{matt}}(\mathbf{x}) = \sqrt{2}\mathsf{G}_{\text{F}} n_e(\mathbf{x}) \text{diag}[1, 0, 0], \tag{3.31}$$

where $n_e = \rho_{\text{matt}} Y_e / m_{\text{u}}$ is the electron number density, determined by the matter density ρ_{matt} and electron fraction Y_e.

Similarly, we consider neutrino coherent forward scattering off neutrinos which introduces the non-linear nature of the problem,

$$\mathsf{H}_{\nu\nu}(\mathbf{p}', \mathbf{x}) = \sqrt{2}\mathsf{G}_{\text{F}} \int \frac{\mathrm{d}^3 p}{(2\pi)^3} \left(1 - \hat{\mathbf{p}}' \cdot \hat{\mathbf{p}}\right) \left(\rho(\mathbf{p}, \mathbf{x}) - \bar{\rho}(\mathbf{p}, \mathbf{x})\right), \tag{3.32}$$

where $\hat{\mathbf{p}}' = \mathbf{p}'/|\mathbf{p}'|$ and $\hat{\mathbf{p}} = \mathbf{p}/|\mathbf{p}|$ denote unit vectors. In the self-interaction Hamiltonian, the so-called multi-angle term $1 - \hat{\mathbf{p}}' \cdot \hat{\mathbf{p}} = 1 - \cos \Theta_{\hat{\mathbf{p}}'\hat{\mathbf{p}}}$ reflects the current-current structure of weak interactions in the low-energy limit, cf. eq. (3.1). In particular, this shows the directional dependence and consequently, the anisotropic nature of the neutrino background[15].

In eq. (3.32) $\rho(\mathbf{p}, \mathbf{x})$ can be decomposed [110, 111] according to

$$\frac{\mathrm{d}^3 p}{(2\pi)^3} \rho(\mathbf{p}, \mathbf{x}) = \sum_{\alpha = e, \mu, \tau} \mathrm{d}n_{\nu_{\underline{\alpha}}}(\mathbf{p}, \mathbf{x}) \, \rho_{\nu_{\underline{\alpha}}}(\mathbf{p}, \mathbf{x}) \tag{3.33}$$

for neutrinos in a differential volume element $\mathrm{d}^3 p$ centered at momentum $\mathbf{p}$. A similar relation holds for antineutrinos. In eq. (3.33) we introduced the initial (i.e., at the neutrino surface, denoted by an underline) differential neutrino number density $\mathrm{d}n_{\nu_{\underline{\alpha}}}$ and the single

---

[14] Note that we already subtracted a multiple of the identity matrix which is not relevant for the flavor evolution.
[15] In particular, for neutrinos moving on parallel trajectories, this factor prevents forward scattering [109].

density (3×3)-matrices $\rho_{\nu_{\underline{\alpha}}}(\mathbf{p}, \mathbf{x})$ for a neutrino with initial flavor α and momentum $\mathbf{p}$ at position $\mathbf{x}$. For normalization we choose the trace equal to one. The diagonal elements of the single density matrices correspond to the probabilities that a neutrino with initial flavor α can be found in a particular flavor β, i.e., $(\rho_{\nu_{\underline{\alpha}}})_{\beta\beta} = P(\nu_\alpha \to \nu_\beta)$, while the (complex-valued) off-diagonal elements describe quantum correlations between different neutrino flavors with the same momentum. An analogous relation holds for antineutrinos.

Using eq. (3.33), eq. (3.32) becomes

$$H_{\nu\nu}(\mathbf{p}', \mathbf{x}) = \sqrt{2}G_\mathrm{F} \sum_{\alpha=e,\mu,\tau} \left(\int \mathrm{d}n_{\nu_{\underline{\alpha}}} (1 - \hat{\mathbf{p}}' \cdot \hat{\mathbf{p}}) \rho_{\nu_{\underline{\alpha}}}(\mathbf{p}, \mathbf{x}) - \int \mathrm{d}n_{\bar{\nu}_{\underline{\alpha}}} (1 - \hat{\mathbf{p}}' \cdot \hat{\mathbf{p}}) \bar{\rho}_{\bar{\nu}_{\underline{\alpha}}}(\mathbf{p}, \mathbf{x}) \right). \quad (3.34)$$

If we follow the flavor evolution of neutrinos along a specific trajectory, we can replace $\mathbf{v_p} \cdot \nabla_\mathbf{x}$ by a differential operator $\partial/\partial r$ along their direction of propagation so that the equations of motion (3.28) for the single density flavor matrices become

$$\frac{\partial}{\partial r} \rho_{\nu_{\underline{\alpha}}}(\mathbf{p}', \mathbf{Q}_0, r) = -i[H_\mathrm{vac} + H_\mathrm{matt} + H_{\nu\nu}, \rho_{\nu_{\underline{\alpha}}}(\mathbf{p}', \mathbf{Q}_0, r)], \quad (3.35)$$

$$\frac{\partial}{\partial r} \bar{\rho}_{\bar{\nu}_{\underline{\alpha}}}(\mathbf{p}', \mathbf{Q}_0, r) = -i[-H_\mathrm{vac} + H_\mathrm{matt} + H_{\nu\nu}, \bar{\rho}_{\bar{\nu}_{\underline{\alpha}}}(\mathbf{p}', \mathbf{Q}_0, r)], \quad (3.36)$$

where $\mathbf{Q}_0$ is the emission point of the neutrinos and $r = r(\mathbf{x})$ is the distance they have traveled.

3.4.2 Comments on symmetries and dimensionality

Because of the non-linear nature of the problem and the anisotropic astrophysical environments, numerically solving flavor evolution problems including neutrino self-interactions requires some assumptions. As will be discussed in detail, one typically assumes that the initial symmetry of the system is maintained. Within this assumption, the flavor evolution of neutrinos in a spherically symmetric environment becomes solvable in the so-called "bulb model" [112], which will be introduced in section 3.5.1. This approach is usually called "multi-angle approximation" when the radial coordinate and the angular variable are retained to specify the neutrino propagation. In contrast, "single-angle approximation", which was also often used in studying such problems, further assumes that the flavor evolution of neutrinos only depends on the radial coordinate [110]. It was found that in the context of supernovae, the solutions of single-angle and multi-angle approximations can be similar (e.g., [112, 113]) but sometimes different (e.g., [84, 114]). Note that based on the "bulb model", it was shown that, the matter potential can induce kinematical decoherence, suppress flavor conversion, or the flavor instability could be shifted compared to the single-angle case when performing a multi-angle treatment [112].

In the following we comment on the dimensionality of the problem of tracking the neutrino flavor propagation in astrophysical settings. Thereby, we will focus on the neutrino emission from a proto-neutron star (PNS) in the supernovae context for purely illustrative purposes.

We express the dimensionality in terms of phase space dimensions, i.e., in position and momentum space dimensions. The full problem is a 7-dimensional one, i.e., it consists of 1 time dimension, and (3+3) phase space dimensions. The neutrino ensemble, characterized by density matrices, has the following dependencies: $\rho = \rho(t, r, \Theta, \Phi, \vartheta, \varphi)$, where we parameterized the position ($\mathbf{x}$) and momentum ($\mathbf{p}$) variables using spherical coordinates as $\mathbf{x} = \mathbf{x}(r, \Theta, \Phi)$ and $\mathbf{p} = \mathbf{p}(E, \theta, \phi)$. Here, ϑ and φ specify the emission direction while Θ and Φ specify the emission points on the PNS. Since neutrinos travel approximately with the speed of light, the relevant timescale is much shorter than the evolution of the matter profile[16]. For this reason, we treat the environment as static and neglect the dependence on time. Furthermore, we assume that coherent forward scattering occurs only outside the neutrino surface.

Since we are now considering a static environment, the most general problem is a (3+3)-dimensional and the density matrices depend on the full space and momentum coordinates: $\rho_\nu(r, E, \vartheta, \varphi, \Theta, \Phi)$. We can reduce the spatial dimensionality to (2+3) by assuming rotational symmetry around the z axis: $\rho_\nu(r, E, \vartheta, \varphi, \Theta)$. In this case we get rid of the Φ-dependence. However, this problem is still too complex for numerical studies. In addition, if we assume spherical symmetry around the center we can further reduce the dimensionality to (1+3): $\rho_\nu(r, E, \vartheta, \varphi)$. However, it should be stressed that if neutrinos propagate differently in different φ-angles, the initial spherical symmetry can be broken, i.e., the solutions do not necessarily possess the initial symmetry [115–117]. For this reason, such kind of model is probably not self-consistent. If we apply the previous assumptions and employ axial symmetry around any radial direction, the dimensionality is (1+2): $\rho_\nu(r, E, \vartheta)$. This corresponds to the multi-angle version of the bulb model. Furthermore, if we assume that the flavor evolution does not depend on the trajectory, we end up with a (1+1)-dimensional problem: $\rho_\nu(r, E)$. This corresponds to the single-angle version of the bulb model[17]. Based on [119] we graphically illustrate in figure 3.2 what we said before.

We stress that three-dimensional supernova simulations indicate large deviations from isotropy and spherical symmetry with respect to the matter profiles and the neutrinos emission, e.g., due to hydrodynamical instabilities like SASI or LESA [120, 121]. For completeness, we list some other references were different types of symmetry breaking have been investigated [122–126], see also the reviews [127, 128].

---

[16] Note that the relevant timescale corresponds to the propagation time difference along the pencil of directions. Of course, the conditions on the proto-neutron star surface are quickly changing, but most of the neutrino fluxes are outwardly directed. Indeed, practically one compares the propagation times for a neutrino emitted along the radial direction and tangentially from the surface. Therefore, as long as the differences between these propagation times are small compared to dynamical timescales, the stationary solution should be valid at least for problems where neutrinos are radiated outwardly. Note that the approximation becomes better with increasing distance from the emitting surface.

[17] Note that this is equivalent to a homogeneous and isotropic neutrino gas which expands in time [118] (if we replace r by time t), e.g., in the context of the early universe.
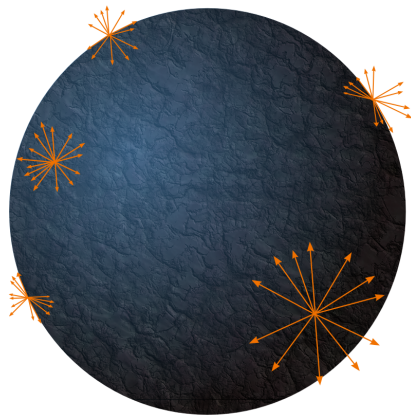
(a) (3+3)-dim.
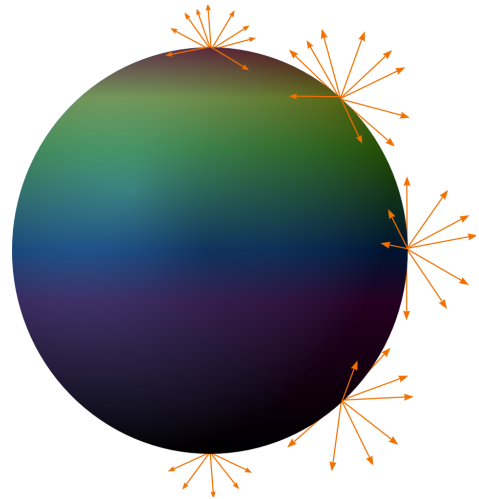
(b) (2+3)dim.: rotational symmetry around z axis.
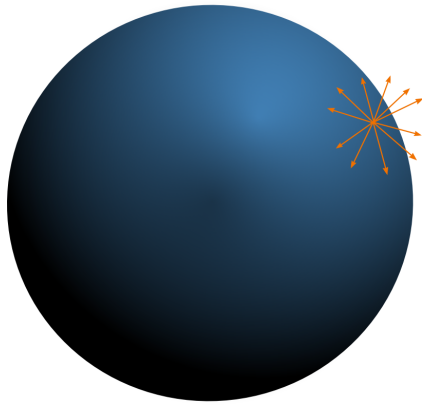
(c) (1+3)-dim.: spherical symmetry around the center.
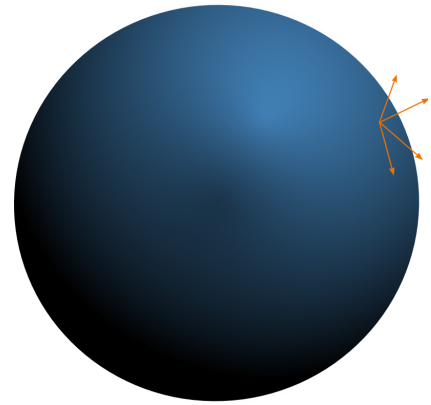
(d) (1+2)-dim.: spherical symmetry around the center and axial symmetry around any radial emission direction. This corresponds to the bulb model (multi-angle case).
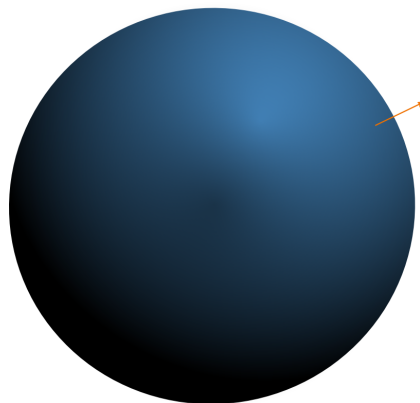
(e) (1+1)-dim.: spherical symmetry around the center and axial symmetry around any radial emission direction + assume that flavor evolution does not depend on the trajectory. This corresponds to the bulb model (single-angle case)

Figure 3.2.: Dimensionality of the problem (in terms of phase-space dimensions).

3.5 Application to core-collapse supernovae

Supernovae mark the end of a massive star's evolution ($M \gtrsim 8 \mathcal{M}_\odot$) which results into an explosion liberating about 10^{53} erg of gravitational binding energy. While only 1% of this energy is released as kinetic energy of the ejecta, the major part (99%) streams off in form of neutrinos. Remarkably, the visible light carries just 0.01% of the energy and can outshine the stars of the supernova's home galaxy [129].

The notion supernova (SN) was established by the pioneers Walter Baade and Fritz Zwicky. In 1934 they already suggested [130, 131] that the source of the enormous amount of energy released in SNe is a result of the gravitational collapse of a star, where the inner part develops to a neutron star. Today this is the accepted model for a type II SN. Note that there are also other types of supernovae, e.g., type Ia SNe occurring in binary systems consisting at least of one white dwarf. So far the explosion mechanism for type Ia SNe is not fully understood, but it is widely assumed that the explosion is due to thermonuclear reactions. For this type, neutrinos only play a minor part in contrast to type Ib, Ic, and type II SNe which are the result of a collapse of a massive star ($M \gtrsim 8\,\mathcal{M}_\odot$) where almost all the energy is released in form of neutrinos. This latter types where the explosion is powered by gravitational energy are referred to as core-collapse supernovae (CCSNe). Depending on the progenitor star mass, CCSNe leave a black hole or a neutron star as a remnant. During the explosion the major part of the energy is released by neutrinos appearing in all types of flavors. The spectra of the emitted neutrinos imprint crucial information about the core collapse, but they can also provide further insides of their own fundamental properties (e.g., neutrino mass hierarchy) [132].

The last supernova in the vicinity of our galaxy was discovered on 24 February 1987 (23:00 UTC) in the Large Magellanic Cloud at a distance of about 50 kpc from the solar system and is denoted by SN1987A. The burst of neutrinos (which lasted less than 13s) was recorded by three neutrino detectors on the Earth [39]:

- Kamiokande-II in Japan,

- Irvine-Michigan-Brookhaven (IMB) detector in the United States of America,

- Baksan Neutrino Observatory (BNO) in Russia.

The observation of neutrinos arising from the SN1987A explosion was a key achievement in both neutrino physics and neutrino astronomy. It provided a strong support for the modern theory of SN explosions and implied that despite the Sun, there exists another cosmic neutrino source.

As a cosmic laboratory for studying fundamental aspects of physics, supernovae provide a rich phenomenology that is crucial for stellar evolution, nucleosynthesis, and neutrino physics. In what follows we will focus on CCSNe, but we will leave the complex details which are explained in the extensive literature, see, e.g., [39, 133–136] and the references given there.

3.5.1 Neutrino bulb model

In this section we briefly describe the so-called bulb model, introduced in [112], which is widely used to follow the neutrino flavor evolution in core-collapse supernovae. The emission geometry is described in figures 3.3 and 3.4. The model assumes spherical symmetry and is characterized by three properties [112]:

1. Neutrinos are emitted uniformly and half-isotropically[18] from the surface of the neutrino sphere of radius R_ν.

2. At any point outside the neutrino sphere, the physical conditions (e.g., baryon density n_B and temperature T) depend only on the distance r from this point to the center of the proto-neutron star.

3. Neutrinos are emitted from the neutrino-sphere in pure flavor eigenstates and with Fermi-Dirac type energy spectra.

We stress that the radius R_ν is defined to be the distance where the neutrino radiation field is assumed to be half-isotropic [138] and fixes an inner boundary condition for the flavor evolution. As was pointed out in [138], this definition for the decoupling sphere is not necessarily equivalent to the usual definition of the neutrino sphere, where its radius corresponds to the distance where the optical depth equals[19] 2/3. However, with regard to flavor transformations, neutrinos are usually assumed[20] to be in a free-streaming regime, because typical onset-radii are much larger than the assumed R_ν [138, 140]. Because of this latter fact, it is not necessary to know the exact location of the inner boundary condition [138, 141], which simplifies the discussion enormously. Otherwise we would be forced to solve the full quantum kinetic equations including charged and neutral current collisions [141].

We follow a neutrino leaving the neutrino sphere with momentum **p** through an infinitesimal small surface area (the red colored area in figure 3.4):

$$\mathrm{d}A = R_\nu^2 \sin\Theta \mathrm{d}\Theta \mathrm{d}\Phi, \tag{3.37}$$

with an emission angle ϑ_0 corresponding to the angle between the normal direction $\hat{\mathbf{n}}$, which is defined to be perpendicular (and pointing outwards the proto-neutron star) to the surface area element and the propagation direction $\hat{\mathbf{p}}$ of the emitted neutrino with momentum **p**: $\hat{\mathbf{n}} \cdot \hat{\mathbf{p}} = \cos\vartheta_0$. Note that vectors with a ˆ denote unit vectors.

---

[18] Neutrinos are emitted half-isotropically, i.e., isotropic in the outward radial direction of the surface [137].

[19] In the usual definition of the neutrino sphere a value of 2/3 is used. Note, however, that most of neutrinos last scatter in some range, e.g., $1/3 \lesssim \tau \lesssim 1$ [139]. The value 2/3 is usually taken, to incorporate the fact that neutrinos are emitted by some angle (not necessarily radially) [133].

[20] This assumption is probably not justified and needs to be re-evaluated.
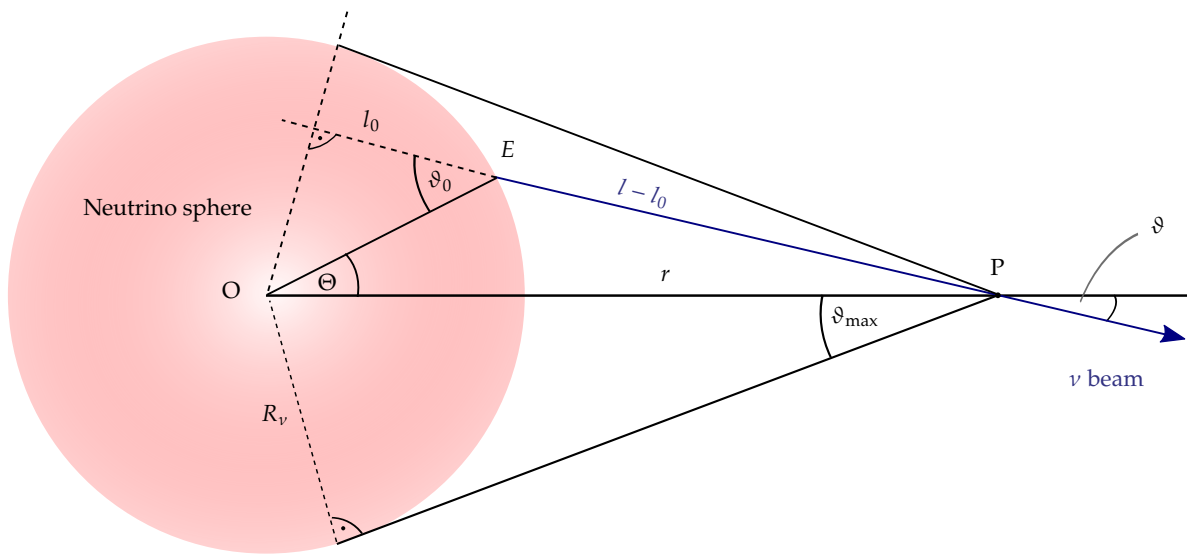
Figure 3.3.: Schematic overview of the neutrino emission process from the neutrino sphere in the bulb model. The background neutrinos originate from the part of the neutrino sphere located inside the cone with opening angle ϑ_{max}. Reproduced and modified from [112].
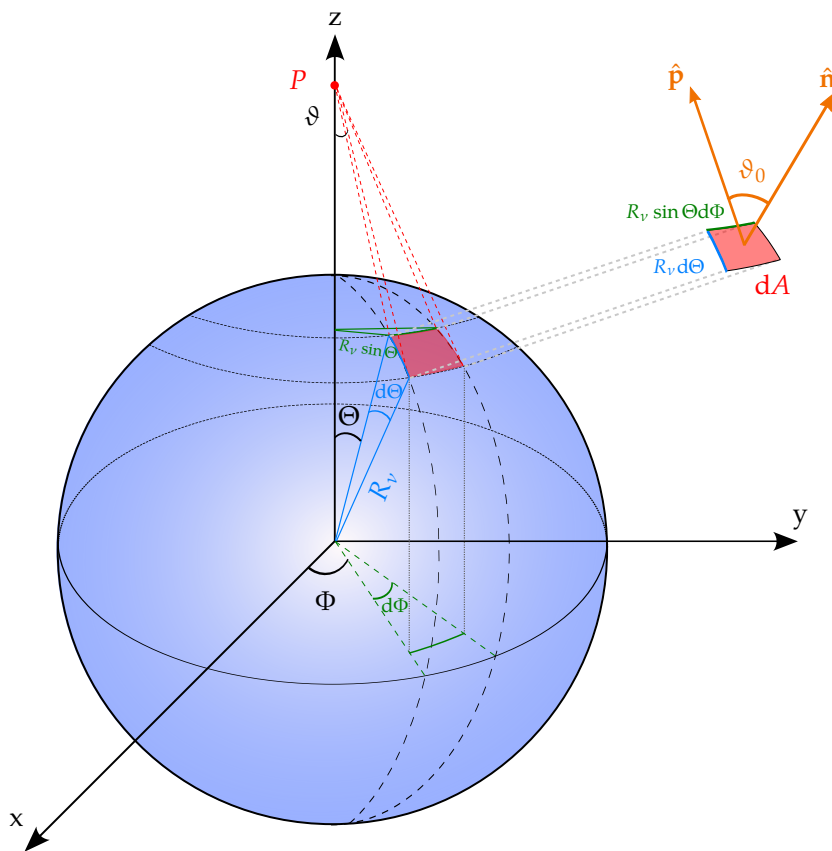
Figure 3.4.: Three-dimensional view of the emission geometry of the bulb model. Polar angle Θ, azimuthal angle Φ.

We introduce the differential neutrino number density $dn_{\nu_\alpha}(\mathbf{p})$ at radius r which includes all ν_α with energy $E = |\mathbf{p}|$ propagating within the range of directions $\hat{\mathbf{p}} + d\hat{\mathbf{p}}$. Explicitly, it turns out to be [112]

$$dn_{\nu_\alpha}(\mathbf{p}) = \frac{j_{\nu_\alpha}(E)\cos\vartheta_0 R_\nu^2 d(\cos\Theta)d\Phi}{(l - l_0)^2},\tag{3.38}$$

where ϑ and ϕ characterize the direction $\hat{\mathbf{p}}$ of the neutrino momentum $\mathbf{p}$, $l \equiv r\cos\vartheta$, and $l_0 \equiv R_\nu\cos\vartheta_0$. Furthermore, j_{ν_α} corresponds to the neutrino number flux per unit energy per solid angle of neutrinos ν_α:

$$j_{\nu_\alpha}(E) = \frac{L_{\nu_\alpha}}{4\pi^2 R_\nu^2 \langle E_{\nu_\alpha}\rangle} f_{\nu_\alpha}(E),\tag{3.39}$$

where L_{ν_α} denotes the energy luminosity, $\langle E_{\nu_\alpha}\rangle$ the average neutrino energy and f_{ν_α} corresponds to the normalized energy distribution function for the neutrino ν_α. Note that the geometric factor $\cos\vartheta_0$ in eq. (3.38) accounts for the fact, that we only follow neutrinos propagating through the area dA in the direction of point P, or in other words, we only consider the neutrino beam inside the cone defined by the opening angle ϑ. By geometric considerations, $d\Phi = d\phi$, and

$$\cos\vartheta_0 R_\nu d\Theta = (l - l_0)d\vartheta\tag{3.40}$$

we find

$$dn_{\nu_\alpha}(\mathbf{p}) = j_{\nu_\alpha}(E)d(\cos\theta)d\phi,\tag{3.41}$$

The opening angle ϑ is restricted to the interval $[0, \vartheta_{\max}]$, where $\vartheta_{\max} = \arcsin(R_\nu/r)$. Note that an equivalent restriction for the emission angle is given by $\vartheta_R \in [0, \pi/2]$.

The distribution function f_{ν_α} can be fitted to supernova neutrino transport calculations [142]. Often the distribution function f_{ν_α} is commonly assumed to be of Fermi-Dirac shape and is described by two parameters T_ν, η_ν:

$$f_{\nu_\alpha}(E_{\nu_\alpha}) = \frac{1}{F_2(\eta_{\nu_\alpha})}\frac{1}{T_{\nu_\alpha}^3}\frac{E_\nu^2}{\exp(E_{\nu_\alpha}/T_{\nu_\alpha} - \eta_{\nu_\alpha}) + 1},\tag{3.42}$$

where we set the neutrino energy $E_{\nu_\alpha} \equiv p$ and F_2. In this expression F_2 corresponds to the Fermi-Dirac integral of order k,

$$F_k(\eta_{\nu_\alpha}) \equiv \int_0^\infty dx\,\frac{x^k}{\exp(x - \eta_{\nu_\alpha}) + 1},\tag{3.43}$$

for $k = 2$, T_{ν_α} denotes the effective temperature at the neutrino sphere and η_{ν_α} is the effective degeneracy parameter (also called: pinching parameter)[21].

Note that the spectra do not follow perfectly a Fermi-Dirac distribution, but are pinched, i.e., both the low- and the high-energy tails are suppressed with respect to the tails of the Maxwell-Boltzmann spectrum with the same mean energy [32, 39, 53]. This pinching is based on the observation that with increasing radius in a SN, the temperature decreases and hence, neutrinos with higher energies have lower temperatures [32]. There are also other fitting functions (cf. [39]). We just mention another, namely the so-called alpha-fit [53, 143]. This is a two-parameter fit

$$f_\alpha(E) = N \left(\frac{E}{\langle E \rangle} \right)^\alpha e^{-(\alpha+1)E/\langle E \rangle}, \tag{3.44}$$

$$N^{-1} \equiv \int_0^\infty dE \left(\frac{E}{\langle E \rangle} \right)^\alpha e^{-(\alpha+1)E/\langle E \rangle} = (\alpha + 1)^{-(\alpha+1)} \Gamma(\alpha + 1) \langle E \rangle, \tag{3.45}$$

where Γ denotes the gamma function. The parameter α controls the pinching of the function while $\langle E \rangle$ denotes the mean energy. The analytical structure of the alpha-fit is simpler than the structure of a Fermi-Dirac like fit while the shapes of both distributions are similar.

3.5.2   Single-angle approximation

If we now use the relation

$$dn_{\nu_\alpha}(\mathbf{q}) = j_{\nu_\alpha}(\mathbf{q})dE \, d(\cos \vartheta)d\phi. \tag{3.46}$$

with $d\Omega_{\mathbf{p}} = \sin \vartheta d\vartheta d\phi$, where $\vartheta \in [0, \vartheta_{\max}]$ and $\phi \in [0, 2\pi]$ and express $\mathbf{q}$ in terms of spherical coordinates, where the direction of $\hat{\mathbf{q}}$ is specified by its polar angle ϑ and azimuthal angle ϕ, i.e,

$$\mathbf{q}' = E \left(\sqrt{1 - \mu'^2} \cos \phi', \sqrt{1 - \mu'^2} \sin \phi', \mu' \right), \tag{3.47}$$

with $\mu' \equiv \cos \vartheta'$ and $E \equiv |\mathbf{q}'|$, we obtain

$$H_{\nu\nu} = \sqrt{2}G_F \sum_{\alpha=e,\mu,\tau} \int_0^\infty dE \int_{\mu_{\max}}^{+1} d\mu' \int_0^{2\pi} d\phi$$
$$\times (1 - \cos \theta) \left(j_{\nu_\alpha} \rho_{\nu_\alpha}(E, \mu', \phi') - j_{\bar{\nu}_\alpha} \bar{\rho}_{\bar{\nu}_\alpha}(E, \mu', \phi') \right) \tag{3.48}$$

with the cosine of the scattering angle θ given by

$$\cos \theta = \mu\mu' + \sqrt{(1 - \mu^2)(1 - \mu'^2)} \cos \varphi, \tag{3.49}$$

---

[21] The parameters T_ν and η_ν should be considered as effective parameters, because the spectra are in general not in thermal equilibrium and therefore, the temperature and the degeneracy parameter are not well-defined [83].

where $\varphi \equiv \phi' - \phi$ denotes the azimuthal angle of one neutrino relative to the other.

If we assume cylindrical symmetry around the z axis, i.e., $\rho_{\nu_\alpha} = \rho_{\nu_\alpha}(q', \mu')$, we obtain for some arbitrary function ξ depending on the energy E and the cosine of ϑ' the relation

$$\int_{\mu_{\max}}^{+1} d\mu' \int_0^{2\pi} d\phi \, (1 - \cos\theta) \xi(E, \mu') = 2\pi \int_{\mu_{\max}}^{+1} d\mu' \, (1 - \mu\mu') \, \xi(E, \mu'). \tag{3.50}$$

In the so-called single-angle approximation [112], it is assumed that the flavor evolution is independent of the trajectory, i.e., $\rho_{\nu_\alpha} = \rho_{\nu_\alpha}(q')$ and therefore the evolution will not differ from the situation where neutrinos are propagating in radial direction, $\mu = 1$. This further simplifies the integration and we obtain the neutrino-neutrino forward scattering part of the Hamiltonian in the single-angle approximation

$$\mathsf{H}_{\nu\nu} = \sqrt{2} G_F \, 2\pi \, D(r) \sum_{\alpha = e, \mu, \tau} \int_0^\infty dE \left(j_{\nu_\alpha}(E) \rho_{\nu_\alpha}(E) - j_{\bar{\nu}_\alpha}(E) \bar{\rho}_{\bar{\nu}_\alpha}(E) \right), \tag{3.51}$$

where the geometric factor

$$D(r) \equiv \int_{\mu_{\max}}^{+1} d\mu' \, (1 - \mu') \tag{3.52}$$

$$= \frac{1}{2} - \mu_{\max} + \frac{1}{2}\mu_{\max}^2 \tag{3.53}$$

$$= \frac{1}{2}(1 - \mu_{\max})^2 \tag{3.54}$$

$$= \frac{1}{2}\left[1 - \sqrt{1 - \left(\frac{R_\nu}{r}\right)^2} \right]^2, \tag{3.55}$$

with the geometric relation $\mu_{\max} \equiv \cos\vartheta_{\max} = \sqrt{1 - (R_\nu/r)^2}$ used in the last step, will partially take the angle effect into account[22] [118]. Note that D only depends on the ratio r/R_ν.

3.5.3 Collective Modes

Neutrinos streaming off a supernovae core can experience different kinds of collective behaviors [118]. Inside the region where the neutrino number density exceeds the ordinary matter number density, neutrinos experience a collective behavior that is called synchronized oscillations [93, 147]: Neutrinos and antineutrinos of different energy modes couple and oscillate with a common frequency. Necessary for this type of collective behavior, is a domination of the scale set by the neutrino self-interaction potential over all other relevant oscillation scales (due to the vacuum and matter) and an asymmetry between the initial

---

[22] Far away from the proto-neutron star, we have $D(r) \propto r^{-4}$ which is the expected behavior: One factor of r^{-2} accounts for the geometric dilution of flux [134, 144, 145] while another factor of r^{-2} originates from the increasing collinearity [144, 146], i.e., $\langle 1 - \cos\theta \rangle \approx (R_\nu/r)^2$, where $\vartheta_{\max} = \arcsin(R_\nu/r) \approx R_\nu/r$ for $r \gg R_\nu$.

neutrino and antineutrino fluxes [86]. In more realistic settings like core-collapse supernovae, the synchronized regime is expected close to the neutrino emitting surface. Because neutrinos are essentially locked in their flavor states, flavor conversion is suppressed. In figure 3.5 this behavior is shown about a distance of 11 km from the center of the core. The energy-averaged survival probability $\langle P(\nu_e \to \nu_e) \rangle$ performs small amplitude oscillations close to 1. Because typical oscillation lengths lie in the centi- or millimeter regime, numerical schemes are often forced to use a high resolution, i.e., one has to choose very small initial step sizes. If we assume that there are no MSW-like resonances, which could in principle be present [148–151], nothing of physical interest is happening.
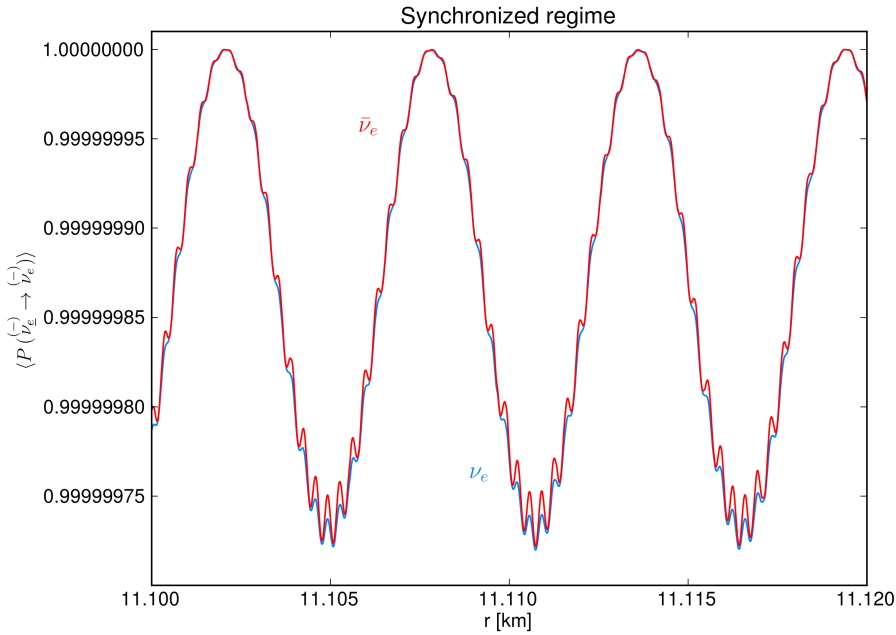
Figure 3.5.: Synchronized regime

Farther outside the neutrino sphere, when the strength of the neutrino potential becomes comparable to the vacuum scale, neutrinos and antineutrinos of one flavor can simultaneously convert into neutrinos and antineutrinos of another flavor. This type of mode is called bipolar [86, 87, 152] and is related to an instability in flavor space, triggered by the non-vanishing vacuum mixing.

In the spinning top analogy, the fact that the neutrino self-interaction potential is not sufficiently strong to keep the ensemble synchronized translates in an decrease of the spin due to friction (the self-interaction potential) and the top begins wobbling. Eventually, there will be a complete turn over [153]. Note that in the bipolar regime, there is usually an effect from both precession and nutation while in the synchronized regime there is only precession.

Depending on the mass hierarchy and the initial neutrino fluxes [86, 114, 145, 154], the gyroscopic pendulum is starting in a stable or unstable equilibrium position and always tries to relax to its stable position (the downwards stable position). Only in the case where the pendulum starts in the unstable position, there can be large flavor conversion. In the

stable case, there are only small oscillations around the equilibrium. It is possible to relate this phenomenon with the classical mechanics analogy of a spinning top or a gyroscopic pendulum precessing in an external field [153].

In [140] it was demonstrated that the onset bipolar instability occurs at different positions if one uses a multi-angle instead of a single-angle treatment. To estimate the onset radius of the bipolar instability, performing stability analysis of the linearized equations of motion turned out to be very fruitful [155–157]. Furthermore, in [158] it was recognized by switching into the matter eigenstate basis that the instability is characterized by a sudden change of the matter phase. Note that the latter is associated with the flavor off-diagonal matrix elements of the Hamiltonian.

Finally, after bipolar oscillations have ceased, a phenomenon can arise where two neutrinos can exchange their flavors at some sharp critical energy. This is called spectral split (or spectral swap) of the neutrino spectra. In [159] this effect was identified by an MSW-like resonance in a co-rotating frame. Note that in [160] it was shown that this effect is similar to a magnetic resonance. In the past, the crucial relevance for core-collapse supernovae was immediately understood: If an electron neutrino would swap its flavor with one of the heavier flavors which have a much harder spectrum, this could increase the neutrino heating rate before the shock, and could potentially provide strong explosion energies [161]. But soon it was realized that the large matter densities could suppress the oscillations at least at the mean-field level [162, 163].

3.5.4 Single-angle calculations

We performed numerical single-angle calculations with two- and three flavors in both mass hierarchies. For the three flavor case, we use, e.g., as in [145, 164], the rotated basis (v_e, v_x, v_y) instead of (v_e, v_μ, v_τ) by effectively setting the mixing angle $\theta_{23} = 0$. For the electron number density, we use the profile as in [165]:

$$n_e(r) = \frac{\rho_{\mathrm{matt},0} Y_e}{m_{\mathrm{u}}} \left(\frac{10\,\mathrm{km}}{r}\right)^3 , \qquad (3.56)$$

where $\rho_{\mathrm{matt},0} = 2 \times 10^8\,\mathrm{gcm}^{-3}$ and $Y_e = 0.5$. As neutrino sphere radius we take $R_\nu = 10\,\mathrm{km}$. Motivated by the studies performed in [83], we choose[23] for the neutrino mean energies $\langle E_\nu \rangle$ and the luminosities L_ν the values listed in table 2.4 and use the alpha-fit function eq. (3.44).

The results show the three distinct regions, synchronized, bipolar and the part, where the MSW effect becomes relevant.

We also compute the fluxes of neutrinos with flavor α and energy E:

$$\mathcal{F}_{\nu_\alpha}(E, r) = \sum_{\beta = e, \mu, \tau} j_{\nu_\beta}(E) P(\nu_\beta \to \nu_\alpha)(E, r). \qquad (3.57)$$

---

[23] This corresponds to $p = 10$ and $q = 3.5$ in table 6 in [83].

65
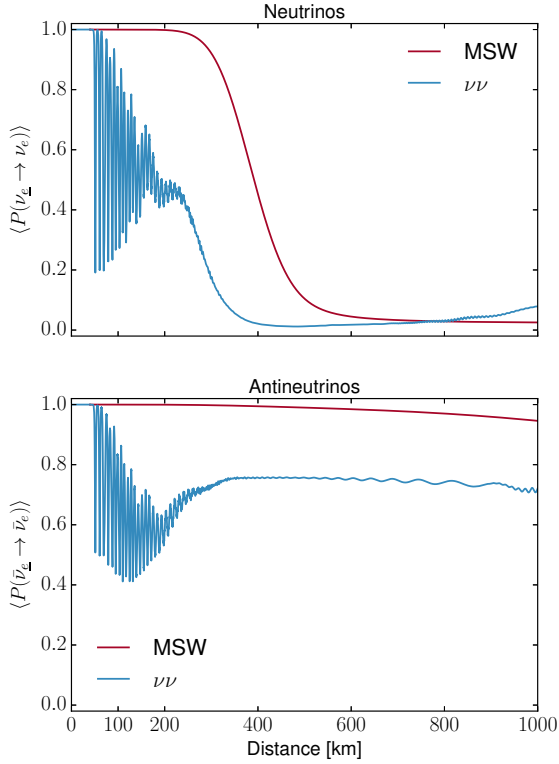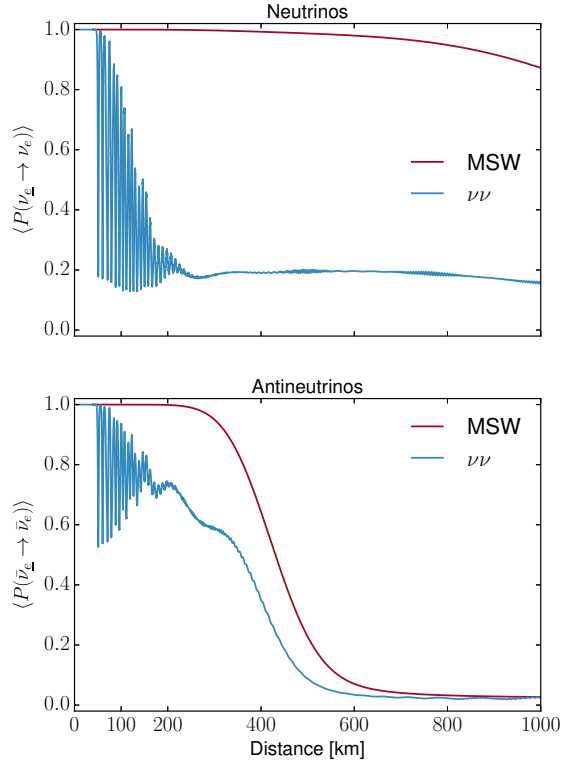
(a) Normal hierarchy.

(b) Inverted hierarchy.
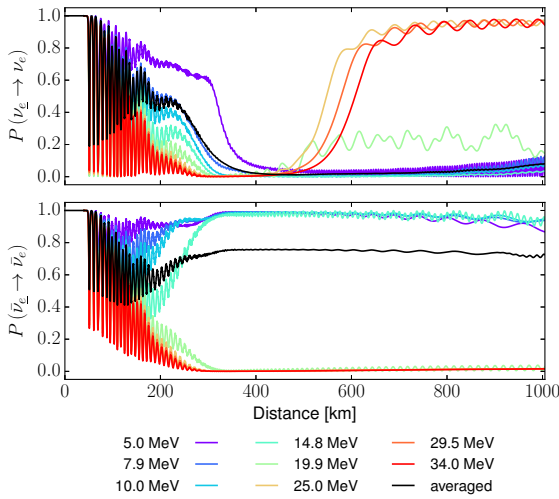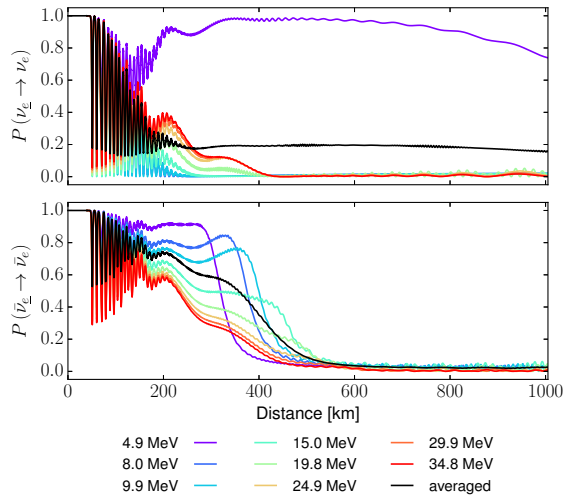
(c) Normal hierarchy.

(d) Inverted hierarchy.

Figure 3.6.: Single-angle calculations for three flavors in normal (left) and inverted (right panels) mass hierarchy. The top panels show the spectral averaged survival probabilities for neutrinos while the middle panels correspond to antineutrinos, respectively. The blue (red) curves correspond to calculations including (without) neutrino self-interactions. In the bottom panels we show energy-dependent survival probabilities along with the averaged ones including neutrino self-interactions.
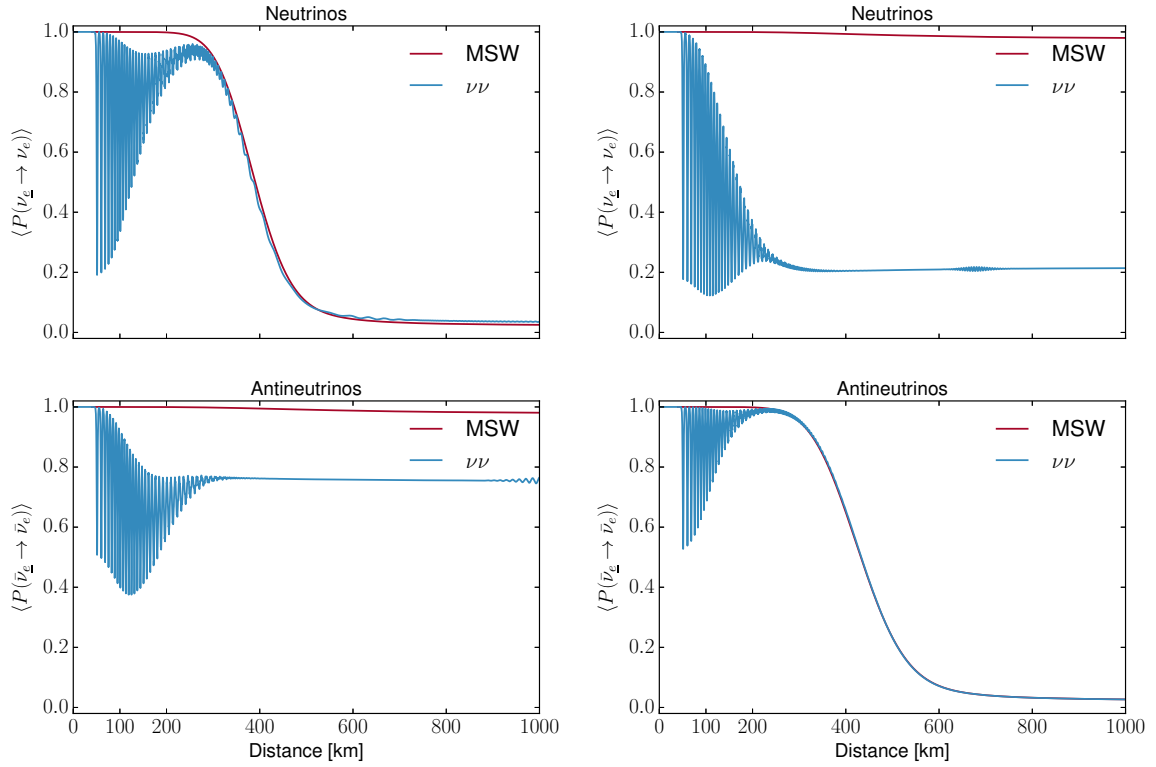
(a) Normal hierarchy.

(b) Inverted hierarchy.
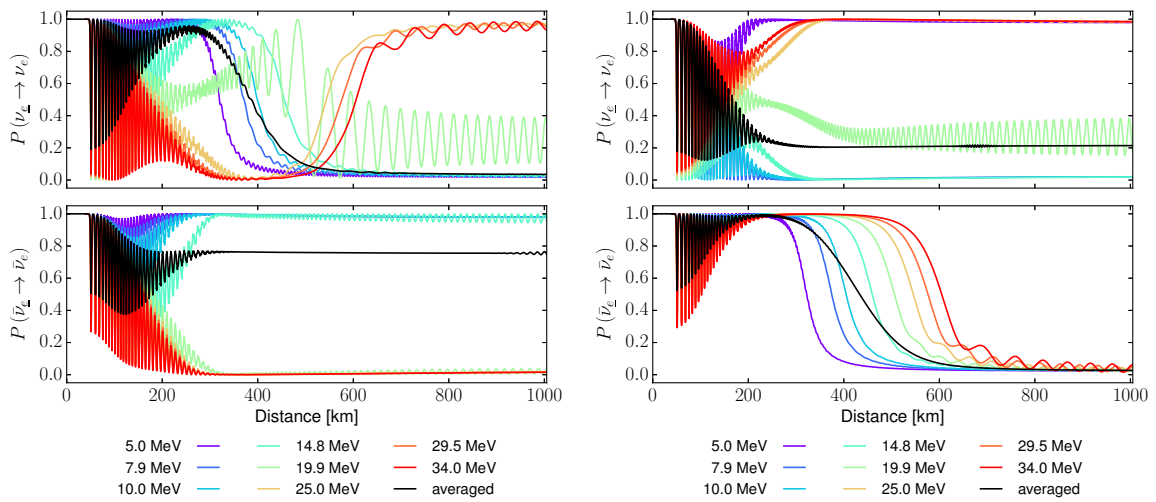
(c) Normal hierarchy.

(d) Inverted hierarchy.

Figure 3.7.: Same as figure 3.6 for the two-flavor case.

In figure 3.8, we show these fluxes at a distance of $r = 400$ km for the three- and two- flavor cases. Some of the results show one, two or even no spectral swaps. We shortly discuss the inverted mass hierarchy case (the normal hierarchy case can be treated similarly). In the three-flavor case, there is only one spectral swap between ν_e and ν_y. In contrast, the two-flavor case shows two spectral splits, one at lower energies ($\simeq 5$ MeV), which is similar to the two flavor case, and another one at higher energies ($\simeq 21$ eV). In the case of antineutrinos, both for two and three flavors, the $\bar{\nu}_e$ swaps are not complete and $\bar{\nu}_e$ mix partially with ν_y. As described in [165], the two-flavor approximation can lead to "artificial" instabilities and one really should use a three-flavor scheme. From the observational point of view, the occurrence of spectral splits has important consequences, since the detection of a split occurring at higher energies could in principle be measurable[24].

---

[24] Note that typical cross sections scale with E_ν^2.
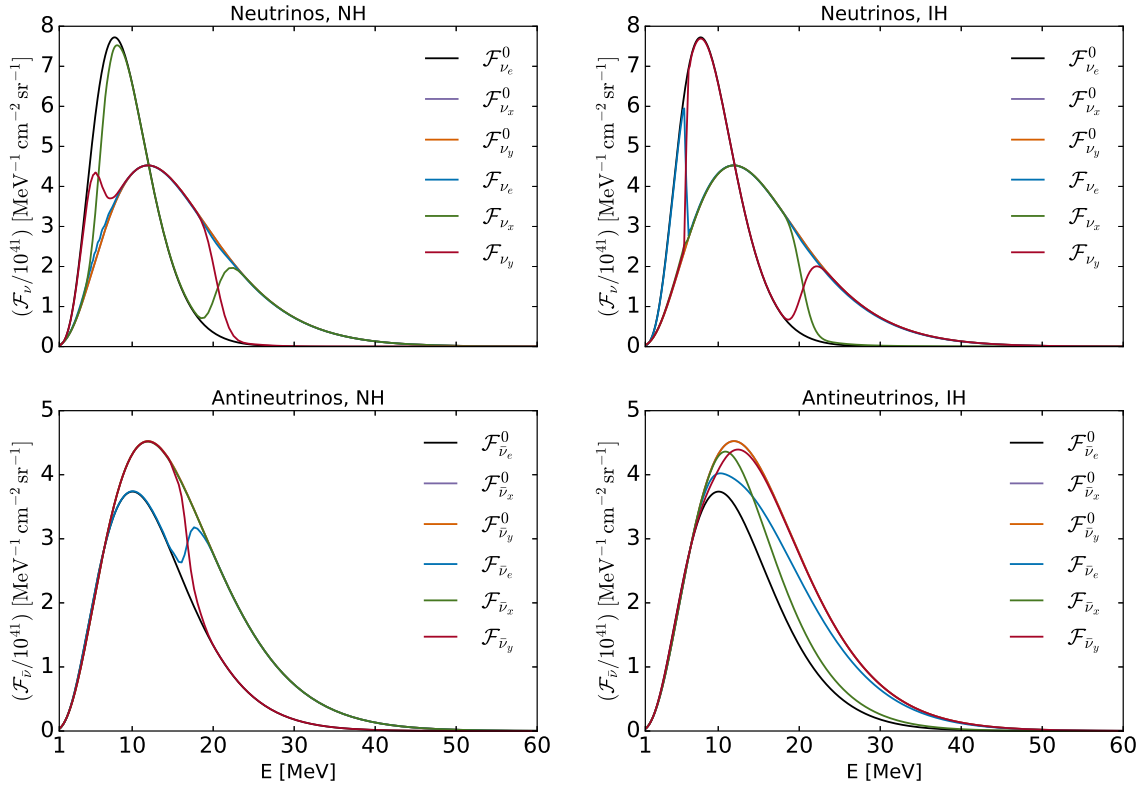
(a) Normal hierarchy.

(b) Inverted hierarchy.
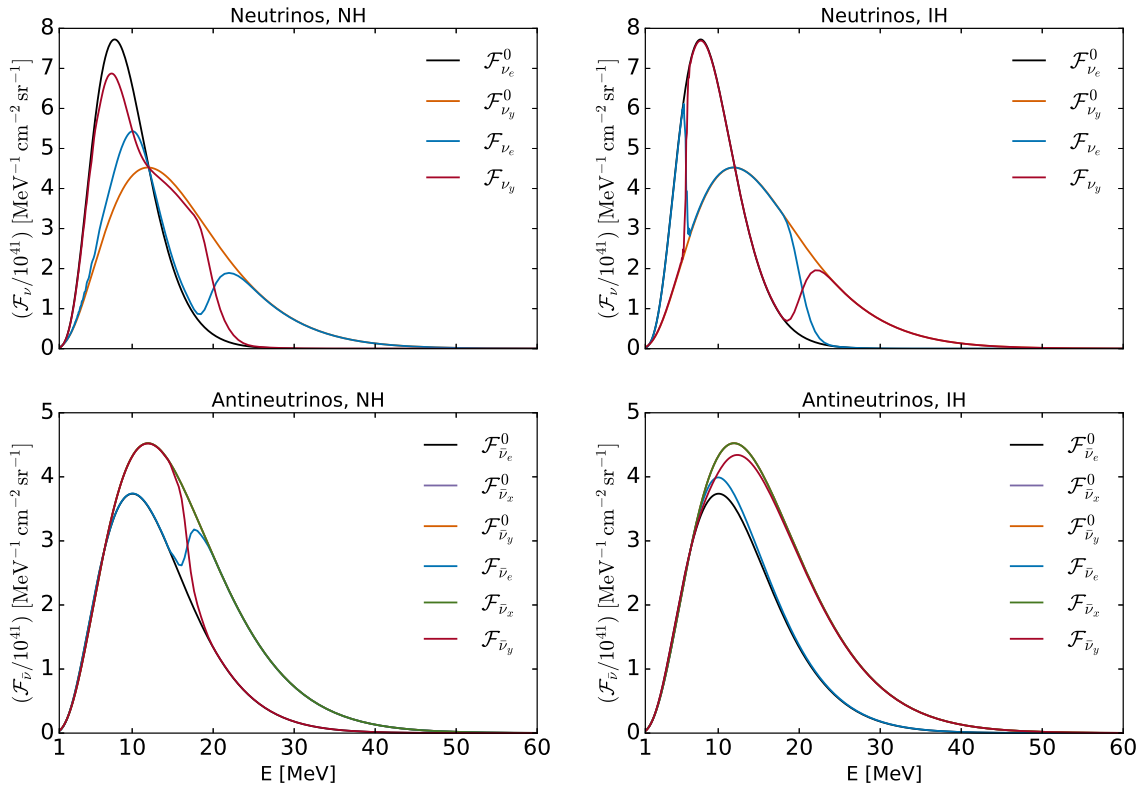
(c) Normal hierarchy.

(d) Inverted hierarchy.

Figure 3.8.: Single-angle calculations for three (top panels (a) and (b)) and two (bottom panels (c) and (d)) flavors in normal (left panels) and inverted (right panels) mass hierarchy. The panels show the fluxes at the neutrino sphere and at a distance $400\,\mathrm{km}$.

3.5.5 General comments

In case of an isotropic neutrino gas, the angular factor $1 - \cos\theta_{\hat{\mathbf{p}}\hat{\mathbf{q}}}$ averages to zero, but in realistic settings neutrinos are usually emitted non-isotropically from the source so that effectively neutrinos propagating on different trajectories possess a different refractive index leading to multi-angle effects. While in case of an isotropic neutrino gas collective flavor oscillations would arise due to self-induced effects, this is not necessarily the case for an anisotropic gas. The multi-angle effects sometimes lead to flavor decoherence, where an equilibration among electron and non-electron (anti)neutrinos fluxes results [141, 155, 166].

The role of dense matter in the development of self-induced flavor conversions was studied in [162] and it turned out that self-induced effects are less sensitive to matter when the number densities fulfill the condition $n_e^- - n_e^+ \ll n_{\bar{\nu}_e} - n_{\bar{\nu}_x}$.

More general, it was realized that the coherent flavor evolution is subject to an instability in flavor space and results in kinematical decoherence in case of a sufficiently small (or vanishing) asymmetry between neutrino and antineutrino number densities. In contrast, a sufficiently large asymmetry can maintain the coherence and in some cases multi-angle angle calculations show a behavior similar to what is obtained in single-angle calculations [113].

Note that if the system under consideration is isotropic, the matter potential will have the same effect on all angular modes and one can transform into a rotating frame such that the matter term is removed[25]. In contrast, in an anisotropic system the matter term is also affected by multi-angle effects and one is not allowed to remove the matter term. The multi-angle matter effects [132] will lead to a wide dispersion between different neutrino momentum modes. As a consequence, this means that if $n_e^- - n_e^+ \gg n_{\bar{\nu}_e} - n_{\bar{\nu}_x}$, self-induced conversion effects are suppressed [162]. In the case of $n_e^- - n_e^+ \sim n_{\bar{\nu}_e} - n_{\bar{\nu}_x}$ multi-angle matter effects could lead to decoherence.

Using hydrodynamics simulations and spherically symmetric one-dimensional models, it has been realized in schematic studies that at relatively early times in case of iron-core supernovae, the dominating matter will block the occurrence of self-induced flavor conversion effects while for lower mass stars with O-Ne-Mg cores there is no complete matter suppression and at least partial flavor conversion effects are found [138, 167–170].

If indeed collective flavor conversion effects are suppressed due to the high matter density, e.g., during the accretion phase for iron-core supernovae, flavor conversions due to the MSW effect are still possible which eases the analysis. This simplifies the problem in the sense that neutrino flavor conversion and neutrino transport can be separated and we can extract information on the neutrino mass hierarchy by detection of the neutrino signal. Self-induced flavor transformations can still be relevant during the cooling phase, since the matter potential decreases and becomes small compared to the neutrino potential.

---

[25] Then, the only effect of matter which would be recognizable, is a suppression of the effective (in-matter) mixing angle if we work in the single-angle approximation.

3.6 Neutrino flavor isospin revisited

In order to describe neutrino self-interactions in the NFIS formalism, we introduce the total NFIS via [87]

$$S := \int_{-\infty}^{+\infty} d\omega \, f_\omega s_\omega, \tag{3.58}$$

where f_ω denotes the normalized neutrino distribution function:

$$\int_0^{+\infty} d\omega \, f_\omega = 1. \tag{3.59}$$

The vector accounting for neutrino self-interactions can then be written as $-2\mu S$, where $\mu \equiv \sqrt{2} G_F n_\nu$ describes the interaction strength and n_ν denotes the total neutrino number density.

Taking into account the previous experience with adiabatic flavor conversion in ordinary matter (see sections 2.6.2, 2.6.3, and 2.7), we can apply the same picture in the presence of neutrino self-interactions. If the matter and neutrino number densities change only sufficiently slowly during the evolution, then the NFIS s_ω should keep its initial alignment with the Hamiltonian vector $\mathbf{H}_\omega$ such that

$$s_\omega = \frac{\epsilon_\omega}{2} \frac{\mathbf{H}_\omega}{H_\omega}, \tag{3.60}$$

where $\epsilon_\omega = +1(-1)$ indicates the (anti-) alignment of the NFIS. If eq. (3.60) is multiplied by f_ω and integrated over ω, then one obtains an equation that can be solved self-consistently:

$$S = \frac{1}{2} \int_{-\infty}^{+\infty} d\omega \, f_\omega \, \epsilon_\omega \, s_\omega. \tag{3.61}$$

It turns out [151] that if $\mathbf{H}_{\text{matt}} \neq 0$, the y-component of the total NFIS vanishes $S_y = 0$.

3.7 Matter-neutrino resonances

In this section we want to investigate the phenomenon of so-called matter-neutrino resonances (MNR). Fur this purpose, we will first focus on simple toy model studies, before we explore the occurrence of MNR in a more realistic setting, namely in a binary neutron star merger remnant, which is one of the purposes of this work.

3.7.1 Two-flavor discussion

In order to simplify the discussion we restrict ourselves to the two-flavor case. We consider a propagation Hamiltonian $H = H_{\text{vac}} + H_{\text{matt}} + H_{\nu\nu}$ which includes a vacuum part

(H_{vac}), a contribution that accounts for coherent neutrino forward scattering off electrons, positrons, nucleons (H_{matt}), and neutrinos ($H_{\nu\nu}$). Such a Hamiltonian is particularly suited for astrophysical settings.

For rendering the physics more transparent, we write the Hamiltonian in its traceless form. Explicitly, the individual contributions are given by eq. (2.47) for the vacuum term, eq. (2.71), $H_{matt} = \mathrm{diag}(V_e, -V_e)/2$, where $V_e = V_{CC}$ corresponds to the refractive energy shift between ν_e and ν_τ due to coherent scattering off ordinary background particles. For the traceless part of the neutrino self-interaction Hamiltonian, we introduce the notation

$$\frac{1}{2} \begin{pmatrix} V_{\nu\nu} & V_{\nu\nu}^{e\tau} \\ (V_{\nu\nu}^{e\tau})^* & -V_{\nu\nu} \end{pmatrix} := H_{\nu\nu} - \frac{1}{2}\mathrm{tr}\,H_{\nu\nu} \tag{3.62}$$

$$= \frac{1}{2} \begin{pmatrix} (H_{\nu\nu})_{ee} - (H_{\nu\nu})_{\tau\tau} & (H_{\nu\nu})_{e\tau} \\ (H_{\nu\nu})_{e\tau}^* & (H_{\nu\nu})_{\tau\tau} - (H_{\nu\nu})_{ee} \end{pmatrix} \tag{3.63}$$

Finally the traceless Hamiltonian takes the form

$$H = \frac{1}{2} \begin{pmatrix} -\omega\cos 2\theta + V_e + V_{\nu\nu} & \omega\sin 2\theta + V_{\nu\nu}^{e\tau} \\ \omega\sin 2\theta + (V_{\nu\nu}^{e\tau})^* & \omega\cos 2\theta - V_e - V_{\nu\nu} \end{pmatrix}. \tag{3.64}$$

Since H is Hermitian, there exists a matrix $\tilde{U} \in SU(2)$ such that the unitary transformation $U^\dagger H U$ diagonalizes the Hamiltonian. The eigenvalues of H are given by $\pm\tilde{\omega}/2 := \Delta\tilde{m}^2/(4E)$ with

$$\frac{\Delta\tilde{m}^2}{2E} = \sqrt{(\omega\cos 2\theta - V_e - V_{\nu\nu})^2 + |\omega\sin 2\theta + V_{\nu\nu}^{e\tau}|^2} \tag{3.65}$$

and we find

$$\tilde{U}^\dagger H \tilde{U} = \frac{\tilde{\omega}}{2} \begin{pmatrix} -1 & 0 \\ 0 & 1 \end{pmatrix}. \tag{3.66}$$

Since, U links flavor and propagation eigenstates,

$$\begin{pmatrix} |\nu_e\rangle \\ |\nu_\tau\rangle \end{pmatrix} = \tilde{U} \begin{pmatrix} |\tilde{\nu}_1\rangle \\ |\tilde{\nu}_2\rangle \end{pmatrix}, \tag{3.67}$$

we are interested in having an explicit form of $\tilde{U}$. Note that a general element $\tilde{U} \in SU(2)$ can be expressed in the following form[26] [172]:

$$\tilde{U} = \begin{pmatrix} e^{i\alpha} \cos\tilde{\theta} & e^{i\beta} \sin\tilde{\theta} \\ -e^{-i\beta} \sin\tilde{\theta} & e^{-i\alpha} \cos\tilde{\theta} \end{pmatrix}, \tag{3.70}$$

where $\alpha, \beta \in \mathbb{R}$ are time and / or space and medium dependent phases. Making use of this expression, we transform back to the flavor basis:

$$H = \frac{\tilde{\omega}}{2} \tilde{U} \begin{pmatrix} -1 & 0 \\ 0 & 1 \end{pmatrix} \tilde{U}^\dagger = \frac{\tilde{\omega}}{2} \begin{pmatrix} -\cos 2\tilde{\theta} & e^{i\phi} \sin 2\tilde{\theta} \\ e^{-i\phi} \sin 2\tilde{\theta} & \cos 2\tilde{\theta} \end{pmatrix}, \tag{3.71}$$

where we set $\phi := \alpha + \beta$.

If we re-define the propagation eigenstates by absorbing phase factors (and not changing the notation),

$$|\tilde{\nu}_1\rangle \mapsto e^{i\alpha} |\tilde{\nu}_1\rangle \tag{3.72}$$

$$|\tilde{\nu}_2\rangle \mapsto e^{-i\alpha} |\tilde{\nu}_2\rangle \tag{3.73}$$

we obtain the relation:

$$\begin{pmatrix} |\nu_e\rangle \\ |\nu_\tau\rangle \end{pmatrix} = \begin{pmatrix} \cos\tilde{\theta} & e^{i\phi} \sin\tilde{\theta} \\ -e^{-i\phi} \sin\tilde{\theta} & \cos\tilde{\theta} \end{pmatrix} \begin{pmatrix} |\tilde{\nu}_1\rangle \\ |\tilde{\nu}_2\rangle \end{pmatrix}. \tag{3.74}$$

We remind that if neutrinos propagate in a neutrino background, the neutrino self-interactions will produce a complex flavor off-diagonal potential $V_{\nu\nu}^{e\tau}$.

Comparing the elements of both forms of the Hamiltonian H, eqs. (3.64) and (3.71), we find the following relationship:

$$e^{i\phi} \tan(2\tilde{\theta}) = \frac{\omega \sin(2\theta) + V_{\nu\nu}^{e\tau}}{\omega \cos(2\theta) - V_e - V_{\nu\nu}}. \tag{3.75}$$

Since $H_{e\tau} = |H_{e\tau}| e^{i\phi}$ and $\tan\phi = \mathfrak{Im}(H_{e\tau})/\mathfrak{Re}(H_{e\tau})$ we can write:

$$\tan\phi = \frac{\mathfrak{Im}(V_{\nu\nu}^{e\tau})}{\omega \sin(2\theta) + \mathfrak{Re}(V_{\nu\nu}^{e\tau})}. \tag{3.76}$$

---

[26] For a Hermitian matrix H we can always introduce two angles $\tilde{\theta}$ and ϕ associated with the matrix elements $H_{\alpha\beta}$ (see e.g., [171]):

$$\tan 2\tilde{\theta} = \frac{2|H_{e\tau}|}{H_{ee} - H_{\tau\tau}}, \qquad 0 \le \tilde{\theta} < \pi, \tag{3.68}$$

$$H_{e\tau} = |H_{e\tau}| e^{i\phi}, \qquad 0 \le \phi < 2\pi, \tag{3.69}$$

where ϕ corresponds to the argument of the complex quantity $H_{e\tau}$.

It is now straightforward to write down the resonance conditions:

$$\omega \cos(2\theta) = V_e + V_{\nu\nu}, \tag{3.77}$$
$$\omega \sin(2\theta) = -\Re(V^{e\tau}_{\nu\nu}). \tag{3.78}$$

At resonance (condition (3.77)), there will be maximal mixing, i.e., $\tilde{\theta}\big|_{\mathrm{res}} = \pi/4$. Note that if this condition is met and $V_e + V_{\nu\nu} > 0$, then there will be a resonance for a neutrino while if $V_e + V_{\nu\nu} < 0$ an antineutrino will encounter a resonance.

The possibility that $V_e + V_{\nu\nu} \approx 0$ was first mentioned in [91], but was not further investigated. This study was concerned with the neutrino evolution in core-collapse supernovae, but as long as only active neutrinos are involved, the condition above is not met[27]. Different from the core-collapse supernovae case, the aftermath of compact object mergers provide a natural environment where $V_e + V_{\nu\nu} \approx 0$ can be fulfilled. Because near the neutrino surface the electron antineutrino fluxes exceed the electron neutrino fluxes, the neutrino self-interaction potential is initially negative. The condition above gives rise to a resonance phenomenon, so-called matter-neutrino resonances (MNR). The first numerical work that encountered such resonances was done in the context of collapsars [173] and subsequent works also found them in compact object mergers [26, 174–176], which we will discuss in the next chapter. In order to capture the essential physics behind the MNR, we study a simple toy model in what follows. For a broader discussion, see [174, 177, 178].

3.7.2 Analytical formulas

In the following we consider a monoenergetic two-flavor system, initially consisting of only ν_e and $\bar{\nu}_e$. We introduce a neutrino asymmetry parameter $\alpha \equiv n_{\bar{\nu}_e}/n_{\nu_e}$ which is the ratio of electron antineutrino number density over electron neutrino number density. Since we are facing a two-flavor problem, it is convenient to employ the NFIS formalism. Positive frequencies correspond to neutrinos while negative frequencies correspond to antineutrinos. The equations of motion can then be formulated as

$$\mathbf{s}_{\pm\omega_0} = \mathbf{s}_{\pm\omega_0} \times \mathbf{H}'_{\pm\omega_0}, \tag{3.79}$$

where we fixed $\omega_0 \in \mathbb{R}_{>0}$ and removed the test neutrino contributions from the self-interaction Hamiltonians:

$$\mathbf{H}'_{\omega_0} := \omega_0 \hat{\mathbf{H}}_{\mathrm{vac}} - V_e \hat{\mathbf{e}}^{\mathrm{f}}_z - 2\mu\alpha\mathbf{s}_{-\omega_0}, \tag{3.80}$$
$$\mathbf{H}'_{\omega_0} := -\omega_0 \hat{\mathbf{H}}_{\mathrm{vac}} - V_e \hat{\mathbf{e}}^{\mathrm{f}}_z - 2\mu\mathbf{s}_{\omega_0}. \tag{3.81}$$

---

[27] The situation is different if sterile neutrinos are incorporated.

If initially $\mu > V_e \gg \omega_0$, the NFISs $\mathbf{s}_{\pm\omega_0}$ are initially aligned with the corresponding Hamiltonians $\mathbf{H}'_{\pm\omega_0}$ and the adiabatic solution is described by

$$\mathbf{s}_{\pm\omega_0} = \frac{1}{2} \frac{\mathbf{H}'_{\pm\omega_0}}{|\mathbf{H}'_{\pm\omega_0}|}, \tag{3.82}$$

with $\mathbf{s}_{\pm\omega_0} \cdot \hat{\mathbf{e}}_y^f = 0$.

Within the resonance region, we can obtain an approximative expression for the survival probabilities if $V_e \gg \omega_0$. If we neglect the vacuum contributions in the effective field, we find

$$s_{\omega_0,z}^f = \mathbf{s}_{\omega_0} \cdot \hat{\mathbf{e}}_z^f = \frac{1}{2} \frac{\mathbf{H}'_{\omega_0}}{|\mathbf{H}'_{\omega_0}|} \tag{3.83}$$

$$\approx -\frac{1}{2} \frac{V_e + 2\mu\alpha s_{-\omega_0,z}^f}{\sqrt{V_e^2 + \mu^2\alpha^2 + 4\mu\alpha V_e s_{-\omega_0,z}^f}}. \tag{3.84}$$

At resonance we have $\mathbf{H}_{\omega_0} \cdot \hat{\mathbf{e}}_z^f = 0$ which is equivalent to $V_e + 2\mu(s_{\omega_0,z}^f + \alpha s_{-\omega_0,z}^f) = 0$ or $2\mu\alpha s_{-\omega_0,z}^f = -V_e - 2\mu s_{\omega_0,z}^f$ if we ignore the vacuum contribution. Then it follows:

$$s_{\omega_0,z}^f \approx \frac{s_{\omega_0,z}^f}{\sqrt{\mu^2\alpha^2 - 4\mu V_e s_{\omega_0,z}^f - V_e^2}} \tag{3.85}$$

and consequently

$$s_{\omega_0,z}^f \approx \frac{\mu^2(\alpha^2 - 1) - V_e^2}{4\mu V_e}. \tag{3.86}$$

The ν_e survival probability is then given by $P(\nu_{\underline{e}} \to \nu_e) = \frac{1}{2} + s_{\omega_0,z}^f$.

Similarly we can find such an approximative expression for antineutrinos

$$s_{-\omega_0,z}^f = \mathbf{s}_{-\omega_0} \cdot \hat{\mathbf{e}}_z^f = \frac{1}{2} \frac{\mathbf{H}'_{-\omega_0}}{|\mathbf{H}'_{-\omega_0}|} \tag{3.87}$$

$$\approx -\frac{1}{2} \frac{V_e + 2\mu s_{\omega_0,z}^f}{\sqrt{V_e^2 + \mu^2 + 4\mu V_e s_{\omega_0,z}^f}} \tag{3.88}$$

At resonance we infer from the expression above that $2\mu s_{\omega_0,z}^f = -V_e - 2\mu\alpha s_{-\omega_0,z}^f$ leading to

$$s_{-\omega_0,z}^f \approx \frac{s_{-\omega_0,z}^f}{\sqrt{\mu^2 - 4\mu\alpha V_e s_{-\omega_0,z}^f - V_e^2}}. \tag{3.89}$$

Finally we arrive at

$$s_{-\omega_0,z}^f \approx -\frac{\mu^2(\alpha^2 - 1) + V_e^2}{4\mu\alpha V_e}. \tag{3.90}$$

and the $\bar{\nu}_e$ survival probability is expressed as $P(\bar{\nu}_e \to \bar{\nu}_e) = \frac{1}{2} - s^f_{-\omega_0,z}$.

Note that the expressions eqs. (3.86) and (3.90) agree with the ones derived in [174], but in contrast, we did not assume $s^f_{\omega_0,x} + \alpha s^f_{-\omega_0,x} \approx 0$ and $s^f_{\omega_0,y} + \alpha s^f_{-\omega_0,y} \approx 0$. In fact it can be shown that the y-component of the total NFIS $\mathbf{S}$ always vanishes in the flavor (and vacuum mass) basis if $V_e \neq 0$ [151]. On the other hand, one can determine S^f_x and S^f_z algebraically from the self-consistent equation:

$$\mathbf{S} = \int_{-\infty}^{\infty} d\omega \, \epsilon_\omega f_\omega \frac{\mathbf{H}_\omega}{|\mathbf{H}_\omega|}. \tag{3.91}$$

For the sake of completeness we also mention the full expression which includes the vacuum contributions (for the neutrino case only):

$$s^f_{\omega_0,z} = \frac{\mu^2(\alpha^2 - 1) - V_e^2 + \omega_0 \cos(2\theta)V_e + 2\omega_0 \mu \alpha \sin(2\theta)s^f_{-\omega_0,x}}{2\mu(2V_e + \omega_0 \cos(2\theta))}. \tag{3.92}$$

3.7.3 Numerical calculations

Like in [174] we choose $\alpha = 4/3$, $V_e = 1000\,\omega_0$, and $\mu(r) = 10000\,\omega_0\,e^{-r\omega_0/10}$. We solve eqs. (3.80) and (3.81) and plot the resulting survival probabilities (denoted as "numerical" solution) in the top panel of figure 3.9. In addition, we show the probabilities predicted by the analytical estimate eqs. (3.86) and (3.90) (denoted as "approximative" solution). We also present the solutions obtained by solving eq. (3.91) algebraically (in figure 3.9 we refer to it as "adiabatic" solution). In the bottom panel of figure 3.9 we present the background potentials which include the flavor evolution obtained by solving eqs. (3.80) and (3.81), and eq. (3.91), respectively.

Note that while the adiabatic solution agrees well with the numerical one, the analytical estimate gives only a good approximation in the resonance regime. Indeed, if we show a more extended region, one can see how the analytical solution diverges (figure 3.10).

Furthermore, we can give an estimate of the transition length as in [174]. At resonance r_{res}, we have approximately $V_e(r_{\mathrm{res}}) + V_{\nu\nu}(r_{\mathrm{res}}) \approx 0$ and after flavor conversion ceased at r_{final} we have $V_e(r_{\mathrm{res}}) + V_{\nu\nu}(r_{\mathrm{res}}) \approx 0$. Written explicitly we have:

$$10^3 \omega_0 + 10^4 \omega_0 e^{-\omega_0 r_{\mathrm{res}}/10}(1 - \alpha) \approx 0, \tag{3.93}$$
$$10^3 \omega_0 - 10^4 \omega_0 e^{-\omega_0 r_{\mathrm{final}}/10}(1 + \alpha) \approx 0. \tag{3.94}$$

Solving these equations for r_{res} and r_{final} we find

$$r_{\mathrm{res}} = \frac{10}{\omega_0} \ln\left(\frac{\alpha - 1}{10}\right), \tag{3.95}$$

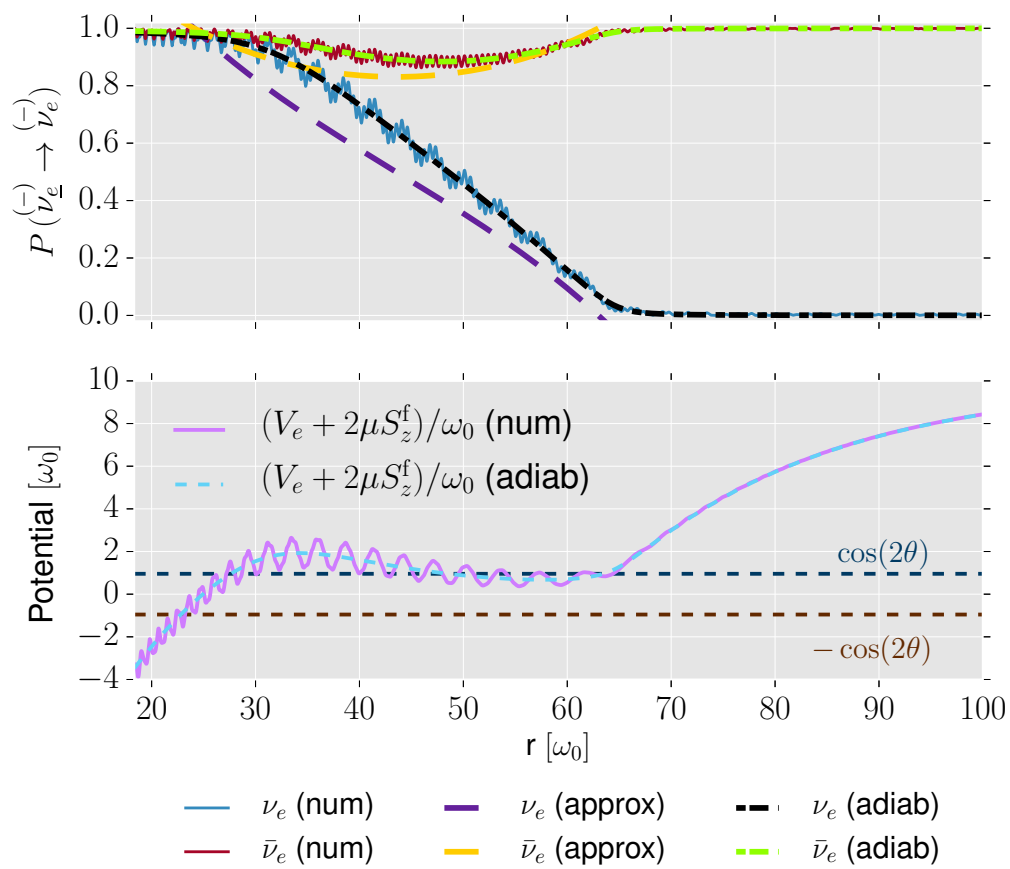$$r_{\mathrm{final}} = \frac{10}{\omega_0} \ln\left(\frac{1 + \alpha}{10}\right). \tag{3.96}$$
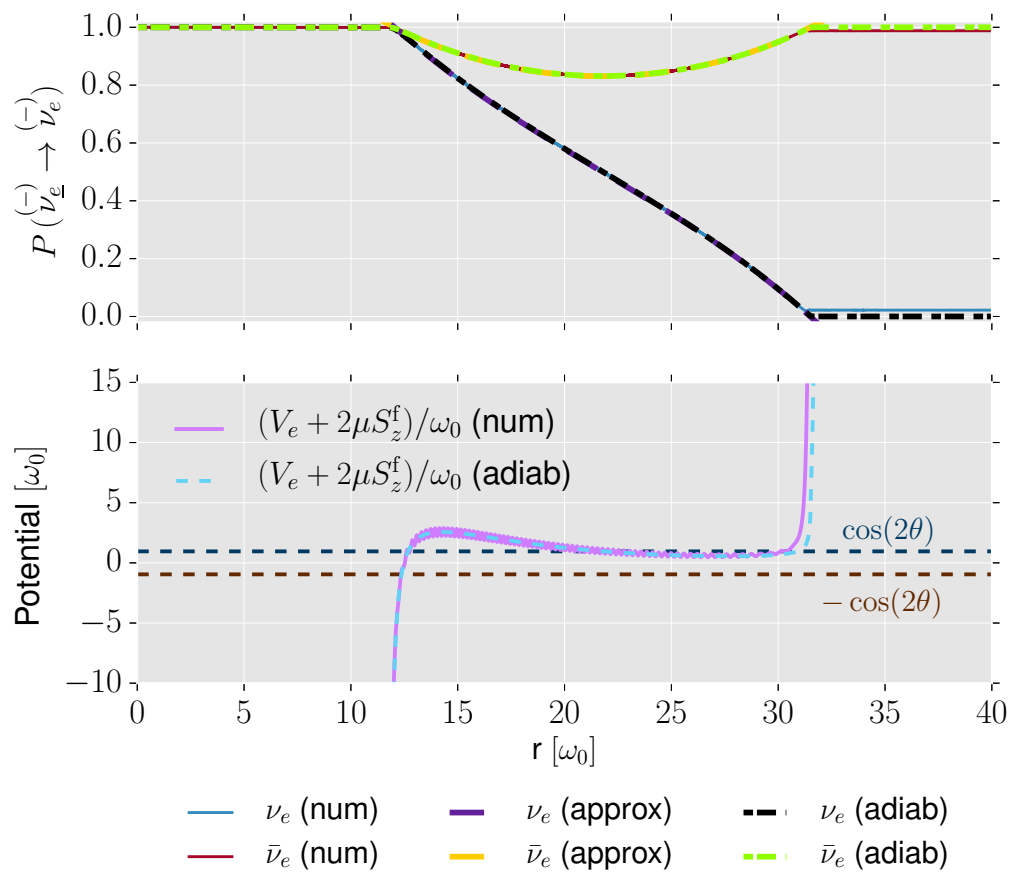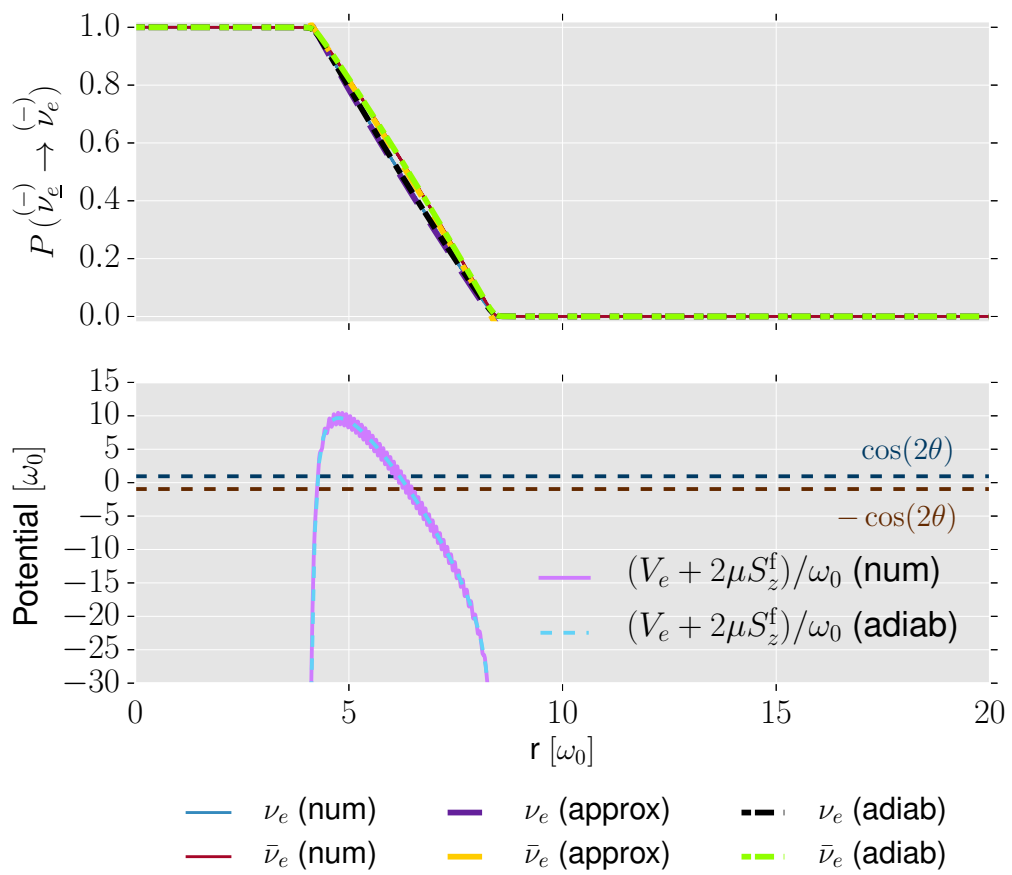
Figure 3.9.: Comparison of numerical solution, the approximation used in [174] and the adiabatic solution. We employed $\alpha = 4/3$, $V_e = 1000\,\omega_0$, and $\mu(r) = 10000\,\omega_0\,\mathrm{e}^{-r\omega_0/10}$.

As an estimate for the transition length we obtain

$$\delta r \approx r_{\text{final}} - r_{\text{res}} \approx \frac{10}{\omega_0} \ln\left(\frac{1+\alpha}{\alpha-1}\right) \approx 19.5\,\omega_0^{-1}. \tag{3.97}$$

We recognize that this agrees with what we observe in figure 3.9. Furthermore, in figure 3.11 we also present the resonance curve, i.e., $\sin^2(2\theta_{\text{eff}})$, where θ_{eff} denotes the effective in-medium mixing angle. It becomes evident that while the effective mixing angle becomes maximal for neutrinos, it is not the case for antineutrinos.
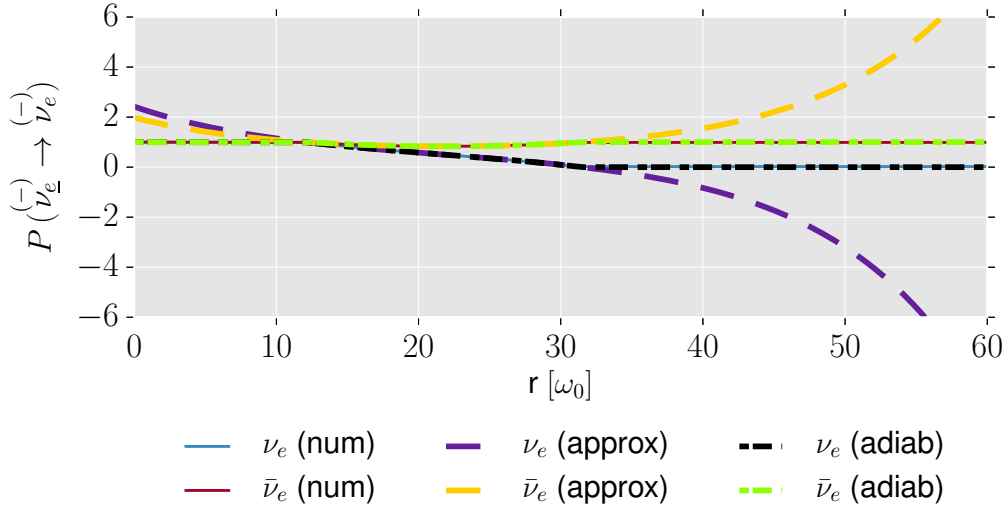
Figure 3.10.: Same as upper panel of figure 3.9, but for an extended region in order to make the deviations of the approximative solution transparent.

In figure 3.12 we present another calculation with $\alpha = 4/3$, $V_e = 10\,\omega_0$, and $\mu(r) = 100\,\omega_0\,e^{-r\omega_0/20}$ as in [177]. Here, again, it is apparent that the adiabatic solution gives a better approximation than the analytical estimate.

While the latter MNR are called standard MNR [174, 175]), there is also another kind of MNR, called symmetric MNR, characterized by a change of sign in the neutrino self-interaction potential when no flavor conversion is included. In order to account for such a sign change, we consider the profile as in [178]: $\alpha(r) = 1.3 - 0.048r$, $V_e = 1000\omega_0$, and $\mu = 10000\omega_0$ and perform the calculations in the normal mass hierarchy. As we can observe in figure 3.13, both neutrinos and antineutrinos undergo efficient flavor transformations. In figure 3.14, we also show the resonance curve. Inspecting figure 3.13 and 3.14 and comparing with figure 3.14, one again realizes that the analytical formula provides a good approximation only during the resonance.

As a final remark, we mention that some numerical schemes might require a high number of energy bins in order to achieve convergence. We shortly comment on this issue in appendix B.
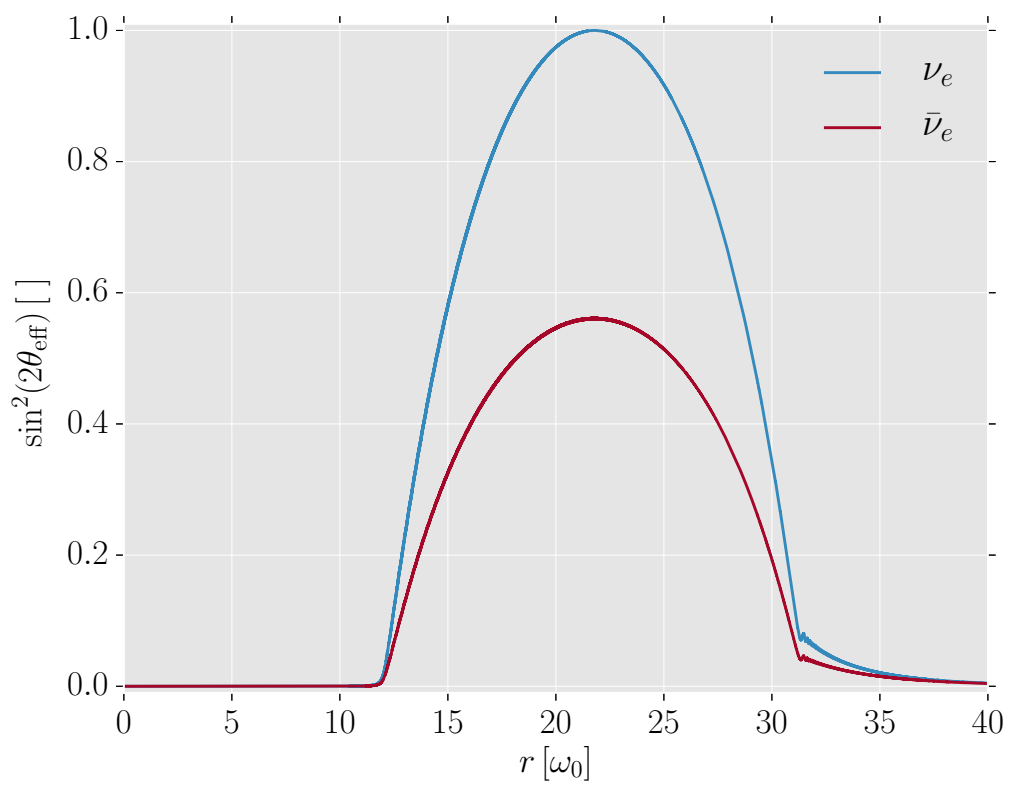
Figure 3.11.: Resonance curve for the profile studied in figure 3.13.

Figure 3.12.: Comparison of numerical solution, the approximation used in [174] and the adiabatic solution. We employed $\alpha = 4/3$, $V_e = 10\,\omega_0$, and $\mu(r) = 100\,\omega_0\,\mathrm{e}^{-r\omega_0/20}$.

Figure 3.13.: Comparison of numerical solution, the approximation used in [174] and the adiabatic solution. We used $\alpha(r) = 1.3 - 0.048r$, $V_e = 1000\omega_0$, and $\mu = 10000\omega_0$.
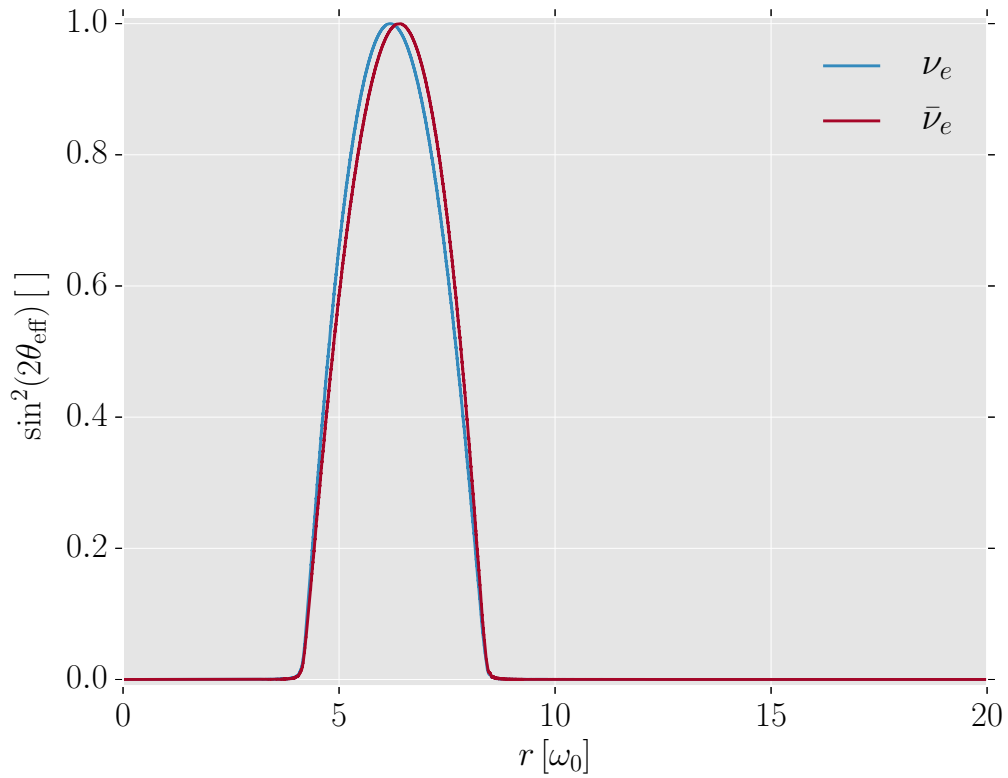
Figure 3.14.: Resonance curve for the profile studied in figure 3.13.
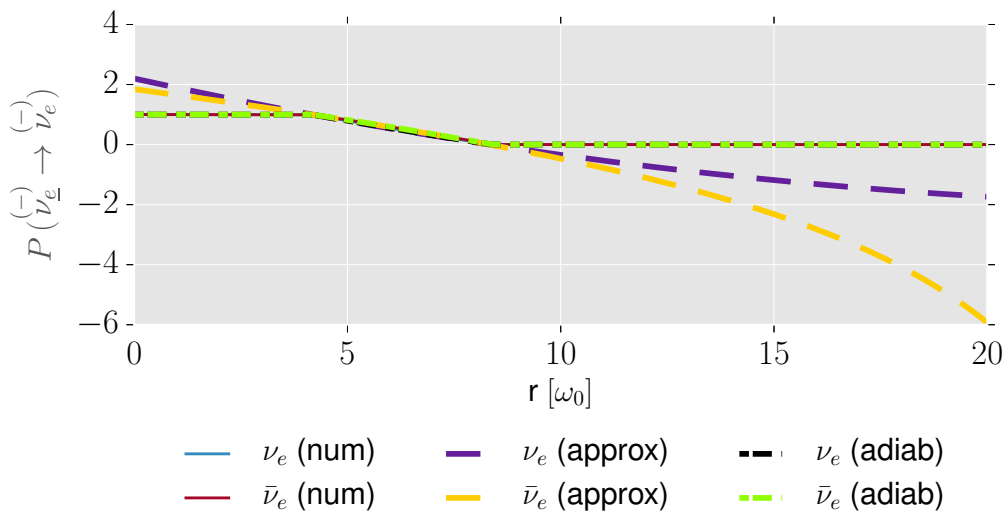
Figure 3.15.: Same as upper panel of figure 3.13, but for an extended region in order to make the deviations of the approximative solution transparent.

Neutrino Flavor Evolution in Binary Neutron Star Merger Remnants

«*There's nothing more romantic than a wedding on DS9 in springtime.*»

«*... when the neutrinos are in bloom.*»

STAR TREK: DEEP SPACE NINE
Episode: You are cordially invited (1997)

4.1 Introduction

The first gravitational wave signal detection from a binary black hole merger observed by the Virgo-LIGO Collaboration has opened the era of gravitational wave astronomy [179]. Since binary neutron star (BNS) mergers [15, 21] are one of the major sources of gravitational waves, a measurement of such a signal is anticipated. Moreover, BNS mergers are considered as the likely production site for *r*-process nucleosynthesis [17, 20] and as a potential source of short gamma-ray bursts [20, 180, 181].

Similar to core-collapse supernovae, the dynamics of such astrophysical environments is expected to be affected by neutrinos. A significant amount of energy is carried by them and their interaction with matter affects the neutron-to-proton ratio (or equivalently, the electron fraction Y_e), which is a crucial element for nucleosynthesis. Since the main processes of transporting energy and altering the composition are neutrino flavor dependent, any mechanism that changes the flavor content of neutrinos should be studied in order to fully access their role in these environments.

Since the first proposals of neutrino oscillations by the pioneering works of Pontecorvo [5, 6, 182], it took almost half a century before neutrino flavor changes were finally discovered by the Super-Kamiokande Collaboration [183] and the Sudbury Neutrino Observatory [184]. It was early recognized that if neutrinos are on their way through a dense background medium, they acquire a refractive index due to coherent forward scattering with the background particles [185]. This can possibly lead to flavor conversions, as in the Sun, where the Mikheyev-Smirnov-Wolfenstein (MSW) effect [71, 185] takes place (see discussion in section 2.6). Furthermore, neutrinos themselves can constitute a significant background. This occurs in the early universe and in astrophysical environments, such as core-collapse supernovae, BNS mergers, and collapsars, where large neutrino fluxes are present so that their number densities are comparable to or larger than that of matter. In these environments, the neutrino coherent

forward scattering off neutrinos produces flavor-diagonal [63, 186] as well as off-diagonal contributions to the neutrino refractive index matrix, as realized by Pantaleone [90, 187]. The neutrino self-interaction contribution couples their flavor evolution non-linearly and causes collective oscillations where different types of collective phenomena (synchronized and bipolar oscillations, spectral splits/swaps) can arise (see [118, 127, 128] and references therein) as discussed in chapter 3.

In environments with a disk geometry (e.g., in collapsars or BNS mergers) another effect associated with neutrino self-interactions was revealed through numerical calculations [173–175]: If the matter and neutrino self-interaction potentials almost cancel each other, matter-neutrino resonances (MNR) can occur and cause flavor conversion in regions above the emitting disk. Different from the case of a deleptonizing proto-neutron star, the material in a binary neutron star merger starts with a huge neutron excess. The prevailing temperatures of the remnant (several mega-electron volts [15]) allow positron captures on neutrons ($n + e^+ \rightarrow p + \bar{\nu}_e$) to increase the electron fraction and to release more electron antineutrinos than electron neutrinos. Initially, this larger number flux of electron antineutrinos causes a different sign in the neutrino self-interaction potential compared to the neutrino-matter potential. Depending on the matter profile, this can allow an almost cancellation of the two potentials at some point. As neutrinos leave the emission surface, the role of geometry becomes more important [175]: Since the electron antineutrinos decouple deeper inside the remnant than electron neutrinos, the latter have a larger emission surface. In the neutrino self-interaction potential this difference in geometry can induce a flip of sign at some point and can allow for symmetric MNR [175], as first found in the context of collapsar-type disks [173]. In [174] another type of MNR, later called standard MNR [175], where the neutrino self-interaction potential does not change its sign, was found. In [175], both the standard and the symmetric MNR were investigated within models with equal and different disk sizes for each neutrino species. In addition, for the symmetric MNR, the possible impact on disk wind nucleosynthesis was investigated and it was found that it could potentially favor the formation of r-process elements [173, 175].

The investigation of this phenomenon in schematic models (like those presented in section 3.6) shows that the underlying mechanism can be understood in terms of adiabatic solutions similar to the MSW flavor transformation [177, 178]. It should be mentioned that the MNR shares common features with the non-linear feedback in conjunction with helicity transformations [188]. Furthermore, we note that the occurrence of the MNR is not restricted to disk scenarios. Since different signs in the matter and neutrino potentials are necessary, this effect could potentially occur in other environments, too, for example, in core-collapse supernovae by incorporating active-sterile neutrino mixing [189] or non-standard neutrino interactions [190].

However, in a system with a disk-like geometry, the problem is intrinsically different from a spherically symmetric one as the disk itself defines a particular direction with the disk center. In this case, one naturally expects that the flavor evolution history of neutrinos emitted from different parts of the disk with different emission angles should be different. In the first flavor

evolution works with a disk geometry [173–175] neutrinos were followed on 45°-trajectories from accretion disks around black holes. The disk model parameters were chosen to be consistent with studies of the collapse of rotating massive stars [173] or the mergers of a black hole and a neutron star [174, 175].

In this chapter, we study the trajectory dependence of the neutrino flavor evolution in the neutrino-driven wind from a binary neutron star merger remnant before black hole formation. To explore the dependence of flavor evolution on the neutrino emission location and angles, we use a "single-trajectory" approximation which assumes that at every point of a given neutrino trajectory, the flavor states of all neutrinos with the same energy identically contribute to the self-interaction. To this aim we use results from the detailed simulations of [25], in particular, matter profiles (density, electron fraction and temperature), neutrino luminosities, and mean neutrino energies. We present numerical results on the flux-averaged neutrino and antineutrino probabilities for several trajectories where neutrino self-interaction and matter potentials differ. We then discuss the potential impact on nucleosynthesis by showing the change in the (anti)neutrino capture rates on free nucleons, relevant for r-process nucleosynthesis, due to flavor evolution along these trajectories. We also investigate the sensitivity of the flavor evolution to different emission characteristics within the same model, or considering uncertainties from available simulations.

In section 4.2, we explain the procedure to determine the neutrino emission surfaces. In section 3.4, we discuss the equations of motion governing the neutrino flavor evolution and the method we adopted in this work to investigate the trajectory dependence. In section 4.5, we describe the unoscillated potentials along chosen trajectories. In section 4.6, we present our numerical results of the trajectory dependence and the impact on the capture rates. We comment on the dependence of the results on the initial emission parameters. We discuss the implications and present a concise comparison of two- vs three flavor results in section 4.7, followed by a first investigation of CP violation in section 4.8.

4.2 Disk structure and neutrino surfaces in BNS merger remnants

4.2.1 BNS merger remnant

Our discussion is based on a long-term three-dimensional Newtonian hydrodynamics simulation of the neutrino-driven wind that emerges from the remnant of the merger of two non-spinning $1.4\,\mathcal{M}_\odot$ neutron stars [25]. As a result of the merging process, a massive neutron star (MNS) forms in the central region, surrounded by an accretion disk. The MNS has a rest mass possibly larger than the maximally allowed rest mass of a non-rotating neutron star [14]. In the case of a gravitational unstable object, its temporary stability against gravitational collapse is expected to be provided primarily by differential rotation [191], but also other mechanisms, such as thermal pressure, could give additional support [191, 192]. For this
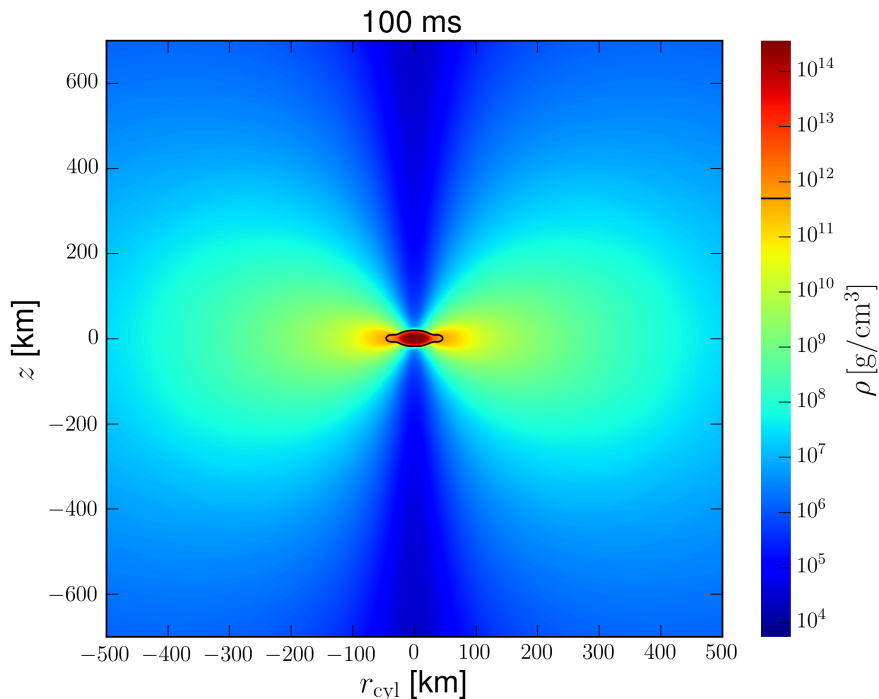
Figure 4.1.: Density profile as a function of cylindrical coordinates z and r_{cyl} at $t = 100\,\mathrm{ms}$ after the merger. The contour $\rho \approx 5 \times 10^{11}\,\mathrm{g/cm^3}$ delimits the innermost part of the disk that is comparable to the surface density of a proto-neutron star [25].

reason, the MNS is assumed to stay stable during the simulation time, $\sim \mathcal{O}(100)$ ms after the merger, and is treated as a stationary rotating object.

Typical timescales of the disk are given by the dynamical timescale $t_{\mathrm{dyn}}^{\mathrm{disk}} \sim \mathcal{O}(10)$ ms and the much longer viscous timescale $t_{\mathrm{visc}}^{\mathrm{disk}} \sim \mathcal{O}(300)$ ms which gives an estimate of the lifetime of the disk [25]. The latter is characterized by a typical radius $R_{\mathrm{disk}} \sim \mathcal{O}(100)$ km and innermost density $\rho_{\mathrm{disk}} \sim 5 \times 10^{11}\mathrm{g\,cm^{-3}}$, while the central density of the MNS is a few $10^{14}\,\mathrm{g\,cm^{-3}}$ as can be inferred from figure 4.1, where we plot the density at $100\,\mathrm{ms}$ after the merger. Because of the high densities of the remnant, neutrinos act as the major cooling source and other particles are essentially trapped on the relevant timescales.

We consider the emission and the absorption of neutrinos from the MNS and the surrounding disk [193]. Similar to the case of a proto-neutron star, those neutrinos can cause a mass outflow, called neutrino-driven wind, by energy deposition via absorption and scattering processes [194, 195]. This wind, together with viscously-driven ejecta, is blown away mainly from the disk [25, 196–199]. Since the rotational period of the accretion disk and of the MNS is much smaller than the neutrino diffusion timescale and the disk lifetime, after a few orbits the remnant approaches a quasi-axisymmetric configuration. Thus, we assume rotational symmetry around the MNS rotational axis and use the axisymmetric averages of hydrodynamical quantities (matter density, temperature and electron fraction) from the simulation [25] for our calculations below. These quantities are shown in figures 4.1 and 4.2.
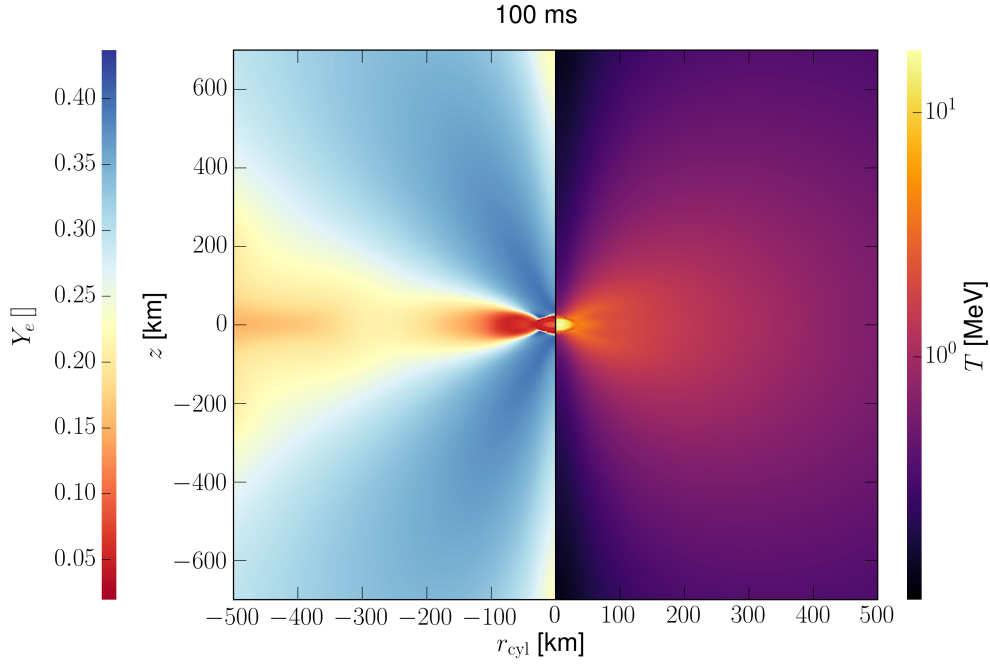
100 ms

Figure 4.2.: Electron fraction (left panel) and matter temperature (right panel) as functions of cylindrical coordinates z and r_{cyl} at $t = 100\,\text{ms}$ after the merger.

	Reaction	Inverse mean free path
(i)	$\nu + N \rightarrow \nu + N$	$\lambda^{-1}_{\nu N,\text{sc}}$
(ii)	$\nu_e + n \rightarrow e^- + p$	$\lambda^{-1}_{\nu_e,\text{ab}}$
(iii)	$\bar{\nu}_e + p \rightarrow e^+ + n$	$\lambda^{-1}_{\bar{\nu}_e,\text{ab}}$

Table 4.1.: Neutrino reactions considered in our model, where $N \in \{n, p\}$. For reaction (i), ν refers to all neutrino species. In the second column we denote the associated mean free paths, where (sc) refers to scattering while (ab) refers to absorption. The corresponding cross sections are taken from [200].

Local deviations of the three-dimensional quantities with respect to the cylindrically averaged values are usually $\lesssim 15\%$ inside the densest part of the remnant.

4.2.2 Neutrino surfaces

In this section, we construct a neutrino emission disk from the simulation result described in section 4.2.1. We first determine the neutrino emission surface by calculating the neutrino opacity in the remnant. The reactions giving the most relevant contributions to the optical depth are listed in table 4.1. For their corresponding cross sections σ we use the expressions described in [200] without weak magnetism corrections (see appendix C).

One main contribution to the opacity for all neutrino species is due to elastic neutrino scattering off free nucleons ($N = n, p$). Because of the presence of neutron-rich matter, the

absorption of ν_es by free neutrons becomes the dominant (though comparable to neutrino-nucleon scattering) opacity source, while absorption of $\bar{\nu}_e$s by free protons is less effective. The ν_xs (short for ν_μ, $\bar{\nu}_\mu$, ν_τ, $\bar{\nu}_\tau$) only scatter off nucleons. As a consequence, matter is most opaque for ν_es and most transparent for ν_xs.

The region where those reactions freeze out and (anti)neutrinos start to stream off freely is called the neutrino surface. Since neutrino opacities have a significant dependence on the neutrino energy, this surface is energy dependent and is usually defined in terms of the neutrino optical depth τ_ν,

$$S_\nu : \left\{ (r_{\text{cyl}}, z) \mid \tau_\nu(E, r_{\text{cyl}}, z) = 2/3 \right\}. \tag{4.1}$$

The spectral optical depth is computed via the line integral

$$\tau_\nu^{\text{d}}(E, r_{\text{cyl}}, z) = \int_{\mathcal{C}_{\text{d}}} \mathrm{d}s \, \lambda_\nu^{-1}(E, r'_{\text{cyl}}, z'), \tag{4.2}$$

where $\mathcal{C}_{\text{d}}$ corresponds to the path of integration,

$$\lambda_\nu^{-1}(E) = \sum_i \lambda_i^{-1} = \sum_i n_i \, \sigma_i(E) \tag{4.3}$$

denotes the inverse mean-free-path and n_i the target number density[1] corresponding to the reaction with cross section σ_i. The index i runs over all reactions in table 4.1 relevant for the neutrino species under consideration.

For the optical depth τ_ν^{d} calculation, we employ a local ray-by-ray approach: At each point (r_{cyl}, z) on the cylindrical domain, we follow a straight line path in one of the seven directions ($d = 1, \ldots, 7$) described in [25] until the edge of the computational domain is reached. Finally, we take the minimum values[2] among all τ_ν^{d} to specify the actual optical depth at one point [201],

$$\tau_\nu(E, r_{\text{cyl}}, z) = \min_{1 \le \text{d} \le 7} \left\{ \tau_\nu^{\text{d}}(E, r_{\text{cyl}}, z) \right\}. \tag{4.4}$$

In principle, we need to distinguish between transport and energy surfaces [53, 202]. From the transport surface, neutrinos can stream off freely while at the energy surface (located deeper inside), neutrinos last exchanged energy with the medium and thermally decouple. Here, it turns out that the actual difference between those is only minor for ν_es, since the opacity is determined by the charged and neutral current processes (i) - (iii) in table 4.1. For $\bar{\nu}_e$s the difference is larger, since we neglected annihilation $\nu_x \bar{\nu}_x \rightarrow e^+ e^-$ and scattering on charged leptons $\nu_x + e^\pm \rightarrow e^\pm + \nu_x$. In addition to these processes, inverse bremsstrahlung

---

[1] Note that $n_p = \rho_{\text{matt}} Y_e / m_{\text{u}}$ for protons and $n_n = \rho_{\text{matt}}(Y_e - 1)/m_{\text{u}}$ for neutrons, where m_{u} denotes the unified atomic mass unit.

[2] We take the minimum, because from the macroscopical (i.e., statistical) point of view, radiation prefers to tend to regions of larger mean free paths (or smaller optical depths) so that it is less likely that the radiated particle interacts with matter [201].
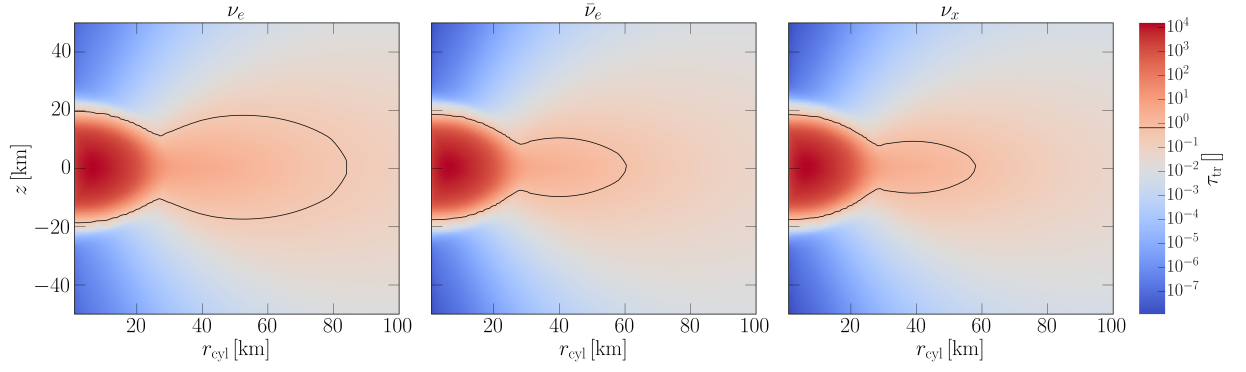
Figure 4.3.: Transport optical depths τ (color coded) as functions of cylindrical coordinates z and r_{cyl} at $t = 100\,\text{ms}$ after the merger. The contours (where $\tau \approx 2/3$) correspond to the neutrino transport surfaces associated with ν_e (left), $\bar{\nu}_e$ (middle), and ν_x (right).

on nucleons $\nu_x + \nu_x + N + N \to N + N$ becomes also relevant for the opacity of ν_xs, which do not possess charged current contributions. These processes make sure that the difference between transport and energy surfaces is large in case of ν_x and they diffuse through a scattering atmosphere that develops between energy and transport surface [202].

But since we are interested in obtaining an estimate of the size of the surface where neutrinos last scatter, we focus on the transport surfaces and perform spectral averages using a (normalized) distribution function of Fermi-Dirac shape with vanishing degeneracy parameter

$$f_\nu(E, T) = \frac{1}{F_2(0)} \frac{1}{T^3} \frac{E^2}{\exp(E/T) + 1}, \tag{4.5}$$

which is completely determined by the local matter temperature $T = T(r_{\text{cyl}}, z)$. In this expression, we have $F_2(0) = \frac{3}{2}\zeta(3) \approx 1.80$, and $F_k(0)$ corresponds to the Fermi-Dirac integral of order k with zero degeneracy parameter,

$$F_k(0) \equiv \int_0^\infty \mathrm{d}x \frac{x^k}{\exp(x) + 1}. \tag{4.6}$$

The results are shown in figure 4.3 and the opacities reflect the density structure of the remnant.

The mean energies are taken from the simulations performed in [25] and are essentially determined at the energy surface. There, we assume thermal equilibrium such that the neutrino temperature can be obtained from the mean energies via the Fermi relation $\langle E_\nu \rangle = (F_3(0)/F_2(0)) T_\nu \approx 3.15 \, T_\nu$, where $F_3(0) = \frac{7\pi^4}{120}$.

t [ms]	R_{ν_e} [km]	$R_{\bar{\nu}_e}$ [km]	R_{ν_x} [km]
60	90	64	61
100	84	60	58

Table 4.2.: Outermost radii of the neutrino surfaces (at 60 ms and 100 ms) (see text).

Neutrino species	$\langle E_\nu \rangle$ [MeV]	$(L_\nu/10^{51})$ [erg/s]
ν_e	10.6	15
$\bar{\nu}_e$	15.3	30
ν_x	17.3	8

Table 4.3.: Emission parameters with $\nu_x \in \{\nu_\mu, \nu_\tau, \bar{\nu}_\mu, \bar{\nu}_\tau\}$.

In the following we construct an infinitely thin disk; i.e., we turn the neutrino surface into a flat disk, assume a constant temperature, and define the neutrino disk radius R_ν as the outermost radius of the neutrino surface,

$$R_\nu \equiv \max_{(r_{\mathrm{cyl}}, z) \in S_\nu} \left\{ \sqrt{r_{\mathrm{cyl}}^2 + z^2} \right\}. \tag{4.7}$$

As can be seen from the results shown in table 4.2, the differences in the neutrino surface radii for the two time snapshots of 60 ms and 100 ms that we have used in our calculations are only minor. The neutrino mean energies and luminosities are approximately stationary during the time of simulation [25]. The values used in our calculations are listed in table 4.3.

4.3 Neutrino self-interaction Hamiltonian in disk geometry

We employ the formalism introduced in [173, 203] and explicitly construct the self-interaction Hamiltonian for neutrinos emitted from a disk. The coordinate system is defined in such a way that the following relations for the basis vectors hold: $\hat{\mathbf{e}}_x = \hat{\mathbf{e}}_{r_{\mathrm{cyl}}}$ and $\hat{\mathbf{e}}_y = \hat{\mathbf{e}}_\phi$. This allows us to identify the x coordinate with the cylindrical radius r_{cyl} (figure 4.4).

At any point $\mathbf{Q}(x, 0, z)$ on the x-z plane, for a neutrino which is emitted from a point $\mathbf{Q}_0$ on the disk and passes through $\mathbf{Q}$, its momentum direction $\hat{\mathbf{p}}$ can be specified by a polar angle θ and an azimuthal angle ϕ in the spherical coordinate system (see figure 4.4),

$$\hat{\mathbf{p}} = (\sin\theta \cos\phi, \sin\theta \sin\phi, \cos\theta), \tag{4.8}$$

or by the polar coordinates r_{d} and φ of the emission point $\mathbf{Q}_0(r_{\mathrm{d}}, \varphi)$ on the disk,

$$\hat{\mathbf{p}} = \frac{\mathbf{Q} - \mathbf{Q}_0}{\Delta^{1/2}}, \tag{4.9}$$
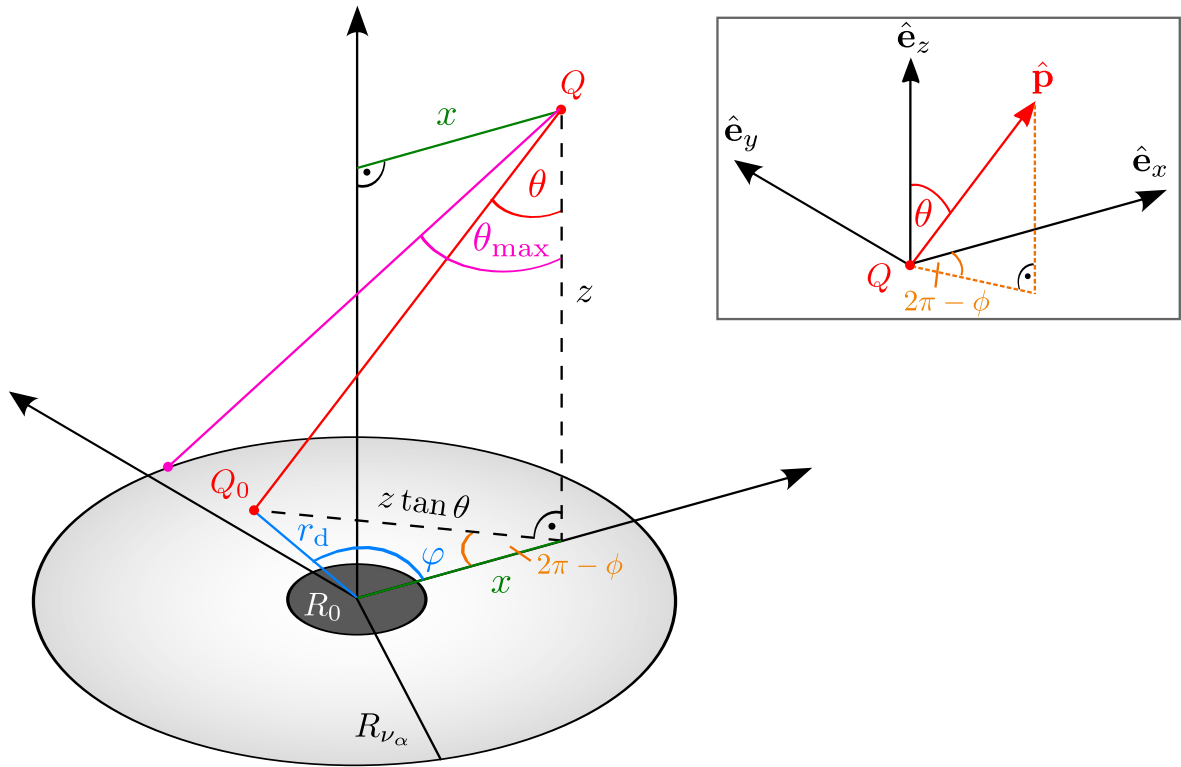
Figure 4.4.: Accretion disk with a central object (black hole or neutron star) located at the origin. In the case of a black hole, the radius R_0 denotes the last stable orbit and defines the inner radius of the disk while for a neutron star, we set $R_0 = 0$. The (outer) flavor dependent radii of the disk are R_{ν_α} for neutrinos and $R_{\bar{\nu}_\alpha}$ for antineutrinos, respectively. The values used in our emission model are based on detailed simulations of a neutron star merger remnant [25] and are given in table 4.2. The polar angle θ and the azimuthal angle ϕ describe the direction of the neutrino momentum $\mathbf{p}$. Neutrinos are emitted from a point Q_0 located in the disk plane at a distance r_d from the origin with a relative angle φ with respect to the positive x axis and propagate to a point Q located at a distance x from the z axis and a vertical distance z from the equatorial plane.

where

$$\Delta \equiv |\mathbf{Q} - \mathbf{Q}_0|^2 = x^2 + r_{\mathrm{d}}^2 - 2xr_{\mathrm{d}}\cos\varphi + z^2. \tag{4.10}$$

A comparison of eq. (4.8) and eq. (4.9) yields the following coordinate transformations:

$$
\begin{aligned}
\cos\theta &= \frac{z}{\Delta^{1/2}}, \qquad \sin\theta = \frac{(\Delta - z^2)^{1/2}}{\Delta^{1/2}}, \\
\cos\phi &= \frac{x - r_{\mathrm{d}}\cos\varphi}{\Delta^{1/2}\sin\theta}, \qquad \sin\phi = -\frac{r_{\mathrm{d}}\sin\varphi}{\Delta^{1/2}\sin\theta}
\end{aligned}
\tag{4.11}
$$

with $\varphi \in [0, 2\pi]$ and $r_{\mathrm{d}} \in [R_0, R_\nu]$. We note that the determinant of the Jacobian $\mathsf{J} \equiv \partial(\cos\theta, \phi)/\partial(r_{\mathrm{d}}, \varphi)$ turns out to be

$$\det \mathsf{J} = \frac{\partial(\cos\theta)}{\partial r_{\mathrm{d}}}\frac{\partial\phi}{\partial\varphi} - \frac{\partial(\cos\theta)}{\partial\varphi}\frac{\partial\phi}{\partial r_{\mathrm{d}}} \tag{4.12}$$

$$= -\frac{zr_{\mathrm{d}}}{\Delta^{3/2}}, \tag{4.13}$$

such that $\mathrm{d}(\cos\theta)\mathrm{d}\phi = |\det\mathsf{J}|\,\mathrm{d}r_{\mathrm{d}}\mathrm{d}\varphi$ holds.

Now, we consider another neutrino with momentum direction

$$\hat{\mathbf{p}}' = (\sin\theta'\cos\phi', \sin\theta'\sin\phi', \cos\theta'). \tag{4.14}$$

The cosine of the scattering angle, $\cos\Theta_{\mathbf{pp}'} \equiv \hat{\mathbf{p}} \cdot \hat{\mathbf{p}}'$, between the two neutrinos is then given by:

$$\cos\Theta_{\mathbf{pp}'} = \cos\theta\cos\theta' + \sin\theta\sin\theta'\left(\cos\phi\cos\phi' + \sin\phi\sin\phi'\right). \tag{4.15}$$

If we make use of the above transformations we find

$$
\begin{aligned}
\cos\Theta_{\mathbf{pp}'} =\ & \frac{z\cos\theta'}{\Delta^{1/2}} + \frac{x\sin\theta'\cos\phi'}{\Delta^{1/2}} \\
& - \frac{r_{\mathrm{d}}\sin\theta'\cos\phi'\cos\varphi}{\Delta^{1/2}} - \frac{r_{\mathrm{d}}\sin\theta'\sin\phi'\sin\varphi}{\Delta^{1/2}}.
\end{aligned}
\tag{4.16}
$$

For neutrinos emitted isotropically from any point on the disk, the differential neutrino number density in eq. (3.34) is given by:

$$\mathrm{d}n_{\nu_\alpha} \equiv \mathrm{d}n_{\nu_\alpha}(\mathbf{p}) = j_{\nu_\alpha}(E)\mathrm{d}E\mathrm{d}\Omega_{\nu_\alpha}, \tag{4.17}$$

where $E = |\mathbf{p}| \equiv p$, $\mathrm{d}\Omega_{\nu_\alpha} \equiv \mathrm{d}\phi\mathrm{d}(\cos\theta)$ and j_{ν_α} denotes the neutrino number flux per unit energy per solid angle for which we assume a Fermi-Dirac shape (see appendix D):

$$j_{\nu_\alpha}(E) = \frac{F_{\nu_\alpha}}{2\pi}f_{\nu_\alpha}(E). \tag{4.18}$$

Here, $F_{\nu_\alpha} = L_{\nu_\alpha}/(\pi R_{\nu_\alpha}^2 \langle E_{\nu_\alpha} \rangle)$ corresponds to the neutrino number flux at the neutrino emitting surface and f_{ν_α} denotes the normalized Fermi-Dirac energy distribution function corresponding to the right hand side of eq. (4.5) with $T = T_{\nu_\alpha}$.

Inserting eqs. (4.17) and (4.18) into eq. (3.34), we rewrite the self-interaction Hamiltonian as

$$
\mathsf{H}_{\nu\nu}(\mathbf{p}', \mathbf{Q}_0, r) = \frac{\sqrt{2}G_\mathrm{F}}{2\pi} \sum_{\alpha = e, \mu, \tau} \int_0^\infty \mathrm{d}E \left(\int_{\Omega_{\nu_\alpha}} \mathrm{d}\Omega \, (1 - \cos\Theta_{\mathbf{pp}'}) \, F_{\nu_\alpha} \rho_{\nu_{\underline{\alpha}}}(\Omega, \mathbf{Q}_0, E, r) f_{\nu_\alpha}(E) \right.
$$
$$
\left. - \int_{\Omega_{\bar{\nu}_\alpha}} \mathrm{d}\Omega \, (1 - \cos\Theta_{\mathbf{pp}'}) \, F_{\bar{\nu}_\alpha} \bar{\rho}_{\bar{\nu}_{\underline{\alpha}}}(\Omega, \mathbf{Q}_0, E, r) f_{\bar{\nu}_\alpha}(E) \right),
$$
(4.19)

where the angular integration is performed with the corresponding limits $\Omega_{\nu_\alpha(\bar{\nu}_\alpha)}$ for neutrinos and antineutrinos, respectively.

4.4 Single-trajectory versus single- and multi-angle approximations

In order to follow the evolution, one should solve eqs. (3.35) and (3.36) for all neutrinos with different $\mathbf{p}$ and $\mathbf{Q}_0$ simultaneously since $\mathsf{H}_{\nu\nu}$ couples them. This is computationally extremely demanding as we will discuss shortly. Instead of solving the full problem we employ a "single-trajectory" approximation which consists in making the assumption that in eq. (4.19) the density matrix is given by

$$
\rho_{\nu_{\underline{\alpha}}}(\Omega, \mathbf{Q}_0, E, r) = \rho_{\nu_{\underline{\alpha}}}(\mathbf{p}', \mathbf{Q}_0, E, r),
$$
(4.20)

that is, it does not dependent on the angular variables. In other words, we suppose that at every point of a given neutrino trajectory with momentum $\mathbf{p}'$, all neutrino states contributing to $\mathsf{H}_{\nu\nu}(\mathbf{p}', \mathbf{Q}_0, r)$ have the same flavor evolution as the one with $\mathbf{p}'$. The approximation given by eq. (4.20) was already used in [173–175]. We emphasize that this approach reduces to the "single-angle approximation" used in the supernova context for a spherically symmetric system, such as the supernova bulb model [112]. Note that the "multi-angle approximation" in the supernova bulb model corresponds to retaining also the θ emission angle dependence in the self-interaction Hamiltonian.

At present, no simulations of neutrino flavor evolution in binary neutron star mergers exist where eqs. (3.35) and (3.36) are solved without making the assumption eq. (4.20). This is due to the fact that it may require computational capabilities beyond the current available resources. In fact, a multi-angle calculation in the supernova neutrino bulb model, which only evolves the flavor content in the radial coordinate with one explicit emission angle variable, requires $\sim \mathcal{O}(10^3)$ CPU hours [112]. Numerical convergence requires a large number of angle bins, typically of the order of $10^3 - 10^4$ [112, 204]. In the disk case, performing a full calculation that preserves the initial symmetry of the system is much more complex than in the supernova bulb model and requires evolving the flavor content in both x and z
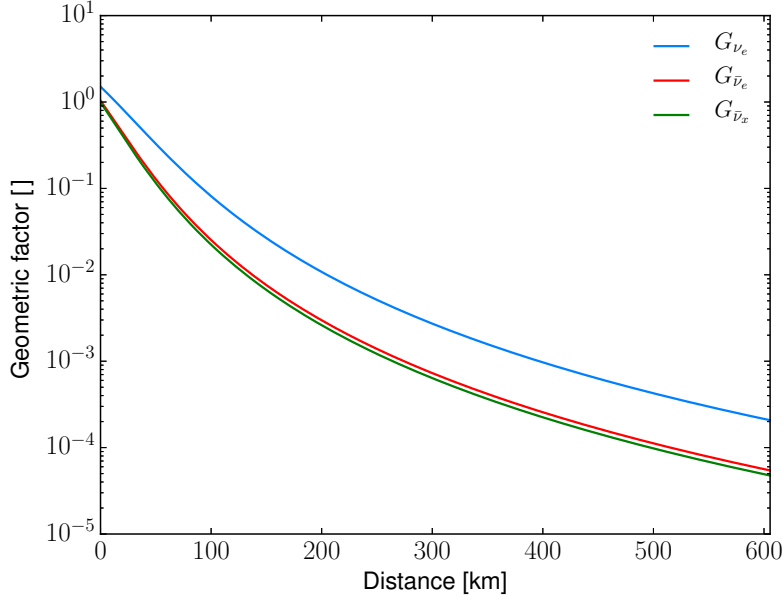
Figure 4.5.: Geometric factors as a function of the distance from the emission point $x_0 = 10\,\mathrm{km}$, $z_0 = 30\,\mathrm{km}$. The emission angles correspond to $\theta = 20°$ and $\phi = 0°$ while the disk radii are taken from table 4.2.

coordinates with three explicit variables: r_d, θ, ϕ specifying the emission location and angles, respectively. As for the possible effect of going from the "single-trajectory" approximation to the full flavor calculation, one can speculate that this will introduce decoherence in the flavor evolution as in the supernova context multi-angle simulations have shown that occurs [84, 114]. Therefore the results presented here can be considered as an upper limit for the effects of flavor evolution on the capture rates since we expect that decoherence is likely to reduce them.

Now, under the single-trajectory approximation, eqs. (3.35) and (3.36) can be solved for each density matrix $\rho_{\nu_{\underline{\alpha}}} = \rho_{\nu_{\underline{\alpha}}}(\theta_0, \phi_0, \mathbf{Q}_0, E, r)$, and the angular integration yields a geometric factor

$$G_{\nu_\alpha}(\theta_0, \phi_0, \mathbf{Q}_0, r) = \int_{\Omega_{\nu_\alpha}} \mathrm{d}\Omega\,(1 - \cos\Theta_{\mathbf{pp'}}), \tag{4.21}$$

whose explicit form is described in appendix E. Here, we fixed the emission angles θ_0 and ϕ_0 describing the direction of momentum $\mathbf{p'}$. In figure 4.5 we show typical sizes for those factors. The ratio $G_{\nu_e}/G_{\bar{\nu}_e}$ increases as a function of distance.

In the following the explicit reference to the angular labels and the emission point will be omitted and the density matrices will be denoted just by $\rho_{\nu_{\underline{\alpha}}}(E, r)$ for notational convenience. Finally, the Hamiltonian eq. (4.19) can be expressed in the compact form,

$$
\begin{aligned}
\mathsf{H}_{\nu\nu}(\theta_0, \phi_0, \mathbf{Q}_0, r) = \sqrt{2}G_\mathrm{F} \sum_{\alpha=e,\mu,\tau} \int_0^\infty \mathrm{d}E\, \Big(& \rho_{\nu_{\underline{\alpha}}}(E, r) j_{\nu_{\underline{\alpha}}}(E) G_{\nu_\alpha}(\theta_0, \phi_0, \mathbf{Q}_0, r) \\
& - \bar\rho_{\bar\nu_{\underline{\alpha}}}(E, r) j_{\bar\nu_{\underline{\alpha}}}(E) G_{\bar\nu_\alpha}(\theta_0, \phi_0, \mathbf{Q}_0, r) \Big).
\end{aligned}
\tag{4.22}
$$

4.5 Trajectory dependence of the unoscillated potentials

Flavor transformation through matter-neutrino resonances is an MSW-like phenomenon. Its occurrence is due to the almost cancellation of the matter and the neutrino self-interaction potentials, that have opposite signs. This condition is met in our model, since the self-interaction potential starts negative due to the dominating electron antineutrino fluxes (table 4.3). However, for significant flavor conversions to occur, this near cancellation is not sufficient. Similar to the MSW case, it is the adiabaticity of the evolution that determines the flavor conversion efficiency [174, 177, 178] and depends, beside the mixing parameters and the neutrino energy, on the matter profiles and their gradients.

We choose different neutrino emission points (x_0, z_0) on the neutrino surfaces and compute their flavor evolution along trajectories that pass through two different reference points $(x_{\mathrm{ref}}, z_{\mathrm{ref}})$ as given in tables 4.4 and 4.5.

Trajectory	x_0 [km]	z_0 [km]	θ_0 [°]	Distance [km]
1a	10	30	45.0	400
1b	−10	30	47.0	415
1c	−35	25	48.7	436
1d	50	30	40.7	373

Table 4.4.: Parameters that specify the neutrino trajectories: emission coordinates at the neutrino surface (x_0, z_0) and emission angle θ_0. The last column shows the distance between the emission point and the reference point $x_{\mathrm{ref}} = 293\,\mathrm{km}$, $z_{\mathrm{ref}} = 313\,\mathrm{km}$.

Trajectory	x_0 [km]	z_0 [km]	θ_0 [°]	Distance [km]
2a	10	30	20.0	187
2b	−10	30	25.5	195
2c	−35	25	31.1	211
2d	50	30	7.8	178

Table 4.5.: Same as table 4.4 for the reference point $x_{\mathrm{ref}} = 74\,\mathrm{km}$, $z_{\mathrm{ref}} = 206\,\mathrm{km}$.

To simplify the discussion, we implicitly assume that $\phi_0 = 0°$; i.e., we do not explore the trajectory dependence on ϕ_0. The two reference points are chosen to have a temperature $T = 8$ GK in different regions of the wind that give rise to different nucleosynthesis outcomes [205]. Point 1 (2) lies on $\approx 43°$ (20°) from the z axis and is ≈ 429 (219) km away from the center of the MNS. Figure 4.6 shows the chosen neutrino emission points on the disk and the reference points 1 and 2 along with the density structure of the remnant.
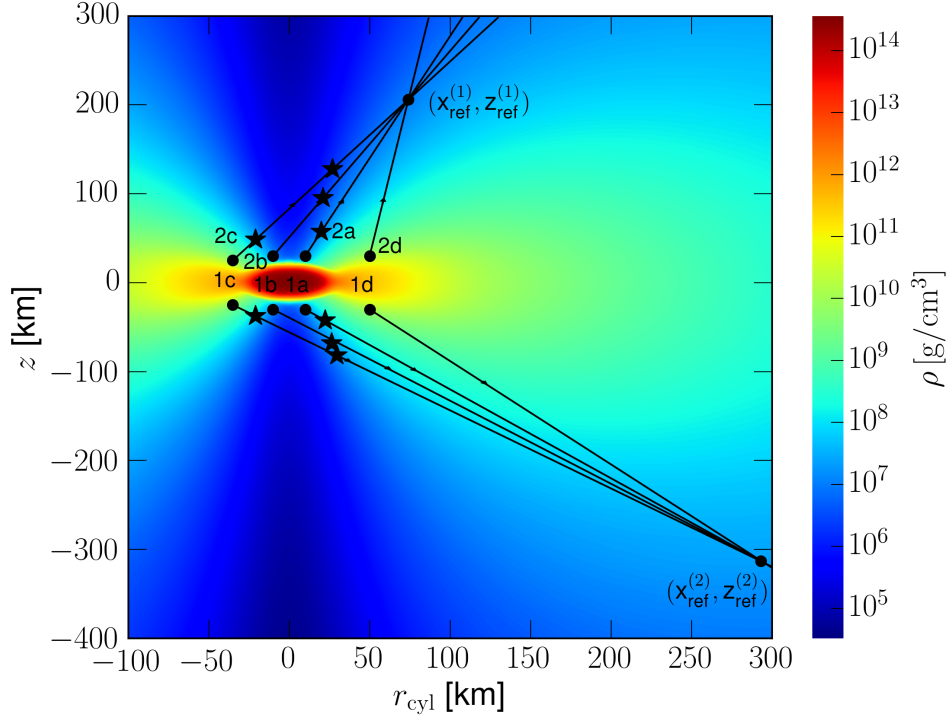
Figure 4.6.: Density profile at 100 ms after the merger as a function of cylindrical coordinates z and r_{cyl}. The neutrino trajectories, shown by the black lines, are specified in tables 4.4 and 4.5. We mirrored the trajectories of table 4.4 for clarity. The two reference points $(x_{ref}^{(i)}, z_{ref}^{(i)})$, $i = 1, 2$, are located at a temperature $T \approx 8$ GK and chosen as representative locations interesting for nucleosynthesis. The points where the matter and unoscillated neutrino self-interaction potentials cancel are marked with $\star$.

For the mixing parameters we take values compatible with current best-fit values, see table 2.3. We use $\delta_{CP} = 0$ for the CP-violating Dirac phase. Since the neutrino mass hierarchy is still unknown [206], we consider both, the normal mass hierarchy (NH), i.e., $\Delta m_{31}^2 > 0$, and inverted mass hierarchy (IH), i.e., $\Delta m_{31}^2 < 0$.

Before presenting the numerical results we introduce the unoscillated potentials associated with the matter and the neutrino self-interaction terms of the Hamiltonian, as done in [173]. The point where the sum of these two quantities cancel already gives an idea for which spatial region MNR are expected to occur. In appendix F we show the cancellation points all over the remnant.

As a measure for the matter strength, we use the refractive energy shift between ν_e and ν_x and define the neutrino-matter potential as follows:

$$\lambda(r) \equiv \sqrt{2}G_F n_e(r). \tag{4.23}$$

For the neutrino self-interaction, the individual contributions from ν_x exactly cancel at any point when flavor transformations have not occurred yet, since we assume the same initial fluxes and surface sizes. Hence, it is convenient to introduce the unoscillated neutrino self-interaction potential as follows:

$$\mu(r) \equiv \frac{\sqrt{2}G_F}{4\pi^2} \left\{ \frac{L_{\nu_e}}{\langle E_{\nu_e} \rangle R_{\nu_e}^2} G_{\nu_e}(\theta_0, \phi_0, r) - \frac{L_{\bar{\nu}_e}}{\langle E_{\bar{\nu}_e} \rangle R_{\bar{\nu}_e}^2} G_{\bar{\nu}_e}(\theta_0, \phi_0, r) \right\}. \tag{4.24}$$

Note that the scales set by the vacuum potentials $\omega \equiv \Delta m^2/(2E)$ ($|\omega_{31}| \approx 0.4\,\mathrm{km}^{-1}$ and $\omega_{21} \approx 0.01\,\mathrm{km}^{-1}$ for a 15 MeV neutrino) are well below $\lambda(r)$ and $\mu(r)$.

Let us discuss the trajectories listed in tables 4.4 and 4.5 taken as representatives over the large set we explored. In the top panels of figures 4.7 and 4.8 we present the matter and unoscillated neutrino self-interaction potentials eqs. (4.23) and (4.24) for these trajectories shown in figure 4.6. To guide the eye we highlight the region around the location of the reference point with a color band. The initial points of 1a (2a) and 1b (2b) are located in the low density polar region, where the matter potential λ is around $3 \times 10^3\,\mathrm{km}^{-1}$ ($\rho_{\mathrm{matt}} \sim 2 \times 10^7\,\mathrm{g\,cm}^{-3}$, $Y_e \sim 0.39$), while trajectory 1c (2c) starts in a low density regime of the wind, where the matter potential is much stronger $9 \times 10^5\,\mathrm{km}^{-1}$ ($\rho_{\mathrm{matt}} \sim 7 \times 10^9\,\mathrm{g\,cm}^{-3}$, $Y_e \sim 0.31$). The starting point of trajectory 1d (2d) is located deeper inside the wind where $\lambda \sim 1 \times 10^6\,\mathrm{km}^{-1}$ ($\rho_{\mathrm{matt}} \sim 2 \times 10^{10}\,\mathrm{g\,cm}^{-3}$, $Y_e \sim 0.18$). Neutrinos on their way on trajectories 1a initially experience an increasing matter potential. When the wind becomes more dilute, the potential decreases until they reach the reference point. In case of trajectories 1b and 2b, neutrinos will first pass the funnel above the MNS pole where the density is very low compared to the emission region. When it enters the wind region the density increases. Afterwards neutrinos proceed similarly as in 1a; i.e., they go through the dilute part of the wind (matter potential is decreasing) and arrive at the reference point. For trajectories 1c and 2c, neutrinos will first need to cover some distance through the dense part of the wind before entering the funnel. Afterwards, they propagate in an analogous way as in cases 1b and 2b. The transition between wind and funnel leads to a rapid drop in the density which is clearly visible in figures 4.7 and 4.8 for trajectories 1b, 1c, 2b, and 2c. A different behavior will be experienced by neutrinos following trajectories 1d, 2a, and 2d. They encounter a monotonically decreasing matter potential until they reach the reference point.

In the self-interaction potential, the relative contribution of ν_e and $\bar{\nu}_e$ changes as a function of distance, due to the interplay of j_{ν_α} and G_{ν_α}. In particular this means that initially, the neutrino self-interaction potential is negative, because it is dominated by the larger electron antineutrino fluxes. Later, the fact that the neutrino surface for electron neutrinos is larger than that of electron antineutrinos may lead to a change of sign in the self-interaction potential
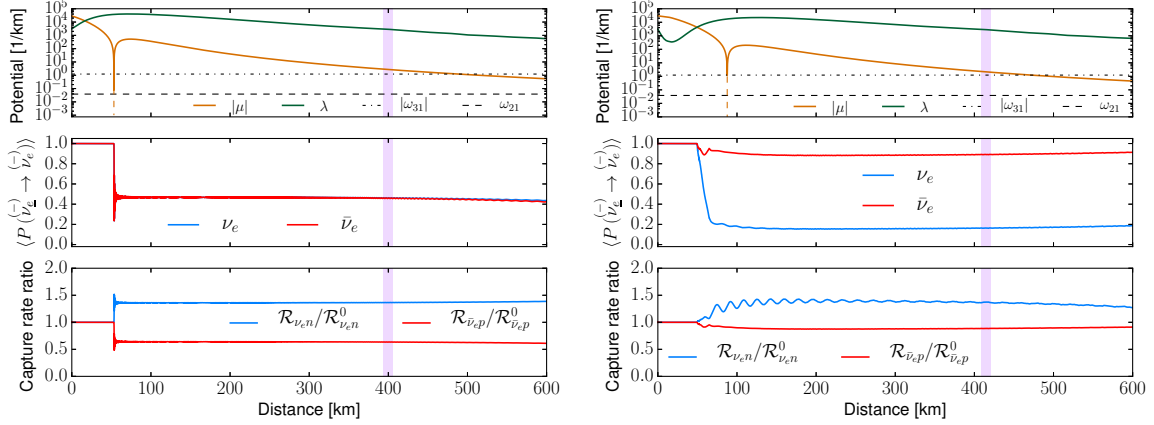
(a) 1a (NH): $x_0 = 10\,\mathrm{km}$, $z_0 = 30\,\mathrm{km}$, $\theta_0 = 45.0°$

(b) 1b (NH): $x_0 = -10\,\mathrm{km}$, $z_0 = 30\,\mathrm{km}$, $\theta_0 = 47.0°$
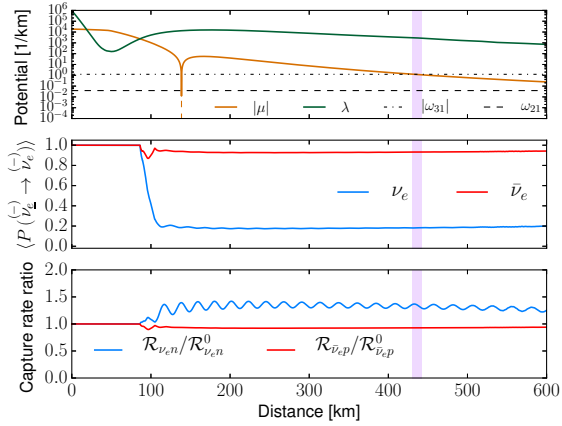
(c) 1c (NH): $x_0 = -35\,\mathrm{km}$, $z_0 = 25\,\mathrm{km}$, $\theta_0 = 48.7°$
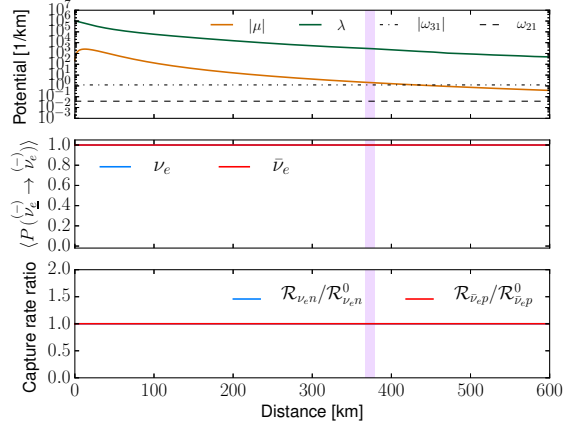
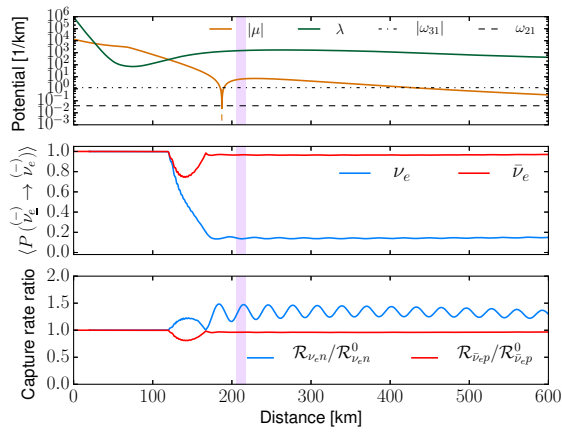(d) 1d (NH): $x_0 = 50\,\mathrm{km}$, $z_0 = 30\,\mathrm{km}$, $\theta_0 = 40.7°$

Figure 4.7.: Results for selected trajectories specified in table 4.4 as functions of the distance for the normal mass hierarchy. The location of the reference point is highlighted by a vertical color band. Top panels: matter potentials (λ) and absolute values of the unoscillated neutrino potentials ($|\mu|$). The middle panels show the spectral averaged survival probabilities for the electron flavor. The blue curves correspond to ν_e and the red curves to $\bar{\nu}_e$, respectively. In the bottom panels, the ratios of capture rates per solid angle for electron neutrinos (blue lines) and antineutrinos (red lines) are presented.
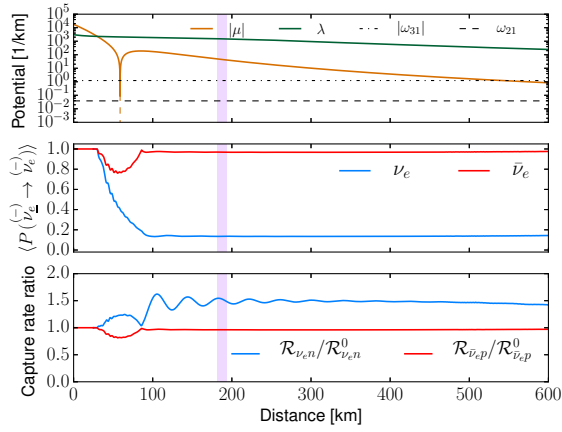
(a) 2a (NH): $x_0 = 10\,\text{km}$, $z_0 = 30\,\text{km}$, $\theta_0 = 20.0°$
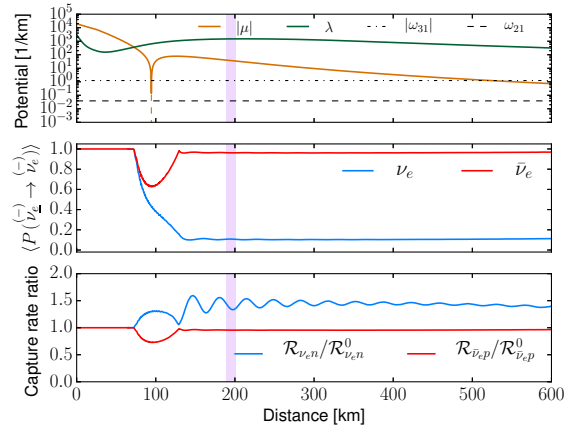
(b) 2b (NH): $x_0 = -10\,\text{km}$, $z_0 = 30\,\text{km}$, $\theta_0 = 25.5°$

(c) 2c (NH): $x_0 = -35\,\text{km}$, $z_0 = 25\,\text{km}$, $\theta_0 = 31.1°$
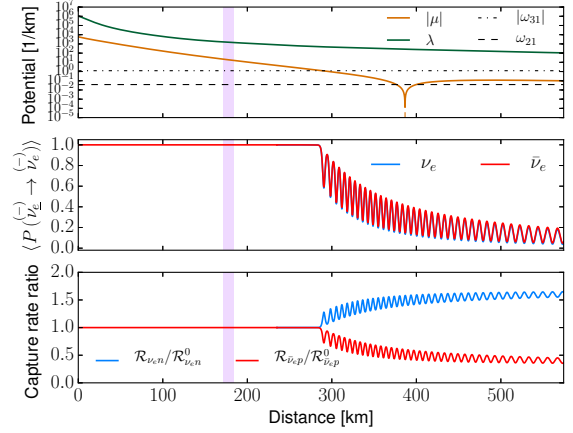
(d) 2d (NH): $x_0 = 50\,\text{km}$, $z_0 = 30\,\text{km}$, $\theta_0 = 7.8°$

Figure 4.8.: Same as figure 4.7 for the trajectories specified in table 4.5.

(as we will see in section 4.6.4). For all trajectories we considered here, the absolute value of the unoscillated neutrino potentials decrease monotonically as a function of distance. The values of $|\mu(r)|$ decrease from $\sim 10^4\,\mathrm{km}^{-1}$ initially and $\sim 10^2\,\mathrm{km}^{-1}$ at $600\,\mathrm{km}$ The relative magnitude of the matter and neutrino potentials and the possible presence of crossings will determine the flavor evolution as we will see in section 4.6.1. We find that the crossings happen at the edge of the funnel (see figure 4.6). This means that for neutrinos emitted around the central region and from the opposite side of the disk, their trajectories cross the funnel so that MNR may occur.

Finally, in our simulations, we find that for some of the examined trajectories, additional MNR occur also at very large distances from the remnant ($r \gtrsim 10^3\,\mathrm{km}$). This behavior is associated with the transition between the expanding neutrino-driven wind ($\rho_{\mathrm{wind}} \gtrsim 5 \times 10^4\,\mathrm{g\,cm}^{-3}$) and the low density atmosphere used in the numerical simulation ($\rho_{\mathrm{atm}} \approx 4 \times 10^3\,\mathrm{g\,cm}^{-3}$). Since the merger of two neutron stars is expected to significantly pollute the funnel above and below the merger remnant (e.g., [207]), the atmosphere in which the wind expands could be denser than the one used in our reference simulation. Since we focus on the neutrino flavor evolution inside the neutrino-driven wind, we can safely neglect this uncertainty.

4.6 Numerical Results

Our goal is to show the trajectory dependence of flavor evolution for neutrinos from the disk by presenting spectral-averaged flavor conversion probabilities (section 4.6.1). As we will discuss we find a variety of flavor conversion behaviors. Furthermore, we explore the potential impact on nucleosynthesis in the neutrino-driven wind by showing ratios of oscillated and unoscillated capture rates per solid angle (section 4.6.2). We present results based on hydrodynamical profiles obtained at 100 ms. We discuss possible variations with a different time snapshot (60 ms) in section 4.6.3. Finally, we show the sensitivity of the flavor evolution when employing different assumptions for the initial luminosities, or considering uncertainties on the neutrino fluxes from simulations available in the literature.

In our calculations of the flavor evolution we assume that all (anti)neutrinos are prepared in flavor eigenstates. The flavor evolution of neutrinos with different energies is then followed by numerically solving eqs. (3.35) and (3.36) with the Hamiltonian components given by eqs. (3.30), (3.31), and (4.22) for a given trajectory with emission angle θ_0. We employed different discretization schemes to check for convergence of the results.

4.6.1 Flavor conversion results and general behavior

After obtaining the flavor evolution of neutrinos along each trajectory, $\rho_{\nu_\alpha}(E, r)$ and $\rho_{\bar\nu_\alpha}(E, r)$, we compute spectral averages of the neutrino survival probability, i.e.,

$$\langle P(\nu_{\underline{e}} \to \nu_e) \rangle(r) = \int_0^\infty \mathrm{d}E \, f_{\nu_{\underline{e}}}(E) P(\nu_{\underline{e}} \to \nu_e)(E, r). \tag{4.25}$$

Notice that $P(\nu_{\underline{\alpha}} \to \nu_\beta) = (\rho_{\nu_{\underline{\alpha}}})_{\beta\beta}$ as defined in section 3.4.1.

As examples, we show the averaged survival probabilities of electron neutrinos and antineutrinos for the trajectories 1a to 1d in the middle panels of figure 4.7 and 2a to 2d in figure 4.8. These results are obtained in NH.

As can be seen from figures 4.7 and 4.8 (top panels), the structure of some profiles allows the unoscillated potentials to cancel at more than one spatial location such as trajectories 1c and 2c. We indicate these locations in figure 4.6 for the trajectories defined in tables 4.4 and 4.5. If the resonance condition is fulfilled, flavor conversion occurs only if the strength of the neutrino self-interaction[3] is larger than the matter contribution ($\lambda < |\mu|$) prior to it. If the matter term dominates the self-interaction term ($\lambda > |\mu|$), before a cancellation point, the resonances are extremely non-adiabatic and nearly no flavor transformation can happen [174, 177]. The characteristic feature of the standard MNR is that electron neutrinos can undergo significant flavor change, while electron antineutrinos only experience a little flavor conversion. This is due to the fact that the latter go through their resonances extremely non-adiabatically at either the beginning or the end of the MNR, depending on the hierarchy, in a way similar to the results shown in [177] with 2-flavor toy models. In NH, we find that survival probabilities for neutrinos propagating along trajectories 1b, 1c, 2a, 2b, and 2c exhibit the standard MNR features discussed above. We note that in all MNR cases, high energy ν_e are only partially converted at the end of the MNR region, resulting in $\sim 20\%$ averaged survival probabilities.

For trajectory 1a, despite the MNR condition being fulfilled, the flavor transformation is extremely non-adiabatic and nearly no flavor conversion happens immediately after the MNR location. However, at ~ 50 km, we see that both ν_e and $\bar\nu_e$ undergo simultaneous flavor conversions when $\lambda(r) \gg |\mu(r)|$. This is due to the fact that the $\nu\nu$ coupling introduces a synchronization frequency[4] [208],

$$\omega_{\mathrm{sync}}^{ij}(r) \approx \frac{\sqrt{2} G_{\mathrm{F}} \int \mathrm{d}E \, \omega_{ij}[j_{\nu_e}(E) G_{\nu_e}(r) + j_{\bar\nu_{\underline{e}}}(E) G_{\bar\nu_e}(r)]}{\mu(r)}. \tag{4.26}$$

As $|\mu(r)| \to 0$ when it changes sign, $|\omega_{\mathrm{sync}}^{ij}(r)| \propto |1/\mu(r)|$ can be very large. Thus, a synchronized MSW effect (see, e.g., [209, 210]) happens when $\omega_{\mathrm{sync}}^{ij} \cos\theta_{ij} \sim \lambda$ so that all

---

[3] We remind the reader that because of the dominance of the electron antineutrino number fluxes over the neutrino one, the neutrino self-interaction term starts negative.

[4] Note that in eq. (4.26) we suppressed the angular dependence in the geometric factors to simplify the notation.

neutrinos and antineutrinos with different momenta are bound together and simultaneously go through the MSW-like flavor conversion. We note here that the flavor transformation is actually due to the resonance of $\omega_{\text{sync}}^{21}$ with $\lambda(r)$ as the larger mixing angle θ_{12} provides enough adiabaticity.

For 1d and 2d, the MNR condition is not met and there is no flavor conversion in 1d. However, 2d shows synchronized type oscillations starting at ~ 285 km, resulting in both ν_e and $\bar{\nu}_e$ flavor conversions. In figure 4.9 we plot along trajectories 1a and 2d energy-dependent survival probabilities for ν_e and $\bar{\nu}_e$ showing the typical synchronization behavior.

(a) 1a   (b) 2d
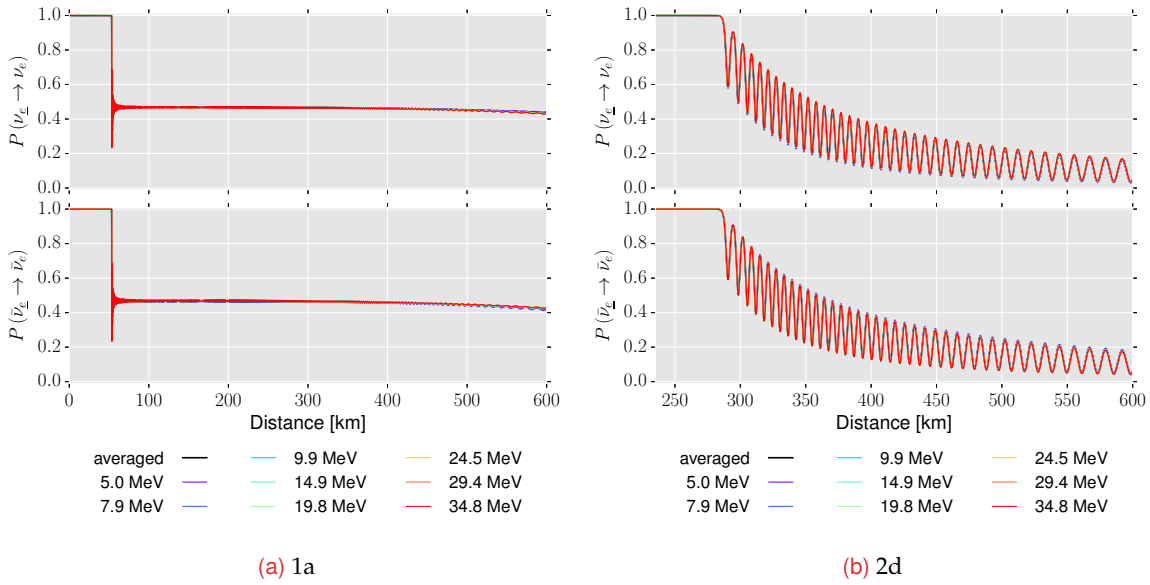
Figure 4.9.: Flavor evolution results obtained in NH along trajectories 1a (left) and 2d (right). The top panels show the spectral averaged along with energy-dependent survival probabilities for ν_e while the bottom panel shows the survival probabilities for $\bar{\nu}_e$, respectively.

For IH, the qualitative behaviors are the same as in NH when MNR occurs (1b, 1c, 2a, 2b, 2c). The only difference is the slightly more adiabatic flavor transformation near the end of the MNR region (see figure 4.10 for the example of trajectory 2a). Regarding the other trajectories, we find for 1a (as in NH) the same synchronized MSW conversion while 1d and 2d, now show the "bipolar" type of flavor transformation (see e.g., [118]) so that both ν_e and $\bar{\nu}_e$ are transformed, but their averaged survival probabilities are different (see figure 4.10 for the example of 2d).

We provide a summary of the results in table 4.6, where we report the type of flavor conversion mechanism.

(a) 2a

(b) 2d
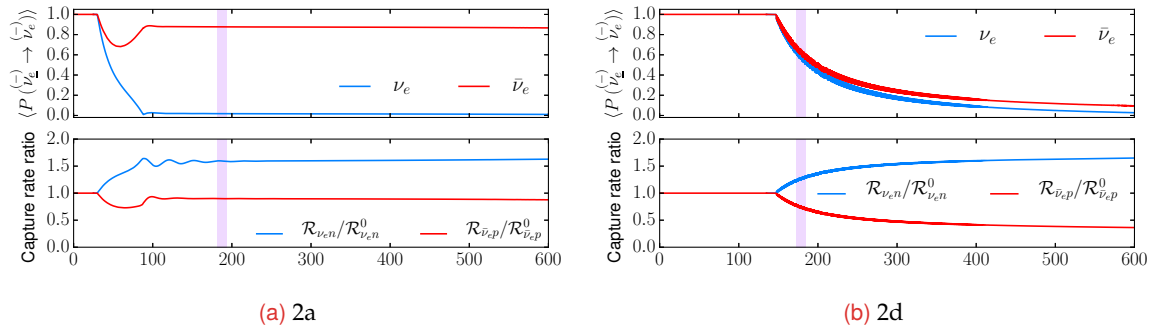
Figure 4.10.: Flavor evolution results obtained in IH along trajectories 2a (left) and 2d (right). The top panels show the spectral averaged survival probabilities for the electron flavor. The blue curves correspond to ν_e and the red ones to $\bar{\nu}_e$, respectively. In the bottom panels the ratios of capture rates per solid angle for electron neutrinos (blue curves) and antineutrinos (red curves) are presented.

Trajectory	Flavor conversion		Capture rate ratio			
	NH	IH	NH		IH	
			ν_e	$\bar{\nu}_e$	ν_e	$\bar{\nu}_e$
1a	sync.	sync.	+36%	-36%	+67%	-67%
1b	MNR	MNR	+37%	-11%	+46%	-12%
1c	MNR	MNR	+33%	-7%	+43%	-7%
1d	-	bipolar	-	-	+46%	-49%
2a	MNR	MNR	+52%	-4%	+59%	-10%
2b	MNR	MNR	+39%	-4%	+56%	-8%
2c	MNR	MNR	+37%	-4%	+53%	-6%
2d	sync.	bipolar	-	-%	+26%	-25%

Table 4.6.: For the given trajectories, we list the flavor conversion mechanism (MNR, synchronized MSW (sync.), bipolar, and no conversion (-)) and capture rate ratios for ν_e and $\bar{\nu}_e$ (distance-averaged around the location of the reference point ($T = 8\,\mathrm{GK}$)) and both mass hierarchies.

4.6.2 Differential capture rates

We calculate the rate per solid angle for electron neutrino captures on free neutrons with both the oscillated and unoscillated neutrino spectra. The oscillated rate is given by,

$$
\mathcal{R}_{\nu_e n}(r) = \frac{1}{2\pi} \sum_{\alpha=e,\mu,\tau} F_{\nu_\alpha} \int_0^\infty dE\, f_{\nu_{\underline{\alpha}}}(E)
$$
$$
\times \sigma_{\nu_e n,\mathrm{abs}}(E) P(\nu_{\underline{\alpha}} \to \nu_e)(E, r). \tag{4.27}
$$

For the unoscillated capture rate we use,

$$
\mathcal{R}^0_{\nu_e n} = \frac{F_{\nu_e}}{2\pi} \int_0^\infty dE\, f_{\nu_e}(E) \sigma_{\nu_e n,\mathrm{abs}}(E). \tag{4.28}
$$

Similar expressions ($\mathcal{R}_{\bar{\nu}_e p}$, $\mathcal{R}^0_{\bar{\nu}_e p}$) hold for electron antineutrino capture on free protons with $\sigma_{\bar{\nu}_e p,\mathrm{abs}}$, where the lower bound of the integrals has to be replaced by the threshold $m_e + \Delta_{np}$, i.e., the sum of the electron mass $m_e \approx 0.5\,\mathrm{MeV}$ and the neutron-proton mass difference Δ_{np}. We compute the ratio between oscillated $\mathcal{R}$ and unoscillated $\mathcal{R}^0$ capture rates.

From eq. (4.27), one can see that when calculating $\mathcal{R}$, the electron neutrino appearance probabilities will be weighted by the ν_μ/ν_τ fluxes (eq. (D.37)) and the cross section (eq. (C.1)). We note that the fluxes j_{ν_α} are peaked around $2.2\,T_{\nu_\alpha}$ while the rates ($j_{\nu_\alpha}\sigma$) around $4.1\,T_{\nu_\alpha}$ (figure 4.11). Therefore, for $\mathcal{R}_{\nu_e n}$, the contribution of the initial non-electron flavors will enhance it when efficient $\nu_e \leftrightarrow \nu_x$ flavor conversion takes place, as the high energy tail of the initial ν_x dominates the capture rates indicated in figure 4.11. For $\mathcal{R}_{\bar{\nu}_e p}$, from figure 4.11 we see that since $(j_{\bar{\nu}_e}\sigma_{\bar{\nu}_e p,\mathrm{abs}}) > (j_{\nu_{\mu,\tau}}\sigma_{\bar{\nu}_e p,\mathrm{abs}})$ for the whole energy spectrum, any flavor conversion of $\bar{\nu}_e \leftrightarrow \bar{\nu}_x$ will suppress it.

Based on the above discussions, we see from the bottom panels of figures 4.7, 4.8, and 4.10 that for ν_e which undergo efficient flavor conversions due to MNR (1b, 1c, 2a, 2b, 2c), the ν_e capture rates are largely enhanced by up to $\sim 59\%$ after the end of the MNR region while the $\bar{\nu}_e$ capture rates are slightly decreased by up to $\sim 12\%$ in those cases. For the trajectories showing the synchronized MSW flavor transformation (1a), the ν_e ($\bar{\nu}_e$) capture rates are increased (decreased) by up to $\sim 67\%$ (67%) as both are simultaneously transformed. As for the cases with a bipolar type of flavor conversion (1d and 2d in IH), the capture rates for ν_e ($\bar{\nu}_e$) are gradually changed up to $\sim 65\%$ (-62%) at 600 km. In most cases where flavor conversion takes place, the capture rates are affected in regions with temperature $T \gtrsim 8\,\mathrm{GK}$ before all nucleons recombine into α-particles. We provide a summary of the capture rate ratio, $\mathcal{R}/\mathcal{R}^0$, in table 4.6 at the reference locations ($T = 8\,\mathrm{GK}$) for all trajectories.
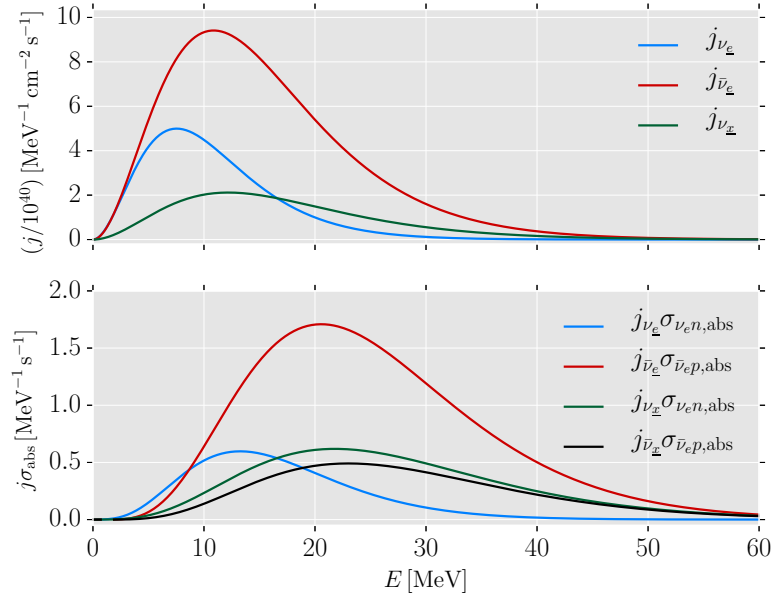
Figure 4.11.: Neutrino number fluxes [see eq. (4.18)] (upper panel) and number fluxes times cross sections (lower panel). All quantities are per unit energy per solid angle.

4.6.3 Comparison between different post-merger times

Although the neutrino luminosities and average energies remain nearly stationary over the disk evolution time, the wind density profiles change substantially. In figure 4.12, we compare the matter potentials for trajectories 2a (upper panel) and 2c (lower panel) at different times (60 and 100 ms). For both cases, the matter potentials are larger at 100 ms compared to the one at 60 ms and show a similar overall behavior as a function of distance. This is because the expanding wind drives the surrounding area less neutron-rich at later times, as can be inferred from figures 4.2 and 4.13. Consequently, the MNR locations at 100 ms are shifted to smaller distances. However, such differences do not result in qualitative changes in the overall flavor evolution behavior.

4.6.4 Impact of input neutrino emission characteristics

For the results presented so far, the calculations are performed based on the neutrino luminosities and mean energies given in table 4.3. These values are obtained at distances far away from the disk, which are called "net luminosities" in [25] (see figure 8 of [25]). However, neutrinos do not completely travel unhindered from the neutrino surfaces in a realistic environment. Their luminosities can be higher in regions close to the neutrino surfaces and reduce to the net luminosities due to charged-current neutrino absorptions
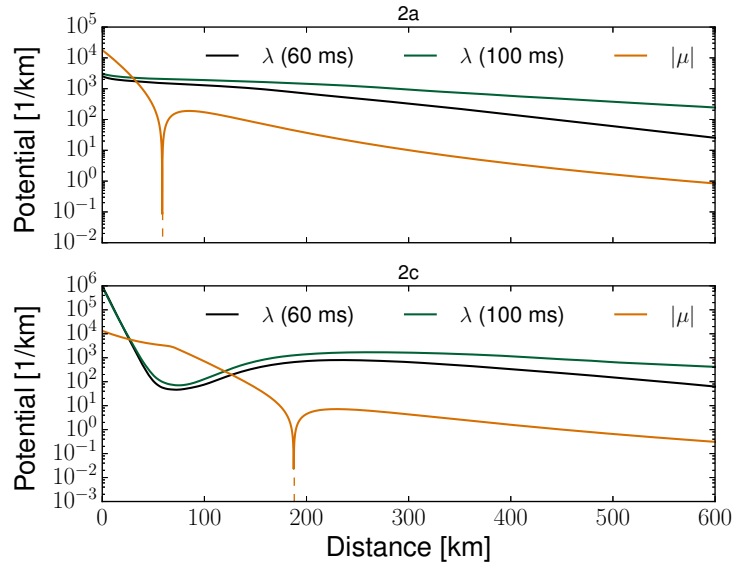
Figure 4.12.: Comparison of the unoscillated potentials between the time snapshots for trajectories 2a (upper) and 2c (lower panel).
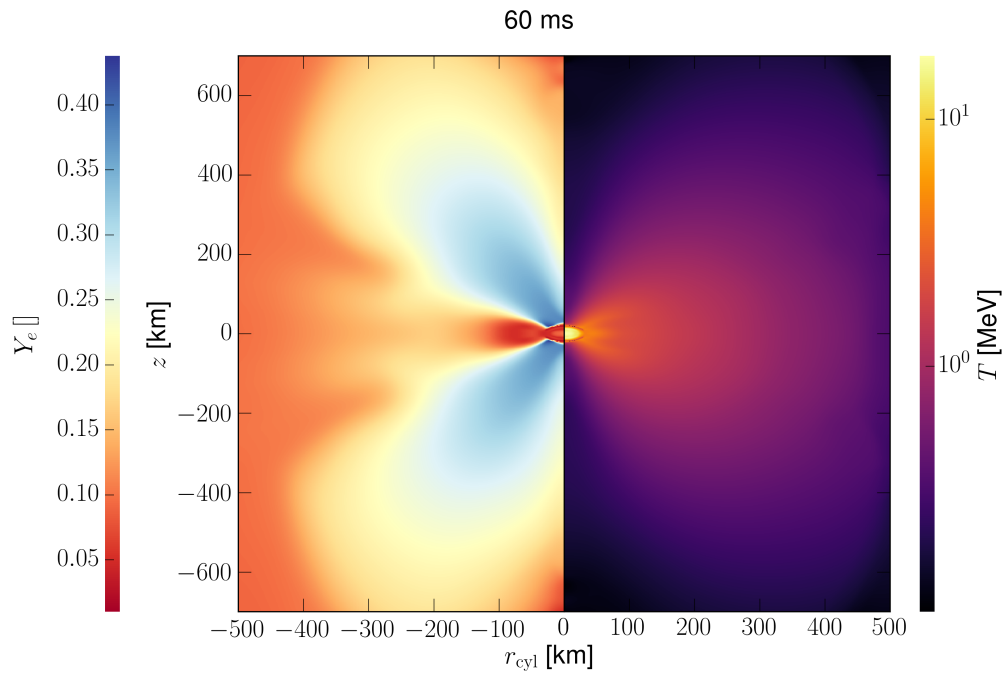
Figure 4.13.: Electron fraction (left panel) and matter temperature (right panel) as functions of cylindrical coordinates z and r_{cyl} at $t = 60\,\mathrm{ms}$ after the merger.
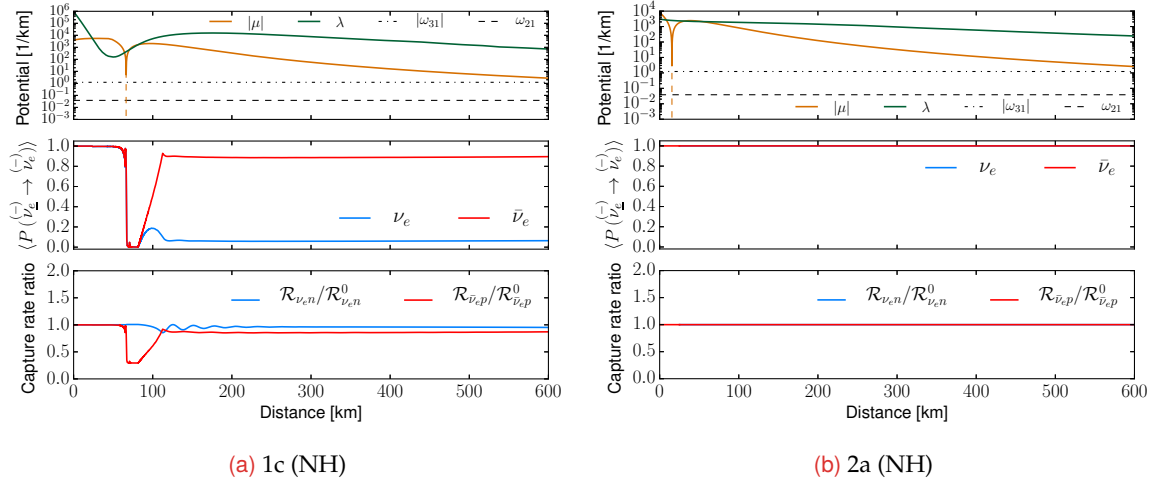
Figure 4.14.: Same as figure 4.7 for trajectories 1c (left) and 2a (right) with cooling luminosities (see text).

above the surfaces[5]. Since the environment is neutron-rich, the decrease of L_{ν_e} is larger than that of $L_{\bar{\nu}_e}$ and L_{ν_x}. Consequently, a less negative $\mu(r)$ compared to the values obtained with net luminosities in regions close to the neutrino surfaces may be obtained. If for a trajectory, $|\mu(r)| > \lambda(r)$ initially close to the neutrino surfaces, one expects MNR to occur closer to the emission point.

We explore this effect by performing additional calculations for all trajectories using the "cooling" neutrino luminosities from [25], calculated by neglecting charged-current neutrino absorptions above the neutrino surfaces: $L_{\nu_e,\text{cool}} = 25 \times 10^{51}$ erg s^{-1}, $L_{\bar{\nu}_e,\text{cool}} = 33 \times 10^{51}$ erg s^{-1}, and $L_{\nu_x,\text{cool}} = L_{\nu_x} = 8 \times 10^{51}$ erg s^{-1}. Compared to the net luminosities (see table 4.3), $L_{\nu_e,\text{cool}} = 1.67 L_{\nu_e}$ and $L_{\bar{\nu}_e,\text{cool}} = 1.1 L_{\bar{\nu}_e}$. Figure 4.14 shows the results with cooling luminosities for trajectories 1c and 2a. In both cases, the MNR locations with a larger $L_{\nu_e,\text{cool}}$ are indeed closer to their emission points when compared to figures 4.7 and 4.8. In 1c, MNR now occurs at ~ 66 km immediately prior to the point where μ changes sign. This results in a complete flavor transformation for both ν_e and $\bar{\nu}_e$, or symmetric MNR [173, 175]. After the symmetric MNR, another standard MNR occurs at a distance of ~ 82 km so that antineutrinos go through nearly complete flavor conversion as discussed in [175]. For the capture rate ratio of ν_e, it changes only slightly due to a much higher $L_{\nu_e,\text{cool}}$. For $\bar{\nu}_e$, the capture rate ratio is largely suppressed in the region between the symmetric MNR and the second standard MNR. For case 2a, the position where MNR occurs is also largely shifted to a smaller distance at ~ 10 km. However, we find a strongly non-adiabatic behavior resulting in no flavor transformation.

The model we have considered is based on one particular simulation of the remnant from the merger of BNS with equal mass. The large variety of possible initial conditions of the merger (NS masses and spins, mass ratios) is expected to translate into a wide range of both the neutrino luminosities and the mean energies for different systems. Also, the neutrino

---

[5] In appendix H we discuss the issue of cooling and net luminosities in more detail and comment on the role of absorption.
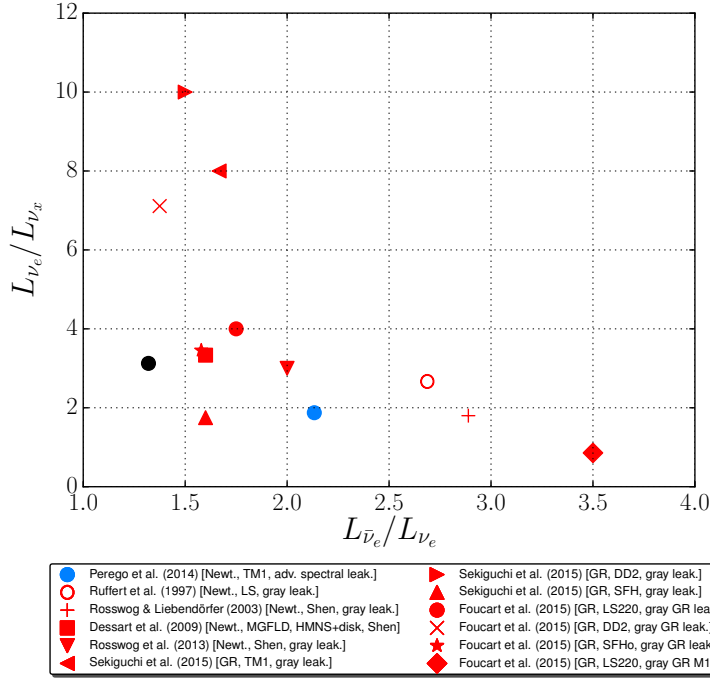
Figure 4.15.: Ratio of luminosities: L_{ν_e}/L_{ν_x} vs $L_{\bar{\nu}_e}/L_{\nu_e}$. The corresponding values are given in table G.1. The black point refers to the cooling luminosities of [25] (see text).

emissions can be significantly influenced by the thermodynamical properties of the dense nuclear matter, which is subject to the large uncertainties in the nuclear EOS (see e.g., [211, 212] for the potential impact of the nuclear EOS on the neutrino luminosities). Finally, the different numerical techniques and levels of approximations that are used to model hydrodynamics, gravity and weak interactions can all lead to quantitatively different predictions of the relevant neutrino quantities. To quantify these uncertainties in our input parameters, we have collected published values of neutrino luminosities and mean energies (when available) from several different simulations of BNS merger and of the merger aftermath in the presence of a long lived MNS. We show these values in table G.1 in appendix G. We see that the luminosities may differ by 1 order of magnitude while the differences in mean energies are within a factor of 2. We show in figures 4.15 and 4.16 the ratio of luminosities, $L_{\bar{\nu}_e}/L_{\nu_e}$ and L_{ν_e}/L_{ν_x}, and the ratio of mean energies, $\langle E_{\bar{\nu}_e}\rangle/\langle E_{\nu_e}\rangle$ and $\langle E_{\nu_e}\rangle/\langle E_{\nu_x}\rangle$. We emphasize that our goal is not to compare the results of the different simulations, but to show the variety of possible ranges for these ratios.

Note that the neutrino self-interaction potential depends on the difference between the fluxes of neutrinos and antineutrinos, which are proportional to the neutrino number luminosities $\sim L_{\nu_\alpha}/\langle E_{\nu_\alpha}\rangle$. We further show the corresponding ratios, $(L_{\bar{\nu}_e}/\langle E_{\bar{\nu}_e}\rangle)/(L_{\nu_e}/\langle E_{\nu_e}\rangle)$ and $(L_{\nu_e}/\langle E_{\nu_e}\rangle)/(L_{\nu_x}/\langle E_{\nu_x}\rangle)$ in figure 4.17.

To explore the impact of different flux ratios on the neutrino flavor evolution, we have varied the neutrino luminosities of table 4.3 by: $L_{\nu_e} \mapsto 0.65\,L_{\nu_e}$ and $L_{\nu_x} \mapsto 1.16\,L_{\nu_x}$. This change gives a similar $(L_{\bar{\nu}_e}/\langle E_{\bar{\nu}_e}\rangle)/(L_{\nu_e}/\langle E_{\nu_e}\rangle)$ to the value obtained in Foucart *et al.* (2016) [GR,
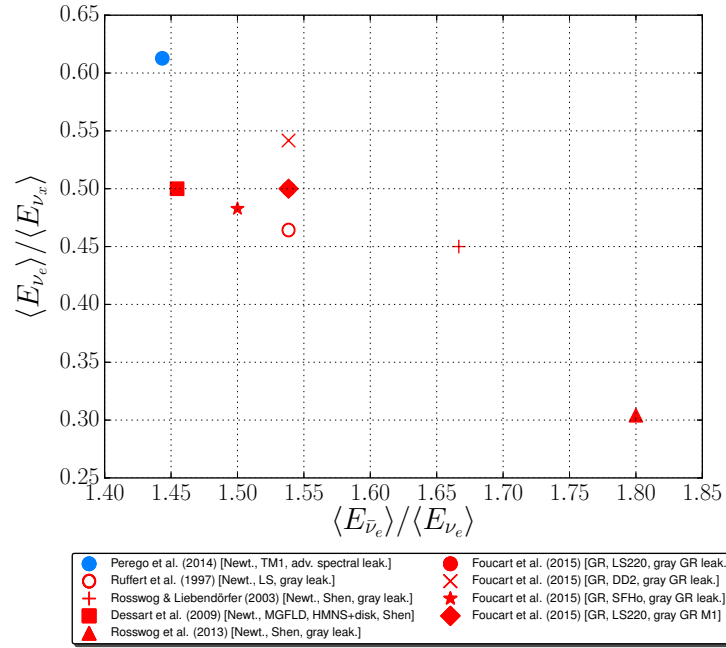
Figure 4.16.: Ratio of mean energies: $\langle E_{\nu_e}\rangle/\langle E_{\nu_x}\rangle$ vs $\langle E_{\bar{\nu}_e}\rangle/\langle E_{\nu_e}\rangle$. The corresponding values are given in table G.1.
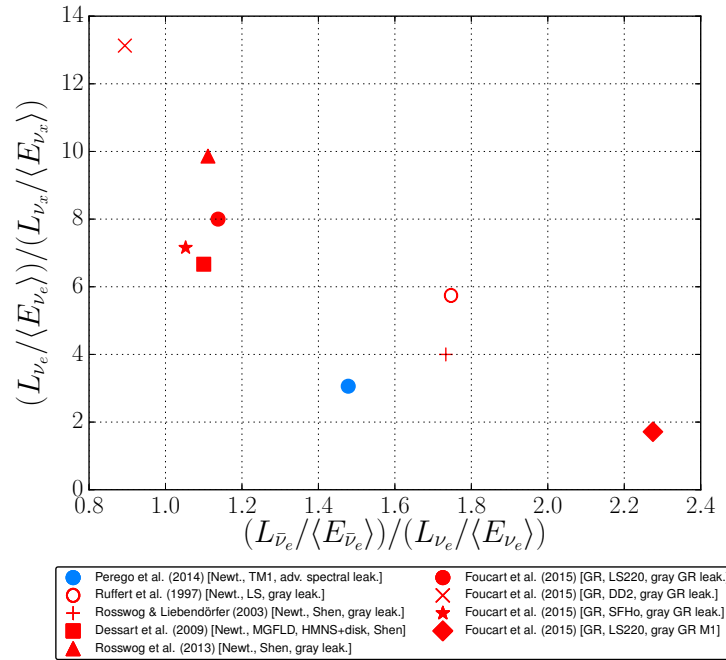
Figure 4.17.: Ratio of emission rates: $(L_{\nu_e}/E_{\nu_e})/(L_{\nu_x}/E_{\nu_x})$ vs $(L_{\bar{\nu}_e}/E_{\bar{\nu}_e})/(L_{\nu_e}/E_{\nu_e})$. The corresponding values are given in table G.1.

gray GR M1, LS220 EOS] [212]. The results with such luminosities for trajectories 1c and 2a in NH are shown in figure 4.18. Contrary to the previously discussed exploration with cooling luminosities, the differences between the fluxes of electron neutrinos and electron antineutrinos become larger. This affects the self-interaction potential in such a way that no change of sign in $\mu(r)$ occurs anymore.

(a) 1c (NH): $x_0 = -35\,\text{km}$, $z_0 = 25\,\text{km}$, $\theta_0 = 48.7°$ (b) 2a (NH): $x_0 = 10\,\text{km}$, $z_0 = 30\,\text{km}$, $\theta_0 = 20.0°$
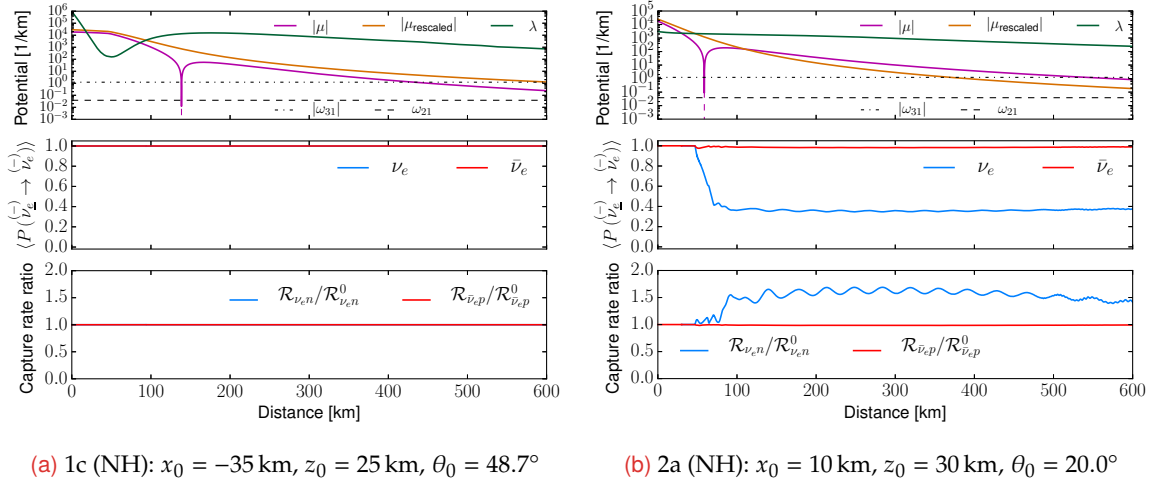
Figure 4.18.: Same as figure 4.7 for trajectories 1c and 2a with rescaled fluxes (see text).

For trajectory 1c, the flavor evolution becomes strongly non-adiabatic when compared to the result shown in figure 4.7c. For trajectory 2a, the flavor evolution becomes less adiabatic.

4.7   Comparison between two- and three-flavor cases

In this section we report on results obtained in a two-flavor approximation by setting $\Delta m_{21}^2 = 0$, $\theta_{12} = 0$, and $\theta_{23} = 0$. Since the MNR has not been discussed in detail like flavor conversions due to oscillations of the bipolar type and the synchronized MSW mechanism, we will focus on the MNR only and show results obtained along trajectories 2a and 2c showing a typical behavior. In particular, we present matter and unoscillated self-interaction potentials and averaged survival probabilities in figures 4.19 and 4.22 in both mass hierarchies and for both three- and two-flavor cases. In addition, we show in figures 4.20, 4.21, 4.23, and 4.24 energy-dependent survival probabilities for ν_e and $\bar{\nu}_e$, respectively.

For both trajectories and in both mass hierarchies, we observe a good agreement between results obtained in the two-flavor approximation and in the three-flavor case. In particular, we verified that the energy-dependent probabilities show a similar behavior as well.

In order to get a clearer picture of the adiabaticity, we focus on the two-flavor case and apply the NFIS formalism. Thereby, we use the adiabatic solution eq. (3.82), where we assume that the NFIS $\mathbf{s}_\nu$ possesses a certain alignment with its effective field $\mathbf{H}$. Then, we can relate the effective mixing angle to the survival probabilities as $P(\nu_{\underline{e}} \rightarrow \nu_e) = (1 + \cos(2\theta_{\text{eff}}))/2$. Furthermore, we can introduce the angle $\tilde{\theta}$ via

$$\mathbf{s}_\nu \cdot \mathbf{H} = \frac{1}{2}|\mathbf{H}|\cos(2\tilde{\theta}), \tag{4.29}$$

which describes the alignment between the NFIS $\mathbf{s}_\nu$ and the field $\mathbf{H}$.

We present the results in figures 4.25 and 4.26. In the numerical calculations, we excluded the contributions in the Hamiltonian H of the test neutrino under consideration[6]. This will not change the equations of motion,

$$\frac{\mathrm{d}\rho_{\nu_\alpha}(\mathbf{p}',r)}{\mathrm{d}r} = \left[\mathsf{H}(\mathbf{p}',r) - [\mathsf{H}_{\nu\nu}(\mathbf{p}',r)]_{\nu_\alpha}, \rho_{\nu_\alpha}(\mathbf{p}',r) \right] \tag{4.30}$$

$$= \left[\mathsf{H}(\mathbf{p}',r), \rho_{\nu_\alpha}(\mathbf{p}',r) \right], \tag{4.31}$$

since $[\mathsf{H}_{\nu\nu}(\mathbf{p}',r)]_{\nu_\alpha}$ commutes with $\rho_{\nu_\alpha}(\mathbf{p}',r)$.

As we can observe, for lower energies $\lesssim 15\,\mathrm{MeV}$, the adiabatic solution agrees with the numerical solution obtained by solving the equations of motion. At energies between 15 and 25 MeV, the adiabatic solution still provides a good approximation for distances up to 90 km. The results suggest that the simple picture emerging from toy models like discussed in section 3.6 can be employed to understand the numerical results obtained from the detailed simulations of [25].

---

[6]   Note that in the original formulation by Pantalone [90] the test neutrino contribution was explicitly removed from the background Hamiltonian $\mathsf{H}_{\nu\nu}$.
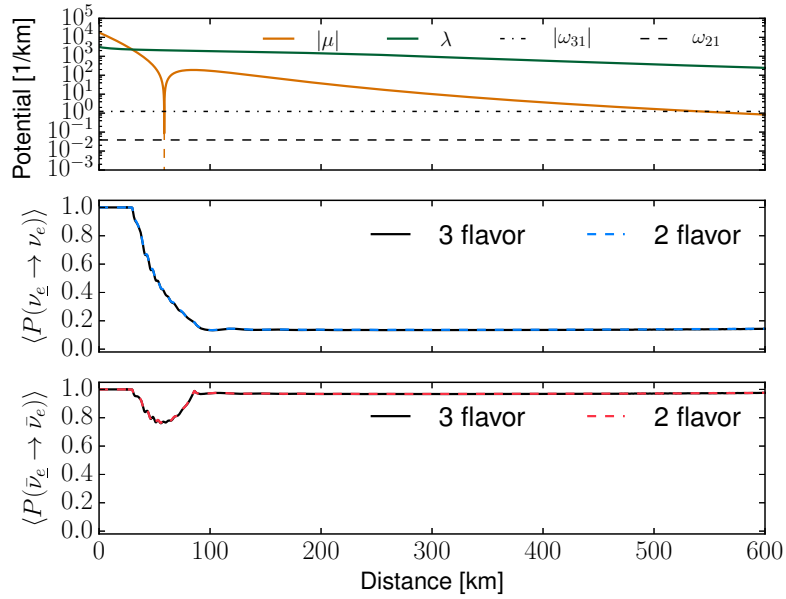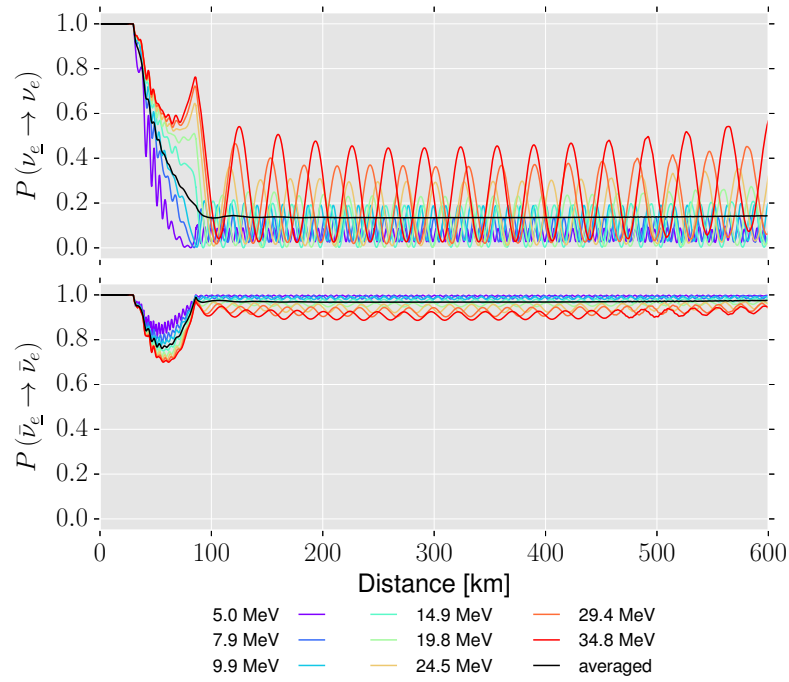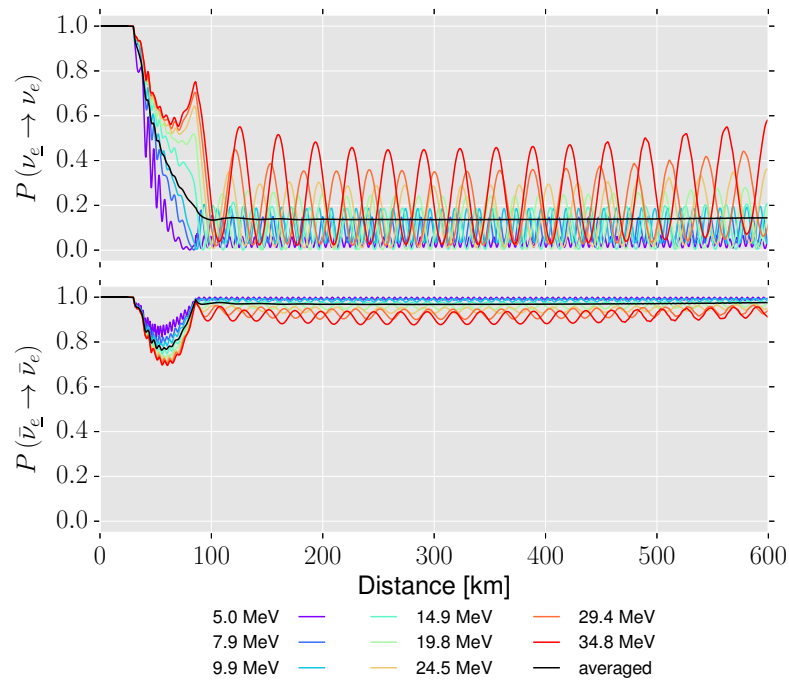
(a) Normal hierarchy
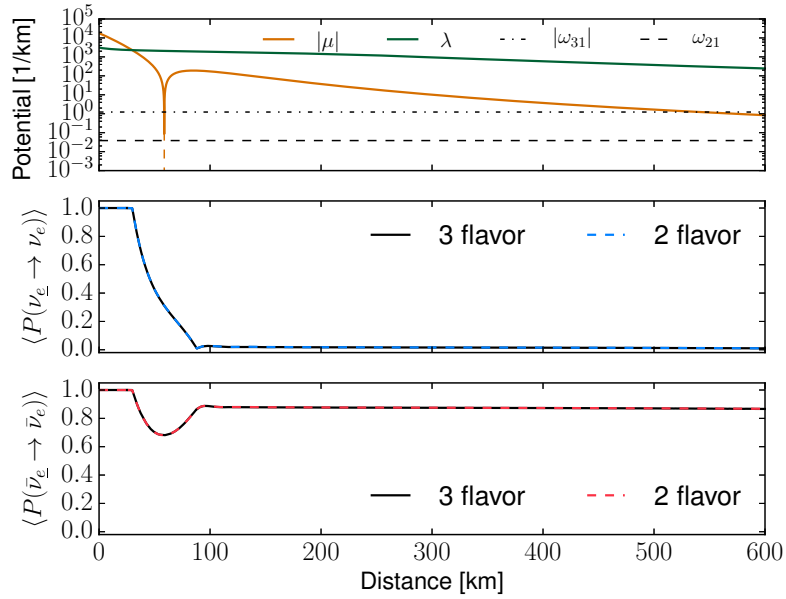
(b) Inverted Hierarchy

Figure 4.19.: Flavor evolution results along trajectory 2a: $x_0 = 10\,\text{km}$, $z_0 = 30\,\text{km}$, $\theta_0 = 20.0°$ in NH (a) and IH (b). We show matter potential, unoscillated neutrino self-interaction potential, and vacuum potentials (for a neutrino energy of $5\,\text{MeV}$) (top panel), averaged survival probabilities for electron neutrinos (middle panel) and electron antineutrinos (bottom panel) obtained in three-flavor (solid curves) and two-flavor calculations (dashed curves).
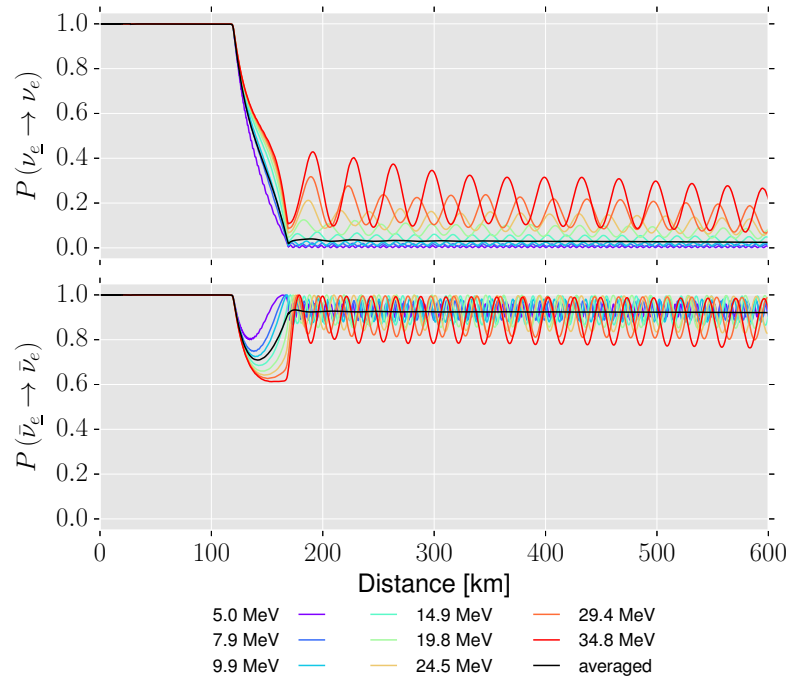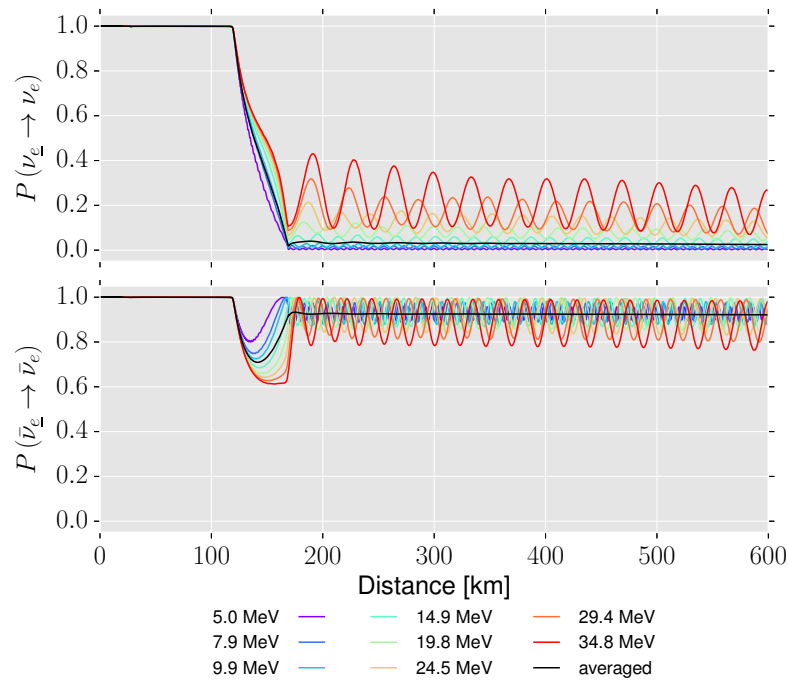
(a) 3-flavor

(b) 2-flavor

Figure 4.20.: Normal hierarchy. 2a: $x_0 = 10 \, \text{km}$, $z_0 = 30 \, \text{km}$, $\theta_0 = 20.0°$. Survival probabilities for electron neutrinos (top panels) and electron antineutrinos (bottom panels) for selected energies for the three-flavor (a) and two-flavor (b) cases.
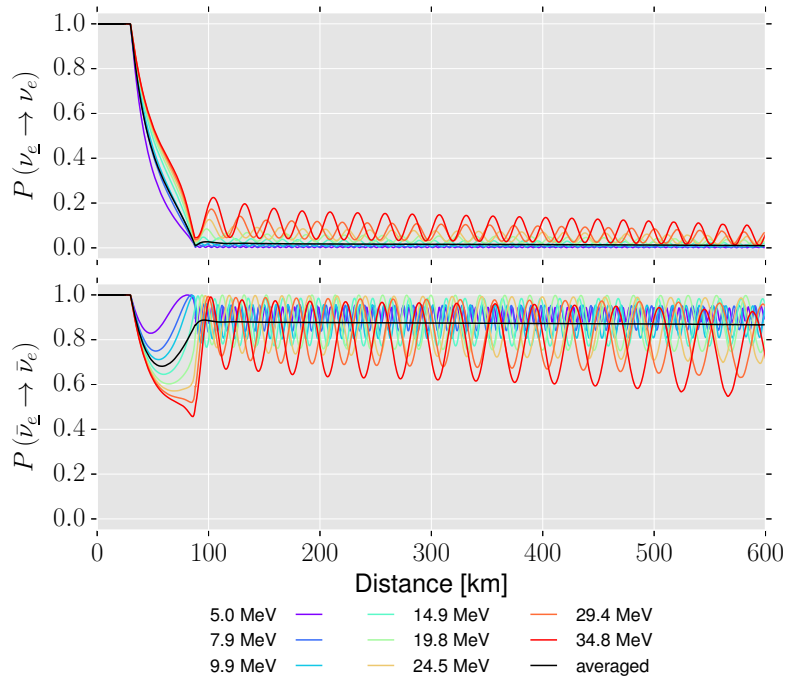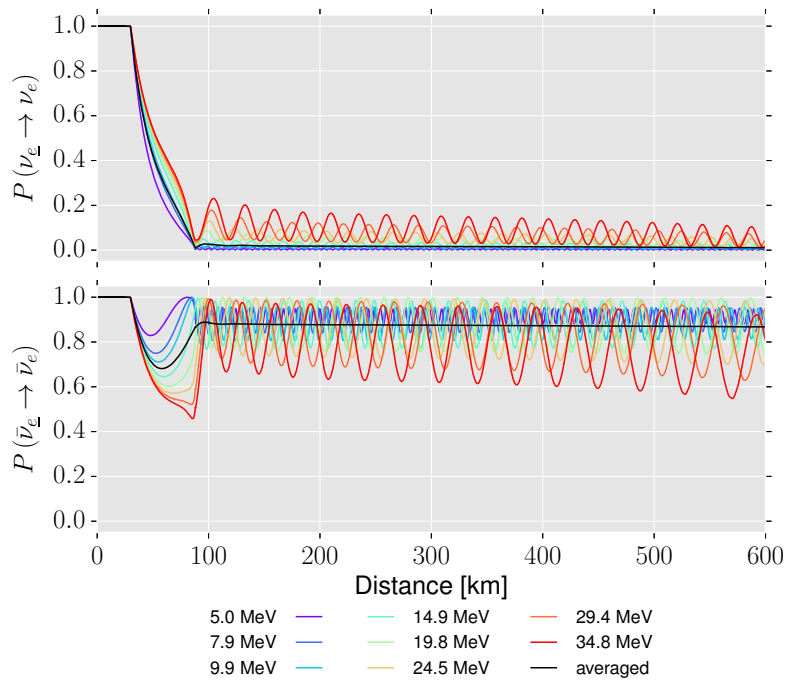
(a) 3-flavor

(b) 2-flavor

Figure 4.21.: Inverted hierarchy. 2a: $x_0 = 10\,\text{km}$, $z_0 = 30\,\text{km}$, $\theta_0 = 20.0°$. Survival probabilities for electron neutrinos (top panels) and electron antineutrinos (bottom panels) for selected energies for the three-flavor (a) and two-flavor (b) cases.
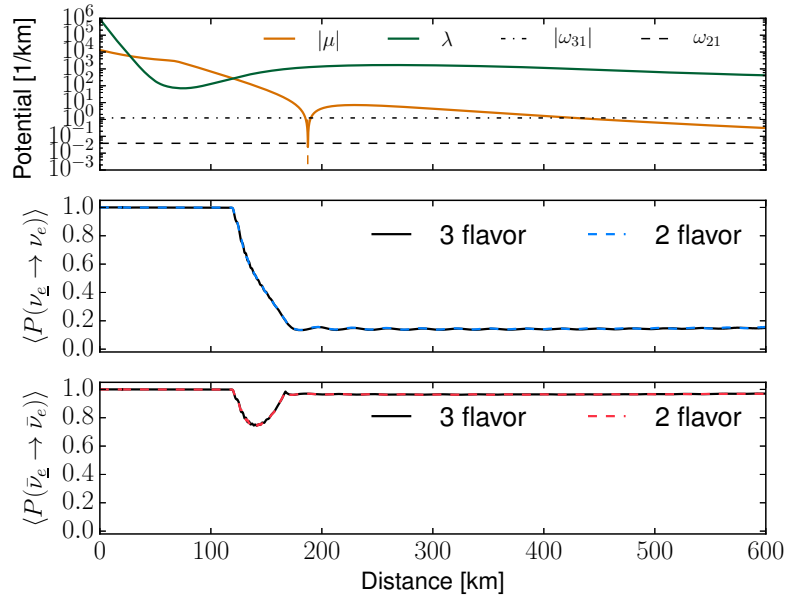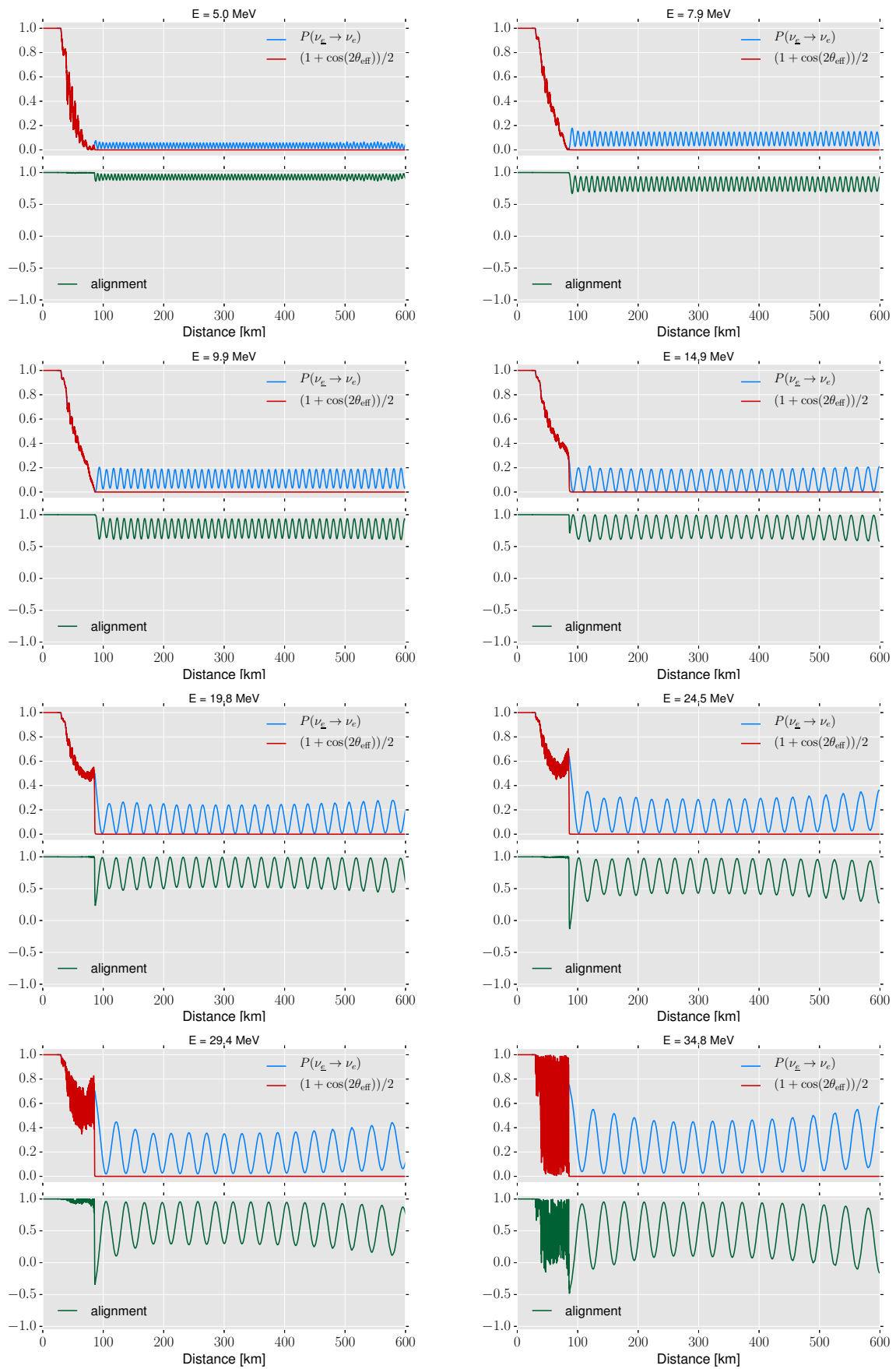
(a) Normal hierarchy
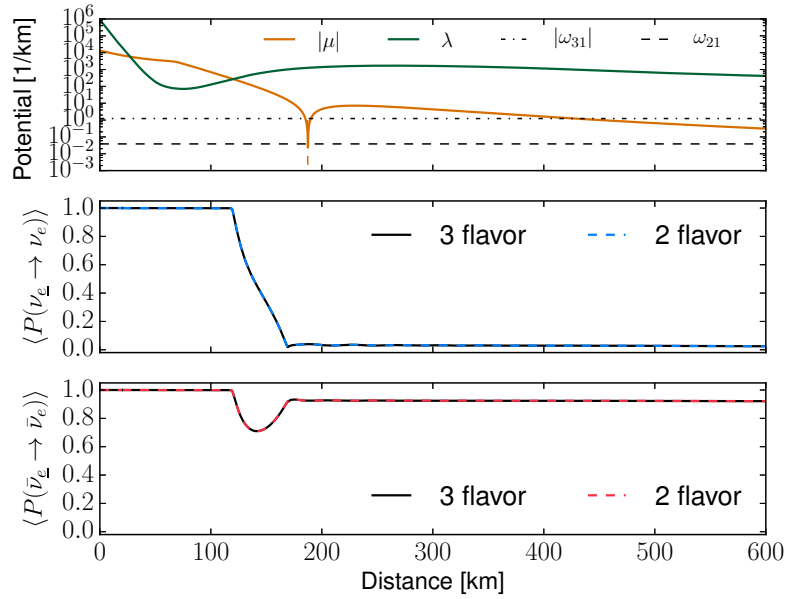
(b) Inverted Hierarchy

Figure 4.22.: Flavor evolution results along trajectory 2c: $x_0 = -35\,\mathrm{km}$, $z_0 = 25\,\mathrm{km}$, $\theta_0 = 31.1°$ in NH (a) and IH (b). We show matter potential, unoscillated neutrino self-interaction potential, and vacuum potentials (for a neutrino energy of $5\,\mathrm{MeV}$) (top panel), averaged survival probabilities for electron neutrinos (middle panel) and electron antineutrinos (bottom panel) obtained in three-flavor (solid curves) and two-flavor calculations (dashed curves).
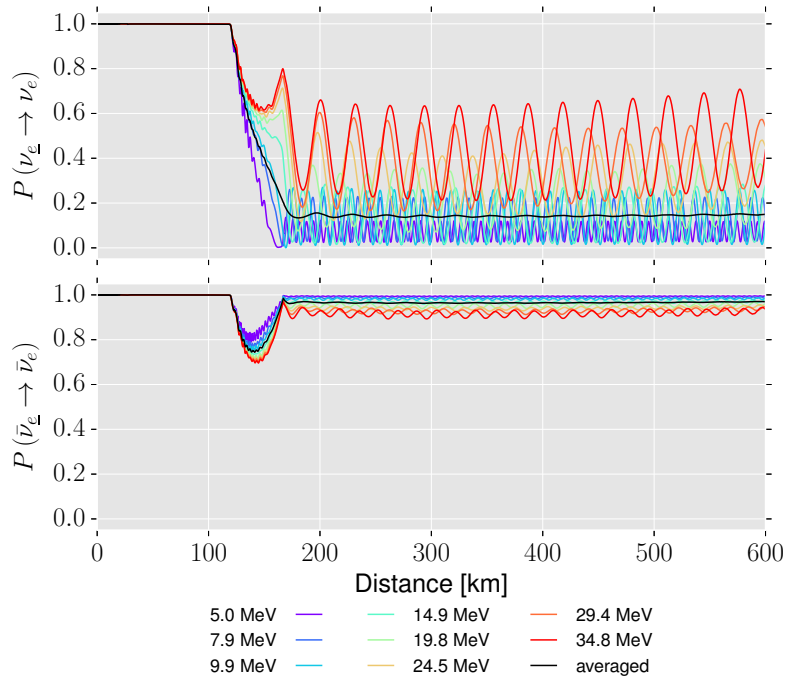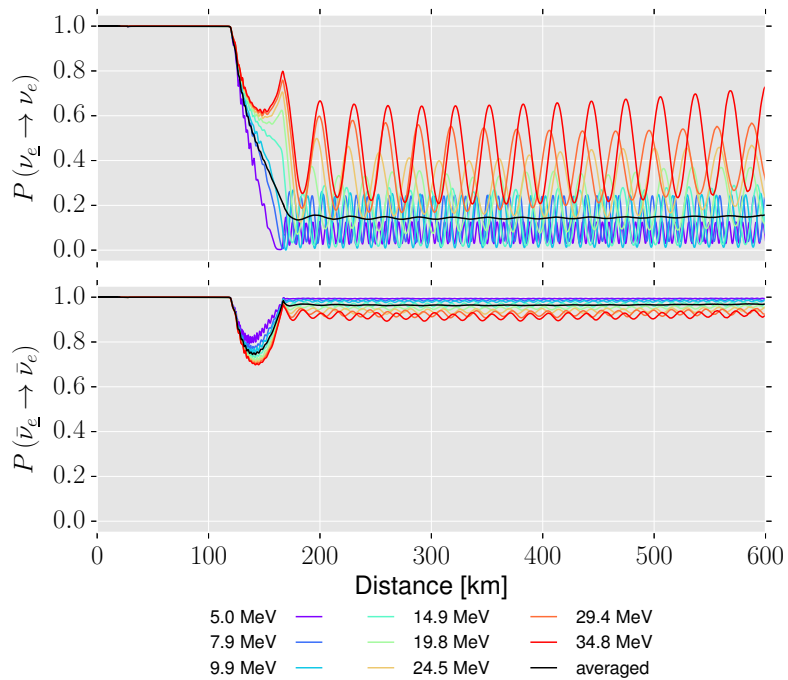
(a) 3-flavor

(b) 2-flavor

Figure 4.23.: Normal hierarchy. 2c: $x_0 = -35\,\mathrm{km}$, $z_0 = 25\,\mathrm{km}$, $\theta_0 = 31.1°$. Survival probabilities for electron neutrinos (top panels) and electron antineutrinos (bottom panels) for selected energies for the three-flavor (a) and two-flavor (b) cases.

(a) 3-flavor

(b) 2-flavor

Figure 4.24.: Inverted hierarchy. 2c: $x_0 = -35\,\text{km}$, $z_0 = 25\,\text{km}$, $\theta_0 = 31.1°$. Survival probabilities for electron neutrinos (top panels) and electron antineutrinos (bottom panels) for selected energies for the three-flavor (a) and two-flavor (b) cases.

Figure 4.25.: Normal hierarchy. 2a: $x_0 = 10\,\text{km}$, $z_0 = 30\,\text{km}$, $\theta_0 = 20.0°$. Effective mixing angle (top panels) and alignment (bottom panels) for different neutrino energies.
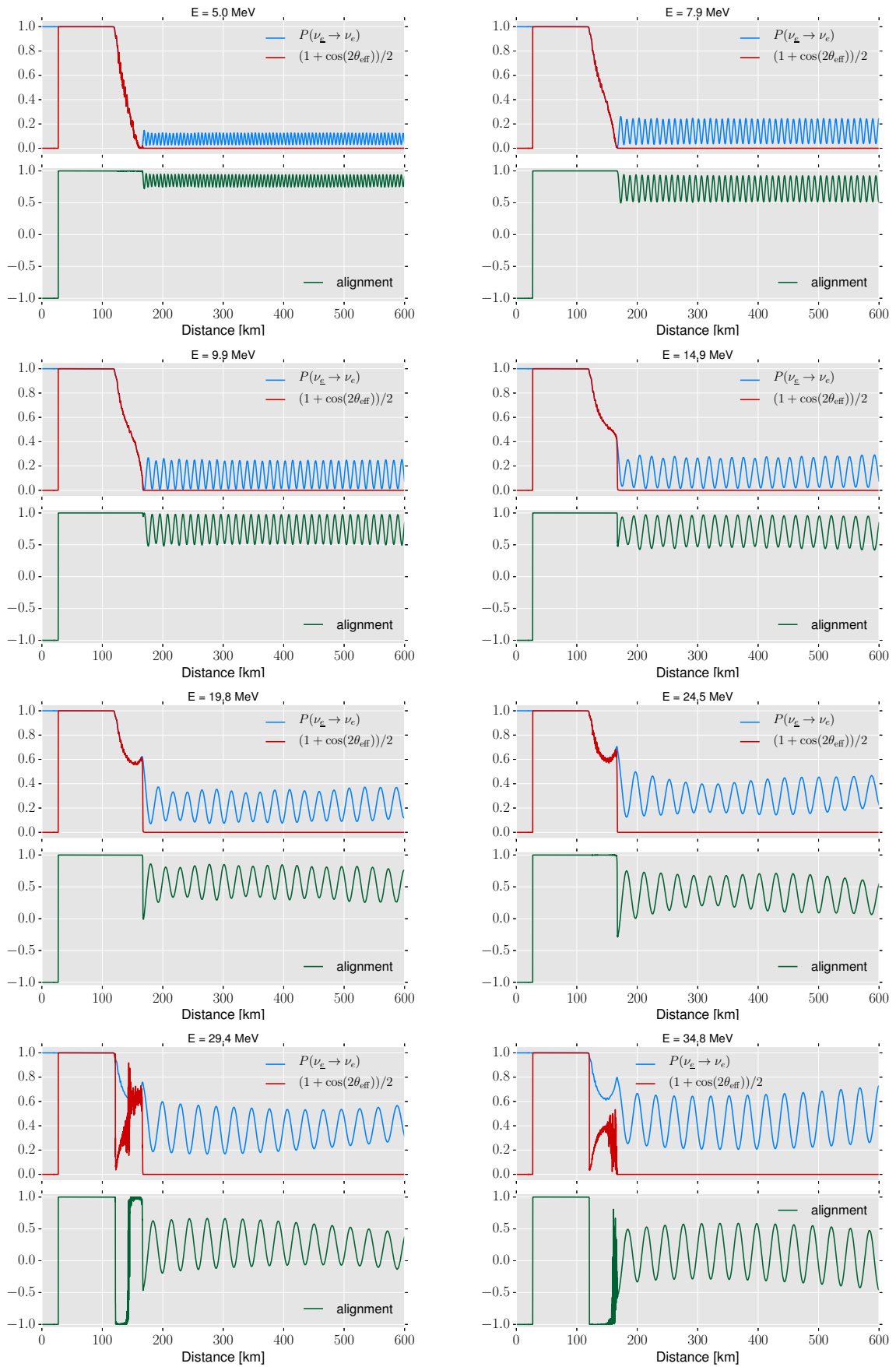
Figure 4.26.: Normal hierarchy. 2c: $x_0 = -35\,\mathrm{km}$, $z_0 = 25\,\mathrm{km}$, $\theta_0 = 31.1°$. Effective mixing angle (top panels) and alignment (bottom panels) for different neutrino energies.
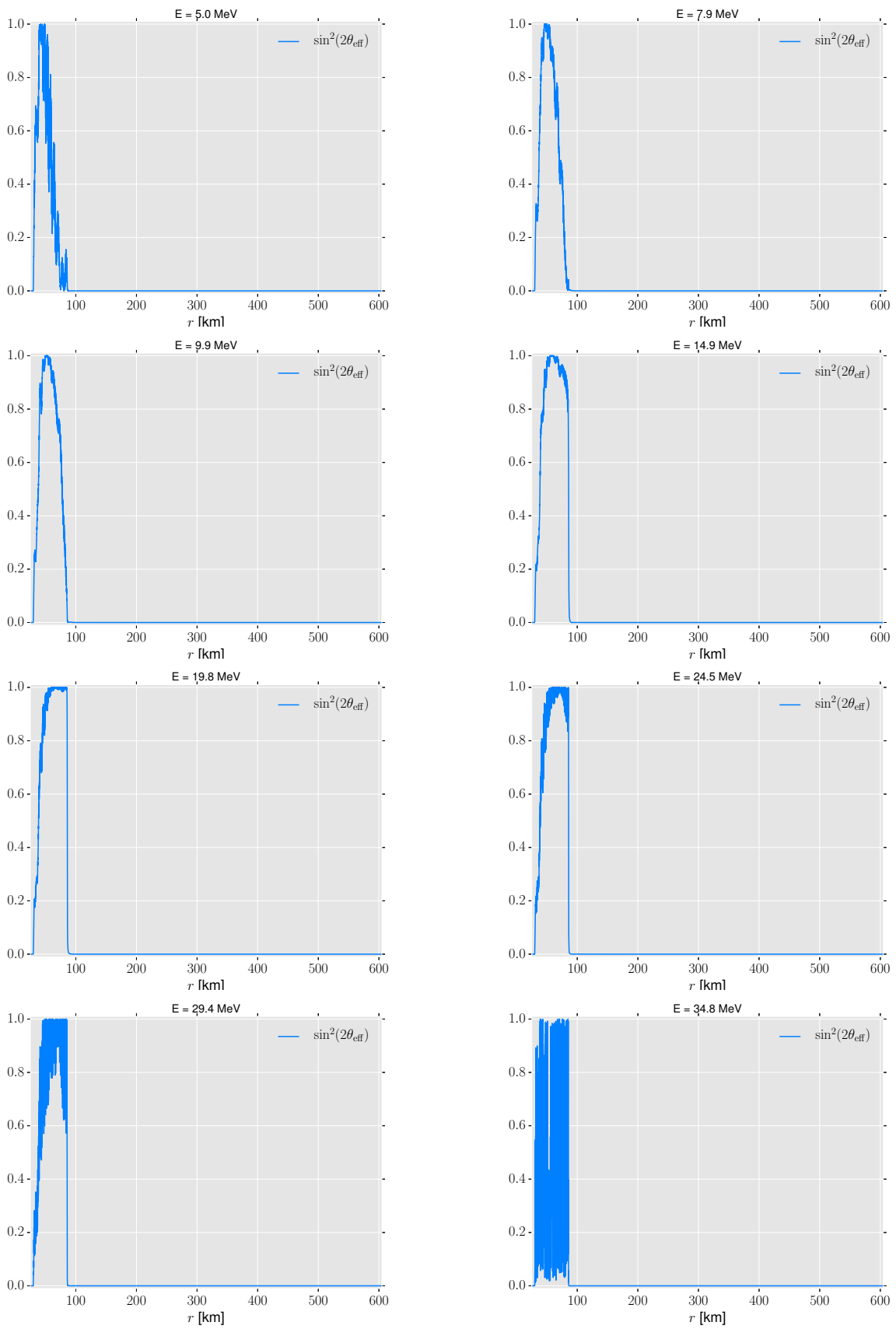
Figure 4.27.: Normal hierarchy. 2a. Effective mixing angle and resonance curve for different neutrino energies.

4.8 CP violation

The presence of CP violation in the quark sector has already been established in decays of neutral kaons in 1964 [213] (for a review, see [31]). Beside obtaining a more complete picture of elementary particles and their interactions, having a deeper knowledge on CP violation is indeed crucial for our understanding of the matter domination over antimatter in our universe as well. As first stressed by Andrei Sakharov [214] in 1966, CP violation is one necessary condition for the dynamical production of an asymmetry between matter and antimatter from an initially symmetric state (baryogenesis [215]). Since neither the standard model of particle physics nor the λCDM (Lambda cold dark matter) model, i.e., the "standard model" of Big Bang cosmology, can explain this asymmetry, extensions to present theories and/or new approaches are necessary.

A useful way to quantify CP-violation represents the so-called Jarlskog invariant J [216, 217] (see also [218, 219]) introduced via[7]

$$\mathfrak{Im}(U_{\alpha j}U_{\beta k}U_{\alpha k}^{*}U_{\beta j}^{*}) = J \sum_{\gamma \in \{e,\mu,\tau\}} \epsilon_{\alpha\beta\gamma} \sum_{l=1}^{3} \epsilon_{jkl}, \tag{4.32}$$

or

$$J = \mathfrak{Im}(U_{e1}U_{\mu 2}U_{e2}^{*}U_{\mu 1}^{*}), \tag{4.33}$$

where $\epsilon_{\alpha\beta\gamma}$ and ϵ_{jkl} denote the Levi-Civita symbol with $\epsilon_{e\mu\tau} = 1$ and $\epsilon_{123} = 1$, respectively. Note that J is independent of the parametrization of the mixing matrix and it is rephasing-invariant, i.e., phase-transformations of the form

$$U_{\alpha j}' \equiv e^{-i\eta}U_{\alpha j}e^{+i\xi}, \tag{4.34}$$

where $\xi, \eta \in \mathbb{R}$, leave J invariant.

In the standard parametrization of the mixing matrix, eq. (2.28), one finds

$$J = s_{12}c_{12}s_{23}c_{23}s_{13}c_{13}^{2} \sin \delta. \tag{4.35}$$

The latter equation shows that finding CP violation via a measurement of J requires that all mixing angles do not vanish. The invariant J will vanish in the CP-preserving cases $\delta = 0$ or $\delta = \pi$. As discussed in section 2.3, it was not clear if $\theta_{13} \neq 0$ at the time when neutrino oscillations were discovered. However, the results of the recent years suggest a finite value θ_{13} and therefore opens opportunities for searching of possible CP-violating effects in neutrino oscillation experiments.

---

[7] We employ a notation consistent for neutrino flavor mixing, but the Jarlskog invariant can be introduced for quarks as well, or more generally for any unitary (3×3)-matrix.

In case of the quark mixing matrix, the Cabibbo-Kobayashi-Maskawa (CKM) matrix [220, 221], it turns out that the values for the involved mixing angles are relatively small and the current best-fit results of the CKM elements [31] suggest a Jarlskog invariant of $J_{\text{quark}} = (3.04^{+0.21}_{-0.20}) \times 10^{-5}$. However, such a small value is not sufficient to explain the observed baryon asymmetry [44].

Instead, a possible violation of the CP symmetry in the lepton sector could offer the starting point for alternative explanations of the asymmetry and there exist various attractive theories. In the lepton sector, the current values of the mixing angles give rise to a much larger Jarlskog constant compared to the quark sector. Using the best-fit values from [31], one obtains $J \simeq -0.0291$ in the normal hierarchy and $J \simeq -0.0276$ in the inverted hierarchy case, respectively. Such values would indicate a relatively large effect if the Dirac phase turns out to be $\delta \simeq 3\pi/2$ (the currently favored value).

4.8.1 Three-flavor probabilities

In what follows, we want to derive an expression for the flavor conversion and survival probabilities in a form convenient for probing CP-violation. First we re-express eq. (2.64) in terms of the Jarlskog invariant:

$$
\begin{aligned}
P(\nu_{\underline{\alpha}} \to \nu_\beta)(E, L) = \delta_{\alpha\beta} &- 4 \sum_{k>j} \mathfrak{Re}(\mathsf{U}_{\alpha j}\mathsf{U}^*_{\alpha k}\mathsf{U}^*_{\beta j}\mathsf{U}_{\beta k}) \sin^2\left(\frac{\pi L}{L^{\text{osc}}_{kj}}\right) \\
&+ 2J \sum_\gamma \epsilon_{\alpha\beta\gamma} \sum_{k>j} \sum_l \epsilon_{jkl} \sin\left(\frac{2\pi L}{L^{\text{osc}}_{kj}}\right).
\end{aligned}
\tag{4.36}
$$

From the latter equation, it becomes obvious that the survival probabilities $P(\nu_{\underline{\alpha}} \to \nu_\alpha)$ are independent on CP violation.

Using the identity [222]

$$
\begin{aligned}
4\sin(x)\sin(y)\sin(z) = \sin(x + y - z) &+ \sin(x + z - x) \\
&+ \sin(z + x - y) - \sin(x + y + z)
\end{aligned}
\tag{4.37}
$$

with $x \equiv -\pi L/L^{\text{osc}}_{21}$, $y \equiv -\pi L/L^{\text{osc}}_{32}$, $z \equiv \pi L/L^{\text{osc}}_{31}$ one finds

$$
\sin\left(\frac{2\pi L}{L^{\text{osc}}_{21}}\right) + \sin\left(\frac{2\pi L}{L^{\text{osc}}_{32}}\right) - \sin\left(\frac{2\pi L}{L^{\text{osc}}_{31}}\right) = 4\sin\left(\frac{\pi L}{L^{\text{osc}}_{21}}\right)\sin\left(\frac{\pi L}{L^{\text{osc}}_{32}}\right)\sin\left(\frac{\pi L}{L^{\text{osc}}_{31}}\right),
\tag{4.38}
$$

which allows to turn the term involving J in eq. (4.36) into

$$2J \sum_\gamma \epsilon_{\alpha\beta\gamma} \sum_{k>j} \sum_l \epsilon_{jkl} \sin\left(\frac{2\pi L}{L_{kj}^{\text{osc}}}\right) = 2J \sum_\gamma \epsilon_{\alpha\beta\gamma} \left\{ \sin\left(\frac{2\pi L}{L_{21}^{\text{osc}}}\right) \right.$$
$$\left. + \sin\left(\frac{2\pi L}{L_{32}^{\text{osc}}}\right) - \sin\left(\frac{2\pi L}{L_{31}^{\text{osc}}}\right) \right\} \tag{4.39}$$
$$= 8J \sum_\gamma \epsilon_{\alpha\beta\gamma} \sin\left(\frac{\pi L}{L_{21}^{\text{osc}}}\right) \sin\left(\frac{\pi L}{L_{32}^{\text{osc}}}\right) \sin\left(\frac{\pi L}{L_{31}^{\text{osc}}}\right). \tag{4.40}$$

Finally, the probability assumes the form

$$P(\nu_{\underline{\alpha}} \to \nu_\beta)(E, L) = \delta_{\alpha\beta} - 4 \sum_{k>j} \Re(\mathsf{U}_{\alpha j} \mathsf{U}_{\alpha k}^* \mathsf{U}_{\beta j}^* \mathsf{U}_{\beta k}) \sin^2\left(\frac{\pi L}{L_{kj}^{\text{osc}}}\right)$$
$$+ 8J \sum_\gamma \epsilon_{\alpha\beta\gamma} \sin\left(\frac{\pi L}{L_{21}^{\text{osc}}}\right) \sin\left(\frac{\pi L}{L_{32}^{\text{osc}}}\right) \sin\left(\frac{\pi L}{L_{31}^{\text{osc}}}\right). \tag{4.41}$$

An indication for CP violation gives the difference (or asymmetry) [223]

$$\mathcal{A}_{\alpha\beta}^{\mathsf{CP}} = P(\nu_{\underline{\alpha}} \to \nu_\beta) - P(\bar{\nu}_{\underline{\alpha}} \to \bar{\nu}_\beta). \tag{4.42}$$

For antineutrinos ($P(\bar{\nu}_{\underline{\alpha}} \to \bar{\nu}_\beta)$) one needs to replace U by its complex conjugate U^* resulting in a different sign in front of the CP-violating term ($J \mapsto -J$) in eq. (4.41). The difference turns out to be

$$\mathcal{A}_{\alpha\beta}^{\mathsf{CP}} = 16J \sum_\gamma \epsilon_{\alpha\beta\gamma} \sin\left(\frac{\pi L}{L_{21}^{\text{osc}}}\right) \sin\left(\frac{\pi L}{L_{32}^{\text{osc}}}\right) \sin\left(\frac{\pi L}{L_{31}^{\text{osc}}}\right). \tag{4.43}$$

Note that if CPT invariance[8] holds, then the difference $P(\nu_{\underline{\alpha}} \to \nu_\beta) - P(\nu_{\underline{\beta}} \to \nu_\alpha)$ which is an indicator for T violation, is equal to $\mathcal{A}_{\alpha\beta}^{\mathsf{CP}}$. Therefore, $\mathcal{A}_{\alpha\beta}^{\mathsf{CP}}$ serves as a probe for the violation of the CP symmetry and T symmetry as well [223].

From the phenomenological point of view, only oscillation experiments measuring flavor transition probabilities allow to study CP or T violations. This is a crucial consequence of the CPT symmetry which demands the relation $P(\nu_{\underline{\alpha}} \to \nu_\beta) = P(\bar{\nu}_{\underline{\beta}} \to \bar{\nu}_\alpha)$, in particular one has $P(\nu_{\underline{\alpha}} \to \nu_\alpha) = P(\bar{\nu}_{\underline{\alpha}} \to \bar{\nu}_\alpha)$ [32, 39].

Also, in order to search for possible CP violation in neutrino oscillations, experiments require a sufficiently large sensitivity and for the oscillation phases one needs $2\pi L/L_{kj}^{\text{osc}} \equiv \Delta m_{kj}^2 L/(2E) \sim \mathcal{O}(1)$ for $kj \in \{21, 32, 31\}$ which allows to resolve the oscillatory behavior[9] [39]. As can be

---

[8] The invariance of physical laws under a combined transformation of charge, parity, and time-reversal is considered as a fundamental symmetry of nature. So far, no deviations from this symmetry have been observed. The validity of the CPT invariance in relativistic local quantum field theories (like the electroweak theory) is ensured by the CPT theorem (or Lüders-Pauli theorem) [224]. The individual symmetries do not need to be respected, as it is the case, e.g., in electroweak interactions.

[9] Note that averaging over the baseline distance L or the energy E will lead to $\mathcal{A}_{\alpha\beta}^{\mathsf{CP}} = 0$.

inferred from eq. (4.43), the violation of CP and T is an three-flavor effect: If one of the mass-squared differences vanish, $\mathcal{A}_{\alpha\beta}^{\text{CP}} = 0$. Long-baseline experiments with sufficiently high beam intensities like T2K, NovA, and DUNE/LBNF are promising candidates for probing CP violation.

So far, we based our discussion on the vacuum case. However, in neutrino oscillations the presence of matter can mimic violations of the C, CP, and CPT symmetries, even if the effective neutrino mass matrix conserves these symmetries [225–227]. As a consequence, experimental studies need to be capable of distinguishing between matter-induced (also called extrinsic or fake) and fundamental (also called intrinsic) violations of CP.

Still, it is possible to find relations that are useful for practical applications. Due to the unitarity of the mixing matrix, the following sum rules (which expresses probability conservation) hold:

$$\sum_{\beta=e,\mu,\tau} P(\nu_{\underline{\alpha}} \to \nu_\beta) = 1, \tag{4.44}$$

$$\sum_{\alpha=e,\mu,\tau} P(\nu_{\underline{\alpha}} \to \nu_\beta) = 1. \tag{4.45}$$

In particular, it follows that the sum of the ν_e appearance probabilities can be expresses by the ν_e-survival probability

$$P(\nu_{\underline{\mu}} \to \nu_e) + P(\nu_{\underline{\tau}} \to \nu_e) = 1 - P(\nu_{\underline{e}} \to \nu_e). \tag{4.46}$$

Note that if there is a violation of the T-symmetry (intrinsic or matter-induced), we have $P(\nu_{\underline{\alpha}} \to \nu_\beta) \neq P(\nu_{\underline{\beta}} \to \nu_\alpha)$ ($\alpha \neq \beta$), but the sum rules above still hold.

In a medium consisting of ordinary matter, one can show [228] that the ν_e survival probability and the ν_e appearance probability do not depend on δ, i.e., the relations

$$P(\nu_{\underline{e}} \to \nu_e)(\delta \neq 0) = P(\nu_{\underline{e}} \to \nu_e)(\delta = 0) \tag{4.47}$$

$$P(\nu_{\underline{\mu}} \to \nu_e)(\delta \neq 0) + P(\nu_{\underline{\tau}} \to \nu_e)(\delta \neq 0) = P(\nu_{\underline{\mu}} \to \nu_e)(\delta = 0)$$
$$+ P(\nu_{\underline{\tau}} \to \nu_e)(\delta = 0), \tag{4.48}$$

hold as in the vacuum case, if the ν_μ and ν_τ interactions with matter are not different. Furthermore, it has been demonstrated [229] that the relations, eqs. (4.47) and (4.48), are valid if neutrino self-interactions are involved as long as the initial fluxes for ν_μ and ν_τ are the same.

In the following section, we want to give a first exploration of CP-violation in BNS mergers. We study the effect of the Dirac phase δ on the neutrino flavor evolution and discuss the impact on probabilities and neutrino fluxes by varying δ over a set of different values.

4.8.2 Impact of the Dirac CP-violating phase

In this section we want to perform a first investigation on the possibility of CP violation by studying a non-vanishing Dirac-phase δ. We show that it can indeed induce modifications of the neutrino flavor evolution and of the interaction rates on neutrons and protons that determine the election fraction.

To study the impact of a non-vanishing Dirac phase δ, we want the relations, shown in eqs. (4.47) and (4.48), to become sensitive on δ. As outlined in the previous section 4.8.1, this can be achieved by using different fluxes for ν_μ and ν_τ and/or by including loop corrections for the corresponding matter potentials. For the latter, we consider the effective neutrino-matter potential

$$\mathsf{H}_{\mathrm{matt}}(r) = \sqrt{2}\mathsf{G}_{\mathrm{F}}n_{\mathrm{b}}(r)\mathrm{diag}[Y_e(r), 0, Y_\tau^{\mathrm{eff}}(r)], \tag{4.49}$$

where $n_{\mathrm{b}} = \rho_{\mathrm{matt}}/m_{\mathrm{u}}$ is the baryon number density, determined by the matter density ρ_{matt}, Y_e denotes the electron fraction and Y_τ^{eff} is the effective tau lepton fraction [230]

$$Y_\tau^{\mathrm{eff}} = \frac{3\sqrt{2}\mathsf{G}_{\mathrm{F}}m_\tau^2}{(2\pi)^2}\left[\ln\left(\frac{m_W^2}{m_\tau^2}\right) - 1 + \frac{Y_n}{3}\right] \tag{4.50}$$

due to one-loop radiative corrections leading to a shift in the $\nu_\mu - \nu_\tau$ energy splitting. In the latter expression, $m_W \approx 80.4\,\mathrm{GeV}$ and $m_\tau \approx 1.8\,\mathrm{GeV}$ denote the masses of the W boson and τ lepton, respectively.

In an electrically neutral medium, the neutron fraction can be expressed by the electron fraction Y_e, i.e., $Y_n = 1 - Y_e$, since $n_p = n_e$. This allows us to write:

$$Y_\tau^{\mathrm{eff}} = \frac{3\sqrt{2}\mathsf{G}_{\mathrm{F}}m_\tau^2}{(2\pi)^2}\left[\ln\left(\frac{m_W^2}{m_\tau^2}\right) - \frac{2}{3} - \frac{Y_e}{3}\right], \tag{4.51}$$

$$\approx 2.8 \times 10^{-5}\left(1 - \frac{Y_e}{21.0}\right). \tag{4.52}$$

Note that the term proportional to Y_e provides only a correction at the level of a few percent.

The quantitative estimates performed so far in the context of core-collapse supernovae show that CP violating effects are at the level of a few percent in presence of radiative corrections [228, 229], and are larger when neutrino magnetic moments are considered [231].

In our numerical calculations, we vary the CP-violating phase $\delta \in \{0, \frac{\pi}{4}, \frac{\pi}{3}, \frac{3\pi}{2}, \pi\}$, where the currently favored value corresponds to $\delta \simeq 3\pi/2$, but still lacks a sufficient statistical significance.

Besides electron neutrino survival probabilities as function of distance for four different neutrino energies, we compute fluxes of neutrinos with flavor α,

$$\mathcal{F}_{\nu_\alpha}(\delta, E, r) = \sum_{\beta=e,\mu,\tau} j_{\nu_\beta}(E) P(\nu_{\underline{\beta}} \to \nu_\alpha)(\delta, E, r), \tag{4.53}$$

where $j_{\nu_\beta}(E)$ denotes the initial flux eq. (4.18). Like in [228, 229], we also show the flux ratios $\mathcal{F}_{\nu_\alpha}(\delta, E, r)/\mathcal{F}_{\nu_\alpha}(\delta = 0, E, r)$ as function of the neutrino energy at two different distances.

Thereby we study three cases:

1. $Y_\tau^{\text{eff}} \neq 0$ and equal initial fluxes for ν_μ and ν_τ,

2. $Y_\tau^{\text{eff}} \neq 0$ and different initial fluxes for ν_μ and ν_τ: $j_{\nu_{\underline{\tau}}}(E) = 1.01\, j_{\nu_{\underline{\mu}}}(E)$,

3. $Y_\tau^{\text{eff}} = 0$ and equal initial fluxes for ν_μ and ν_τ: $j_{\nu_{\underline{\tau}}}(E) = 1.01\, j_{\nu_{\underline{\mu}}}(E)$,

where in case of different initial fluxes we changed the ν_τ luminosity by a small amount, $L_{\nu_{\underline{\tau}}} = 1.01\, L_{\nu_{\underline{\mu}}}$, and apply the same change onto the corresponding antineutrino quantity ($L_{\bar{\nu}_\tau}$).

In figures 4.28, 4.32, and 4.36 we present our results on the survival probabilities for ν_e and $\bar{\nu}_e$ for both mass hierarchies. It turns out that in all cases a similar picture emerges. In both mass hierarchies the energy-dependent survival probabilities of ν_e and $\bar{\nu}_e$ show almost no change or only very small differences in form of small shifts of the probabilities with respect to the case of a vanishing Dirac phase ($\delta = 0$). In scenario 2 above where we include radiative corrections and a rescaling of the ν_τ luminosities, we encounter the largest shifts for $P(\nu_{\underline{e}} \to \nu_e)$ in the normal mass hierarchy.

For the flux ratios at a distance of 500 km, shown in figures 4.29, 4.33, and 4.37, some differences are present in case of very low and high neutrino energies. The largest impact is found in the normal mass hierarchy for $\mathcal{F}_{\nu_e}$. In particular in the second case, the ν_e-fluxes becomes strongly enhanced for $\delta = 3\pi/2$. But even in the third case, where we only introduced a small difference between the ν_μ and ν_τ fluxes, we can observe an maximal effect at the level of $\mathcal{O}(10)\%$ in the flux ratios. This is reasonable if we keep in mind that the presence of the neutrino self-interaction potential and the non-linearity of the problem can lead to an enhancement of the CP violating effects as first demonstrated in [229] in the context of core-collapse supernovae. Since shifts can result in a huge effect when plotting ratios, we also show the fluxes (not ratios) next to each other in figures 4.30, 4.34, and 4.38 for $\delta = 0$ and $\delta = 3\pi/2$. From these plots the modifications due to a non-trivial CP phase seem to be only minor.

As can be seen from the flux ratios, the results also show a sensitivity on the chosen value for the Dirac phase δ that is very different in each of the three cases. In addition, we encounter a hierarchy dependence that still needs to be understood.

Finally, in all cases the differential capture rate ratios, presented in figures 4.31, 4.35, 4.39, remain practically unaffected. The maximal effect ($\lesssim 3\%$) shows up in case of including radiative corrections along with the luminosity rescaling.

From the theory point of view, we still need to understand the energy dependence[10] of our results. On the other hand, it is difficult to observe such energy-dependent effects in experiments. While the low energy effects appear in a narrow energy range requiring a fine energy resolution of the detector, the features at higher energies appear at a broader range of neutrino energies. However, we saw that even if we change the ν_τ fluxes by only 1%, the outcome can be very different. Regarding this sensitivity on the initial fluxes and keeping in mind the large experimental uncertainties, a measurement appears to be impractical at the present stage. Furthermore, the statistics is rather poor when studying neutrinos from astrophysical sources other than the Sun.

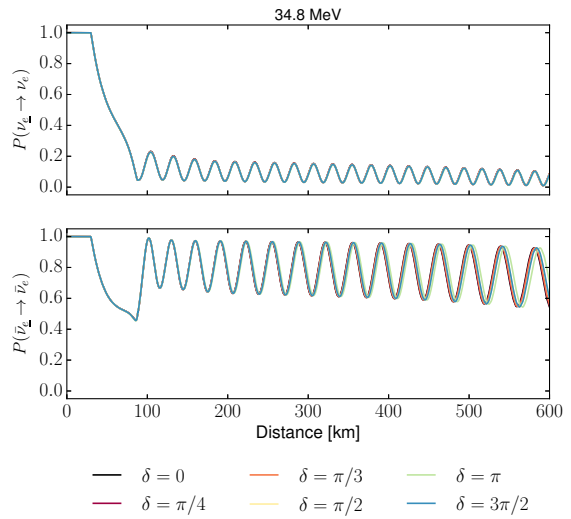[10] Note that such a dependence was already observed in the context of SNe [229].
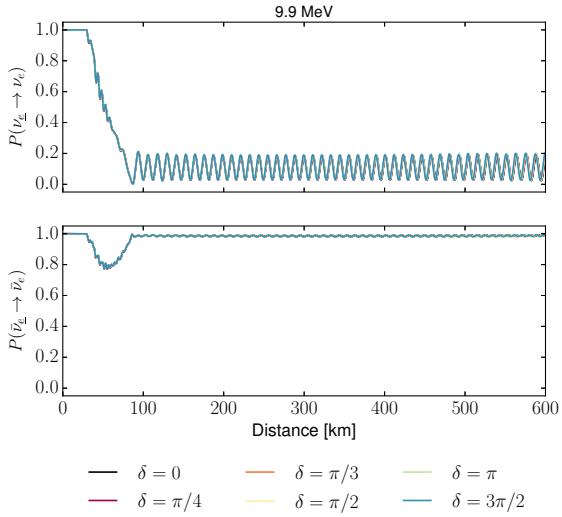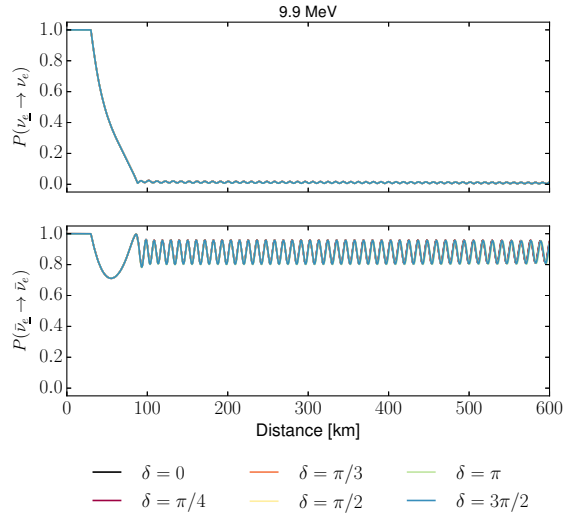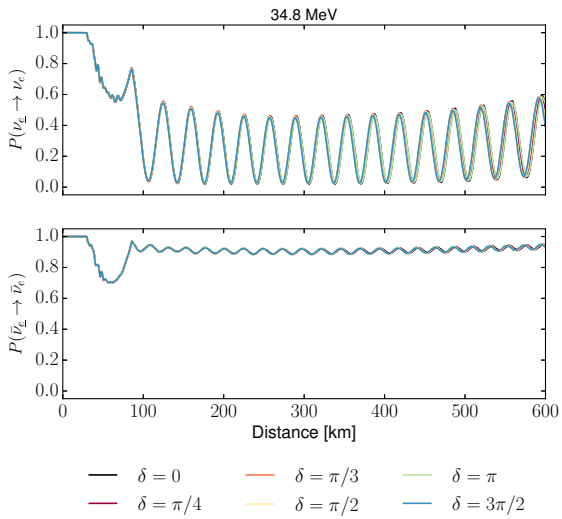
Figure 4.28.: Electron neutrino survival probabilities for different values of δ as function of distance for different energies in normal (left) and inverted hierarchy (right panels). The results are obtained with $Y_\tau^{\text{eff}} \neq 0$ and equal initial fluxes for ν_μ and ν_τ.
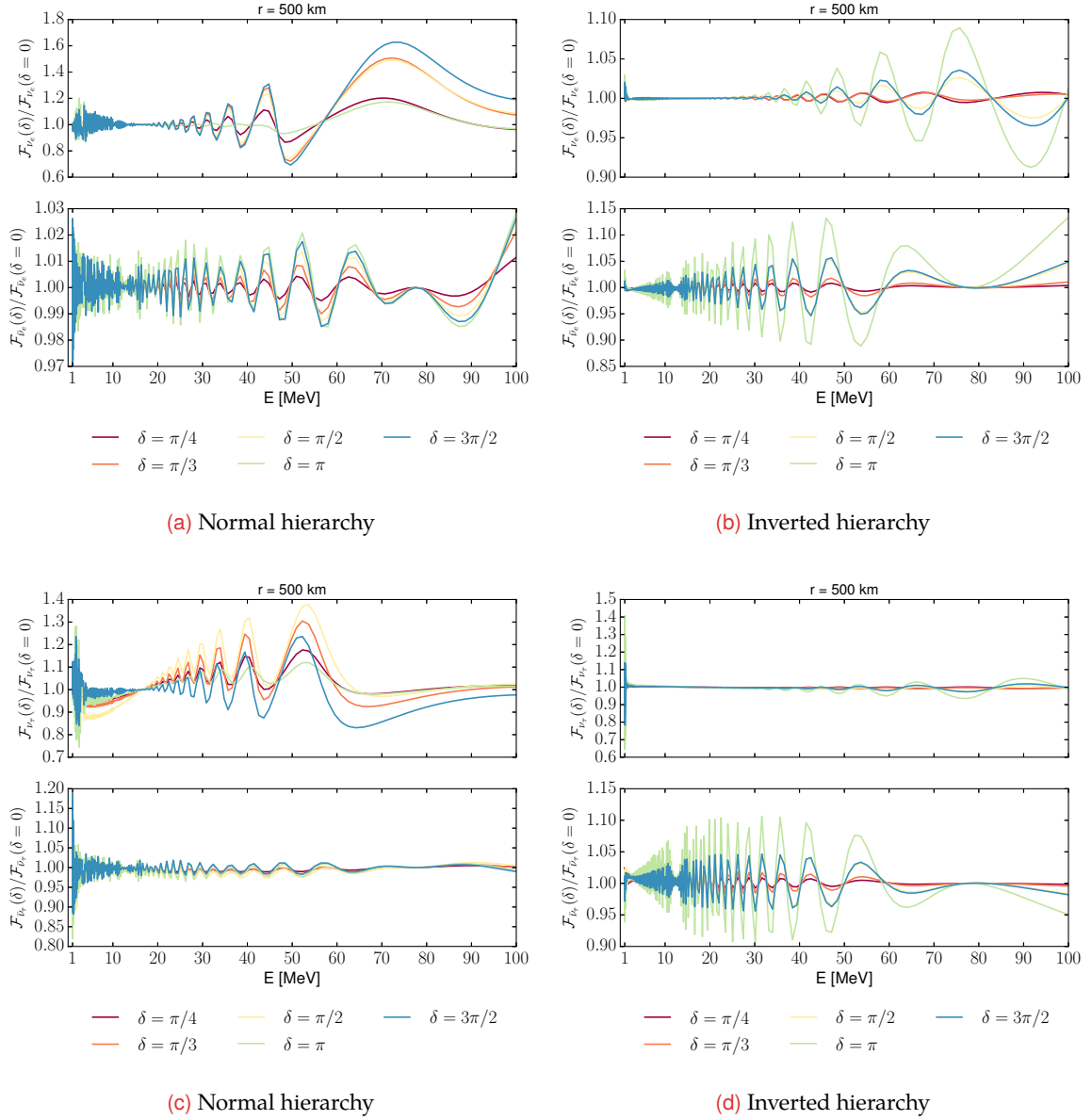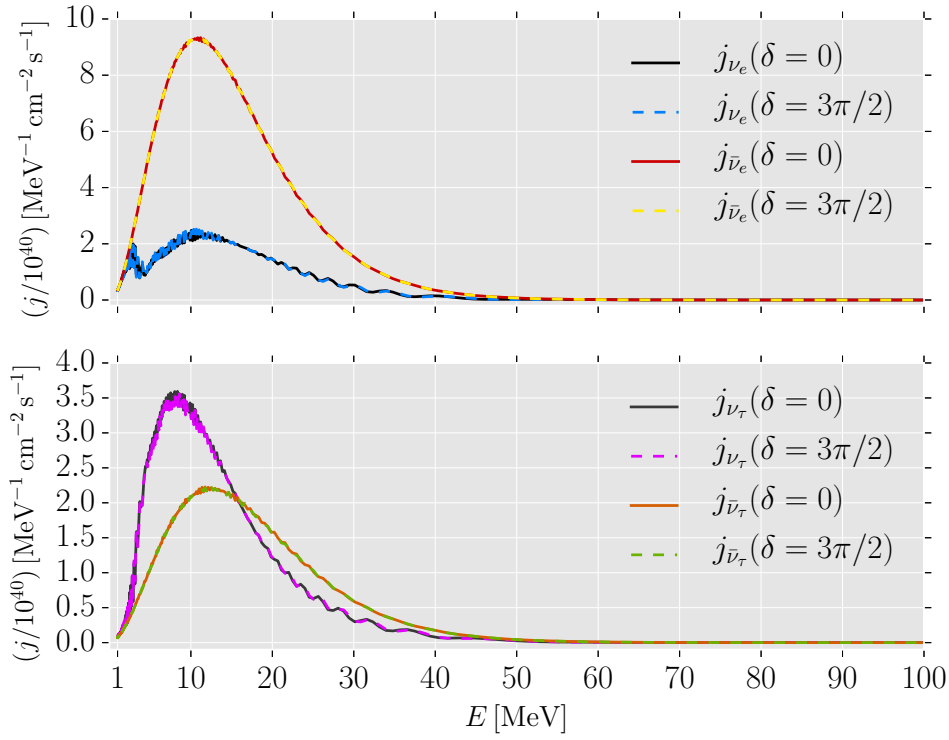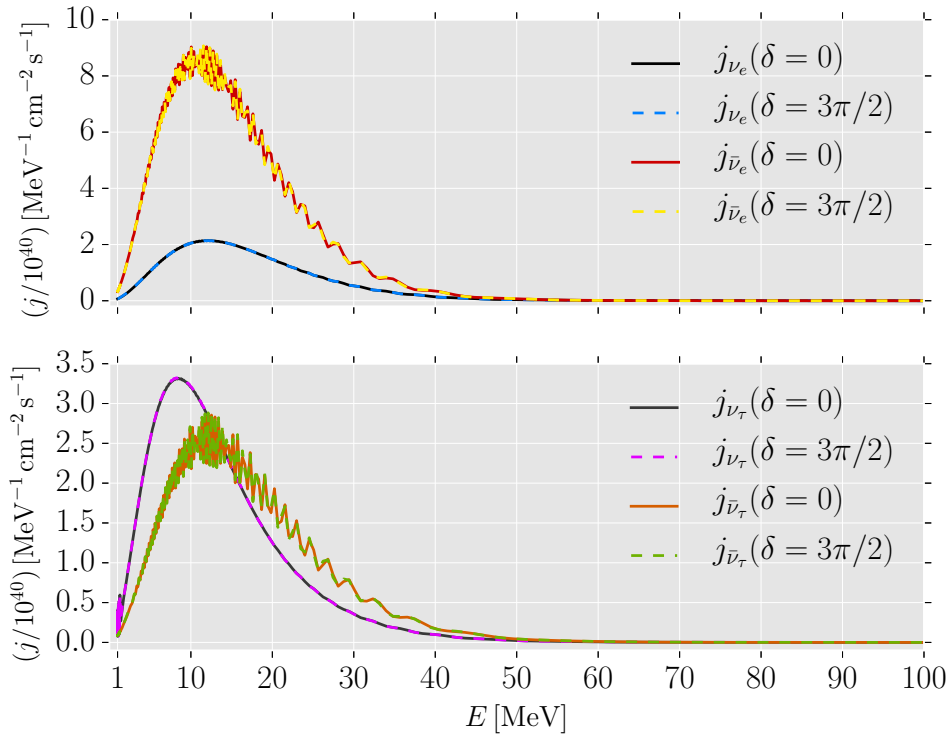
Figure 4.29.: Ratios of fluxes for $\delta \neq 0$ over $\delta = 0$ for ν_e and $\bar{\nu}_e$ (upper panel) and ν_τ and $\bar{\nu}_\tau$ (lower panel) as function of neutrino energy at $500\,\mathrm{km}$. The results are obtained with $Y_\tau^{\mathrm{eff}} \neq 0$ and equal initial fluxes for ν_μ and ν_τ.

(a) Normal hierarchy

(b) Inverted hierarchy

Figure 4.30.: Fluxes for $\delta = 0$ and $\delta = 3\pi/2$ for ν_e and $\bar{\nu}_e$ (upper panel) and ν_τ and $\bar{\nu}_\tau$ (lower panel) as function of neutrino energy at $500\,\mathrm{km}$. Figure (a) corresponds to the normal hierarchy case while in (b) shows the results obtained in the inverted hierarchy. The results are obtained with $\Upsilon_\tau^{\mathrm{eff}} \neq 0$ and equal initial fluxes for ν_μ and ν_τ.

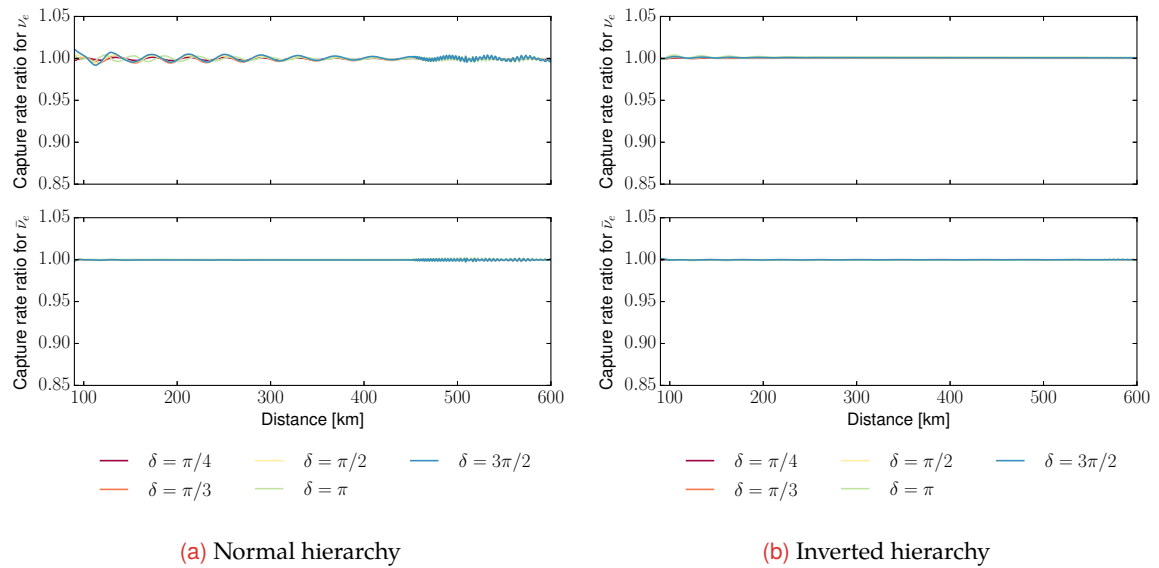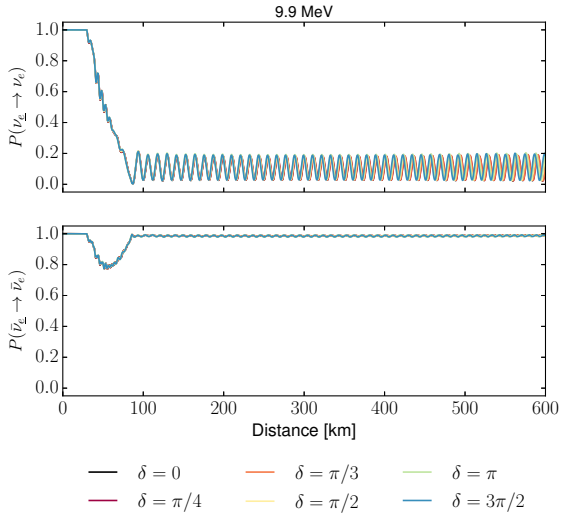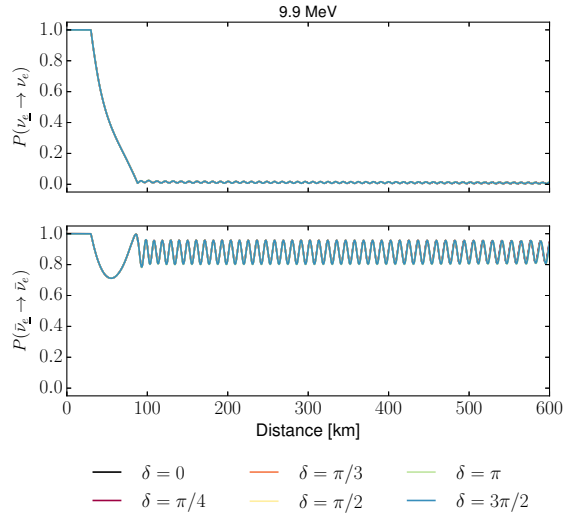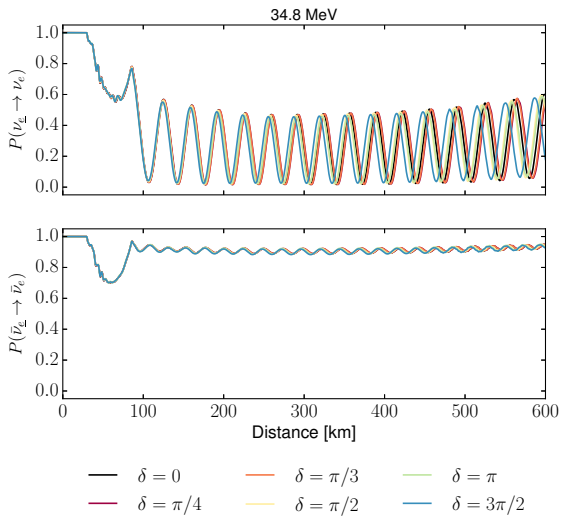(a) Normal hierarchy

(b) Inverted hierarchy

Figure 4.31.: Ratios of capture rate ratios for different values of δ as function of distance for different energies. The results are obtained with $Y_\tau^{\mathrm{eff}} \neq 0$ and equal initial fluxes for ν_μ and ν_τ.
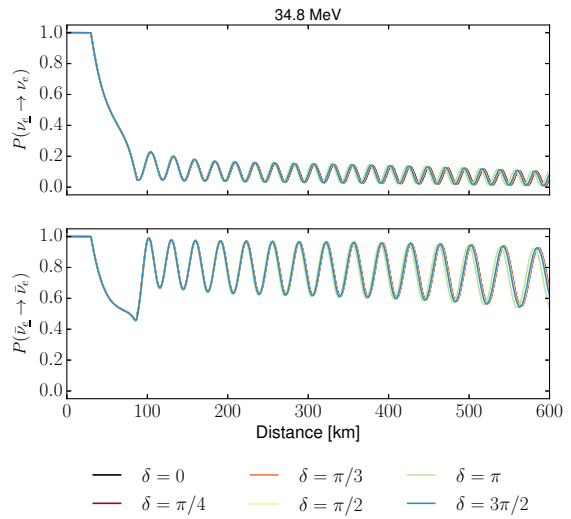
(a) Normal hierarchy

(b) Inverted hierarchy

(c) Normal hierarchy

(d) Inverted hierarchy

Figure 4.32.: Electron neutrino survival probabilities for different values of δ as function of distance for different energies in normal (left) and inverted hierarchy (right panels). The results are obtained with $Y_\tau^{\text{eff}} \neq 0$ and different initial fluxes for ν_μ and ν_τ.

(a) Normal hierarchy   (b) Inverted hierarchy

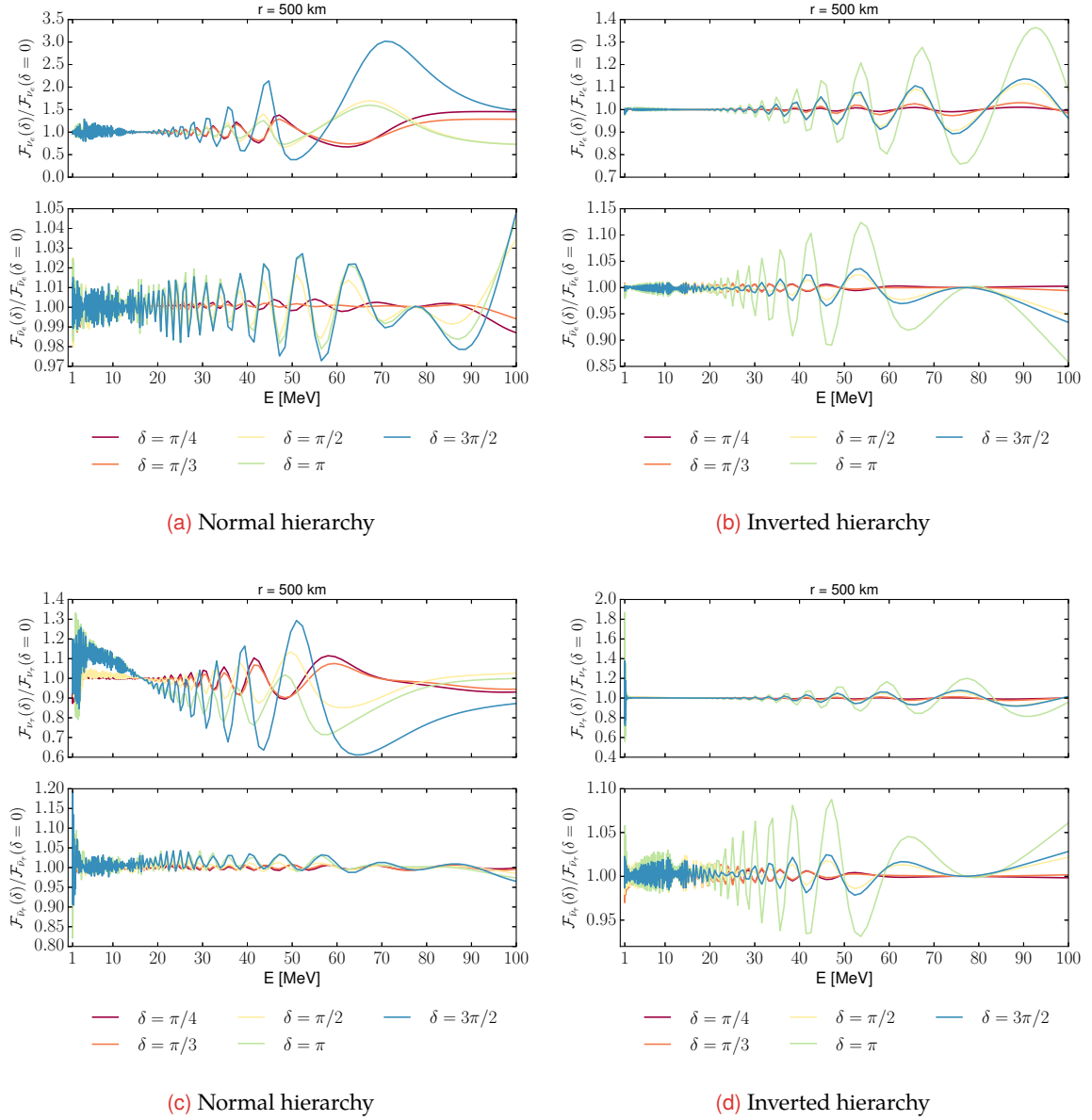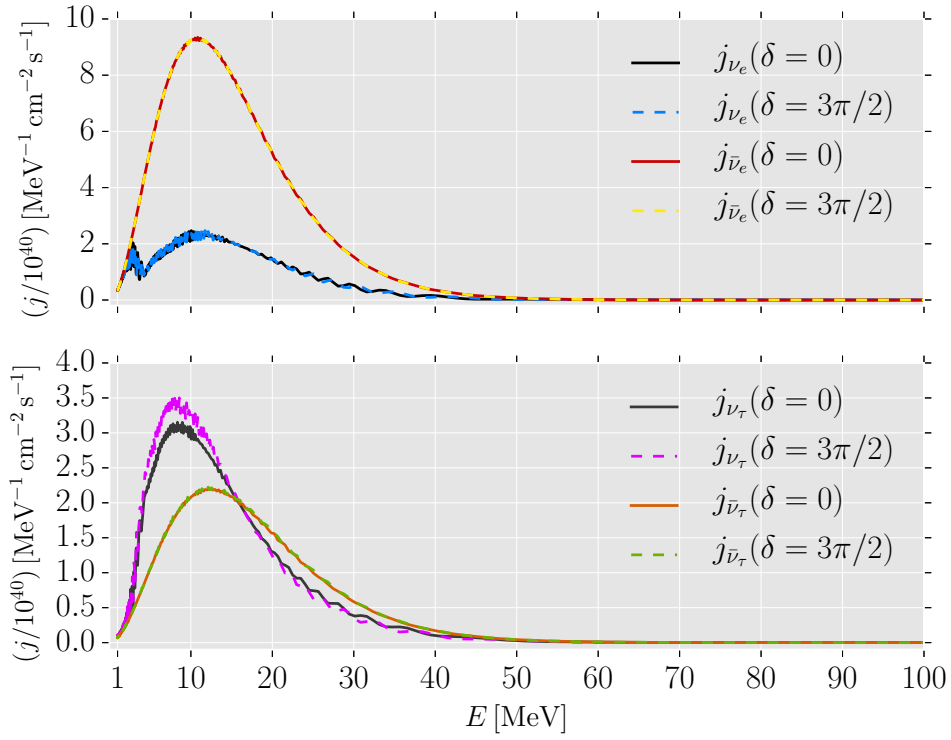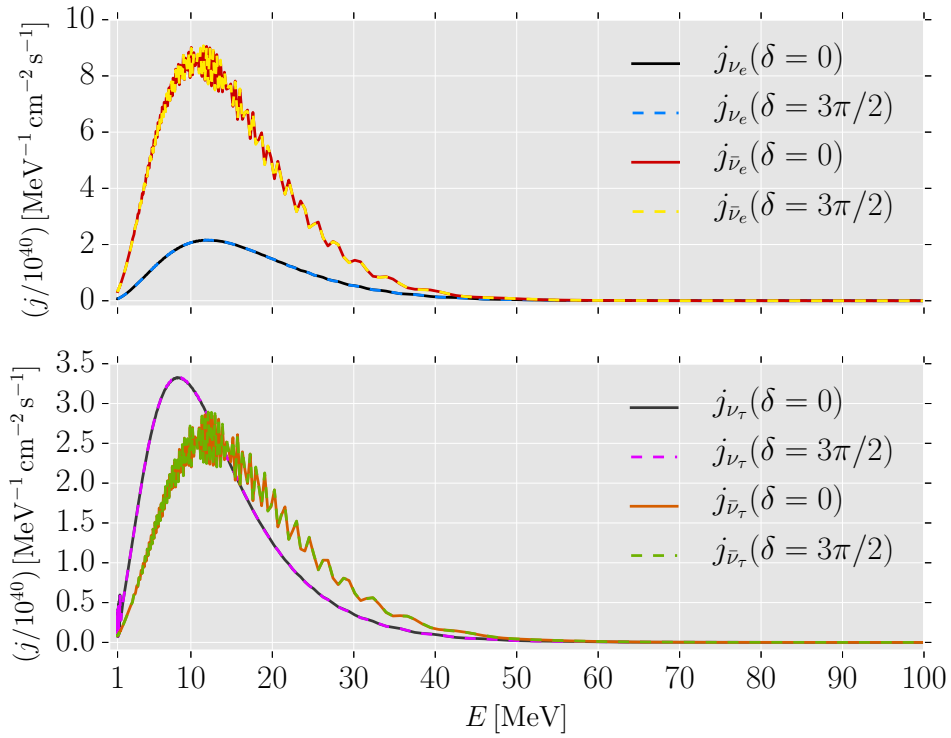(c) Normal hierarchy   (d) Inverted hierarchy

Figure 4.33.: Ratios of fluxes for $\delta \neq 0$ over $\delta = 0$ for ν_e and $\bar{\nu}_e$ (upper) and ν_τ and $\bar{\nu}_\tau$ (lower panels) as function of neutrino energy at $500\,\mathrm{km}$. The results are obtained with $Y_\tau^{\mathrm{eff}} \neq 0$ and different initial fluxes for ν_μ and ν_τ.

(a) Normal hierarchy

(b) Inverted hierarchy

Figure 4.34.: Fluxes for $\delta = 0$ and $\delta = 3\pi/2$ for ν_e and $\bar{\nu}_e$ (upper panel) and ν_τ and $\bar{\nu}_\tau$ (lower panel) as function of neutrino energy at $500\,\mathrm{km}$. Figure (a) corresponds to the normal hierarchy case while in (b) shows the results obtained in the inverted hierarchy. The results are obtained with $Y_\tau^{\mathrm{eff}} \neq 0$ and different initial fluxes for ν_μ and ν_τ.

(a) Normal hierarchy

(b) Inverted hierarchy

Figure 4.35.: Ratios of capture rate ratios for different values of δ as function of distance for different energies. The results are obtained with $Y_\tau^{\text{eff}} \neq 0$ and different initial fluxes for ν_μ and ν_τ.
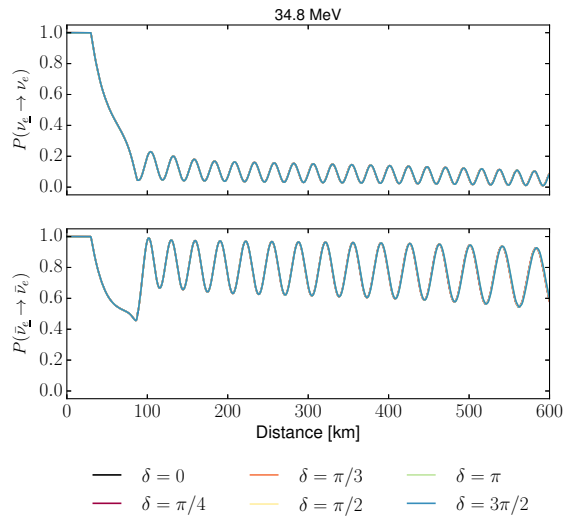
Figure 4.36.: Electron neutrino survival probabilities for different values of δ as function of distance for different energies in normal (left) and inverted hierarchy (right panels). The results are obtained with $Y_\tau^{\mathrm{eff}} = 0$ and different initial fluxes for ν_μ and ν_τ.

(a) Normal hierarchy

(b) Inverted hierarchy

(c) Normal hierarchy

(d) Inverted hierarchy
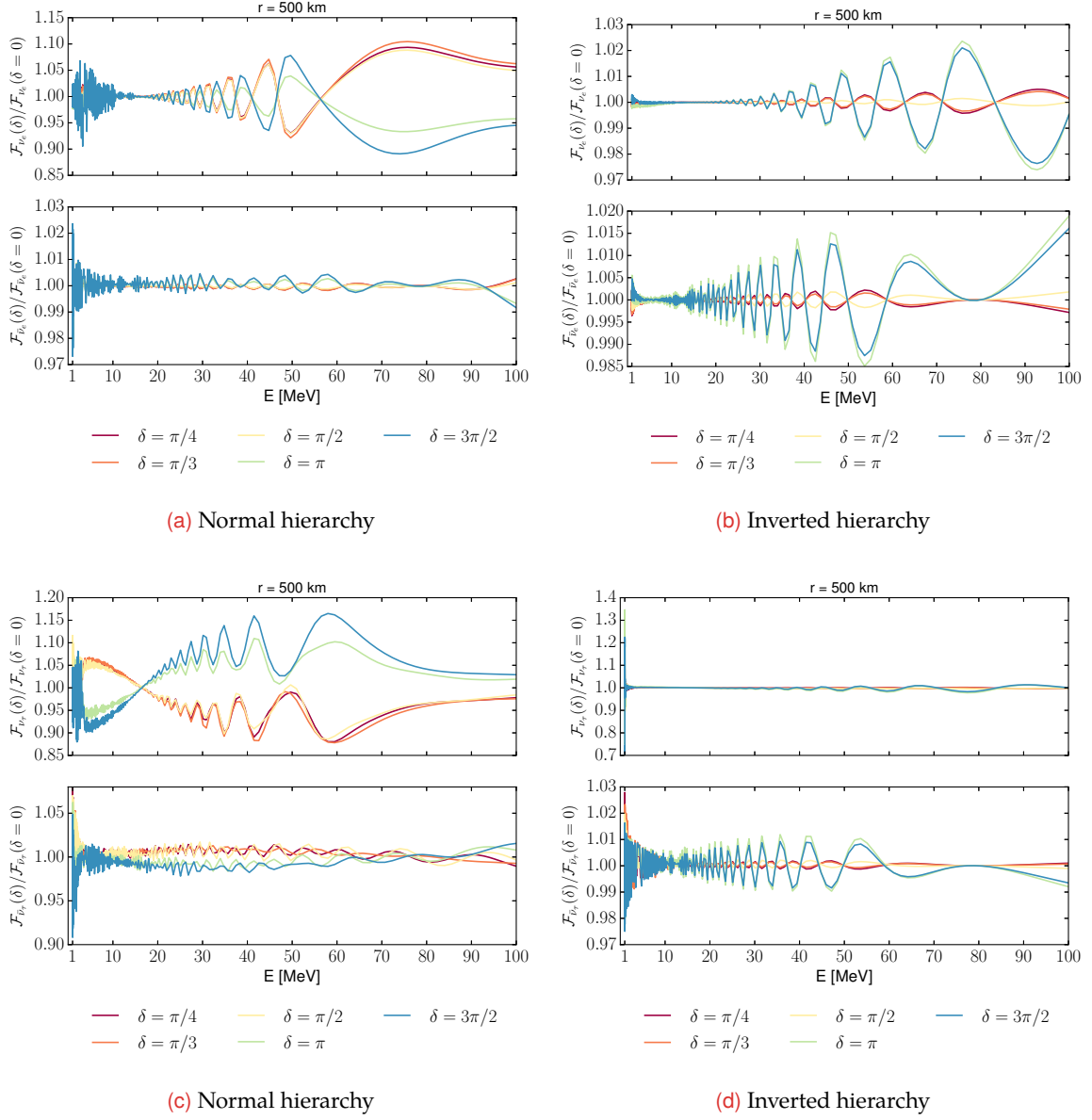
Figure 4.37.: Ratios of fluxes for $\delta \neq 0$ over $\delta = 0$ for ν_e and $\bar{\nu}_e$ (upper) and ν_τ and $\bar{\nu}_\tau$ (lower panels) as function of neutrino energy at $500\,\mathrm{km}$. The results are obtained with $Y_\tau^{\mathrm{eff}} = 0$ and different initial fluxes for ν_μ and ν_τ.
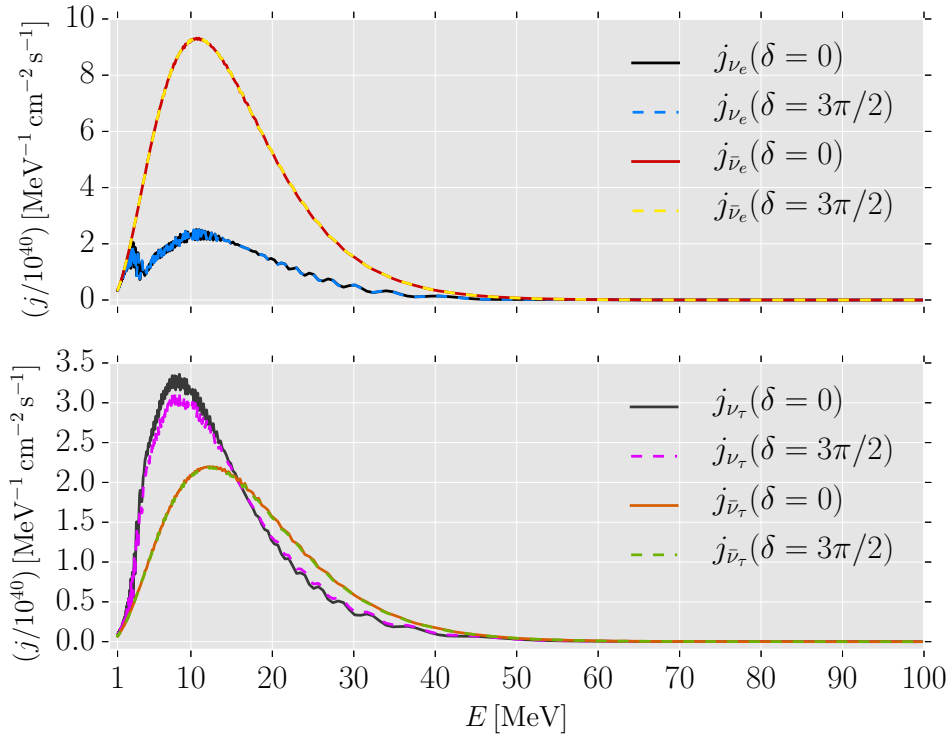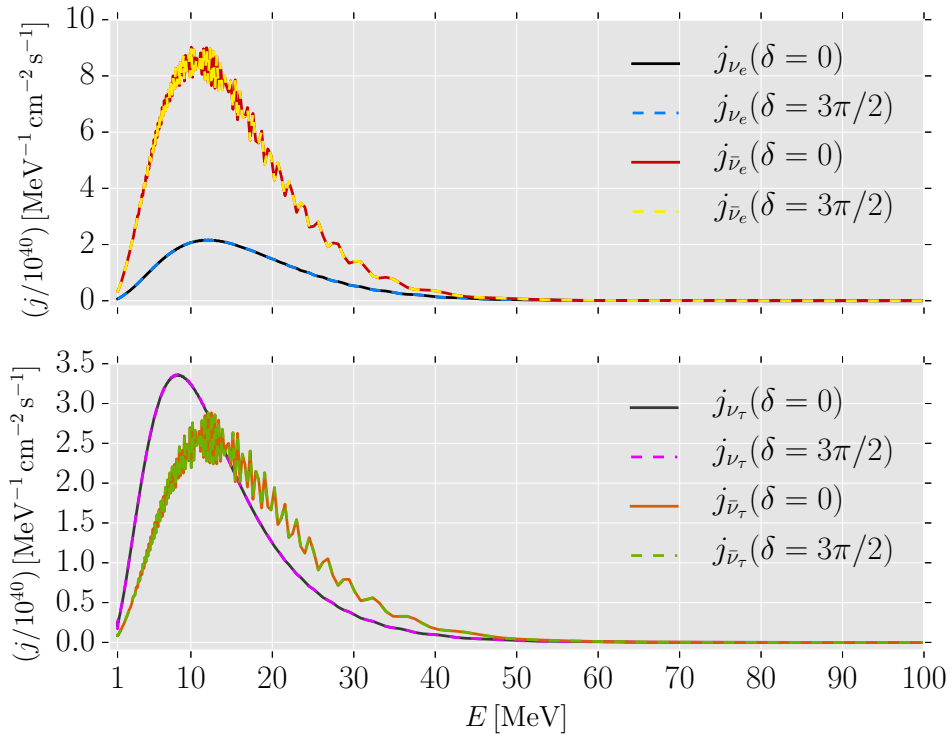
(a) Normal hierarchy

(b) Inverted hierarchy

Figure 4.38.: Fluxes for $\delta = 0$ and $\delta = 3\pi/2$ for ν_e and $\bar{\nu}_e$ (upper panel) and ν_τ and $\bar{\nu}_\tau$ (lower panel) as function of neutrino energy at $500\,\mathrm{km}$. Figure (a) corresponds to the normal hierarchy case while in (b) shows the results obtained in the inverted hierarchy. The results are obtained with $Y_\tau^{\mathrm{eff}} = 0$ and different initial fluxes for ν_μ and ν_τ.
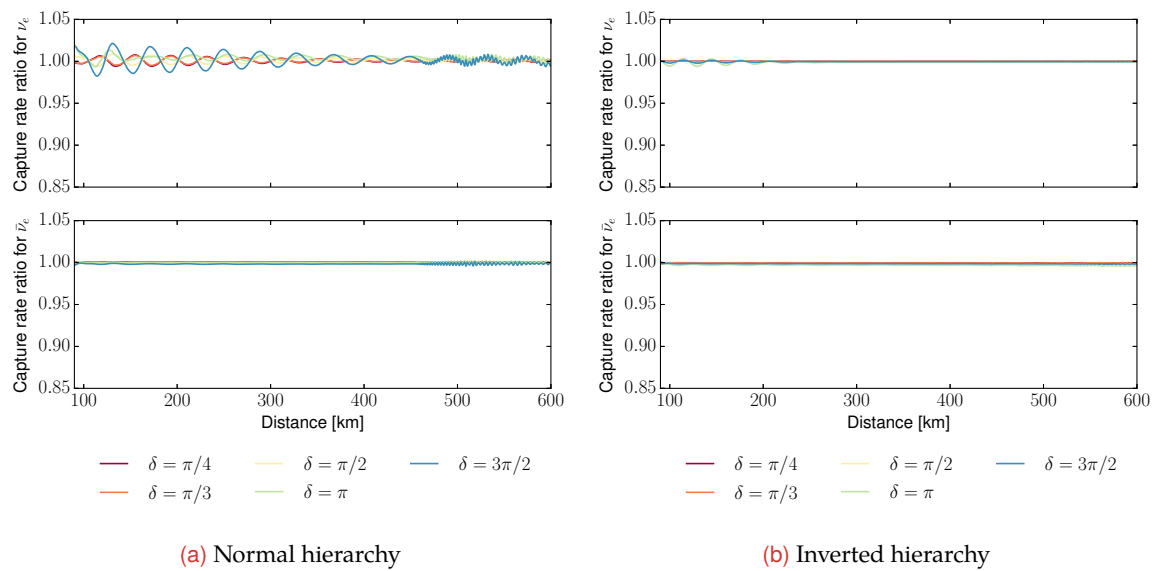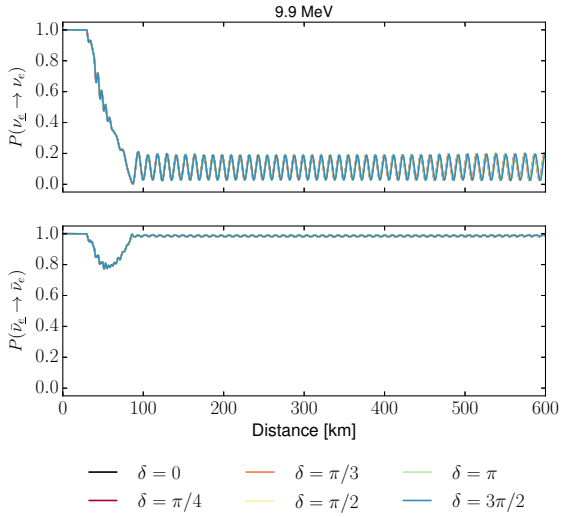
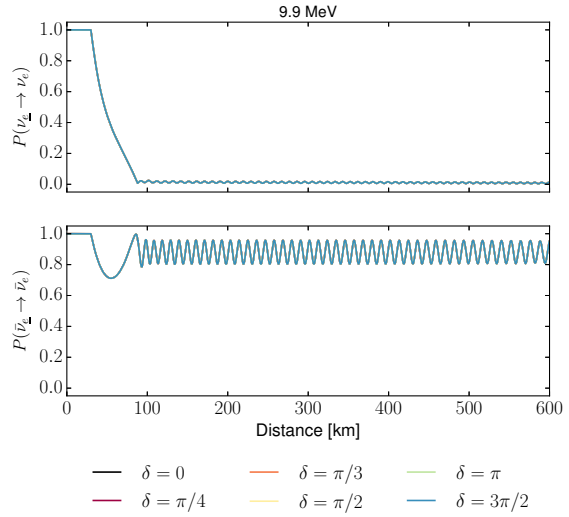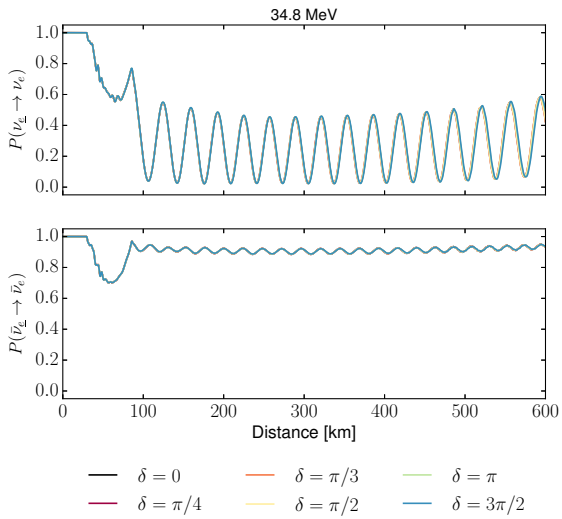(a) Normal hierarchy

(b) Inverted hierarchy

Figure 4.39.: Ratios of capture rate ratios for different values of δ as function of distance for different energies. The results are obtained with $Y_\tau^{\mathrm{eff}} = 0$ and different initial fluxes for ν_μ and ν_τ.

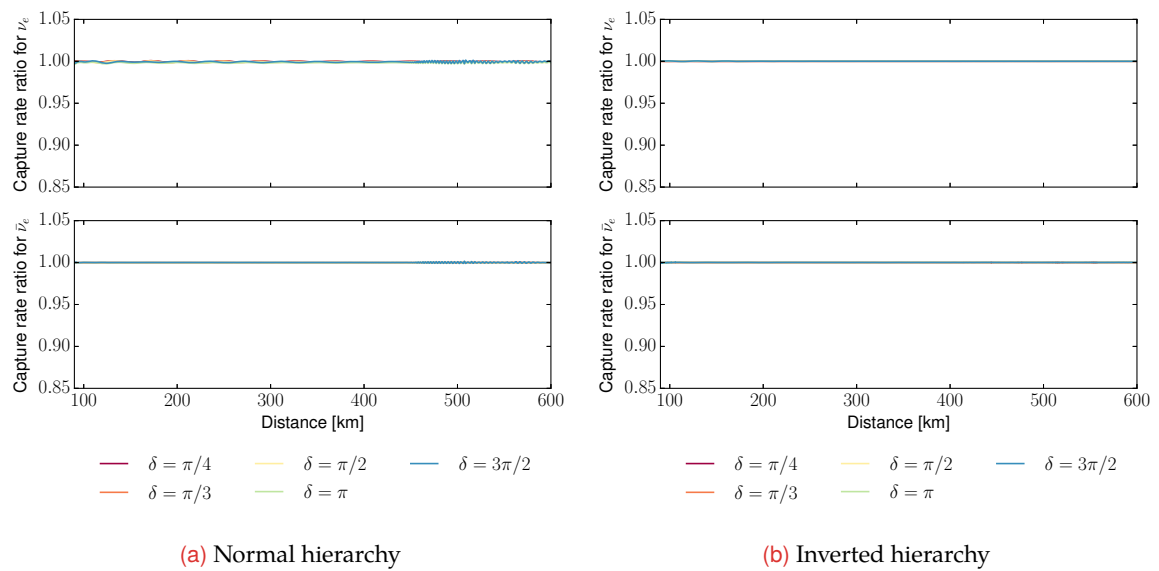# Summary and Outlook

> "
>
> *Où finit le télescope, le microscope commence.*
> *Lequel des deux a la vue la plus grande?*
>
> VICTOR HUGO
> Les Misérables (1862)[1]

In the present work, we investigated the trajectory dependence of the neutrino flavor evolution in a BNS merger remnant. This work represents an improvement compared to previous investigations, in various aspects, and can serve as the initial point for future studies. To be more precise, we followed neutrinos emitted from different emission points along various angles, and determined the flavor transformation properties. We found that depending on which location and which polar angle neutrinos are emitted, the outcome can be different. In particular, we observed that flavor conversion through MNR can occur for most neutrinos traveling through the low density funnel. For cases without flavor conversion across MNR due to the non-adiabaticity, a synchronized MSW transformation can take place afterwards. For neutrinos that do not encounter MNR, bipolar type of flavor oscillations may occur for the IH. We note that future investigations should also explore the dependence on the azimuthal emission angle that was omitted in this work.

We found that flavor evolution can significantly affect the neutrino capture rates on protons and neutrons at the regions with $T \gtrsim 8\,\mathrm{GK}$. This may change the r-process abundances in the neutrino wind. In our work we presented capture rates which do not take into account the solid angle contributions. This treatment is consistent with our single-trajectory approximation and we found that the oscillated ν_e ($\bar{\nu}_e$) capture rates can increase (decrease) up to almost 67% (67%).

If we apply flavor conversion probabilities derived with the single-trajectory approximation to all neutrinos emitted from the disk and integrate over the solid angle (see, e.g., Fig. D.2), we find the ν_e capture rates instead always decrease. This behavior is due to the fact that the solid angle for ν_e is larger so that the relative contribution from ν_x reduces. We speculate that the use of the "single-trajectory" assumption is maximizing the impact of flavor conversion we find on the capture rates.

The initial luminosities are a key input for the flavor evolution as we observed. In fact, a change in the luminosities can produce different flavor conversion results. In particular, we have shown this fact in two ways: either by taking the cooling luminosities as input

---

[1] Where the telescope ends, the microscope begins. Which of the two has the grander view?

instead of the net luminosities, or by rescaling the number luminosity ratios of different neutrino species according to BNS merger model predictions. With cooling luminosities, we obtained flavor conversions for ν_e and, for most cases also for $\bar{\nu}_e$, that occur closer to the neutrino emission surface. Using rescaled luminosities, we also obtained standard MNR albeit the flavor transformation becomes less adiabatic. If future realistic initial fluxes happen to produce flavor conversion very close to the neutrino surface, the presence of neutrino absorption in the region above the disk might require, in the long run, the investigation of the competition between collisions and flavor evolution in an improved treatment of the neutrino propagation.

Whether there is efficient flavor conversion through MNR depends crucially on the way how neutrinos go through the resonance and the adiabaticity. We discussed these points in a two-flavor treatment and compared to the three-flavor calculations. In particular, we showed that even in detailed simulations [25], three flavor results can be understood, at least to some extend, within a two flavor framework in the cases with MNR. Hereby, we compared the adiabatic solution to the solutions obtained directly by solving the equations of motion. In most cases, we found a rather good agreement. However, we also observed increasing discrepancies for increasing neutrino energies. These need to be investigated in future studies. Also the adiabaticity for the three flavor case should be analyzed in more detail, e.g., by computing the non-adiabaticity parameter discussed in [158].

Furthermore, we performed a first exploration of CP violation in BNS mergers. In our numerical calculations, we probed distinct values for the Dirac-phase and studied different fluxes for ν_μ and ν_τ neutrinos and radiative corrections to the neutrino-matter potential. We found effects that are partially consistent with similar studies in the core-collapse supernova context. However, there are also differences, in particular between the mass hierarchies and neutrino energies which are not fully understood yet. With respect to observations a measurement of these effects appears to be impractical at the moment. For the possible impact on nucleosynthesis, we did not observe a relevant change of the differential capture rates. However, it is difficult to make a reliable statement with the employed level of approximations. Because these investigation was only preliminary, additional studies are necessary. The latter can also involve further radiative corrections, e.g., corrections to the neutrino self-interaction potential [232] or physics beyond the standard model like flavor changing neutral currents.

Besides CP violation, future investigations should also examine the role of neutrino non-standard interactions and sterile neutrinos in BNS mergers. In particular the role of the MNR, which can be relevant in such scenarios, should be analyzed.

In our work we illuminated in more detail some of the employed approximations used in our and in previous works and commented on their limitations. Demanding simulations beyond the currently used approximations will tell us how the implementation of the full coupling of the self-interaction Hamiltonian will modify the results presented in this work. From the studies performed in the supernova context one may speculate that this may introduce decoherence and possibly change the starting points of flavor conversions. Also symmetry

breaking effects (e.g., [124, 128]) or fast flavor conversions (see [128, 233] and references therein) appearing very close to the neutrino emission surface which require a non-trivial angular dependence for the neutrino distribution function, could have a strong impact on our studies and need to be addressed in future studies. To follow the dynamics of the flavor evolution one needs to study the feedback of neutrino flavor conversions on the hydrodynamics as well [189]. In particular this means that if the amount of ν_e ($\bar{\nu}_e$) changes, the electron fraction will be altered. In turn, the hydrodynamics needs to be updated and the corresponding equations have to be solved accordingly. Moreover, one should also include general relativistic effects which produce a redshift and the bending of the neutrino trajectory [234]. With respect to simulations of binary neutron star mergers and their aftermath (in particular the formation of the neutrino-driven wind), future numerical codes should cover a wide range of physical ingredients at the same time like full general relativistic hydrodynamics and a sophisticated spectral neutrino transport treatment including all flavor neutrinos. These steps (among others) beyond the approximations employed in this work may be necessary to assess the impact of flavor conversions on the r-process elements produced in the neutrino-driven wind and the actual contribution from neutron star mergers to the observed heavy element abundances.

Ongoing and future experiments will settle some of the open issues, in particular they will reveal the neutrino mass ordering and clarify if there is CP violation in the lepton sector. Furthermore, the expected gravitational wave signals and measurements from electromagnetic counterparts from binary neutron star mergers will provide valuable information that a necessary to understand the origin of heavy elements.

Acknowledgments

I would like to thank my advisor Friedrich-Karl Thielemann for giving me the opportunity to work on this fascinating and challenging topic in a very stimulating group where I always felt like being part of a family. For his continuous support, advice, encouragement, and for his patience throughout this work, I want to express my deepest gratitude. In particular his advice, not only on physics related issues, but on science in general were always of great value for me. Furthermore, I adopted his very optimistic way of thinking during the past years and I always enjoyed his very special sense of humor. Last but not least, I thank him for giving me the chance to participate on workshops, conferences, schools and discussion meetings and thereby meet interesting and great people.

One of them is Cristina Volpe which I met in Erice. To her, I want to express my greatest gratitude as well. Especially, for her continuous support, the time she spend and ongoing advice which shaped the basis of this thesis. In particular, I enjoyed the discussions we had when we met several times in Paris. It really helped me to quickly progress and to work on different aspects presented in this work. I always benefited from her expertise knowledge which left a deep impression to me. From her I also learned how science works in practice and what is really important in research. She was always willing to listen to my questions and provided me with many valuable physical insights. The discussions with her always turned out to be very fruitful in many ways. In addition, I want to thank her for being the co-referee for this work.

Another person I met in Erice, was Meng-Ru Wu. Despite on neutrino physics, I learned a lot from him about numerical aspects and on solving numerical issues related to the non-linear flavor evolution. In addition, I want to thank him and my former office mate Albino Perego for lots of discussions and our collaboration, which we started during the "Brainstorming and Fun" meeting in Basel in 2014. I also like to thank Albino for providing his simulation data. It was his data that made this work possible.

I would like to use the opportunity to give special thanks to Andreas Aste. I always admired his broad mathematical knowledge and his way of thinking about physics. It was a pleasure to be the tutor for his exercises on mathematical physics issues. In a very unique way, he taught me various aspects on fundamental physics for which I am truly grateful. He was also the one who encouraged me to switch to astrophysics in the first place.

Moreover, I am grateful to

- Sofie Fehlmann for the after-lunch conversations we had about physics and topics beyond that. I always enjoyed it.

- My office colleagues Marius Eichler, Kevin Ebinger, Julia Reichert and Benjamin Wehmeyer for a great working atmosphere. We had a lot of fun together. In particular, I would like to thank Kevin for our extensive discussions we had about broad aspects of physics and mathematics. It was always a great pleasure for me. I also thank him for proof-reading parts of this thesis.

- Chiara Biscaro for her delicious cakes.

Of course, I thank all other members (former and current) of our astrophysics group: Oliver Heinimann, Matthias Hempel, Matthias Liebendörfer, Rubén Cabezón, Kuo-Chuan Pan, Marco Pignatari, Umberto Battino, Takami Kuroda, and Thomas Rauscher.

Zudem möchte ich mich ganz herzlich bei meiner Familie bedanken, die immer für mich da war, wenn ich sie brauchte. Ganz besonders bei meinen Grosseltern Annemarie und Walter, denen ich diese Arbeit von ganzem Herzen widme. Sie haben mich mein ganzes Leben begleitet und auf so vielfältige Arten unterstützt, gefördert und immer an mich geglaubt. Auch möchte ich mich bei meiner Schwester Cindy, vor allem für ihren liebevollen psychologischen Beistand, bedanken. Sie hat immer Zeit für mich gefunden und mich durch ihre positive Denkweise immer wieder unterstützt. Natürlich danke ich meiner Nichte Clara-Sophie, die es immer wieder schafft mir ein Lächeln ins Gesicht zu zaubern.

Maik

Neutrino Refractive Index

In this chapter we want to elaborate on what we actual mean when a neutrino propagating in a medium acquires a refractive index. For this purpose, we apply simple arguments from quantum mechanical scattering theory. However, it should be stressed that a more complete treatment should rather be based on quantum field theory.

One of the key quantities in scattering theory is the so-called scattering amplitude f_E. In general, it is a complex function and accounts for the strength and angular dependency of a scattering process. Its dimension corresponds to a length and depends on the initial energy of the particle beam and the polar and azimuthal angles θ and ϕ, respectively, but not on the details of the experimental setting. In the following we assume elastic and isotropic scattering. In particular the scattering amplitude is azimuthally symmetric: $f_E = f_E(\theta)$. We consider plane waves incident normally on a foil of some uniform material with number density n and with infinitesimal thickness δ at $\mathbf{x} = (\rho, \varphi, z)$, where we employed cylindrical coordinates. The foil extends infinitely in the x-y plane. The small thickness ensures that at most single scattering inside the foil occurs [235, 236]. The incident wave interacts with the scattering centers and thereby produces a scattered wave. The situation is depicted in figure A.1. Now,
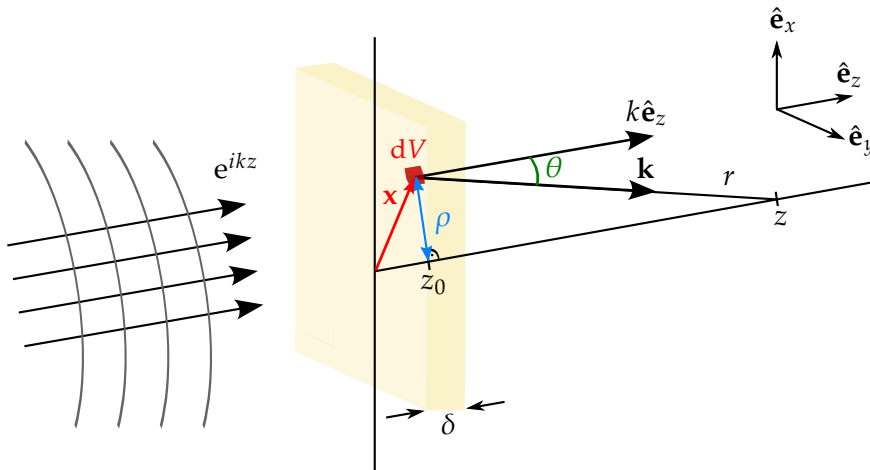
Figure A.1.: Plane waves incident normally on a thin foil.

we are interested in calculating the wave function at a distance $\Delta \equiv z - z_0 \gg 1/k$ far away from the foil at an observation point $(0, 0, z)$. For this purpose, we have to build a coherent sum of the incident wave and all scattered waves. The latter are found by taking all the contributions of the individual scatterers and multiply the scattering amplitude $f_E(\theta)$ with the number density n and finally perform the integration over the foil area [236]. The scattered

wave function observed at $(0, 0, z)$ with $n\mathrm{d}V$ scattering centers inside the volume element $\mathrm{d}V = \delta\,\mathrm{d}\varphi\,\mathrm{d}\rho\,\rho$ is then found to be:

$$\mathrm{e}^{ikz_0}\frac{\mathrm{e}^{ikr}}{r}f_E(\theta)n\mathrm{d}V, \tag{A.1}$$

where the e^{ikz_0}-factor accounts for the position of the scatterers at $\mathbf{x}$. If we use the relation $r = \sqrt{\rho^2 + \Delta^2}$, the total scattered wave is given by

$$\psi_\mathbf{k}^{\mathrm{sc}} \sim n\delta \int_0^{2\pi}\mathrm{d}\varphi\,\mathrm{e}^{ikz_0}\int_0^\infty \mathrm{d}\rho\,\frac{\rho}{\sqrt{\rho^2 + \Delta^2}}f_E(\theta)\mathrm{e}^{ik\sqrt{\rho^2 + \Delta^2}} \tag{A.2}$$

and as a consequence, the total wave function at the point $(0, 0, z)$ corresponds to

$$\psi_\mathbf{k} \sim \mathrm{e}^{ikz}\left(1 + n\delta\int_0^{2\pi}\mathrm{d}\varphi\,\mathrm{e}^{ikz_0}\int_0^\infty\mathrm{d}\rho\,\frac{\rho}{\sqrt{\rho^2 + \Delta^2}}f_E(\theta)\mathrm{e}^{ik\left(\sqrt{\rho^2 + \Delta^2} - z\right)}\right). \tag{A.3}$$

Note that the φ-integration becomes trivial, because we assumed isotropic scattering. If we now expand the square root in the exponent for $\rho/\Delta \ll 1$, we obtain

$$k\sqrt{\rho^2 + \Delta^2} \approx k\Delta\left(1 + \frac{1}{2}\frac{\rho^2}{\Delta^2}\right) \tag{A.4}$$

and therefore,

$$\mathrm{e}^{ik(\sqrt{\rho^2 + \Delta^2} - z)} \approx \mathrm{e}^{-ikz_0}\mathrm{e}^{ik\rho^2/(2\Delta)}. \tag{A.5}$$

The argument appearing in the second exponent leads to rapid oscillations for $k\rho^2/\Delta \gg 1$ [236] and therefore the upper limit of integration is of order Δ/k. As a consequence and because of $k\Delta \gg 1$ we find $\theta = \arcsin(\rho/\Delta) \approx 0$, leading to

$$\psi_\mathbf{k} \sim \mathrm{e}^{ikz}\left(1 + \frac{2\pi n\delta}{\Delta}f_E(0)\int_0^\infty\mathrm{d}\rho\,\frac{\rho}{\sqrt{\rho^2 + \Delta^2}}\mathrm{e}^{ik\rho^2/(2\Delta)}\right). \tag{A.6}$$

The remaining integration yields:

$$\int_0^\infty\mathrm{d}\rho\,\rho\mathrm{e}^{ik\rho^2/(2\Delta)} = \frac{1}{2}\int_0^\infty\mathrm{d}(\rho^2)\,\mathrm{e}^{ik\rho^2/(2\Delta)} \tag{A.7}$$

$$= \lim_{\epsilon\to 0^+}\frac{1}{2}\int_0^\infty\mathrm{d}(\rho^2)\,\mathrm{e}^{i(k+i\epsilon)\rho^2/(2\Delta)} \tag{A.8}$$

$$= \frac{i\Delta}{k}. \tag{A.9}$$

In the first step we made a change of variables ($\rho \mapsto \rho^2$) and in the second step we employed the method of adiabatic regularization [237, 238], i.e., we multiplied the integrand by a regularization factor $e^{-\epsilon \rho^2 / (2\Delta)}$ [236] and computed the limit[1] $\epsilon \to 0^+$. This yields

$$\psi_{\mathbf{k}} \sim e^{ikz} \left(1 + \frac{2\pi i n \delta}{k} f_E(0) \right). \tag{A.10}$$

Finally, if we want to study the case with finite thickness d, we consider N layers of infinitesimal thickness and take the continuum limit $N \to \infty$ such that $d \equiv N \cdot \delta < \infty$ holds [32, 240]:

$$\psi_{\mathbf{k}} \sim \lim_{N \to \infty} e^{ikz} \left(1 + \frac{2\pi i \, nd}{Nk} f_E(0) \right)^N \tag{A.11}$$

$$= e^{ikz} e^{2\pi i n d f_E(0)/k}. \tag{A.12}$$

Therefore, after the scattering process, the initial wave picked up an additional phase factor. To interpret the latter, we use the well-known relation from the classical theory of scattering [235, 241–245]

$$n_{\text{refr}} = 1 + \frac{2\pi}{k^2} n f_E(0) \tag{A.13}$$

which allows us to establish a connection between the exponent and the refractive index of the medium [53]

$$\psi_{\mathbf{k}} \sim e^{ik[z + (n_{\text{refr}} - 1)d])}. \tag{A.14}$$

Now the physical interpretation becomes evident: After traveling through the medium, the wave experienced refraction.

In the following, let us consider a beam of free streaming neutrinos with momentum $\mathbf{k}$ propagating in z-direction, described by a plane wave $e^{ik\hat{\mathbf{e}}_z \cdot \mathbf{x}}$. After the neutrinos interacted with some scatterer at $\mathbf{x} = (\rho, \varphi, z)$, the scattered wave is expected to fulfill the asymptotic condition[2] $f_E(\theta, \phi) e^{ipr}/r$ at large distances r from the scattering region [246, 247], where p denotes the corresponding momentum[3]. In this case the total distorted wave function assumes the asymptotic form

$$\psi_{\mathbf{k}} \sim e^{ikz} + f_E(\theta, \phi) \frac{e^{ikr}}{r}. \tag{A.15}$$

In case of elastic scattering we have $f_E = f_E(\theta)$ and the following relation for the elastic differential cross section holds

$$\left(\frac{d\sigma}{d\Omega} \right)_{\text{el}} = |f_E(\theta)|^2. \tag{A.16}$$

---

[1] Note that the regularization factor could be interpreted as an artificial "absorption" factor [239].
[2] The so-called Sommerfeld radiation condition.
[3] Note that $\rho \equiv \sqrt{x^2 + y^2}$, φ and z denote cylindrical coordinates (as before).

In perturbative quantum field theories, however, the scattering amplitude corresponds essentially to the matrix element $\mathcal{M}$ that can be computed using Feynman rules. In the center-of-momentum frame, one finds for a two-body elastic scattering process [248]:

$$\left(\frac{d\sigma}{d\Omega}\right)_{el} = \frac{|\mathcal{M}|^2}{64\pi^2 E^2},$$ (A.17)

where E denotes the energy in that frame. If we compare both expressions for the differential cross section, it is convenient to define the scattering amplitude for elastic scattering as [249]

$$f_E(\theta) = \frac{1}{8\pi E}\mathcal{M},$$ (A.18)

where our choice of phase is just convention. If we use eq. (A.13) with k^2 replaced by E^2, we can link the scattering of a single scatterer to the macroscopic properties of the medium (with a large number of scattering centers) described by the (complex) index of refraction[4,5] n_{refr}. The Feynman amplitude $\mathcal{M}$ for the charged current contribution of the elastic neutrino-electron scattering process $\nu_e + e^- \rightarrow \nu_e + e^-$ at tree-level can be found by a straightforward calculation yielding [43, 250]

$$f_E(0) = -\frac{G_F E}{\sqrt{2}\pi}$$ (A.19)

and the refractive index is given by

$$n_{refr} = 1 - \frac{\sqrt{2}G_F n_e}{E},$$ (A.20)

where n_e denotes the electron number density[6]. Thus, the neutrinos acquire a non-trivial (i.e. $\neq 1$) refractive index n_{refr}, i.e., their dispersion relation is altered in matter:

$$|\mathbf{p}| \approx E \mapsto |\mathbf{p}| \approx E\, n_{refr}.$$ (A.21)

Consequently, also the neutrino flavor propagation phenomenology is expected to change. The scattered waves may coherently interfere in the forward direction. This can be described by an effective potential which can be introduced via

$$V \equiv E - E n_{refr} = -(n_{refr} - 1)E.$$ (A.22)

Because the interaction of the neutrinos with such a medium is flavor dependent, the medium is called "flavor birefringent" [53]. For example, if the medium consists only of electrons, the scattering amplitudes for $\nu_{\mu,\tau}$-e-scattering will be different from ν_e-e-scattering, because the

---

[4] Note that the imaginary part of $f_E(0)$ is associated with the so-called absorption coefficient. Because the interaction is weak, we will neglect absorption for convenience [61, 250].

[5] At non-zero temperature, we need to replace $n f_E(0)$ by its thermal average [251]: $\langle n f_E(0)\rangle$.

[6] In a full discussion one should consider both the charged current and the neutral current contributions to $f_E(0)$. But since for the flavor evolution only the difference between the refractive indices matters, we can focus on the charged current part only.

latter can proceed through the charged-current channel in addition to the neutral-current channel. If we limit our discussion on charged current contributions, we find for the effective potential of electron neutrinos in an electron background $V \equiv \sqrt{2} G_{\mathrm{F}} n_e$. One should keep in mind that the refractive indices are computed within the SM where neutrinos are assumed to be massless and lepton number is conserved. Therefore, it seems natural to ask if the use of those refractive indices is appropriate. Though we know that neutrinos have non-vanishing masses, high precision experiments of weak processes indicate that neutrino interactions with particles of the SM are reasonably well described within the SM. Thus, at least in a first approximation to possible extensions of the SM, the calculation of the neutrino refractive indices seems to be admissible [31, 32].

To get a feeling of the size of the refractive index, we make some estimates. In supernovae with a matter density of $\rho \simeq 10^8 \mathrm{g}\,\mathrm{cm}^{-3}$, electron fraction $Y_e = 0.4$, the electron number density corresponds to $n_e = \rho Y_e / m_{\mathrm{u}} \sim \mathcal{O}(10^{31})\,\mathrm{cm}^{-3}$ and for the refractive index we find $|n_{\mathrm{refr}-1}| \sim \mathcal{O}(10^{-13})$. In the neutrino driven wind in the aftermath of a binary neutron star merger, it is possible to encounter conditions with $\rho \simeq 2 \times 10^{10}\,\mathrm{cm}^{-3}$, $Y_e = 0.18$, and a refractive index of $|n_{\mathrm{refr}-1}| \sim \mathcal{O}(10^{-11})$. Though these tiny values might suggest that refractive effects are practically negligible[7], the impact on the flavor evolution can be crucial.

As a final remark, we stress that although the situation here shares similarities with the case of photons traveling through a medium, the situation significantly changes if neutrinos travel through a medium consisting of other neutrinos: The resulting potential that describes how neutrinos change their flavor, will then depend on the flavor states of the background neutrinos. Clearly, this turns the problem into a non-linear one (see Chapter 3).

---

[7] Indeed, if we would employ a model with only one single flavor, refractive effects are not important.

Energy Binning

During a matter-neutrino resonance, the matter and neutrino self-interaction potentials cancel each other at the order of the vacuum potential which is proportional to the inverse energy, $1/E$. Numerically, the problem becomes very sensitive to any remainder. It turns out that if we switch to the inverse energy space[252], we can reach convergence (with respect to accuracy) with a lower number of energy bins. To be specific, instead of performing integrations over energies E, we substitute the corresponding energy integrals and switch to the inverse-energy space $1/E$, i.e., for a function $f = f(E)$ we have:

$$\int_0^\infty \mathrm{d}E \, f(E) = \int_0^\infty \frac{\mathrm{d}\omega}{\omega^2} \, f(1/\omega), \tag{B.1}$$

with the substitution $\omega \equiv 1/E$. In figure B.1 we show different numerical integration schemes used in this work. We employed a simple midpoint rule or a Gauss-Legendre quadrature for the integration over energies or inverse energies. While by integration over E, many bins are used for higher energies, where the energy distribution function f_ν (here we assume a Fermi-Dirac function) has a wide tail which is almost vanishing (see eq. (4.5)). In contrast, if we integrate over $1/E$, most of the energy bins are used in the region where the distribution function is most relevant.
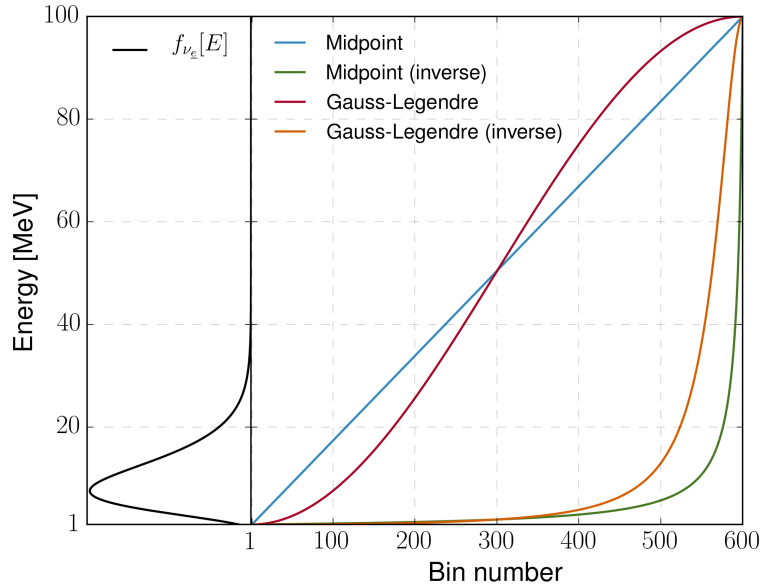

Figure B.1.: Different numerical schemes (midpoint rule and Gauss-Legendre quadrature) for integration over energies and inverse energies. We show the energy binning, i.e., energy as a function of the numbers of bin (right) and on the left we plot a Fermi-Dirac distribution as function of the neutrino energy.

Cross Sections

In the following we list explicit expressions from [200] for the cross sections without weak magnetism corrections.

Neutrino absorption on free nucleons ($N \in \{n, p\}$):

$$\sigma_{\nu N,\text{abs}} = \sigma_0 \left(\frac{1 + 3g_A^2}{4}\right) \left(\frac{E \pm \Delta_{np}}{m_e c^2}\right)^2 \left[1 - \left(\frac{m_e c^2}{E \pm \Delta_{np}}\right)^2\right]^{1/2} , \tag{C.1}$$

where $\nu \in \{\nu_e, \bar{\nu}_e\}$, $\sigma_0 = \approx 1.705 \times 10^{-44}\,\text{cm}^2$, $g_A \approx -1.23$, $\Delta_{np} = (m_n - m_p)c^2 \approx 1.29\,\text{MeV}$, and E corresponds to the neutrino energy. The plus sign refers to electron neutrino absorption on free neutrons ($\sigma_{\nu_e n,\text{abs}}$), while the minus sign refers to electron antineutrino absorption on free protons ($\sigma_{\bar{\nu}_e p,\text{abs}}$).

For the elastic neutrino-nucleon scattering, the momentum-transfer cross section is the relevant cross section for our calculations of the (transport) optical depth. It is obtained from the differential cross section weighted by a factor $(1 - \cos\Theta)$ and integrated over the solid angle. Here, Θ denotes the scattering angle. Explicitly, the momentum-transfer cross sections for neutrino-neutron scattering turns out to be

$$\sigma_{\nu n,\text{tr}} = \frac{\sigma_0}{4} \left(\frac{E}{m_e c^2}\right)^2 \left(\frac{1 + 5g_A^2}{6}\right) \tag{C.2}$$

and for neutrino-proton scattering

$$\sigma_{\nu p,\text{tr}} = \frac{\sigma_0}{6} \left(\frac{E}{m_e c^2}\right)^2 \left[(C_V' - 1)^2 + 5g_A^2(C_A' - 1)^2\right] , \tag{C.3}$$

where

$$C_V' = \frac{1}{2} + 2\sin^2\theta_W \approx 0.96, \tag{C.4}$$

$$C_A' = \frac{1}{2}. \tag{C.5}$$

Luminosities and Neutrino Fluxes

In this chapter we derive an expression for the neutrino luminosities for an infinitesimal thin disk explicitly writing the constants $\hbar$ and c. For this purpose, we assume that the disk behaves like a blackbody source at a fixed temperature T_ν and take the neutrino number flux per unit energy per solid angle to be of Fermi-Dirac shape,

$$\mathcal{J}_\nu(E) = \frac{c}{(2\pi\hbar c)^3} \frac{E^2}{e^{E/T_\nu} + 1}. \tag{D.1}$$

The differential neutrino number flux per unit energy in a beam with differential solid angle $d\Omega = dA \cos(\Theta)/\delta^2$ at $Q(x, 0, z)$ with a distance l from the center of the disk is then given by (see figure D.1)

$$d\Phi_\nu(l, \vartheta, E) = \mathcal{J}_\nu(E) \frac{dA \cos\Theta}{\delta^2}, \tag{D.2}$$

where

$$\delta \equiv |\mathbf{Q} - \mathbf{Q}_0| = \sqrt{x^2 + r_d^2 - 2xr_d \cos\varphi + z^2} \tag{D.3}$$

corresponds to the distance from the differential area dA to Q. The $\cos(\Theta)$-factor accounts for the fact that a distant observer at Q sees only an effective area which accordingly reduces the flux. An integration over the disk yields the neutrino number flux per unit energy at Q:

$$\Phi_\nu(l, \vartheta, E) = \mathcal{J}_\nu(E) \int_0^{2\pi} d\varphi \int_0^{R_\nu} dr_d r_d \frac{\cos\Theta}{\delta^2}. \tag{D.4}$$

Using $\cos\Theta = z/\delta$ and $z = l\cos\vartheta$, it follows:

$$\Phi_\nu(l, \vartheta, E) = l\cos\vartheta\, \mathcal{J}_\nu(E) \int_0^{R_\nu} dr_d r_d \int_0^{2\pi} \frac{d\varphi}{\delta^3}. \tag{D.5}$$

For the explicit calculation, it is convenient [173] to introduce the quantities

$$L \equiv (x - r_d)^2 + z^2, \qquad M \equiv (x + r_d)^2 + z^2 \tag{D.6}$$

so that

$$\delta = \sqrt{\frac{L + M}{2} - \frac{M - L}{2} \cos\varphi}. \tag{D.7}$$

With the relation

$$\int_0^{2\pi} \frac{\mathrm{d}\varphi}{\delta^3} = \frac{4E\left(\sqrt{\frac{M-L}{M}}\right)}{L\sqrt{M}}, \tag{D.8}$$

where

$$E(k) \equiv \int_0^{\pi/2} \mathrm{d}\theta \sqrt{1 - k^2 \sin^2 \theta} \tag{D.9}$$

denotes Legendre's complete elliptic integral of the second kind [253], we find

$$\Phi_\nu(l, \vartheta, E) = 4l \cos \vartheta \, \mathcal{J}_\nu(E) \int_0^{R_\nu} \mathrm{d}r_\mathrm{d} \, r_\mathrm{d} \, \frac{E\left(\sqrt{\frac{M-L}{M}}\right)}{L\sqrt{M}}. \tag{D.10}$$

For an observer located at infinity, we compute the isotropized luminosity, i.e., the luminosity
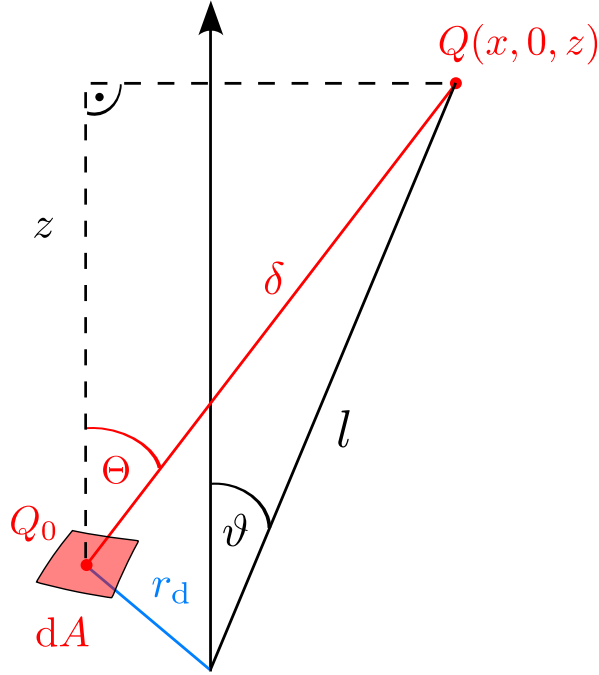
Figure D.1.: Geometry: $Q_0(r_\mathrm{d} \cos \varphi, r_\mathrm{d} \sin \varphi, 0)$, $x = l \sin \vartheta$, $z = l \cos \vartheta$, $\mathrm{d}A = \mathrm{d}r_\mathrm{d} \, r_\mathrm{d} \, \mathrm{d}\varphi$.

obtained by assuming an isotropically emitted flux,

$$L_\nu(\vartheta) = 2\pi l^2 \int_0^\infty \mathrm{d}E \, E \, \Phi_\nu(l, \vartheta, E)\Big|_{l\to\infty} \tag{D.11}$$

$$= \frac{7}{120} \frac{\pi^2 c}{(\hbar c)^3} T_\nu^4 \, l^3 \, \cos \vartheta \int_0^{R_\nu} \mathrm{d}r_\mathrm{d} \, r_\mathrm{d} \, \frac{E\left(\sqrt{\frac{M-L}{M}}\right)}{L\sqrt{M}}\Bigg|_{l\to\infty}, \tag{D.12}$$

where we used

$$\int_0^\infty dE \, \frac{E^3}{e^{E/T_\nu} + 1} = \frac{7\pi^4}{120} T_\nu^4.$$ (D.13)

The asymptotic relation

$$\frac{E\left(\sqrt{\frac{M-L}{M}}\right)}{L\sqrt{M}} = \frac{\pi}{2}\frac{1}{l^3} + \mathcal{O}(1/l^5) \qquad (l \to \infty),$$ (D.14)

yields

$$L_\nu(\vartheta) = \frac{7\pi}{4} \sigma_{SB} T_\nu^4 \cos\vartheta \int_0^{R_\nu} dr_d \, r_d$$ (D.15)

$$= \frac{7\pi}{8} \sigma_{SB} T_\nu^4 R_\nu^2 \cos\vartheta,$$ (D.16)

where $\sigma_{SB} \equiv \pi^2 k_B^4 / (60\hbar^3 c^2)$ denotes the Stefan-Boltzmann constant.

Note that in the equations above, we considered a neutrino moving in the upward direction ($\cos\vartheta > 0$). If we want to follow a neutrino moving downwards, we have to replace $\cos\vartheta$ by $-\cos\vartheta$, i.e., if $\frac{\pi}{2} < \vartheta < \pi$.

An integration over the upper hemisphere leads to the total neutrino luminosity

$$L_\nu = \int_0^1 d(\cos\vartheta) \, L_\nu(\vartheta)$$ (D.17)

$$= \frac{7\pi}{16} \sigma_{SB} T_\nu^4 R_\nu^2.$$ (D.18)

As an additional check, we also compute the total neutrino energy flux emitted from dA,

$$\mathcal{F}_\nu = \int_0^\infty dE \, E^2 \, \mathcal{J}_\nu(E) \int d\Omega \cos\vartheta$$ (D.19)

$$= \frac{7}{8} \frac{\pi}{120\hbar^3 c^2} T_\nu^4 \, 2\pi \int_0^1 d(\cos\vartheta) \cos\vartheta$$ (D.20)

$$= \frac{7}{16} \sigma_{SB} T_\nu^4$$ (D.21)

and from that, we infer the total neutrino luminosity

$$L_\nu = \pi R_\nu^2 \mathcal{F}_\nu$$ (D.22)

$$= \frac{7\pi}{16} \sigma_{SB} T_\nu^4 R_\nu^2.$$ (D.23)

This expression agrees with the one derived above (see eq. (D.17)). For a simple estimate, it is useful to express this in the convenient form

$$L_\nu \sim 15 \times 10^{51} \text{ erg/s} \left(\frac{T_\nu}{3.4\,\text{MeV}}\right)^4 \left(\frac{R_\nu}{90\,\text{km}}\right)^2. \tag{D.24}$$

If we use the neutrino disk radii at 60 ms from table 4.2 and the temperatures from table 4.3, we obtain $L_{\nu_e} \approx 15 \times 10^{51}$ erg/s, $L_{\bar\nu_e} \approx 33 \times 10^{51}$ erg/s and $L_{\nu_x} \approx 48 \times 10^{51}$ erg/s. While the values for L_{ν_e} and $L_{\bar\nu_e}$ are compatible with the luminosities obtained in [25], the value of L_{ν_x} is about 6 times larger.

Similarly, we compute the isotropized neutrino number luminosity

$$L_{N,\nu}(\vartheta) = 2\pi l^2 \int_0^\infty dE\, \Phi_\nu(l,\vartheta,E)\bigg|_{l\to\infty} \tag{D.25}$$

$$= \frac{c}{(\hbar c)^3} \frac{F_2(0)}{4\pi} \cos\vartheta\, T_\nu^3 R_\nu^2 \tag{D.26}$$

and neutrino number luminosity

$$L_{N,\nu} = \int_0^1 d(\cos\vartheta)\, L_{N,\nu}(\vartheta) \tag{D.27}$$

$$= \frac{c}{(\hbar c)^3} \frac{F_2(0)}{8\pi} T_\nu^3 R_\nu^2. \tag{D.28}$$

In local thermal equilibrium we can relate the mean energy, defined [25] via $\langle E_\nu \rangle = L_\nu/L_{N,\nu}$, to the effective temperature

$$\langle E_\nu \rangle = \frac{F_3(0)}{F_2(0)} T_\nu. \tag{D.29}$$

However, we stress that the mechanism behind the spectra formation is rather demanding, since neutrinos decouple at different energy-dependent surfaces, and therefore our assumption of a thermal spectra which is determined by an effective temperature represents only a coarse approximation. In order to account for deviations from thermal equilibrium, one could examine different shapes of the spectral function similar to studies that have been done in the context of core-collapse supernovae (e.g., [83]).

If we multiply the neutrino number flux,

$$F_\nu = \int_0^\infty dE\, \mathcal{J}_\nu(E) \int d\Omega\, \cos\vartheta \tag{D.30}$$

$$= \frac{\pi c}{(2\pi\hbar c)^3} F_2(0) T_\nu^3, \tag{D.31}$$

by the disk area πR_ν^2, the same expression for the neutrino number luminosity $L_{\mathrm{N},\nu} = \pi R_\nu^2 F_\nu$ as above is obtained:

$$L_{\mathrm{N},\nu} = \frac{c}{(\hbar c)^3} \frac{F_2(0)}{8\pi} T_\nu^3 R_\nu^2. \tag{D.32}$$

Finally, we express the neutrino number flux in terms of the luminosity and mean neutrino energy,

$$F_\nu = \frac{1}{\pi R_\nu^2} \frac{L_\nu}{\langle E_\nu \rangle}, \tag{D.33}$$

and define the neutrino number flux per unit energy per solid angle as follows:

$$c \frac{\mathrm{d}^2 n_\nu}{\mathrm{d}\Omega \mathrm{d}E} \equiv \frac{F_\nu}{\pi} f_\nu(E), \tag{D.34}$$

where

$$f_\nu(E) = \frac{1}{F_2(0)} \frac{1}{T_\nu^3} \frac{E^2}{\mathrm{e}^{E/T_\nu} + 1} \tag{D.35}$$

denotes the normalized Fermi-Dirac distribution function with vanishing degeneracy parameter.

Consequently, the neutrino flux per unit energy corresponds to

$$\Phi_\nu(E, x, z) = \int_{\Omega_\nu} \mathrm{d}\Omega \left(c \frac{\mathrm{d}^2 n_\nu}{\mathrm{d}\Omega \mathrm{d}E} \right) \tag{D.36}$$

$$= \frac{F_\nu}{4\pi} f_\nu(E) \Omega_\nu, \tag{D.37}$$

where the solid angle is given by

$$\Omega_\nu = 4z \int_{R_0}^{R_\nu} \mathrm{d}r_{\mathrm{d}} r_{\mathrm{d}} \frac{E(\sqrt{\frac{M-L}{M}})}{L\sqrt{M}}. \tag{D.38}$$

We show a typical form of the solid angle in figure D.2 along trajectory 2a. Since the neutrino disk radii for $\bar{\nu}_e$ and ν_x are similar, the difference in their corresponding solid angles is minor.
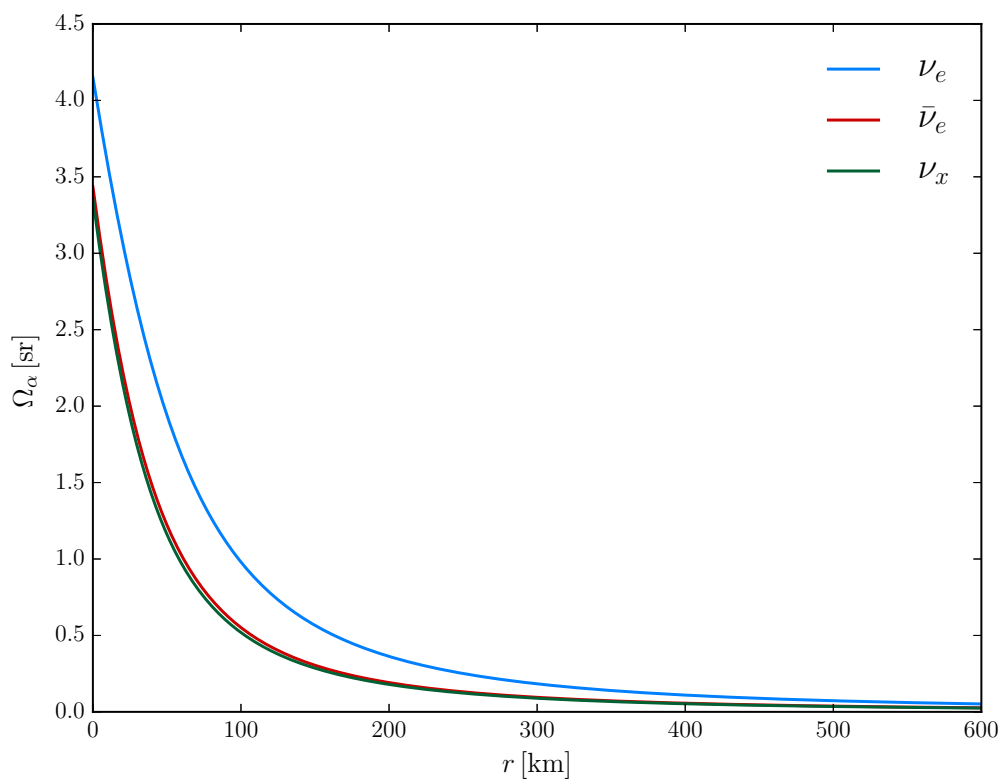
Figure D.2.: Solid angle for each neutrino species computed along trajectory 2a.

Geometric Factor

In this chapter we show the explicit structure of the geometric factor eq. (4.21) used in the neutrino self-interaction Hamiltonian eq. (4.22). An analytical calculation yields

$$\int_{\Omega_{\nu_\alpha}} \mathrm{d}\Omega \left(1 - \cos\Theta_{\mathbf{pp'}}\right) = \int_{\cos\theta_{\max,\nu_\alpha}}^{+1} \mathrm{d}(\cos\theta) \int_0^{2\pi} \mathrm{d}\phi \left(1 - \cos\Theta_{\mathbf{pp'}}\right) \tag{E.1}$$

$$= \int_{R_0}^{R_{\nu_\alpha}} \mathrm{d}r_{\mathrm{d}} \int_0^{2\pi} \mathrm{d}\varphi \left|\det \mathsf{J}\right| \left(1 - \cos\Theta_{\mathbf{pp'}}\right) \tag{E.2}$$

$$= z \int_{R_0}^{R_{\nu_\alpha}} \mathrm{d}r_{\mathrm{d}} \, r_{\mathrm{d}} \, \Gamma(r_{\mathrm{d}}, \theta_0, \phi_0, x, z) \tag{E.3}$$

$$=: G_{\nu_\alpha}(\theta_0, \phi_0, x, z). \tag{E.4}$$

In the second step, we performed a change of coordinates (as described in eqs. (4.11), (4.13), and (4.16)) and present the explicit calculation of the Jacobian determinant in section E.2. Furthermore, we introduced Γ as

$$\Gamma(r_{\mathrm{d}}, \theta_0, \phi_0, x, z) \equiv \int_0^{2\pi} \mathrm{d}\varphi \left\{ \frac{1}{\delta^3} - \frac{z\cos\theta_0 + x\sin\theta_0\cos\phi_0}{\delta^4} \right.$$
$$\left. + r_{\mathrm{d}}\sin\theta_0\cos\phi_0 \frac{\cos\varphi}{\delta^4} + r_{\mathrm{d}}\sin\theta_0\sin\phi_0 \frac{\sin\varphi}{\delta^4} \right\}, \tag{E.5}$$

with δ defined in eq. (D.7). In the single-trajectory approximation, the geometric factor G_{ν_α} should be understood as an averaging over the angles. The explicit φ-integration in eq. (E.5), shown in Section E.3 yields

$$\Gamma = \frac{4E\left(\sqrt{\frac{M-L}{M}}\right)}{L\sqrt{M}} - \frac{\pi\left\{(L+M)(z\cos\theta_0 + x\sin\theta_0\cos\phi_0) - 4xr_{\mathrm{d}}^2\sin\theta_0\cos\phi_0\right\}}{(LM)^{3/2}}, \tag{E.6}$$

where in the second step, the relation $M - L = 4xr_{\mathrm{d}}$, with M and L defined in eq. (D.6), was used and $E(k)$ denotes Legendre's complete elliptic integral of the second kind [253],

$$E(k) \equiv \int_0^{\pi/2} \mathrm{d}\theta \sqrt{1 - k^2\sin^2\theta}. \tag{E.7}$$

Because of our definition of the angle ϕ that differs from the definition in [173], we note that $-\Gamma/2$ with the replacement $\phi_0 \mapsto \pi - \phi_0$ corresponds to the geometric factor C given in [173]. Here, one also has to keep in mind the different convention used to denote the elliptic integral.

E.1 Physical behavior at large distances

In this section, we want to study the behavior of the geometric factors at large distances from the disk. As before, we set $\phi = 0°$. If neutrinos propagated sufficiently far away, we find

$$\cos \theta_0 \approx z/r, \qquad \sin \theta_0 \approx x/r. \tag{E.8}$$

and therefore

$$L \approx r^2 - 2r_{\mathrm{d}}r \sin \theta_0 + r_{\mathrm{d}}^2, \tag{E.9}$$

$$M \approx r^2 + 2r_{\mathrm{d}}r \sin \theta_0 + r_{\mathrm{d}}^2, \tag{E.10}$$

$$L + M = 2(r^2 + r_{\mathrm{d}}^2), \tag{E.11}$$

$$M - L = 4r_{\mathrm{d}}r \sin \theta_0. \tag{E.12}$$

Consequently, we approximate

$$z\Gamma(r) \approx \frac{4E\left(\sqrt{\dfrac{M-L}{M}}\right) r \cos \theta_0}{L\sqrt{M}} - \frac{2\pi r^2 \cos \theta_0 \left\{(r^2 + r_{\mathrm{d}}^2) - 2r_{\mathrm{d}}^2 \sin^2 \theta_0\right\}}{(LM)^{3/2}} \tag{E.13}$$

$$= \frac{\pi r_{\mathrm{d}}^2}{2r^4}(1 + \cos \theta_0{}^2 \cos \theta_0) + \mathcal{O}(1/r^6). \tag{E.14}$$

and find

$$G_{\nu_{\underline{\alpha}}}(r) \approx \frac{\pi(1 + \cos \theta_0{}^2 \cos \theta_0)}{8} \left(\frac{r_{\mathrm{d}}}{r}\right)^4. \tag{E.15}$$

Along a trajectory with $\theta_0 = 45°$ this corresponds to

$$G_{\nu_{\underline{\alpha}}}(r) \approx \frac{3\sqrt{2}\pi}{32} \left(\frac{r_{\mathrm{d}}}{r}\right)^4. \tag{E.16}$$

As was pointed out in [101] for disk-like sources, we naturally expect $G_{\nu_{\underline{\alpha}}}$ to drop off with r^{-4} at large distances. One factor of r^{-2} accounts for the geometric dilution of flux while another factor of r^{-2} is due to the increasing collinearity. In figure E.1 we show the geometric factor for electron neutrinos along trajectory 1a (see table 4.4) and the asymptotic behavior described by eq. (E.16). Both match at large distances.

In order to conclude this chapter, we provide a complete derivation of the geometric factor given in eq. (E.6) in the following sections.
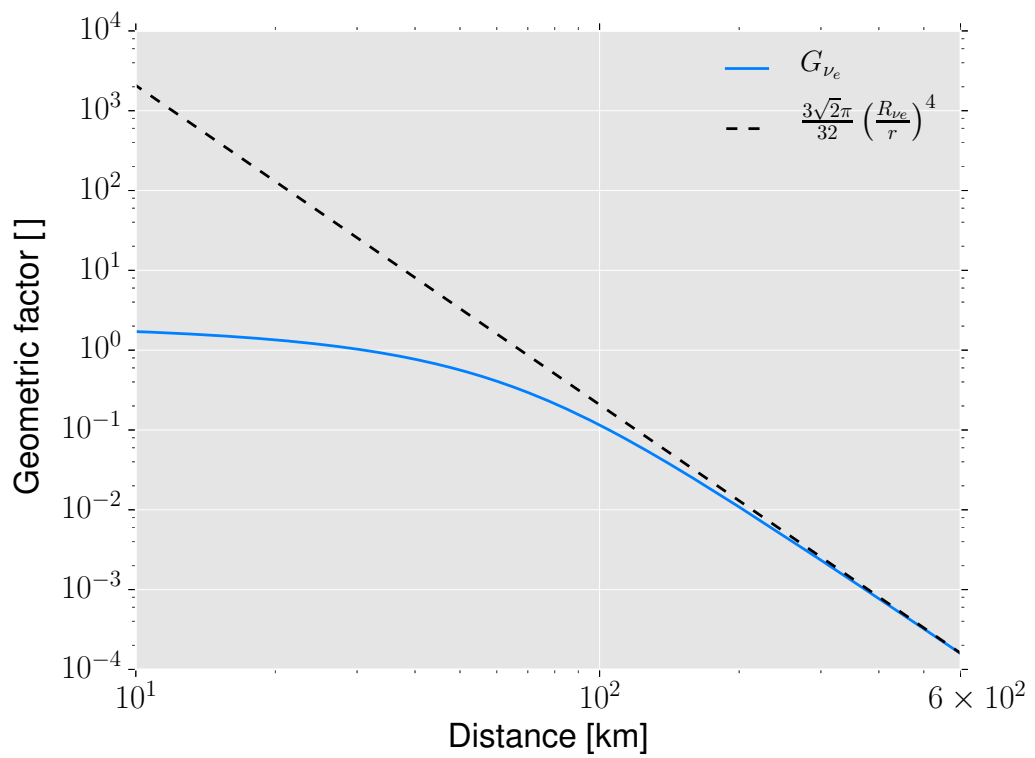
Figure E.1.: Geometric factor for electron neutrinos G_{ν_α} along trajectory 1a (blue curve) together with the expression given in eq. (E.16) (dashed black curve) as a function of distance r. At large distances eq. (E.16) reproduces the asymptotic behavior of the geometric factor.

E.2 Jacobian determinant

Before we calculate all partial derivatives appearing in the Jacobian determinant,

$$\det J = \frac{\partial(\cos\theta)}{\partial r}\frac{\partial\phi}{\partial\varphi} - \frac{\partial(\cos\theta)}{\partial\varphi}\frac{\partial\phi}{\partial r}, \tag{E.17}$$

it is useful to remark the expressions

$$\frac{\partial\Delta}{\partial r} = 2(r - x\cos\varphi), \tag{E.18}$$

$$\frac{\partial(\Delta^{-1/2})}{\partial r} = -\frac{1}{2\Delta^{3/2}}\frac{\partial\Delta}{\partial r} = -\frac{r - x\cos\varphi}{\Delta^{3/2}}, \tag{E.19}$$

$$\frac{\partial\Delta}{\partial\varphi} = 2xr\sin\varphi, \tag{E.20}$$

$$\frac{\partial(\Delta^{-1/2})}{\partial\varphi} = -\frac{xr\sin\varphi}{\Delta^{3/2}}. \tag{E.21}$$

The latter equations allow us to find compact expressions for the following derivatives:

$$\frac{\partial(\cos\theta)}{\partial r} = -z\frac{r - x\cos\varphi}{\Delta^{3/2}}, \tag{E.22}$$

$$\frac{\partial\phi}{\partial\varphi} = -\frac{1}{1 + \frac{r^2\sin^2\varphi}{x - r\cos\varphi}}\frac{\partial}{\partial\varphi}\left(\frac{r\sin\varphi}{x - r\cos\varphi}\right) \tag{E.23}$$

$$= -\frac{xr\cos\varphi - r^2}{\Delta - z^2}, \tag{E.24}$$

$$\frac{\partial(\cos\theta)}{\partial\varphi} = -z\frac{xr\sin\varphi}{\Delta^{3/2}}, \tag{E.25}$$

$$\frac{\partial\phi}{\partial r} = -\frac{(x - r\cos\varphi)^2}{\Delta - z^2}\frac{\partial}{\partial r}\left(\frac{r\sin\varphi}{x - r\cos\varphi}\right) \tag{E.26}$$

$$= -\frac{(x - r\cos\varphi)^2}{\Delta - z^2}\frac{x\sin\varphi}{(x - r\cos\varphi)^2} \tag{E.27}$$

$$= -\frac{x\sin\varphi}{\Delta - z^2}. \tag{E.28}$$

Consequently, we find

$$\det J = z\frac{r - x\cos\varphi}{\Delta^{3/2}}\frac{xr\cos\varphi - r^2}{\Delta - z^2} - z\frac{x^2 r\sin^2\varphi}{\Delta^{3/2}}\frac{1}{\Delta - z^2} \tag{E.29}$$

$$= \frac{zr}{\Delta^{3/2}(\Delta - z^2)}\left\{(r - \cos\varphi)(x\cos\varphi - r) - x^2\sin^2\varphi\right\} \tag{E.30}$$

$$= \frac{zr}{\Delta^{3/2}(\Delta - z^2)}\left\{xr\cos\varphi - r^2 - x^2\cos^2\varphi + xr\cos\varphi - x^2\sin^2\varphi\right\} \tag{E.31}$$

$$= \frac{zr}{\Delta^{3/2}(\Delta - z^2)}\left\{x^2 + r^2 - 2xr\cos\varphi\right\} \tag{E.32}$$

$$= -\frac{zr}{\Delta^{3/2}}. \tag{E.33}$$

E.3 φ-integration

We split eq. (E.5) into four parts

$$\Gamma = \int_0^{2\pi} d\varphi \frac{1}{\delta^3} - (z \cos \theta_0 + x \sin \theta_0 \cos \phi_0) \int_0^{2\pi} d\varphi \frac{1}{\delta^4}$$
$$+ r_d \sin \theta_0 \cos \phi_0 \int_0^{2\pi} d\varphi \frac{\cos \varphi}{\delta^4} + r_d \sin \theta_0 \sin \phi_0 \int_0^{2\pi} d\varphi \frac{\sin \varphi}{\delta^4} \tag{E.34}$$
$$=: \Gamma_1 - (z \cos \theta_0 + x \sin \theta_0 \cos \phi_0)\Gamma_2 + r_d \sin \theta_0 \cos \phi_0 \Gamma_3 + r_d \sin \theta_0 \sin \phi_0 \Gamma_4 \tag{E.35}$$

and compute Γ_1, Γ_2, Γ_3, and Γ_4 in what follows.

E.3.1 Γ_1

Inserting the explicit expression for δ in eq. (D.3) allows us to write

$$\Gamma_1 \equiv \int_0^{2\pi} d\varphi \frac{1}{(\frac{L+M}{2} - \frac{M-L}{2} \cos \varphi)^{3/2}} \tag{E.36}$$

$$= \int_{-\pi}^{+\pi} d\varphi \frac{1}{(\frac{L+M}{2} - \frac{M-L}{2} \cos \varphi)^{3/2}}. \tag{E.37}$$

Using the Weierstrass substitution $\xi := \tan \frac{\varphi}{2}$ we find[1]

$$\Gamma_1 = 2 \int_{-\infty}^{+\infty} d\xi \frac{1}{1 + \xi^2} \frac{1}{(\frac{L+M}{2} - \frac{M-L}{2} \frac{1-\xi^2}{1+\xi^2})^{3/2}} \tag{E.38}$$

$$= 2 \int_{-\infty}^{+\infty} d\xi \frac{\sqrt{1 + \xi^2}}{[(1 + \xi^2)\frac{L+M}{2} - \frac{M-L}{2}(1 - \xi^2)]^{3/2}} \tag{E.39}$$

$$= 2 \int_{-\infty}^{+\infty} d\xi \frac{\sqrt{1 + \xi^2}}{(L + M\xi^2)^{3/2}}. \tag{E.40}$$

---

[1] Note that $\varphi = 2 \arctan \xi$, $d\varphi = 2d\xi/(1 + \xi^2)$, $\cos \varphi = (1 - \xi^2)/(1 + \xi^2)$ and $\tan(x) \to \pm\infty$ for $x \to \pm\pi/2$.

Now we substitute $\rho := \sqrt{M/L}\xi$ yielding

$$\Gamma_1 = 2\sqrt{\frac{L}{M}} \int\limits_{-\infty}^{+\infty} \mathrm{d}\rho \, \frac{\sqrt{1 + \frac{L}{M}\rho^2}}{[l(1 + \rho^2)]^{3/2}} \tag{E.41}$$

$$= \frac{2}{L\sqrt{M}} \int\limits_{-\infty}^{+\infty} \mathrm{d}\rho \, \frac{\sqrt{1 + \frac{L}{M}\rho^2}}{(1 + \rho^2)^{3/2}}. \tag{E.42}$$

With the substitution $u := \arctan\rho$ we arrive at[2]

$$\Gamma_1 = 2\sqrt{\frac{L}{M}} \int\limits_{-\infty}^{+\infty} \mathrm{d}\rho \, \frac{\sqrt{1 + \frac{L}{M}\rho^2}}{[l(1 + \rho^2)]^{3/2}} \tag{E.43}$$

$$= \frac{2}{L\sqrt{M}} \int\limits_{-\pi/2}^{+\pi/2} \mathrm{d}u \, \frac{\sqrt{1 + \frac{L}{M}\tan^2 u}}{\sqrt{1 + \tan^2 u}}. \tag{E.44}$$

Because $\sqrt{1 + \tan^2 u} = 1/\cos(u)$ on $[-\frac{\pi}{2}, +\frac{\pi}{2}]$ we finally find

$$\Gamma_1 = \frac{2}{L\sqrt{M}} \int\limits_{-\pi/2}^{+\pi/2} \mathrm{d}u \, \cos(u) \sqrt{1 + \frac{L}{M}\frac{\sin^2 u}{\cos^2 u}} \tag{E.45}$$

$$= \frac{2}{L\sqrt{M}} \int\limits_{-\pi/2}^{+\pi/2} \mathrm{d}u \, \sqrt{1 - \left(1 - \frac{L}{M}\right)\sin^2 u} \tag{E.46}$$

$$=: \frac{2}{L\sqrt{M}} \int\limits_{-\pi/2}^{+\pi/2} \mathrm{d}u \, f(u) \tag{E.47}$$

$$= \frac{4}{L\sqrt{M}} \int\limits_{0}^{+\pi/2} \mathrm{d}u \, \sqrt{1 - \frac{M - L}{M}\sin^2 u} \tag{E.48}$$

$$= \frac{4}{L\sqrt{M}} E\left(\sqrt{\frac{M - L}{M}}\right). \tag{E.49}$$

Note that in the first step we used the relation

$$\int_0^{2\pi} \mathrm{d}\varphi \, \Delta^{-3/2} = \int_0^{+\pi} \mathrm{d}\varphi \, \Delta^{-3/2} + \int_{+\pi}^{+2\pi} \mathrm{d}\varphi \, \Delta^{-3/2} \tag{E.50}$$

$$= \int_{-\pi}^{+\pi} \mathrm{d}\varphi \, \Delta^{-3/2}, \tag{E.51}$$

---

[2] Where the relations $\mathrm{d}u = \mathrm{d}\rho/(1 + \rho^2)$ and $u(x) \to \pm\pi/2$ for $x \to \pm\infty$ hold.

where

$$\int_{+\pi}^{+2\pi} d\varphi \, \Delta^{-3/2} = \int_{-\pi}^{0} d\varphi \, \Delta^{-3/2} \tag{E.52}$$

with the substitution $\varphi \mapsto \varphi - 2\pi$.

E.3.2 Γ_2

Starting from

$$\Gamma_2 \equiv \int_{0}^{2\pi} d\varphi \, \frac{1}{(\frac{L+M}{2} - \frac{M-L}{2} \cos \varphi)^2} \tag{E.53}$$

$$= \int_{-\pi}^{+\pi} d\varphi \, \frac{1}{(\frac{L+M}{2} - \frac{M-L}{2} \cos \varphi)^2} \tag{E.54}$$

and using the Weierstrass substitution $\xi := \tan \frac{\varphi}{2}$ again, we find

$$\Gamma_2 = 2 \int_{-\infty}^{+\infty} d\xi \, \frac{1 + \xi^2}{(L + M\xi^2)^2} \tag{E.55}$$

$$= 2 \int_{-\infty}^{+\infty} d\xi \, \frac{\sqrt{1 + \xi^2}}{(L + M\xi^2)^2}. \tag{E.56}$$

Now we substitute $\rho := \sqrt{M/L}\xi$ and obtain

$$\Gamma_2 = \frac{2}{L\sqrt{LM}} \int_{-\infty}^{+\infty} d\rho \, \frac{1 + \frac{L}{M}\rho^2}{(1 + \rho^2)^2} \tag{E.57}$$

$$= \frac{2}{L\sqrt{M}} \left\{ \frac{L}{M} \int_{-\infty}^{+\infty} d\rho \, \frac{1}{1 + \rho^2} + \left(1 - \frac{L}{M}\right) \int_{-\infty}^{+\infty} d\rho \, \frac{1}{(1 + \rho^2)^2} \right\} \tag{E.58}$$

$$= \frac{2\pi}{L\sqrt{M}} \left\{ \frac{L}{M} + \frac{1}{2} - \frac{1}{2}\frac{L}{M} \right\} \tag{E.59}$$

$$= \frac{\pi(L + M)}{(LM)^{3/2}}. \tag{E.60}$$

In the second step we performed the partial fraction decomposition

$$\frac{1 + \frac{L}{M}\rho^2}{(1 + \rho^2)^2} = \frac{\frac{L}{M}}{1 + \rho^2} + \frac{1 - \frac{L}{M}}{(1 + \rho^2)^2} \tag{E.61}$$

and in the third step we made use of the relation[3]

$$\int_{-\infty}^{+\infty} d\rho \, \frac{1}{1+\rho^2} = \int_{-\pi/2}^{+\pi/2} du = \pi, \tag{E.62}$$

and

$$\int_{-\infty}^{+\infty} d\rho \, \frac{1}{(1+\rho^2)^2} = \frac{\pi}{2}. \tag{E.63}$$

E.3.3 Γ_3

For Γ_3 we proceed similarly as in the previous cases. Beginning from

$$\Gamma_3 \equiv \int_0^{2\pi} d\varphi \, \frac{\cos\varphi}{(\frac{L+M}{2} - \frac{M-L}{2}\cos\varphi)^2} \tag{E.64}$$

$$= \int_{-\pi}^{+\pi} d\varphi \, \frac{\cos\varphi}{(\frac{L+M}{2} - \frac{M-L}{2}\cos\varphi)^2} \tag{E.65}$$

and using the Weierstrass substitution $\xi := \tan\frac{\varphi}{2}$, we find

$$\Gamma_3 \equiv \int_{-\infty}^{+\infty} d\xi \, \frac{1-\xi^2}{(1+\xi^2)^2} \frac{1}{(\frac{L+M}{2} - \frac{M-L}{2}\frac{1-\xi^2}{1+\xi^2})^2} \tag{E.66}$$

$$= \int_{-\infty}^{+\infty} d\xi \, \frac{1-\xi^2}{(L+M\xi^2)^2} =: \Gamma_3^{(1)} + \Gamma_3^{(2)}. \tag{E.67}$$

The letter expression is split into two integrals, which we evaluate as follows. For the first one, we obtain

$$\Gamma_3^{(1)} = 2\int_{-\infty}^{+\infty} d\xi \, \frac{1}{(L+M\xi^2)^2} \tag{E.68}$$

$$= \frac{2}{L\sqrt{LM}} \int_{-\infty}^{+\infty} d\rho \, \frac{1}{(1+\rho^2)^2} \tag{E.69}$$

$$= \frac{\pi}{L\sqrt{LM}} \tag{E.70}$$

---

[3] along with the substitution $du := d(\arctan\rho) = d\rho/(1+\rho^2)$.

while the second integral reduces to

$$\Gamma_3^{(2)} = -2 \int_{-\infty}^{+\infty} d\xi \, \frac{\xi^2}{(L + M\xi^2)^2} \tag{E.71}$$

$$= -\frac{2}{L\sqrt{LM}} \int_{-\infty}^{+\infty} d\rho \, \frac{\frac{L}{M}\rho^2}{(1 + \rho^2)^2} \tag{E.72}$$

$$= -\frac{2}{M\sqrt{LM}} \int_{-\infty}^{+\infty} d\rho \, \frac{\rho^2}{(1 + \rho^2)^2} \tag{E.73}$$

$$= -\frac{2}{M\sqrt{LM}} \left\{ \int_{-\infty}^{+\infty} d\rho \, \frac{1}{1 + \rho^2} - \int_{-\infty}^{+\infty} d\rho \, \frac{1}{(1 + \rho^2)^2} \right\} \tag{E.74}$$

$$= -\frac{\pi}{M\sqrt{LM}}. \tag{E.75}$$

Here we made use of the partial fraction decomposition

$$\frac{\rho^2}{(1 + \rho^2)^2} = \frac{\rho^2}{1 + \rho^2} - \frac{1}{(1 + \rho^2)^2}. \tag{E.76}$$

Finally, addition of $\Gamma_3^{(1)}$ and $\Gamma_3^{(2)}$ leads to

$$\Gamma_3 = \frac{\pi}{L\sqrt{M}} \left(\frac{1}{L} - \frac{1}{M} \right) \tag{E.77}$$

$$= \frac{\pi(M - L)}{(LM)^{3/2}} \tag{E.78}$$

$$= \frac{4\pi x r_\mathrm{d}}{(LM)^{3/2}}, \tag{E.79}$$

with the relation $M - L = 4x r_\mathrm{d}$.

E.3.4 Γ_4

The fourth integral Γ_4 can be evaluated by exploiting some trigonometric relations. We start from

$$\Gamma_4 \equiv \int_0^{2\pi} d\varphi \, \frac{\sin \varphi}{(\frac{L+M}{2} - \frac{M-L}{2} \cos \varphi)^2} \tag{E.80}$$

$$\equiv \int_0^{\pi} d\varphi \, \frac{\sin \varphi}{(\frac{L+M}{2} - \frac{M-L}{2} \cos \varphi)^2} + \int_{\pi}^{2\pi} d\varphi \, \frac{\sin \varphi}{(\frac{L+M}{2} - \frac{M-L}{2} \cos \varphi)^2} \tag{E.81}$$

and perform the substitution $\xi \equiv \pi - \varphi$ on the first integral and $\xi \equiv \varphi - \pi$ on the second integral of the latter expression. We arrive at

$$\Gamma_4 \equiv -\int_{\pi}^{0} d\varphi \, \frac{\sin(\pi - \xi)}{(\frac{L+M}{2} - \frac{M-L}{2} \cos(\pi - \xi))^2} + \int_{0}^{\pi} d\varphi \, \frac{\sin(\pi + \xi)}{(\frac{L+M}{2} - \frac{M-L}{2} \cos(\pi + \xi))^2}. \tag{E.82}$$

Using $\sin(\pi \pm \xi) = \mp \sin \xi$ and $\cos(\pi \pm \xi) = -\cos \xi$, Γ_4 reduces to

$$\Gamma_4 \equiv \int_{0}^{\pi} d\varphi \, \frac{\sin \xi}{(\frac{L+M}{2} + \frac{M-L}{2} \cos \xi)^2} - \int_{0}^{\pi} d\varphi \, \frac{\sin \xi}{(\frac{L+M}{2} + \frac{M-L}{2} \cos \xi)^2} \tag{E.83}$$

$$= 0. \tag{E.84}$$

Matter-Neutrino Resonance Locations

The initial conditions employed in this work are close to the ones used by [176], who also investigated the flavor evolution in BNS mergers. This allows a close comparison between the two different works. In particular, we compute the locations above the remnant where MNR occurs and compare with the results reported by [176] in their figure 6. These locations can be identified as cancellation points, i.e., points where the unoscillated neutrino self-interaction potential cancels with the matter potential along a specific trajectory, $\lambda + \mu \approx 0$. In figure F.1, we represent the cancellation points for several different trajectories starting from the disk (indicated by a ★). Stars with equal colors correspond to the same emission point with the same color, drawn as •. Thereby, we excluded all points where the crossing starts dominated by matter. The emerging picture suggests that the resonances for neutrinos originating from one side of the disk are preferably located at the edge of the funnel. Neutrinos emerging from the MNS will all encounter MNR, probably with some flavor transformations depending on the adiabaticity. In contrast, neutrinos emitted from the disk will encounter MNR only if they propagate through the central regions of the funnel, where the matter density is relatively low. Remarkably, this picture is qualitatively consistent with the results found in [176]. Nevertheless, quantitative differences between the two works can be present and traced back to the different approaches used in the two works to model the radiation field outside the neutrino surfaces. On the one hand, we have assumed a thin disk model, emitting thermal radiation from a spectrally averaged, single-temperature neutrino surface. On the other hand, [176] used an energy-dependent leakage scheme and a ray-tracing algorithm to model the emission from a finite size, thick disk. They also take explicitly into account radiation damping effects outside the neutrino surfaces.

In figure F.2, we show how the MNR distribution is affected if we include the points where the crossing stars matter dominated as well. Compared to figure F.1, the distribution appears more symmetric along the polar axis.

We also show how a rescaling of the luminosities would impact on the MNR distribution. For this purpose, we rescaled the luminosities in order to have a similar number flux ratio consistent with the values obtained in Foucart *et al.* (2016) [GR, gray GR M1, LS220 EOS] [212], see also section 4.6.4. It turns out that the overall form looks similar to the MNR point distribution shown in figure F.1. But compared to our standard case, presented in figure F.1, the MNR points are "pushed" to higher z values.
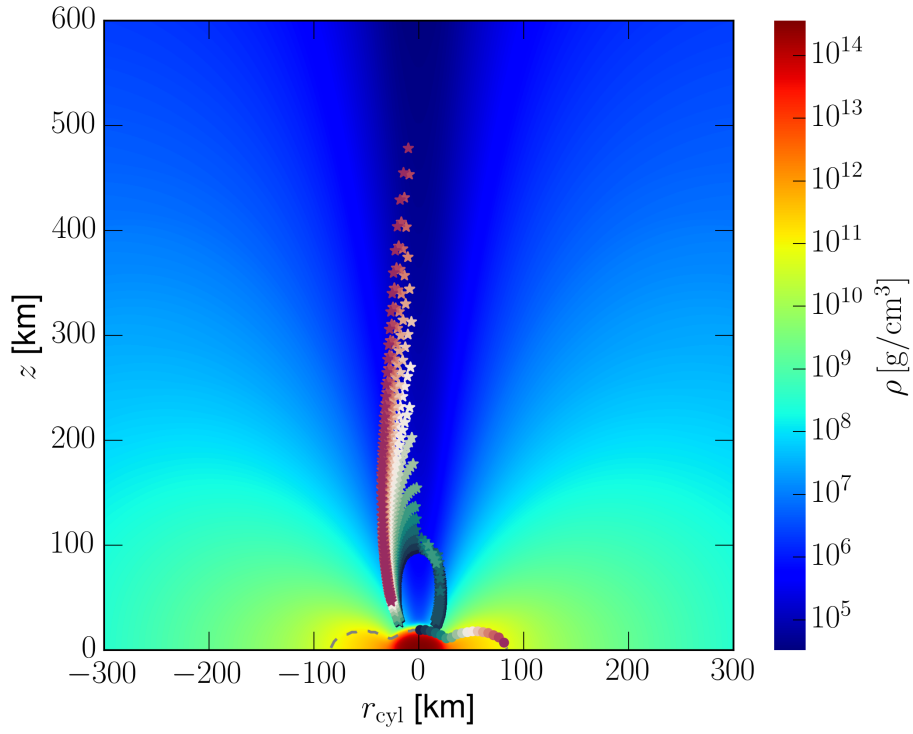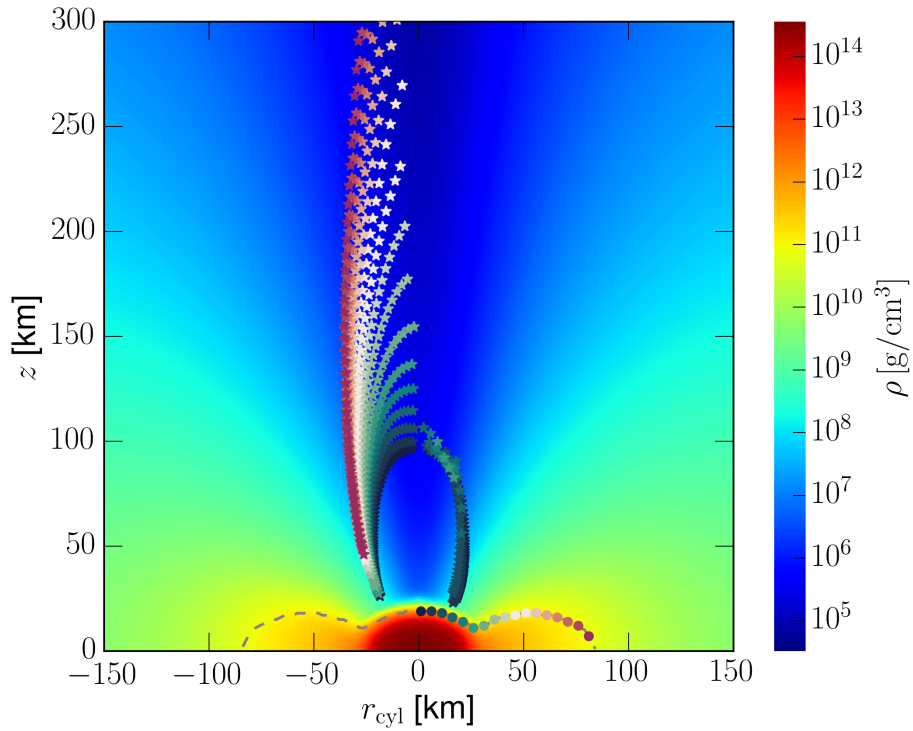
Figure F.1.: Cancellation points ($\star$), i.e. points where $\lambda + \mu \approx 0$, for several trajectories above the BNS merger remnant. The emission points are represented by $\bullet$. Emission and cancellation points with the same color refer to a single trajectory. Points where the crossing starts dominated by matter are excluded. Color coded is the density of matter. The bottom plot (b) shows an enlarged section of a smaller spatial region of (a).
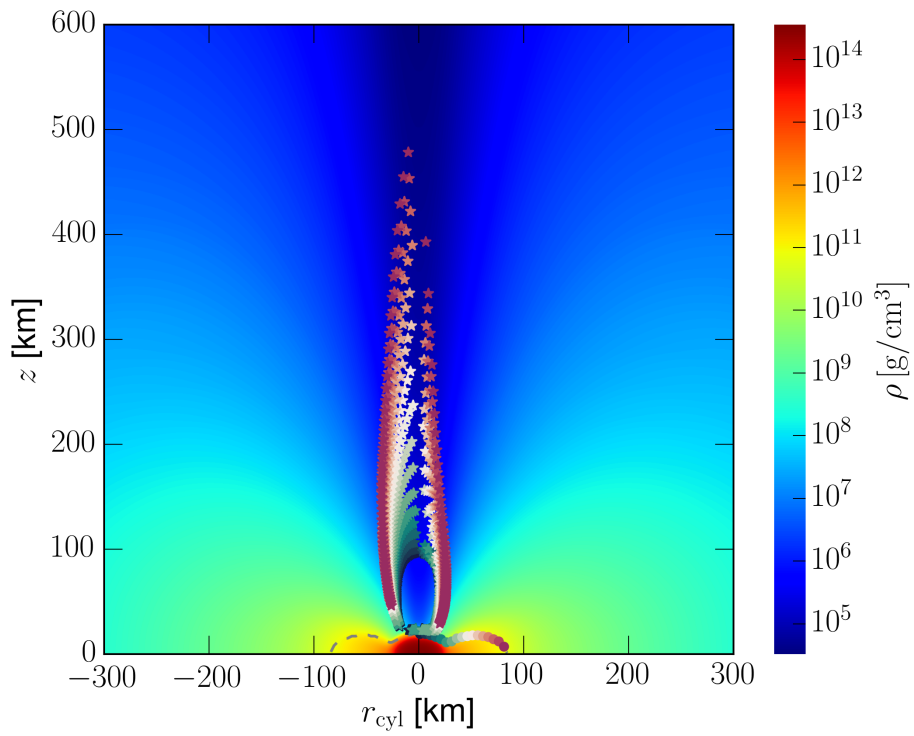
Figure F.2.: Same as figure F.1 (a), but points where the crossing starts dominated by matter are included.
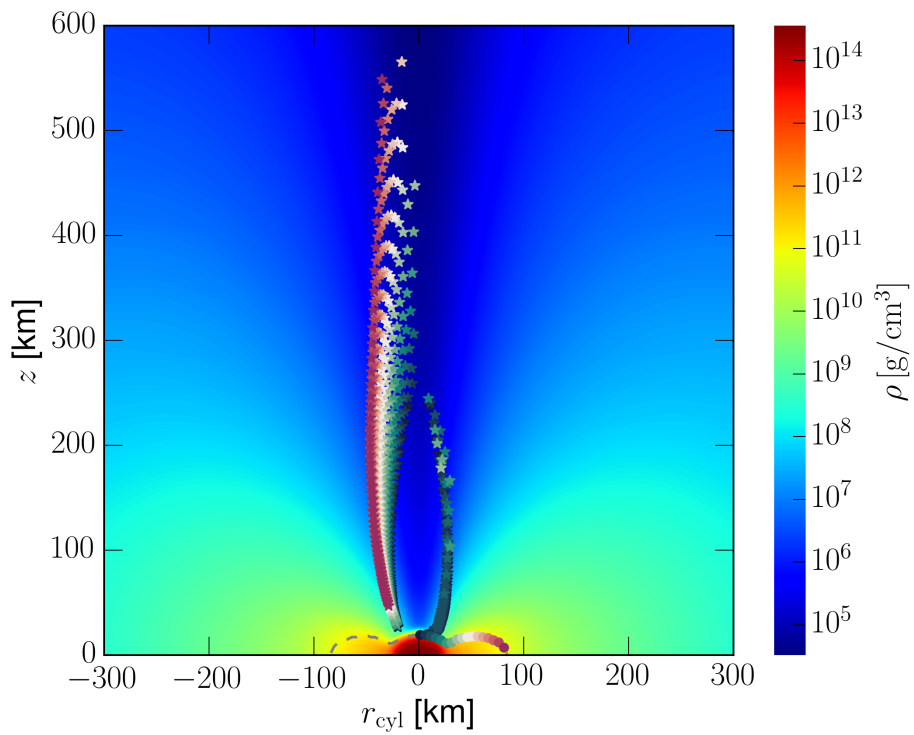
Figure F.3.: Same as figure F.1 (a), but with rescaled luminosities.

Collected Data

In the following table, we report a summary of published data concerning the neutrino luminosities and mean energies of a binary neutron star merger. We considered simulations of binary NS mergers [211, 212, 254–256] or merger aftermaths [25, 197, 198], including neutrino emission as well as characterized by the presence of a (possibly unstable) massive neutron star surrounded by a thick accretion disk. Since they run for very different amounts of time, for the merger simulations we choose the values when the luminosities have reached quasi-stationary values, while for the aftermath simulations the values close to the beginning of the calculation.

Source	$t - t_{\text{merger}}$	L_{ν_e}	$L_{\bar{\nu}_e}$	L_{ν_x}	$\langle E_{\nu_e} \rangle$	$\langle E_{\bar{\nu}_e} \rangle$	$\langle E_{\nu_x} \rangle$	Notes
[25]	–	15	32	8	10.6	15.3	17.3	Grid, Newtonian, spectral leakage, HS(TM1) EOS, MNS + disk.
[254]	8	16	43	6	13	20	28	Grid, Newtonian, gray leakage, LS(180) EOS, $1.65 - 1.65\,\mathcal{M}_\odot$, no spin.
[255]	18	45	130	25	9	15	20	SPH, Newtonian, gray leakage, Shen EOS, $1.4 - 1.4\,\mathcal{M}_\odot$, no spin.
[198]	–	20	32	6	11	16	22	Grid, Newtonian, MGFLD, Shen EOS, MNS + disk.
[256]	16	30	60	10	8	14.4	26.3	SPH, Newtonian, gray leakage, Shen EOS, $1.3 - 1.4\,\mathcal{M}_\odot$, no spin.
[197]	–	55	45	–	12	15	–	Grid, Newtonian, gray leakage, Timmes & Swesty EOS, MNS + disk.
[211]	30	120	200	15	–	–	–	Grid, GR, gray GR leakage + moment formalism for free streaming ν's, HS(TM1) EOS, $1.35 - 1.35\,\mathcal{M}_\odot$, no spin.
[211]	30	100	150	10	–	–	–	Grid, GR, ν's as above, HS(DD2) EOS, $1.35 - 1.35\,\mathcal{M}_\odot$, no spin.
[211]	10	175	280	100	–	–	–	Grid, GR, ν as above, SFHo EOS, $1.35 - 1.35\,\mathcal{M}_\odot$, no spin.
[212]	10	120	210	30	13	20	26	Grid, GR, gray GR leakage, LS(220) EOS, $1.2 - 1.2\,\mathcal{M}_\odot$, no spin.
[212]	10	160	220	22.5	13	20	24	Grid, GR, gray GR leakage, HS(DD2) EOS, $1.2 - 1.2\,\mathcal{M}_\odot$, no spin.
[212]	10	190	300	55	14	21	29	Grid, GR, gray GR leakage, SFHo EOS, $1.2 - 1.2\,\mathcal{M}_\odot$, no spin.
[212]	10	60	210	70	13	20	26	Grid, GR, gray GR M1, LS(220) EOS, $1.2 - 1.2\,\mathcal{M}_\odot$, no spin.

Table G.1.: A summary of published data. We considered simulations of binary NS mergers or of their aftermath. In the former case, we report the time when the data were taken with respect to the beginning of the merger (in ms). In the latter case, we report data close to the beginning of the simulation. For all cases, we list the neutrino luminosities (in $10^{51}\,\text{erg}\,\text{s}^{-1}$), where for ν_x, the values correspond to each single species and, when available, the neutrino mean energies (in MeV, in the case of [212] the quantities provided are the root mean square energies $\sqrt{\langle E_\nu^2 \rangle}$.

Cooling Luminosities and Role of Absorption

In our model, the neutrino flavor evolution from a BNS merger depends on the emission characteristics at the neutrino surfaces and no absorption processes are explicitly modeled outside them. In particular, the number flux is expressed as $F_\nu \propto L_\nu / \langle E_\nu \rangle$ (see expression below eq. (4.18)), where L_ν and $\langle E_\nu \rangle$ are assumed to be the luminosity and mean energies at the neutrino surfaces.

The luminosity values used in our calculations were obtained in the simulation of [25]. Two kinds of luminosities were considered in this work. The cooling luminosities $L_{\nu,\text{cool}}$, where neutrino absorption outside the neutrino surfaces is neglected, and the net luminosities $L_{\nu,\text{net}}$, where absorption processes are taken into account everywhere. Thus, in the latter case, the damping of the luminosities due to the absorption from the disk outside the last scattering surfaces was taken into account.

According to these definitions, at the neutrino surface ($\tau \approx 2/3$) the two luminosities coincide, while outside it the cooling luminosity is always larger than the net one. In figure H.1 we show, for purely illustrative purposes, a schematic behavior[1] for $L_{\nu,\text{net}}$ and $L_{\nu,\text{cool}}$. Outside, but close to the neutrino surface, neutrino cooling dominates while farther away neutrino heating becomes the dominant process.

Reference [25] provides only information about the luminosity values far away from the neutrino surface (symbolically we write $r \to \infty$). This introduces a potential ambiguity in the choice of the values of L_ν and $\langle E_\nu \rangle$ at the neutrino surfaces in our model. For our calculations, we have chosen $L_{\nu,\text{net}}$ (table 4.3) and in the following we will reason why our choice is consistent with our assumptions and results.

In radiative transport theory (see, e.g., [257]), one phenomenologically describes the intensity loss in a beam as it propagates a distance $\mathrm{d}r$ by the following transfer equation (where we consider absorption only):

$$\frac{\mathrm{d}I(E,r)}{\mathrm{d}r} = -\alpha I(E,r). \tag{H.1}$$

Here, $I(E,r)$ denotes the local, specific intensity (i.e., the intensity per unit energy per solid angle) and α corresponds to an absorption coefficient, where we follow the convention that

---

[1] which is not necessarily representative for our BNS merger remnant, but is sufficient to underline the basic concepts involved.
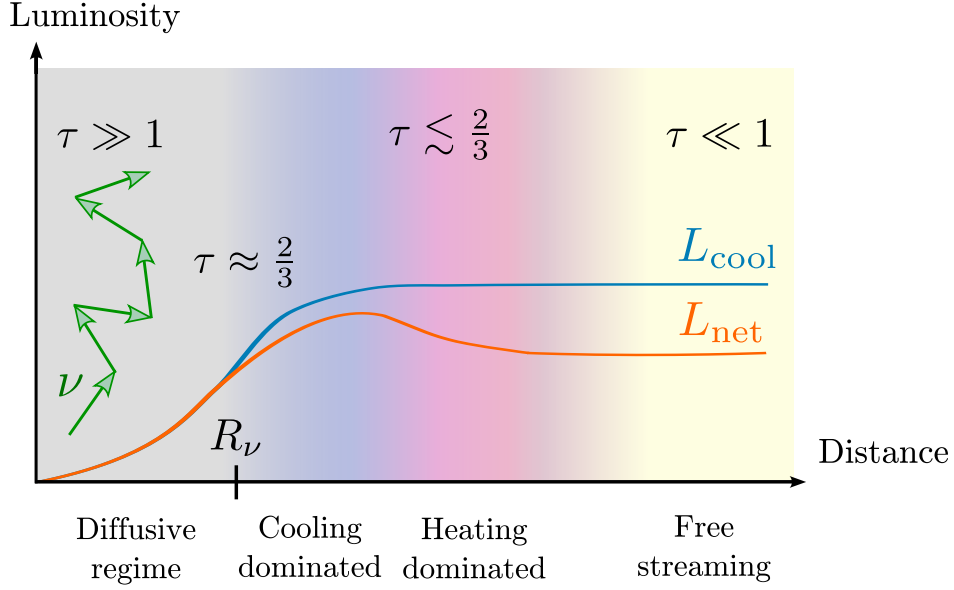
Figure H.1.: Schematic behavior of net and cooling luminosities.

$\alpha > 0$ if energy is removed from the beam (this is why a minus sign appears explicitly in the transfer equation). The equation yields the solution

$$I(E, r) = I(E, r_0)e^{-\int_{r_0}^{r} dr'\, \alpha(E,r')} \tag{H.2}$$

$$= I(E, r_0)e^{-\tau_{\text{abs}}(E,r)}, \tag{H.3}$$

where the integration is performed along the trajectory of the propagating ray and r_0 is an arbitrary point which specifies the zero point of the absorption optical depth[2] [257]

$$\tau_{\text{abs}}(E, r') = \int_{r_0}^{r} dr'\, \alpha(E, r'). \tag{H.4}$$

The solution above shows that the specific intensity is decreasing along a given path. Motivated by this, we model the number of neutrinos at a distance r from the neutrino surface as [258]

$$N_\nu(r) = N_\nu(R_\nu)\, e^{-(\tau_{\text{abs}}(R_\nu)-\tau_{\text{abs}}(r))} \qquad (R_\nu \lesssim r < \infty), \tag{H.5}$$

where the specific form of the exponent makes sure that absorption occurs only outside the neutrino surface ($r \gtrsim R_\nu$). Note that $N_\nu(r \to \infty) = N_\nu(R_\nu)\, e^{-\tau_{\text{abs}}(R_\nu)}$. In analogy to this equation, we write for the luminosities

$$L_{\nu,\text{net}}(r) = L_\nu(R_\nu)\, e^{-(\tau_{\text{abs}}(R_\nu)-\tau_{\text{abs}}(r))}, \tag{H.6}$$

where at the neutrino surface we have[3] $L_\nu(R_\nu) = L_{\nu,\text{cool}}(R_\nu)$.

---

[2] Note that per definition, the following relation between the absorption and scattering optical depth holds: $\tau \geq \tau_{\text{abs}}$.

[3] If absorption was negligible, we would have $L_{\nu,\text{net}}(r) = L_{\nu,\text{cool}}(r) = L_\nu(R_\nu)$.

In [25], the luminosities were computed by integrating over the whole volume and it was demonstrated that absorption is indeed relevant. However, we need the luminosity at the neutrino surface, which is contained in a much smaller volume. Since neutrino heating leads to an effective reduction of the luminosity with respect to the case where only cooling is involved, using net luminosities gives a better estimate of $L(R_\nu)$. Using $L_{\nu,\text{cool}}^\infty$ instead would result in an overestimate of the luminosities.

Inside the funnel, the neutrino number densities are high, but due to the relatively low matter density ($\rho_{\text{matt}} \lesssim 10^7\,\text{g}\,\text{cm}^{-3}$) the impact of neutrino absorption on the remnant dynamics is negligible here. However, with increasing cylindrical radius the net neutrino heating can deposit energy efficiently [25], since the matter density increases and matter is rotating inside the disk around the MNS.

To distinguish among these two different behaviors and to check if absorption is relevant along the trajectories we studied, we computed the absorption optical depth τ_{abs} based on our disk model. Thereby, we took into account (anti)neutrino absorption by nucleons only and performed the calculations along the neutrino trajectory. Note that we did not follow the same approach as before in determining the neutrino surfaces (see section 4.2.2). In case of the latter, we computed the optical depth along rays in different directions from a given point and took the minimum, which is appropriate in regions where neutrinos undergo many scattering events and are not nearly free-streaming. If we now assume that only absorption occurs and we track a neutrino along a specific trajectory, the latter approach will not work anymore, since neutrinos do not change their directions. For this reason, it is more reasonable to consider only the direction along the ray that represents this particular path.

In the explicit calculations, presented in figure H.2, it turns out that τ_{abs} is quickly decreasing with increasing distance and absorption could be relevant only very close to the neutrino surface (where τ_{abs} is still small and could have only minor effects). However, in the regions where we observe flavor conversion, absorption is practically negligible.

It is important to stress that if absorption was relevant, this would have crucial consequences: Treating the region outside the neutrino surface as free-streaming is not admissible anymore, and we need to employ a different approach to track the neutrino flavor evolution, i.e., we need to include collision terms in the quantum-kinetic equations (see [102, 103]).
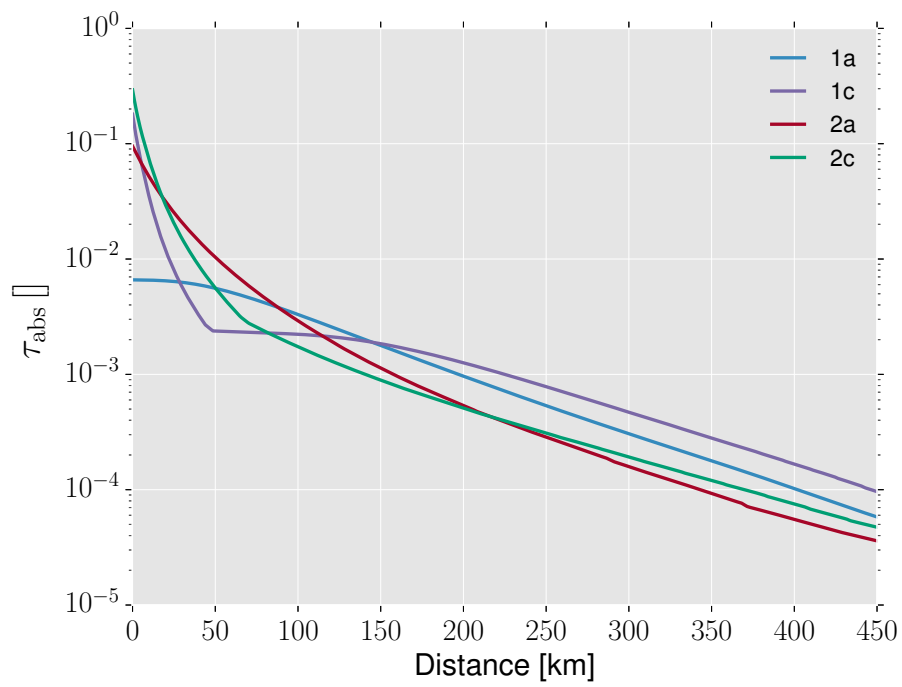
Figure H.2.: Absorption optical depth along trajectories 1a, 1c, 2a, and 2c.

Bibliography

[1] E. Amaldi, *From the discovery of the neutron to the discovery of nuclear fission*, Phys. Rept. **111**, 1–332 (1984).

[2] C. L. Cowan, F. Reines, F. B. Harrison, H. W. Kruse, and A. D. McGuire, *Detection of the free neutrino: A Confirmation*, Science **124**, 103–104 (1956).

[3] G. Danby, J. M. Gaillard, K. A. Goulianos, L. M. Lederman, N. B. Mistry, M. Schwartz, and J. Steinberger, *Observation of High-Energy Neutrino Reactions and the Existence of Two Kinds of Neutrinos*, Phys. Rev. Lett. **9**, 36–44 (1962).

[4] W. C. Haxton, R. G. Hamish Robertson, and A. M. Serenelli, *Solar Neutrinos: Status and Prospects*, Ann. Rev. Astron. Astrophys. **51**, 21–61 (2013).

[5] B. Pontecorvo, *Mesonium and anti-mesonium*, Sov. Phys. JETP **6**, 429 (1957), Zh. Eksp. Teor. Fiz. 33, 549 (1957).

[6] B. Pontecorvo, *Inverse beta processes and nonconservation of lepton charge*, Sov. Phys. JETP **7**, 172–173 (1958), Zh. Eksp. Teor. Fiz. 34, 247 (1957).

[7] Z. Maki, M. Nakagawa, and S. Sakata, *Remarks on the unified model of elementary particles*, Prog. Theor. Phys. **28**, 870–880 (1962).

[8] Y. Katayama, K. Matumoto, S. Tanaka, and E. Yamada, *Possible unified models of elementary particles with two neutrinos*, Prog. Theor. Phys. **28**, 675 (1962).

[9] V. Gribov and B. Pontecorvo, *Neutrino astronomy and lepton charge*, Physics Letters B **28**, 493–496 (1969).

[10] M. Maggiore, *Gravitational Waves. Volume 1: Theory and Experiments* (Oxford University Press Inc., New York, 2008).

[11] J. Aasi et al., *Advanced LIGO*, Class. Quant. Grav. **32**, 074001 (2015).

[12] F. Acernese et al., *Advanced Virgo: a second-generation interferometric gravitational wave detector*, Class. Quant. Grav. **32**, 024001 (2015).

[13] P. Amaro-Seoane et al., *eLISA/NGO: Astrophysics and cosmology in the gravitational-wave millihertz regime*, GW Notes **6**, 4–110 (2013).

[14] K. Hotokezaka, K. Kiuchi, K. Kyutoku, T. Muranushi, Y.-i. Sekiguchi, M. Shibata, and K. Taniguchi, *Remnant massive neutron stars of binary neutron star mergers: Evolution process and gravitational waveform*, Phys. Rev. **D88**, 044026 (2013).

[15] S. Rosswog, *The multi-messenger picture of compact binary mergers*, Int. J. Mod. Phys. **D24**, 1530012 (2015).

[16] M. Shibata, *Numerical relativity*, 100 Years of General Relativity (World Scientific Publishing Company Pte Limited, 2015).

[17] J. M. Lattimer and D. N. Schramm, *Black-hole-neutron-star collisions*, ApJL. **192**, L145–L147 (1974).

[18] J. M. Lattimer and D. N. Schramm, *The tidal disruption of neutron stars by black holes in close binaries*, ApJ **210**, 549–567 (1976).

[19] B. S. Meyer, *Decompression of initially cold neutron star matter - A mechanism for the r-process?*, ApJ **343**, 254–276 (1989).

[20] D. Eichler, M. Livio, T. Piran, and D. N. Schramm, *Nucleosynthesis, Neutrino Bursts and Gamma-Rays from Coalescing Neutron Stars*, Nature **340**, 126–128 (1989).

[21] J. A. Faber and F. A. Rasio, *Binary Neutron Star Mergers*, Living Rev. Rel. **15**, 8 (2012).

[22] L.-X. Li and B. Paczynski, *Transient events from neutron star mergers*, Astrophys. J. **507**, L59 (1998).

[23] S. R. Kulkarni, *Modeling supernova-like explosions associated with gamma-ray bursts with short durations*, arXiv: 0510256 [astro-ph] (2005).

[24] M. Tanaka, *Kilonova/Macronova Emission from Compact Binary Mergers*, Adv. Astron. **2016**, 6341974 (2016).

[25] A. Perego, S. Rosswog, R. M. Cabezón, O. Korobkin, R. Käppeli, A. Arcones, and M. Liebendörfer, *Neutrino-driven winds from neutron star merger remnants*, MNRAS **443**, 3134–3156 (2014).

[26] M. Frensel, M.-R. Wu, C. Volpe, and A. Perego, *Neutrino flavor evolution in binary neutron star merger remnants*, Phys. Rev. D **95**, 023011 (2017).

[27] B. Pontecorvo, *Inverse β-Decay*, Chalk River Laboratory Report PD-205 (1946).

[28] H. Georgi and M. Luke, *Neutrino moments, masses and custodial $SU(2)$ symmetry*, Nuclear Physics B **347**, 1–11 (1990).

[29] T. A. Y. Fukuda et al., *Evidence for Oscillation of Atmospheric Neutrinos*, Phys. Rev. Lett. **81**, 1562–1567 (1998).

[30] T. Kajita, E. Kearns, and M. Shiozawa, *Establishing atmospheric neutrino oscillations with Super-Kamiokande*, Nucl. Phys. **B908**, 14–29 (2016).

[31] C. Patrignani et al., *Review of Particle Physics*, Chin. Phys. **C40**, 100001 (2016).

[32] Z.-Z. Xing and S. Zhou, *Neutrinos in Particle Physics, Astronomy and Cosmology* (Zhejiang University Press, Hangzhou and Springer-Verlag Berlin Heidelberg, 2011).

[33] E. Witten, *Lepton number and neutrino masses*, Nucl. Phys. Proc. Suppl. **91**, 3–8 (2001).

[34] A. de Gouvêa, *Neutrino mass models*, Annual Review of Nuclear and Particle Science **66**, 197–217 (2016).

[35] S. Weinberg, *Baryon and Lepton Nonconserving Processes*, Phys. Rev. Lett. **43**, 1566–1570 (1979).

[36] S. Bludman, D. Kennedy, and P. Langacker, *Seesaw model solutions of the solar neutrino problem*, Nuclear Physics B **374**, 373–391 (1992).

[37] R. N. Mohapatra and P. B. Pal, *Massive Neutrinos in Physics and Astrophysics*, 3rd ed. (World Scientific Publishing Co. Pte. Ltd., 2004).

[38] E. Majorana, *Theory of the Symmetry of Electrons and Positrons*, Nuovo Cim. **14**, 171–184 (1937).

[39] C. Giunti and C. W. Kim, *Fundamentals of Neutrino Physics and Astrophysicst* (Oxford University Press, 2007).

[40] C. Giunti, C. W. Kim, and U. W. Lee, *Remarks on the weak states of neutrinos*, Phys. Rev. D **45**, 2414–2420 (1992).

[41] R. Slansky, S. Raby, T. Goldman, G. Garvey, as told to N. G. Cooper, *The Oscillating Neutrino. An Introduction to Neutrino Masses and Mixing*, in Celebrating the Neutrino, Los Alamos Science Number 25 (1997).

[42] T. Kajita, *The Measurement of Neutrino Properties with Atmospheric Neutrinos*, Ann. Rev. Nucl. Part. Sci. **64**, 343–362 (2014).

[43] S. Bilenky, *Introduction to the Physics of Massive and Mixed Neutrinos* (Springer-Verlag Berlin/Heidelberg, 2010).

[44] F. Suekane, *Neutrino Oscillations. A Practical Guide to Basics and Applications* (Springer Japan, 2015).

[45] I. Esteban, M. C. Gonzalez-Garcia, M. Maltoni, I. Martinez-Soler, and T. Schwetz, *Updated fit to three neutrino mixing: exploring the accelerator-reactor complementarity*, arXiv: 1611.01514 [hep-ph] (2016).

[46] L. S. Kisslinger, *Review of Neutrino Oscillations With Sterile and Active Neutrinos*, Int. J. Mod. Phys. **A31**, 1630037 (2016).

[47] A. Palazzo, *Phenomenology of light sterile neutrinos: a brief review*, Mod. Phys. Lett. **A28**, 1330004 (2013).

[48] A. Boyarsky, O. Ruchayskiy, and M. Shaposhnikov, *The Role of sterile neutrinos in cosmology and astrophysics*, Ann. Rev. Nucl. Part. Sci. **59**, 191–214 (2009).

[49] S. M. Bilenky, *Some comments on high precision study of neutrino oscillations*, Phys. Part. Nucl. Lett. **12**, 453–461 (2015).

[50] P. Vogel, L. Wen, and C. Zhang, *Neutrino Oscillation Studies with Reactors*, Nature Commun. **6**, 6935 (2015).

[51] X. Qian and P. Vogel, *Neutrino mass hierarchy*, Progress in Particle and Nuclear Physics **83**, 1–30 (2015).

[52] T. K. Kuo and J. Pantaleone, *Neutrino oscillations in matter*, Rev. Mod. Phys. **61**, 937–979 (1989).

[53] G. G. Raffelt, *Stars as laboratories for fundamental physics: the astrophysics of neutrinos, axions, and other weakly interacting particles* (University of Chicago Press, 1996).

[54] D. Boyanovsky and C. M. Ho, *Charged lepton mixing and oscillations from neutrino mixing in the early universe*, Astropart. Phys. **27**, 99–112 (2007).

[55] G. G. Raffelt and W. Rodejohann, *Massive neutrinos in astrophysics*, in 4th National Summer School for German-speaking Graduate Students of Theoretical Physics Saalburg, Germany, August 31-September 11, 1998 (1998).

[56] E. K. Akhmedov and A. Yu. Smirnov, *Paradoxes of neutrino oscillations*, Phys. Atom. Nucl. **72**, 1363–1381 (2009).

[57] G. M. Fuller, *Consequences of Neutrino Mass and Flavor Mixing for Core Collapse Supernovae*, in Open Issues in Core Collapse Supernova Theory: An Overview, edited by A. Mezzacappa and G. M. Fuller, Proceedings from the Institute for Nuclear Theory - Vol. 14, University of Washington, Seattle, 22-24 June 2004 (World Scientific Publishing Co. Pte. Ltd., 2005).

[58] A. S. Dighe and A. Y. Smirnov, *Identifying the neutrino mass spectrum from a supernova neutrino burst*, Phys. Rev. D **62**, 033007 (2000).

[59] T. K. Kuo and J. Pantaleone, *Solar-neutrino problem and three-neutrino oscillations*, Phys. Rev. Lett. **57**, 1805–1808 (1986).

[60] J. Lesgourgues, G. Mangano, G. Miele, and S. Pastor, *Neutrino cosmology* (Cambridge University Press, 2013).

[61] L. Wolfenstein, *Neutrino oscillations in matter*, Phys. Rev. D **17**, 2369–2374 (1978).

[62] M. Keil, *Supernova Neutrino Spectra and Applications to Flavor Oscillations*, Dissertation, Technical University of Munich, arXiv: 0308228 [astro-ph], 2003.

[63] D. Nötzold and G. Raffelt, *Neutrino dispersion at finite temperature and density*, Nucl. Phys. B **307**, 924–936 (1988).

[64] D. B. Williams and C. B. Carter, *Transmission Electron Microscopy. A Textbook for Materials Science*, 2nd ed. (Springer Science+Business Media, 2009).

[65] R. Schäfer and P. C. Schmidt, *Methods in Physical Chemistry. Volume 2* (Wiley-VCH Verlag & Co. KGaA, 2012).

[66] Q. Ho-Kim and X.-Y. Pham, *Elementary Particles and Their Interactions: Concepts and Phenomena* (Springer-Verlag Berlin Heidelberg New York, 1998).

[67] J. Kopp, *Theoretical Neutrino Physics*, Lecture notes, Johannes Gutenberg University Mainz (2015).

[68] M. Artin, *Algebra* (Prentice Hall Inc., New Jersey, 1991).

[69] M. Blennow and A. Yu. Smirnov, *Neutrino propagation in matter*, Adv. High Energy Phys. **2013**, 972485 (2013).

[70] S. P. Mikheev and A. Yu. Smirnov, *Resonance Amplification of Oscillations in Matter and Spectroscopy of Solar Neutrinos*, [Yad. Fiz. 42, 1441 (1985)] Sov. J. Nucl. Phys. **42**, 913–917 (1985).

[71] S. Mikheyev and A. Smirnov, *Resonant amplification of ν oscillations in matter and solar-neutrino spectroscopy*, English, Il Nuovo Cim. C **9**, 17–26 (1986).

[72] K. Zuber, *Neutrino Physics* (Taylor & Francis Group, LLC, 2004).

[73] H. A. Bethe, *A Possible Explanation of the Solar Neutrino Puzzle*, Phys. Rev. Lett. **56**, 1305 (1986).

[74] A. Y. Smirnov, *Neutrino Mass and New Physics*, J. Phys. Conf. Ser. **53**, 44–82 (2006).

[75] A. Bellerive, J. R. Klein, A. B. McDonald, A. J. Noble, and A. W. P. Poon, *The Sudbury Neutrino Observatory*, Nucl. Phys. **B908**, 30–51 (2016).

[76] A. Yu. Smirnov, *Solar neutrinos: Oscillations or No-oscillations?*, arXiv: 1609.02386 [hep-ph] (2016).

[77] S. J. Parke, *Nonadiabatic Level Crossing in Resonant Neutrino Oscillations*, Phys. Rev. Lett. **57**, 1275–1278 (1986).

[78] L. Landau, *Zur Theorie der Energieübertragung. II*, Phys. Z. Sowjetunion **2**, 1–13 (1932).

[79] C. Zener, *Nonadiabatic crossing of energy levels*, Proc. Roy. Soc. Lond. **A137**, 696–702 (1932).

[80] E. C. G. Stückelberg, *Theorie der unelastischen Stösse zwischen Atomen*, Helvetica Physica Acta **5**, 369 (1932).

[81] E. Majorana, *Atomi orientati in campo magnetico variabile*, Il Nuovo Cimento (1924-1942) **9**, 43–50 (1932).

[82] F. D. Giacomo and E. E. Nikitin, *The Majorana formula and the Landau-Zener-Stückelberg treatment of the avoided crossing problem*, Physics-Uspekhi **48**, 515 (2005).

[83] M. T. Keil, G. G. Raffelt, and H.-T. Janka, *Monte Carlo Study of Supernova Neutrino Spectra Formation*, Astrophys. J. **590**, 971 (2003).

[84] H. Duan and A. Friedland, *Self-induced suppression of collective neutrino oscillations in a supernova*, Phys. Rev. Lett. **106**, 091101 (2011).

[85] A. Arcones, H.-T. Janka, and L. Scheck, *Nucleosynthesis-relevant conditions in neutrino-driven supernova outflows. 1. Spherically symmetric hydrodynamic simulations*, Astron. Astrophys. **467**, 1227 (2007).

[86] S. Hannestad, G. G. Raffelt, G. Sigl, and Y. Y. Y. Wong, *Self-induced conversion in dense neutrino gases: Pendulum in flavor space*, Phys. Rev. D **74**, 105010 (2006).

[87] H. Duan, G. M. Fuller, and Y.-Z. Qian, *Collective neutrino flavor transformation in supernovae*, Phys. Rev. D **74**, 123004 (2006).

[88] G. M. Fuller, R. W. Mayle, J. R. Wilson, and D. N. Schramm, *Resonant neutrino oscillations and stellar collapse*, Astrophys. J. **322**, 795–803 (1987).

[89] E. G. Flowers and P. G. Sutherland, *Neutrino Neutrino Scattering and Supernovae*, Astrophys. J. **208**, L19–L21 (1976).

[90] J. Pantaleone, *Dirac neutrinos in dense matter*, Phys. Rev. D **46**, 510–523 (1992).

[91] Y.-Z. Qian and G. M. Fuller, *Neutrino-neutrino scattering and matter-enhanced neutrino flavor transformation in supernovae*, Phys. Rev. D **51**, 1479–1494 (1995).

[92] G. Sigl and G. Raffelt, *General kinetic description of relativistic mixed neutrinos*, Nucl. Phys. B **406**, 423–451 (1993).

[93] S. Samuel, *Neutrino oscillations in dense neutrino gases*, Phys. Rev. D **48**, 1462–1477 (1993).

[94] W. Nolting, *Grundkurs Theoretische Physik 7: Viel-Teilchen-Theorie*, 7th ed. (Springer-Verlag, Berlin Heidelberg, 2009).

[95] J. Pantaleone, *Dirac neutrinos in dense matter*, Phys. Rev. D **46**, 510–523 (1992).

[96] L. E. Reichl, *A Modern Course in Statistical Physics* (Edward Arnold, London, 1980).

[97] H. Haug, *Statistische Physik. Gleichgewichtstheorie und Kinetik.* 2nd. ed. (Springer-Verlag, Berlin Heidelberg New York, 2006).

[98] E. Wigner, *On the Quantum Correction For Thermodynamic Equilibrium*, Phys. Rev. **40**, 749–759 (1932).

[99] P. Strack and A. Burrows, *Generalized Boltzmann formalism for oscillating neutrinos*, Phys. Rev. **D71**, 093004 (2005).

[100] R. F. Sawyer, *Neutrino oscillations in inhomogeneous matter*, Phys. Rev. **D42**, 3908–3917 (1990).

[101] B. Dasgupta, A. Dighe, A. Mirizzi, and G. Raffelt, *Collective neutrino oscillations in nonspherical geometry*, Phys. Rev. D **78**, 033014 (2008).

[102] C. Volpe, D. Väänänen, and C. Espinoza, *Extended evolution equations for neutrino propagation in astrophysical and cosmological environments*, Phys. Rev. D **87**, 113010 (2013).

[103] A. Vlasenko, G. M. Fuller, and V. Cirigliano, *Neutrino quantum kinetics*, Phys. Rev. D **89**, 105004 (2014).

[104] J. Serreau and C. Volpe, *Neutrino-antineutrino correlations in dense anisotropic media*, Phys. Rev. D **90**, 125040 (2014).

[105] V. Cirigliano, G. M. Fuller, and A. Vlasenko, *A new spin on neutrino quantum kinetics*, Phys. Lett. B **747**, 27–35 (2015).

[106] A. Kartavtsev, G. Raffelt, and H. Vogel, *Neutrino propagation in media: Flavor-, helicity-, and pair correlations*, Phys. Rev. **D91**, 125020 (2015).

[107] C. Volpe, *Neutrino quantum kinetic equations*, Int. J. Mod. Phys. E **24**, 1541009 (2015).

[108] J. F. Cherry, J. Carlson, A. Friedland, G. M. Fuller, and A. Vlasenko, *Neutrino scattering and flavor transformation in supernovae*, Phys. Rev. Lett. **108**, 261104 (2012).

[109] A. B. Balantekin and Y. Pehlivan, *Neutrino-Neutrino Interactions and Flavor Mixing in Dense Matter*, J. Phys. **G34**, 47–66 (2007).

[110] Y.-Z. Qian and G. M. Fuller, *Neutrino-neutrino scattering and matter-enhanced neutrino flavor transformation in supernovae*, Phys. Rev. D **51**, 1479–1494 (1995).

[111] G. M. Fuller and Y.-Z. Qian, *Simultaneous flavor transformation of neutrinos and antineutrinos with dominant potentials from neutrino-neutrino forward scattering*, Phys. Rev. D **73**, 023004 (2006).

[112] H. Duan, G. M. Fuller, J. Carlson, and Y.-Z. Qian, *Simulation of coherent nonlinear neutrino flavor transformation in the supernova environment: Correlated neutrino trajectories*, Phys. Rev. D **74**, 105014 (2006).

[113] G. L. Fogli, E. Lisi, A. Marrone, and A. Mirizzi, *Collective neutrino flavor transitions in supernovae and the role of trajectory averaging*, JCAP **0712**, 010 (2007).

[114] B. Dasgupta, A. Dighe, G. G. Raffelt, and A. Y. Smirnov, *Multiple spectral splits of supernova neutrinos*, Phys. Rev. Lett. **103**, 051105 (2009).

[115] G. Raffelt, S. Sarikas, and D. d. S. Seixas, *Axial symmetry breaking in self-induced flavor conversion of supernova neutrino fluxes*, Phys. Rev. Lett. **111**, 091101 (2013).

[116] G. Raffelt and D. d. S. Seixas, *Neutrino flavor pendulum in both mass hierarchies*, Phys. Rev. D **88**, 045031 (2013).

[117] A. Mirizzi, *Multi-azimuthal-angle effects in self-induced supernova neutrino flavor conversions without axial symmetry*, Phys. Rev. D **88**, 073004 (2013).

[118] H. Duan, G. M. Fuller, and Y.-Z. Qian, *Collective Neutrino Oscillations*, Annual Review of Nuclear and Particle Science **60**, 569–594 (2010).

[119] H. Duan, *Collective Neutrino Oscillations*, Talk held at the International Summer School on AstroComputing 2014: Neutrino & Nuclear Astrophysics, July 21 - August 1 2014, San Diego Supercomputing Center, University of California, San Diego (2014).

[120] I. Tamborra, F. Hanke, H.-T. Janka, B. Müller, G. G. Raffelt, and A. Marek, *Self-sustained asymmetry of lepton-number emission: A new phenomenon during the supernova shock-accretion phase in three dimensions*, Astrophys. J. **792**, 96 (2014).

[121] I. Tamborra, G. Raffelt, F. Hanke, H.-T. Janka, and B. Müller, *Neutrino emission characteristics and detection opportunities based on three-dimensional supernova simulations*, Phys. Rev. **D90**, 045032 (2014).

[122] A. Mirizzi, *Breaking the symmetries in self-induced flavor conversions of neutrino beams from a ring*, Phys. Rev. D **92**, 105020 (2015).

[123] G. Mangano, A. Mirizzi, and N. Saviano, *Damping the neutrino flavor pendulum by breaking homogeneity*, Phys. Rev. D **89**, 073017 (2014).

[124] H. Duan and S. Shalgar, *Flavor instabilities in the neutrino line model*, Phys. Lett. B **747**, 139–143 (2015).

[125] S. Abbar and H. Duan, *Neutrino flavor instabilities in a time-dependent supernova model*, Phys. Lett. B **751**, 43–47 (2015).

[126] B. Dasgupta and A. Mirizzi, *Temporal instability enables neutrino flavor conversions deep inside supernovae*, Phys. Rev. D **92**, 125030 (2015).

[127] H. Duan, *Collective neutrino oscillations and spontaneous symmetry breaking*, Int. J. Mod. Phys. E **24**, 1541008 (2015).

[128] S. Chakraborty, R. Hansen, I. Izaguirre, and G. Raffelt, *Collective neutrino flavor conversion: Recent developments*, Nucl. Phys. **B908**, 366–381 (2016).

[129] B. W. Carroll and D. A. Ostlie, *An Introduction to Modern Astrophysics*, 2nd ed. (Pearson Education, Inc., 2007).

[130] W. Baade and F. Zwicky, *On super-novae*, Proceedings of the National Academy of Sciences **20**, 254–259 (1934).

[131] W. Baade and F. Zwicky, *Remarks on Super-Novae and Cosmic Rays*, Phys. Rev. **46**, 76–77 (1934).

[132] A. Mirizzi, I. Tamborra, H.-T. Janka, N. Saviano, K. Scholberg, R. Bollig, L. Hudepohl, and S. Chakraborty, *Supernova Neutrinos: Production, Oscillations and Detection*, Riv. Nuovo Cim. **39**, 1–112 (2016).

[133] H. A. Bethe, *Supernova mechanisms*, Rev. Mod. Phys. **62**, 801–866 (1990).

[134] H. T. Janka, F. Hanke, L. Huedepohl, A. Marek, B. Mueller, and M. Obergaulinger, *Core-Collapse Supernovae: Reflections and Directions*, Progress of Theoretical and Experimental Physics **2012**, 01A309 (2012).

[135] K. Kotake, T. Takiwaki, Y. Suwa, W. I. Nakano, S. Kawagoe, Y. Masada, and S.-i. Fujimoto, *Multimessengers from core-collapse supernovae: multidimensionality as a key to bridge theory and observation*, Adv. Astron. **2012**, 428757 (2012).

[136] H.-T. Janka, T. Melson, and A. Summa, *Physics of Core-Collapse Supernovae in Three Dimensions: a Sneak Preview*, Ann. Rev. Nucl. Part. Sci. **66**, 341–375 (2016).

[137] J. F. Cherry Jr., *Neutrino Flavor Transformation in Core-Collapse Supernovae*, PhD thesis, University of California, San Diego, 2012.

[138] S. Chakraborty, T. Fischer, A. Mirizzi, N. Saviano, and R. Tomàs, *Analysis of matter suppression in collective neutrino oscillations during the supernova accretion phase*, Phys. Rev. D **84**, 025002 (2011).

[139] L. Bento, *Instabilities in neutrino plasma density waves*, Phys. Rev. **D63**, 077302 (2001).

[140] H. Duan and A. Friedland, *Self-Induced Suppression of Collective Neutrino Oscillations in a Supernova*, Phys. Rev. Lett. **106**, 091101 (2011).

[141] A. Esteban-Pretel, S. Pastor, R. Tomàs, G. G. Raffelt, and G. Sigl, *Decoherence in supernova neutrino transformations suppressed by deleptonization*, Phys. Rev. D **76**, 125018 (2007).

[142] G. M. Fuller and Y.-Z. Qian, *Simultaneous flavor transformation of neutrinos and antineutrinos with dominant potentials from neutrino-neutrino forward scattering*, Phys. Rev. D **73**, 023004 (2006).

[143] G. G. Raffelt, M. T. Keil, R. Buras, H.-T. Janka, and M. Rampp, *Supernova neutrinos: Flavor-dependent fluxes and spectra*, in Neutrino oscillations and their origin. Proceedings, 4th International Workshop, NOON2003, Kanazawa, Japan, February 10-14, 2003, edited by Y. Suzuki, M. Nakahata, Y. Itow, M. Shiozawa, and Y. Obayashi (World Scientific Publishing Co. Pte. Ltd., 2004).

[144] G. G. Raffelt, *Neutrinos and the stars*, in Proceedings, International School of Physics "Enrico Fermi", 182nd Course, "Neutrino Physics and Astrophysics": Varenna, Italy, July 25-August 5, 2011, Vol. 182 (2012).

[145] B. Dasgupta, A. Mirizzi, I. Tamborra, and R. Tomàs, *Neutrino mass hierarchy and three-flavor spectral splits of supernova neutrinos*, Phys. Rev. D **81**, 093008 (2010).

[146] S. Sarikas, I. Tamborra, G. Raffelt, L. Hüdepohl, and H.-T. Janka, *Supernova neutrino halo and the suppression of self-induced flavor conversion*, Phys. Rev. D **85**, 113007 (2012).

[147] S. Pastor, G. Raffelt, and D. V. Semikoz, *Physics of synchronized neutrino oscillations caused by self-interactions*, Phys. Rev. D **65**, 053011 (2002).

[148] V. A. Kostelecký and S. Samuel, *Neutrino oscillations in the early universe with an inverted neutrino mass hierarchy*, Phys. Lett. **B318**, 127–133 (1993).

[149] V. A. Kostelecký and S. Samuel, *Selfmaintained coherent oscillations in dense neutrino gases*, Phys. Rev. **D52**, 621–627 (1995).

[150] V. A. Kostelecký and S. Samuel, *Neutrino oscillations in the early universe with nonequilibrium neutrino distributions*, Phys. Rev. **D52**, 3184–3201 (1995).

[151] H. Duan, G. M. Fuller, and Y.-Z. Qian, *A Simple Picture for Neutrino Flavor Transformation in Supernovae*, Phys. Rev. **D76**, 085013 (2007).

[152] H. Duan, G. M. Fuller, J. Carlson, and Y.-Z. Qian, *Analysis of collective neutrino flavor transformation in supernovae*, Phys. Rev. D **75**, 125005 (2007).

[153] S. Hannestad, G. G. Raffelt, G. Sigl, and Y. Y. Y. Wong, *Self-induced conversion in dense neutrino gases: Pendulum in flavor space*, Phys. Rev. D **74**, 105010 (2006).

[154] G. Fogli, E. Lisi, A. Marrone, and I. Tamborra, *Supernova neutrinos and antineutrinos: Ternary luminosity diagram and spectral split patterns*, JCAP **0910**, 002 (2009).

[155] R. F. Sawyer, *The multi-angle instability in dense neutrino systems*, Phys. Rev. **D79**, 105003 (2009).

[156] A. Banerjee, A. Dighe, and G. Raffelt, *Linearized flavor-stability analysis of dense neutrino streams*, Phys. Rev. **D84**, 053013 (2011).

[157] D. Väänänen and C. Volpe, *Linearizing neutrino evolution equations including neutrino-antineutrino pairing correlations*, Phys. Rev. **D88**, 065003 (2013).

[158] S. Galais, J. Kneller, and C. Volpe, *The neutrino-neutrino interaction effects in supernovae: the point of view from the matter basis*, J. Phys. **G39**, 035201 (2012).

[159] G. G. Raffelt and A. Yu. Smirnov, *Adiabaticity and spectral splits in collective neutrino transformations*, Phys. Rev. **D76**, 125008 (2007).

[160] S. Galais and C. Volpe, *The neutrino spectral split in core-collapse supernovae: a magnetic resonance phenomenon*, Phys. Rev. **D84**, 085005 (2011).

[161] Y. Suwa, K. Kotake, T. Takiwaki, M. Liebendörfer, and K. Sato, *Impacts of Collective Neutrino Oscillations on Core-collapse Supernova Explosions*, The Astrophysical Journal **738**, 165 (2011).

[162] A. Esteban-Pretel, A. Mirizzi, S. Pastor, R. Tomàs, G. G. Raffelt, P. D. Serpico, and G. Sigl, *Role of dense matter in collective supernova neutrino transformations*, Phys. Rev. D **78**, 085012 (2008).

[163] H. Duan, G. M. Fuller, and Y.-Z. Qian, *Symmetries in collective neutrino oscillations*, J.Phys. **G36**, 105003 (2009).

[164] B. Dasgupta and A. Dighe, *Collective three-flavor oscillations of supernova neutrinos*, Phys. Rev. **D77**, 113002 (2008).

[165] A. Friedland, *Self-Refraction of Supernova Neutrinos: Mixed Spectra and Three-Flavor Instabilities*, Phys. Rev. Lett. **104**, 191102 (2010).

[166] G. G. Raffelt and G. Sigl, *Self-induced decoherence in dense neutrino gases*, Phys. Rev. D **75**, 083002 (2007).

[167] S. Chakraborty, T. Fischer, A. Mirizzi, N. Saviano, and R. Tomas, *No collective neutrino flavor conversions during the supernova accretion phase*, Phys. Rev. Lett. **107**, 151101 (2011).

[168] B. Dasgupta, E. P. O'Connor, and C. D. Ott, *The Role of Collective Neutrino Flavor Oscillations in Core-Collapse Supernova Shock Revival*, Phys. Rev. **D85**, 065008 (2012).

[169] S. Sarikas, G. G. Raffelt, L. Hudepohl, and H.-T. Janka, *Suppression of Self-Induced Flavor Conversion in the Supernova Accretion Phase*, Phys. Rev. Lett. **108**, 061101 (2012).

[170] S. Chakraborty, A. Mirizzi, N. Saviano, and D. d. S. Seixas, *Suppression of the multi-azimuthal-angle instability in dense neutrino gas during supernova accretion phase*, Phys. Rev. **D89**, 093001 (2014).

[171] C. Cohen-Tannoudji, B. Diu, and F. Laloë, *Quantenmechanik. Band 1.* 3rd ed. (Walter De Gruyter GmbH & Co KG, Berlin, 2007).

[172] H. J. Weber and G. B. Arfken, *Essential Mathematical Methods for Physicists* (Harcourt/Academic Press, 2003).

[173] A. Malkus, J. P. Kneller, G. C. McLaughlin, and R. Surman, *Neutrino oscillations above black hole accretion disks: Disks with electron-flavor emission*, Phys. Rev. D **86**, 085015 (2012).

[174] A. Malkus, A. Friedland, and G. C. McLaughlin, *Matter-Neutrino Resonance Above Merging Compact Objects*, arXiv: 1403.5797 [hep-ph] (2014).

[175] A. Malkus, G. C. McLaughlin, and R. Surman, *Symmetric and standard matter neutrino resonances above merging compact objects*, Phys. Rev. D **93**, 045021 (2016).

[176] Y.-L. Zhu, A. Perego, and G. C. McLaughlin, *Matter Neutrino Resonance Transitions above a Neutron Star Merger Remnant*, Phys. Rev. **D94**, 105006 (2016).

[177] M.-R. Wu, H. Duan, and Y.-Z. Qian, *Physics of neutrino flavor transformation through matter-neutrino resonances*, Phys. Lett. B **752**, 89–94 (2016).

[178] D. Väänänen and G. C. McLaughlin, *Uncovering the matter-neutrino resonance*, Phys. Rev. D **93**, 105044 (2016).

[179] B. P. Abbott et al., *Observation of gravitational waves from a binary black hole merger*, Phys. Rev. Lett. **116**, 061102 (2016).

[180] B. Paczynski, *Gamma-ray bursters at cosmological distances*, ApJ **308**, L43–L46 (1986).

[181] E. Nakar, *Short-Hard Gamma-Ray Bursts*, Phys. Rept. **442**, 166–236 (2007).

[182] B. Pontecorvo, *Neutrino Experiments and the Problem of Conservation of Leptonic Charge*, Sov. Phys. JETP **26**, 984–988 (1968), Zh. Eksp. Teor. Fiz.53,1717(1967).

[183] Y. Fukuda et al., *Evidence for oscillation of atmospheric neutrinos*, Phys. Rev. Lett. **81**, 1562–1567 (1998).

[184] Q. R. Ahmad et al., *Direct evidence for neutrino flavor transformation from neutral-current interactions in the sudbury neutrino observatory*, Phys. Rev. Lett. **89**, 011301 (2002).

[185] L. Wolfenstein, *Neutrino oscillations in matter*, Phys. Rev. D **17**, 2369–2374 (1978).

[186] G. M. Fuller, R. W. Mayle, J. R. Wilson, and D. N. Schramm, *Resonant neutrino oscillations and stellar collapse*, Astrophys. J. **322**, 795–803 (1987).

[187] J. Pantaleone, *Neutrino oscillations at high densities*, Phys. Lett. B **287**, 128–132 (1992).

[188] A. Vlasenko, G. M. Fuller, and V. Cirigliano, *Prospects for Neutrino-Antineutrino Transformation in Astrophysical Environments*, arXiv: 1406.6724 [astro-ph.HE] (2014).

[189] M.-R. Wu, G. Martinez-Pinedo, and Y.-Z. Qian, *Linking neutrino oscillations to the nucleosynthesis of elements*, EPJ Web Conf. **109**, 06005 (2016).

[190] C. J. Stapleford, D. J. Väänänen, J. P. Kneller, G. C. McLaughlin, and B. T. Shapiro, *Nonstandard Neutrino Interactions in Supernovae*, Phys. Rev. **D94**, 093007 (2016).

[191] T. W. Baumgarte, S. L. Shapiro, and M. Shibata, *On the maximum mass of differentially rotating neutron stars*, Astrophys. J. **528**, L29 (2000).

[192] J. D. Kaplan, C. D. Ott, E. P. O'Connor, K. Kiuchi, L. Roberts, and M. Duez, *The Influence of Thermal Pressure on Equilibrium Models of Hypermassive Neutron Star Merger Remnants*, Astrophys. J. **790**, 19 (2014).

[193] A. Perego, R. M. Cabezón, and R. Käppeli, *An Advanced Leakage Scheme for Neutrino Treatment in Astrophysical Simulations*, Astrophys. J. Suppl. **223**, 22, 22 (2016).

[194] R. C. Duncan, S. L. Shapiro, and I. Wasserman, *Neutrino-driven winds from young, hot neutron stars*, ApJ **309**, 141–160 (1986).

[195] Y. Z. Qian and S. E. Woosley, *Nucleosynthesis in neutrino driven winds: 1. The Physical conditions*, Astrophys. J. **471**, 331–351 (1996).

[196] O. Just, A. Bauswein, R. A. Pulpillo, S. Goriely, and H.-T. Janka, *Comprehensive nucleosynthesis analysis for ejecta of compact binary mergers*, MNRAS **448**, 541–567 (2015).

[197] B. D. Metzger and R. Fernández, *Red or blue? A potential kilonova imprint of the delay until black hole formation following a neutron star merger*, Mon. Not. Roy. Astron. Soc. **441**, 3444–3453 (2014).

[198] L. Dessart, C. Ott, A. Burrows, S. Rosswog, and E. Livne, *Neutrino signatures and the neutrino-driven wind in Binary Neutron Star Mergers*, Astrophys. J. **690**, 1681 (2009).

[199] R. Surman, G. C. McLaughlin, M. Ruffert, H. T. Janka, and W. R. Hix, *r-Process Nucleosynthesis in Hot Accretion Disk Flows from Black Hole - Neutron Star Mergers*, Astrophys. J. **679**, L117–L120 (2008).

[200] A. Burrows, S. Reddy, and T. A. Thompson, *Neutrino opacities in nuclear matter*, Nucl. Phys. A **777**, 356–394 (2006).

[201] A. Perego, E. Gafton, R. Cabezón, S. Rosswog, and M. Liebendörfer, *MODA: a new algorithm to compute optical depths in multidimensional hydrodynamic simulations*, A&A **568**, A11 (2014).

[202] G. G. Raffelt, *Mu- and Tau-Neutrino Spectra Formation in Supernovae*, Astrophys. J. **561**, 890 (2001).

[203] B. Dasgupta, A. Dighe, A. Mirizzi, and G. Raffelt, *Collective neutrino oscillations in nonspherical geometry*, Phys. Rev. D **78**, 033014 (2008).

[204] S. Sarikas, D. de Sousa Seixas, and G. Raffelt, *Spurious instabilities in multiangle simulations of collective flavor conversion*, Phys. Rev. D **86**, 125020 (2012).

[205] D. Martin, A. Perego, A. Arcones, F.-K. Thielemann, O. Korobkin, and S. Rosswog, *Neutrino-driven Winds in the Aftermath of a Neutron Star Merger: Nucleosynthesis and Electromagnetic Transients*, ApJ **813**, 2 (2015).

[206] X. Qian and P. Vogel, *Neutrino mass hierarchy*, Prog. Part. Nuc. Phys. **83**, 1–30 (2015).

[207] O. Just, M. Obergaulinger, H.-T. Janka, A. Bauswein, and N. Schwarz, *Neutron-star Merger Ejecta as Obstacles to Neutrino-powered Jets of Gamma-Ray Bursts*, ApJ **816**, L30 (2016).

[208] S. Pastor and G. Raffelt, *Flavor oscillations in the supernova hot bubble region: Nonlinear effects of neutrino background*, Phys. Rev. Lett. **89**, 191101 (2002).

[209] Y. Y. Y. Wong, *Analytical treatment of neutrino asymmetry equilibration from flavor oscillations in the early universe*, Phys. Rev. **D66**, 025015 (2002).

[210] K. N. Abazajian, J. F. Beacom, and N. F. Bell, *Stringent constraints on cosmological neutrino anti-neutrino asymmetries from synchronized flavor transformation*, Phys. Rev. **D66**, 013008 (2002).

[211] Y. Sekiguchi, K. Kiuchi, K. Kyutoku, and M. Shibata, *Dynamical mass ejection from binary neutron star mergers: radiation-hydrodynamics study in general relativity*, Phys. Rev. D **91**, 064059 (2015).

[212] F. Foucart, R. Haas, M. D. Duez, E. O'Connor, C. D. Ott, L. Roberts, L. E. Kidder, J. Lippuner, H. P. Pfeiffer, and M. A. Scheel, *Low mass binary neutron star mergers : gravitational waves and neutrino emission*, Phys. Rev. **D93**, 044019 (2016).

[213] J. H. Christenson, J. W. Cronin, V. L. Fitch, and R. Turlay, *Evidence for the 2π Decay of the K_2^0 Meson*, Phys. Rev. Lett. **13**, 138–140 (1964).

[214] A. D. Sakharov, *Violation of CP Invariance, C Asymmetry, and Baryon Asymmetry of the Universe*, Pisma Zh. Eksp. Teor. Fiz. **5**, 32–35 (1967), Sov. Phys. JETP Lett. **5**, 24 (1967).

[215] L. Canetti, M. Drewes, and M. Shaposhnikov, *Matter and Antimatter in the Universe*, New J. Phys. **14**, 095012 (2012).

[216] C. Jarlskog, *Commutator of the Quark Mass Matrices in the Standard Electroweak Model and a Measure of Maximal CP Violation*, Phys. Rev. Lett. **55**, 1039 (1985).

[217] C. Jarlskog, *A Basis Independent Formulation of the Connection Between Quark Mass Matrices, CP Violation and Experiment*, Z. Phys. **C29**, 491–497 (1985).

[218] L.-L. Chau and W.-Y. Keung, *Comments on the Parametrization of the Kobayashi-Maskawa Matrix*, Phys. Rev. Lett. **53**, 1802 (1984).

[219] D.-d. Wu, *The Rephasing Invariants and CP*, Phys. Rev. **D33**, 860 (1986).

[220] N. Cabibbo, *Unitary Symmetry and Leptonic Decays*, Phys. Rev. Lett. **10**, 531–533 (1963).

[221] M. Kobayashi and T. Maskawa, *CP Violation in the Renormalizable Theory of Weak Interaction*, Prog. Theor. Phys. **49**, 652–657 (1973).

[222] E. Zeidler, ed., *Springer-Handbuch der Mathematik I: Begründet von I.N. Bronstein und K.A. Semendjaew, weitergeführt von G. Grosche, V. Ziegler und D. Ziegler, herausgegeben von E. Zeidler*, Springer-Handbuch der Mathematik (Springer Fachmedien Wiesbaden, 2013).

[223] Z.-z. Xing, *Flavor mixing and CP violation of massive neutrinos*, Int. J. Mod. Phys. **A19**, 1–80 (2004).

[224] R. Streater and A. Wightman, *PCT, spin and statistics, and all that*, Mathematical physics monograph series (W.A. Benjamin, 1964).

[225] S. Pakvasa, *CPT and Lorentz violations in neutrino oscillations*, in Proceedings of the Second Meeting on CPT and Lorentz symmetry, Bloomington, USA, Aug 15-18, 2001, edited by V. A. Kostelecký (World Scientific Publishing Co. Pte. Ltd., 2002).

[226] E. K. Akhmedov, *Neutrino oscillations beyond two flavours*, Nuclear Physics B - Proceedings Supplements **118**, edited by F. von Feilitzsch and N. Schmitz, 245–254 (Elsevier Science B.V., 2003).

[227] M. Jacobson and T. Ohlsson, *Extrinsic CPT violation in neutrino oscillations in matter*, Phys. Rev. **D69**, 013003 (2004).

[228] A. B. Balantekin, J. Gava, and C. Volpe, *Possible CP-Violation effects in core-collapse Supernovae*, Phys. Lett. **B662**, 396–404 (2008).

[229] J. Gava and C. Volpe, *Collective neutrinos oscillation in matter and CP-violation*, Phys. Rev. **D78**, 083007 (2008).

[230] F. J. Botella, C. S. Lim, and W. J. Marciano, *Radiative Corrections to Neutrino Indices of Refraction*, Phys. Rev. **D35**, 896 (1987).

[231] A. de Gouvea and S. Shalgar, *Transition Magnetic Moments and Collective Neutrino Oscillations:Three-Flavor Effects and Detectability*, JCAP **1304**, 018 (2013).

[232] A. Mirizzi, S. Pozzorini, G. G. Raffelt, and P. D. Serpico, *Flavour-dependent radiative correction to neutrino-neutrino refraction*, JHEP **10**, 020 (2009).

[233] R. F. Sawyer, *Neutrino cloud instabilities just above the neutrino sphere of a supernova*, Phys. Rev. Lett. **116**, 081101 (2016).

[234] O. L. Caballero, G. C. McLaughlin, and R. Surman, *Neutrino Spectra from Accretion Disks: Neutrino General Relativistic Effects and the Consequences for Nucleosynthesis*, Astrophys. J. **745**, 170 (2012).

[235] J. D. Jackson, *Classical Electrodynamics*, 3rd ed. (John Wiley & Sons, Inc., New York, London, Sydney, 1999).

[236] S. Weinberg, *Lectures on Quantum Mechanics* (Cambridge University Press, 2013).

[237] E. Zeidler, *Quantum Field Theory I, Basics in Mathematics and Physics, a Bridge Between Mathematicians and Physicists* (Springer-Verlag, Berlin/Heidelberg/New York, 2006).

[238] E. Zeidler, *Quantum Field Theory II, Quantum Electrodynamics, a Bridge Between Mathematicians and Physicists* (Springer-Verlag, Berlin/Heidelberg/New York, 2009).

[239] B. R. Holstein, *Topics in Advanced Quantum Mechanics* (Addison-Wesley Pub Co, 1992).

[240] J. J. Sakurai, *Advanced Quantum Mechanics* (Addison Wesley Pub Co Inc, 1967).

[241] L. Wolfenstein and K. Lande, *Solar neutrinos*, in Symmetries and Fundamental Interactions in Nuclei, edited by Haxton, W. C. and Henley, E. M. (World Scientific Publishing Co. Pte. Ltd., 1995).

[242] M. L. Goldberger and K. M. Watson, *Collision Theory* (John Wiley & Sons, Inc., New York, London, Sydney, 1964).

[243] W. von Sellmeier, *Zur Erklärung der abnormen Farbenfolge im Spectrum einiger Substanzen*, Annalen der Physik **219**, 272–282 (1871).

[244] Strutt, J.W., *XV. On the light from the sky, its polarization and colour*, Philosophical Magazine Series 4 **41**, 107–120 (1871).

[245] J. Strutt, *XXXIV. On the transmission of light through an atmosphere containing small particles in suspension, and on the origin of the blue of the sky*, Philosophical Magazine Series 5 **47**, 375–384 (1899).

[246] R. Landau, *Quantum Mechanics: A Second Course in Quantum Theory*, 2nd. ed. (WILEY-VCH Verlag GmbH & Co. KGaA, Weinheim, 2004).

[247] L. Landau and E. Lifshitz, *Course of Theoretical Physics Vol. 3. Quantum Mechanics: Non-Relativistic Theory.* 3rd ed. (Pergamon Press, 1977).

[248] M. E. Peskin and D. V. Schroeder, *An Introdcution to Quantum Field Theory* (Westview Press, 1995).

[249] S. Weinberg, *The Quantum Theory of Fields. Volume I: Foundations* (Cambridge University Press, 1995).

[250] F. Boehm and P. Vogel, *Physics of Massive Neutrinos*, 2nd ed. (Cambridge University Press, 1992).

[251] P. Langacker and J. Liu, *Standard model contributions to the neutrino index of refraction in the early Universe*, Phys. Rev. D **46**, 4140–4160 (1992).

[252] M.-R. Wu, private communication (2015).

[253] F. W. J. Olver, D. W. Lozier, R. F. Boisvert, and C. W. Clark, eds., *NIST Handbook of Mathematical Functions* (Cambridge University Press, New York, NY, 2010).

[254] M. Ruffert, H. T. Janka, K. Takahashi, and G. Schaefer, *Coalescing neutron stars: A Step towards physical models. 2. Neutrino emission, neutron tori, and gamma-ray bursts*, Astron. Astrophys. **319**, 122–153 (1997).

[255] S. Rosswog and M. Liebendörfer, *High-resolution calculations of merging neutron stars - ii. neutrino emission*, Mont. Not. R. Astron. Soc. **342**, 673–689 (2003).

[256] S. Rosswog, T. Piran, and E. Nakar, *The multimessenger picture of compact object encounters: binary mergers versus dynamical collisions*, Mon. Not. Roy. Astron. Soc. **430**, 2585 (2013).

[257] G. B. Rybicki and A. P. Lightman, *Radiative Processes in Astrophysics* (Wiley-VCH Verlag GmbH & Co. KGaA, Weinheim, 2004).

[258] A. Perego, private communication (2016).

CURRICULUM VITAE

Maik Uwe Frensel

Hauptstrasse 51   Phone: +49 7622 9140
79689 Maulburg (Germany)   E-Mail: Maik.Frensel@gmail.com
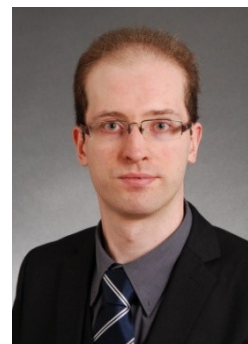
PERSONAL DATA

Date and place of birth	15.03.1986 in Schopfheim (Germany)
Nationality	German, Swiss

EDUCATION

10/2011-12/2016	**PhD IN THEORETICAL PHYSICS** at University of Basel **Grade: SUMMA CUM LAUDE** Advisor: Prof. Dr. Friedrich-Karl Thielemann Title: *"Aspects of neutrino flavor propagation in binary neutron star merger remnants"*
08/2008-02/2010	**MASTER OF SCIENCE (M.SC.) IN PHYSICS,** **Grade: 6.0 ("excellent")** Advisors: PD Dr. Andreas Aste and Prof. Dr. Dirk Trautmann Master thesis title: *"Massless loop diagrams within the framework of causal perturbation theory"*
10/2005-07/2008	**BACHELOR OF SCIENCE (B.SC.) IN PHYSICS,** **Grade: 5.4 ("good")** Bachelor studies of physics at University of Basel
09/2002-06/2005	**ABITUR** **with distinction. Grade: 1.3 ("very good")** Technisches Gymnasium at Gewerbeschule Lörrach (Germany) with focus on information technology

WORK EXPERIENCE

09/2012-12/2016	Teaching assistant at Institute of Physics, University of Basel
	Tutoring mathematical methods in particle physics and occasional lecturing
01/2002-12/2016	Management assistant at IBC-Frensel (Informations-, Beratungs- und Ausbildungscenter für Arbeitssicherheit und Flurförderzeuge), Maulburg
	Main tasks: Writing of measurement reports, risk assessments, safety instructions for operating machines and handling hazardous materials, preparation of courses and safety briefings, solving individual client problems (technical and legal questions), written correspondence
09/2001-12/2008	Development and maintenance of the website of the municipality Maulburg

TEACHING

Ausgewählte Kapitel der theoretischen Teilchenphysik	(Autumn semester 2012)
Symmetrien und Felder	(Fall semester 2013)
Mathematische Methoden der Teilchenphysik	(Autumn semester 2013)
Symmetrien, Teilchen und Felder	(Fall semester 2014)
Mathematische Methoden der Teilchenphysik	(Autumn semester 2014)
Symmetrien, Teilchen und Felder	(Fall semester 2015)
Mathematische Methoden der Teilchenphysik	(Autumn semester 2015)
Co-supervision of master studies semester project	(Fall semester 2016)
Mathematische Methoden der Teilchenphysik	(Autumn semester 2016)

AWARDS

Teaching award "Goldener Korrekturstift" for best tutor, awarded by the student council "Fachgruppe 14" (autumn semester 2012, 2013, 2016 and fall semester 2014).

IT-Skills

Programming languages	Java, Fortran, Python, C/C++
Parallele Programmierung	OpenMP (shared memory)
	Message Passing Interface (MPI) (distributed memory)
Software Engineering	Unified Model Language (UML),
	Entity-relationship model (ER model)
Computer algebra systems	Maple, Mathematica, Matlab
Databases	MySQL
Web development	HTML, JavaScript, Adobe Flash
Office tools	Microsoft Office: Word, Excel, PowerPoint, Access
Image manipulation tools	Adobe Photoshop, Gimp
Operating systems	Unix-like operating systems, Microsoft Windows

Language Skills

German (native)	English (fluent)	French (basic knowledge)

Publications and Preprints

2017   Maik Frensel, Meng-Ru Wu, Cristina Volpe und Albino Perego:
"*Neutrino Flavor Evolution in Binary Neutron Star Merger Remnants*"
Physical Review **D** 95, 023011 (2017)

2015   Andreas Aste und Maik Frensel:
"Localization properties and causality aspects of massless and massive scalar particles"
arXiv:1510.05106 [hep-th]

Meetings, Conferences, Workshops, Schools

29. September - 01. October 2016
Brainstorming and Fun: Compact objects, their equation of state, related explosive events, and their nucleosynthesis
Workshop; Basel

18. - 20. July 2016
Discussion meeting with Dr. Cristina Volpe
Université Paris Diderot-Paris 7, Laboratoire APC, Paris

04. - 09. July 2016
Poster: "Neutrino flavor evolution in a binary neutron star merger remnant"
Neutrino 2016: XXVII International Conference on Neutrino Physics and Astrophysics,
Royal Geographical Society, London

04. - 05. February 2015
Discussion meeting with Dr. Cristina Volpe
Université Paris Diderot-Paris 7, Laboratoire APC, Paris

---

10. - 11. Dezember 2015
Discussion meeting with Dr. Meng-Ru Wu
Technische Universität Darmstadt, Institut für Kernphysik Theorie-Zentrum S2|11, Schlossgartenstrasse 2, Darmstadt

---

12. - 13. November 2015
Discussion meeting with Dr. Cristina Volpe
Université Paris Diderot-Paris 7, Laboratoire APC, Paris

---

27. September - 02. October 2015
Discussion meeting with Dr. Cristina Volpe
Université Paris Diderot-Paris 7, Laboratoire APC, Paris

---

27. - 31. July 2015
Talk (held on 31. June)
Discussion meeting with Dr. Meng-Ru Wu
Technische Universität Darmstadt, Institut für Kernphysik Theorie-Zentrum S2|11, Schlossgartenstrasse 2, Darmstadt

---

22. - 26. June 2015
Discussion meeting with Dr. Cristina Volpe
Université Paris Diderot-Paris 7, Laboratoire APC, Paris

---

29. - 30. September 2014
Brainstorming and Fun: Stellar Evolution/Explosions, Nuclear/Particle Physics Input
Origin of the Elements and Evolution of Galaxies
Conference; Basel

---

10. - 12. July 2014
Neutrinos in Astro- and Particle Physics (NIAPP) Topical Workshop
Max Planck Institute for Astrophysics and Munich Institute for Astro- and Particle Physics, Garching near Munich

---

16. - 24. September 2013
International School of Nuclear Physics, 35th Course, Neutrino Physics: Present and Future
Ettore Majorana Foundation and Centre for Scientific Culture, Erice

---

08. - 19. July 2013
CSCS-USI Summer School on Computer Simulations in Science and Engineering
Swiss National Supercomputing Centre and University of Lugano

---

16. November 2012
MASCHE Annual Meeting
EuroGENESIS workshop; Goethe University Frankfurt

---

27. - 28. September 2012
Brainstorming and Fun: Nuclear Input, Stellar Simulations, Explosions, Remnants
Chemical Evolution, Observational Constraints
Conference; Basel

During my studies I heard lectures by the following people:

Prof. Dr. Thomas Vetter, Prof. Dr. Ben Schweizer, Prof. Dr. Ernst Meyer, Prof. Dr. Hanspeter Kraft, Prof. Dr. Christian Schönenberger, PD Dr. Mihai Halic, Prof. Dr. Assyr Abdulle, Prof. Dr. Heiko Schuldt, PD Dr. Andreas Aste, Prof. Dr. Dirk Trautmann, Prof. Dr. Hans-Josef Hug, Prof. Dr. Bruno Binggeli, PD Dr. Christoph Luchsinger, PD Dr. Franz-Josef Elmer, Prof. Dr. Friedrich-Karl Thielemann, Prof. Dr. Dominik Zumbühl, Dr. Alexey Neelov, Prof. Dr. Christoph Bruder, Prof. Dr. Bernd Krusche, Prof. Dr. Helmar Burkhart, Prof. Dr. Volker Dittmann, Prof. Dr. Daniel Loss, PD Dr. Ahmad A. Hujeirat, PD Dr. Annette A'Campo-Neuen, Prof. Dr. Gerhard Baur, Dr. Giordano Favi, lic. phil. Philipp Zimmermann